Institute of Experimental Pharmacology and Toxicology
Center for Experimental Medicine
University Medical Center Hamburg Eppendorf

Evaluation of cGMP-driven post-translational microtubule modifications in human cardiomyocytes

Dissertation

Submitted to the
Department of Chemistry
Faculty of Mathematics, Informatics and Natural Sciences
University of Hamburg
in partial fulfillment of the requirements
for the degree of
Doctor of Natural Sciences (Dr. rer. nat.)

by

Moritz Meyer-Jens

Hamburg, October 2025

Reviewers of written thesis:
1st Prof. Dr. Hartmut Schlüter
2nd Prof. Dr. Lucie Carrier

Disputation committee members:
1st Prof. Dr. Hartmut Schlüter
2nd Prof. Dr. Wolfram Brune
3rd Prof. Dr. Friederike Cuello

Disputation: 12th of December 2025
Print approval: 24th of May 2026

The experimental work for this thesis was performed from April 2022 until October 2025 at the Institute for Experimental Pharmacology and Toxicology (Director Prof. Dr. Thomas Eschenhagen) under the direct supervision of Prof. Dr. Lucie Carrier.

List of Publications

1. Alizoti, E., Ewald, L., Parretta, S., **Meyer-Jens, M.**, Orthey, E., Conze, C., Carrier, L., Robbins, J., & Singh, S. R. (2024). Ruxolitinib clears CRYAB p.Arg120Gly aggregates through the ubiquitin-proteasome system. bioRxiv 2024.10.11.615348; doi: https://doi.org/10.1101/2024.10.11.615348
2. Kliesow Remes, A., Ruf, T., Zurashvili, T., Ding, L., **Meyer-Jens, M.**, Schwab, D. M., Hille, S., Matzen, A., Michalewski, S., Kilian, L., Shetty, P. M. V., Fuchs, M. C., Eden, M., Gröne, H. J., Rapti, K., Jungmann, A., Milting, H., Katus, H. A., Carrier, L., Müller, O. J. (2025). AAV-mediated overexpression of CPT1B protects from cardiac hypertrophy and heart failure in a murine pressure overload model. Bas Res Cardiol, 120:975-989. https://doi.org/10.1007/s00395-025-01123-y
3. **Meyer-Jens, M.**, Wenzel, K., Grube, K., Rüdebusch, J., Krämer, E., Bahls, M., Müller, K., Voß, H., Schlüter, H., Felix, S. B., Carrier, L., Könemann, S., & Schlossarek, S. (2024). Sacubitril/valsartan reduces proteasome activation and cardiomyocyte area in an experimental mouse model of hypertrophy. Journal of Molecular and Cellular Cardiology Plus, 7, 100059. https://doi.org/10.1016/J.JMCCPL.2023.100059
4. Singh, S. R., **Meyer-Jens, M.**, Alizoti, E., Bacon, W. C., Davis, G., Osinska, H., Gulick, J., Reischmann-Düsener, S., Orthey, E., McLendon, P. M., Molkentin, J. D., Schlossarek, S., Robbins, J., & Carrier, L. (2021). A high-throughput screening identifies ZNF418 as a novel regulator of the ubiquitin-proteasome system and autophagy-lysosomal pathway. Autophagy, 17(10), 3124–3139. https://doi.org/10.1080/15548627.2020.1856493
5. Zech, A. T. L., Prondzynski, M., Singh, S. R., Pietsch, N., Orthey, E., Alizoti, E., Busch, J., Madsen, A., Behrens, C. S., **Meyer-Jens, M.**, Mearini, G., Lemoine, M. D., Krämer, E., Mosqueira, D., Virdi, S., Indenbirken, D., Depke, M., Salazar, M. G., Völker, U., Carrier, L. (2022). ACTN2 Mutant Causes Proteopathy in Human iPSC-Derived Cardiomyocytes. Cells, 11(17), 1–17. https://doi.org/10.3390/cells11172745

Table of contents

List of abbreviations

A	alanine
A-band	Anisotropic band
ACE	angiotensin converting enzyme
ACM	arrhythmogenic cardiomyopathy
ACTA1	skeletal alpha actin 1
ACTB	beta actinin
ACTN1	actinin alpha 1
ACTN2	alpha actinin 2
ACTN4	actinin alpha 4
ac-tub	acetylated tubulin
ADP	adenosine diphosphate
Adv-cGi500	cGi500 encoding adenovirus
AI	autoinhibitory
Alk EpoY	alkaline EpoY
AMVM	adult mouse ventricular myocytes
Ang(II)	angiotensin(II)
ANKRD1	ankyrin D1
ANP/NPPA	A-type natriuretic peptide
AP	Action potential
ARNI	angiotensin receptor neprilysin inhibitor
ARVM	adult rat ventricular myocytes
AT1R	angiotensin 1 receptor
ATP	adenosine triphosphate
ATP1B4	ATPase Na+/K+ Transporting Family Member Beta 4
AURKB	aurora B kinase
BMP10	bone morphogenic protein 10
BMP4	bone morphogenic protein 4
BNP/NPPB	B-type natriuretic peptide
bp	base pair
BPM	beats per minute
BSA	bovine serum albumin
BTS	N-Benzyl-Toluensulfonamide
BW	body weight
Ca	calcium
CALM1	calmodulin 1
CAPN2	calpain 2
Cas	CRISPR-associated nuclease

CASQ2	calsequestrin 2
CD	core domain
cDNA	complementary DNA
CENPF	centromere protein F
CENPM	centromere protein M
CENPU	centromere protein U
CFP	cyan fluorescent protein
cGMP	cyclic guanosine monophosphate
CM	cardiomyocyte
C-MYC	proto-oncogene c-Myc
CNB-A/B	cyclic nucleotide binding domain A/B
CNP	C-type natriuretic peptide
CO_2	carbon dioxide
CRISPR	clustered regularly interspaced palindromic repeats
CRMP2	collapsin response mediator protein 2
CRYAB	alpha B-Crystallin
CSF	colony stimulating factor
CSRP3	cysteine and glycine rich protein 3
Ct	C-terminal
CTGF	connective tissue growth factor
cTnT	cardiac troponin T
Ctrl.	control
d	day
DCM	dilated cardiomyopathy
ddH_2O	double-distilled water
DES	desmin
DKK1	dickkopf wnt signaling pathway inhibitor 1
DMSO	dimethylsulfoxide
DNA	desoxyribonucleic acid
DSB	double strand breaks
DTT	dithiothreitol
dTyr-tub	detyrosinated tubulin
E	glutamate
EB	embryoid bodies
EF	ejection fraction
EHT	engineered heart tissue
E_m	Membrane potential
ESC	embryonic stem cells
ESRRB	estrogen related receptor beta
ET1	endothelin 1
etc.	et cetera

ETS2	ETS proto-oncogen 2 transcription factor
FACS	fluorescent assisted cell sorting
FCS	fetal calf serum
FGF	fibroblast growth factor
FHL	four and a half LIM domain
FL	full length
FLNA	filamin A
FLNB	filamin B
FLNC	filamin C
FRET	Förster resonance electron transfer
FTDA+	FTDA with Y
FTDA++	FTDA with FGF and Y
GAPDH	glyceraldehyde-3-phosphade dehydrogenase
GATA4	GATA binding protein 4
gDNA	genomic DNA
GDP	guanosine diphosphate
GO	gene ontology
crRNA	guide RNA
GSK3B	glycogen synthase kinase 3 B
GTP	guanosine triphosphate
h	hour
H	Hydrogen
HBSS	Hank's buffered saline solution
HCM	hypertrophic cardiomyopathy
HDR	homology directed repair
HF	heart failure
HFmrEF	heart failure with mildly reduced ejection fraction
HFpEF	heart failure with preserved ejection fraction
HFrEF	heart failure with reduced ejection fraction
hiPSC-CMs	hiPSC-derived CMs
hiPSCs	human induced pluripotent stem cells
HRP	horse radish peroxidase
HS	horse serum
HW	heart weight
Hz	Hertz
I-band	Isotropic band
IBMX	3-Isobutyl-1-methylxanthin
I_{ca}	Inward calcium current
IGF	insulin like growth factor
ISL1	ISL LIM homeobox 1
Iso	isoproterenol

K40	lysine 40
kb	kilobase
KD	knockdown
KIF14	kinesin family member 14
KIF18A	kinesin family member 18A
KIF1C	kinesin family member 1C
KIF20A	kinesin family member 20 A
KLF4	krüppel-like factor 4
KO	knockout
KY	KY02111
LAD	left anterior descending coronary artery
LTCC	L-type calcium channel
LZ	leucine zipper
M	molar
MAP	microtubule associated protein
MAP1B	microtubule associated protein 1 B
MAP4	microtubule associated protein 4
MATCAP1	microtubule associated tyrosine carboxypeptidase 1
M-band	Middle band
MEF2C	myocyte enhancer factor 2 C
MESP1	mesoderm posterior BHLH transcription factor 1
MHC head	Myosin heavy chain head
MI	myocardial infarction
mio	milllion
MLC binding domain	Myosin light chain binding domain
MM	maturation medium
MME	neprilysin
mrtf-a	myocardin related transcription factor A
MS	mass spectrometry analysis
ms	millisecond
MT	microtubule
MTOC	microtubule organizing center
mTORC1	mechanistic target of rapamycin complex 1
MW	molecular weight
MYBPC3/MyBP-C	Myosin binding protein C3
MYH11	myosin heavy chain 11
MYH6	myosin heavy chain 6
MYH7	myosin heavy chain 7
MCD	myocardin
MYOM3	myomesin 3
Na	sodium

NaCl	sodium chloride
NaF	sodium fluoride
Nanog	Nanog homeobox
NCX	Sodium calcium exchanger
NF	non failing
NFAT	calcineurin-nuclear factor of activated T-cells
NHEJ	non homologous end joining
NKM	non-cardiomyocyte medium
NO	nitric oxide
NODAL	growth differentiation factor nodal
NP	natriuretic peptide
NPR	NP receptor
NRAP	nebulin-related anchoring protein
NRG1	neuregulin 1
NRVM	neonatal rat ventricular myocytes
Nt	N-terminal
Nt-proBNP	N-terminal prohormone brain NP
O_2	oxygen
OBSCN	obscurin
OCT	octamer-binding transcription factor
OE	overexpression
O/N	overnight
OT	off target
P/S	penicillin/streptomycin
PAM	protospacer adjacent motif
PBS	phosphate buffered saline
PCR	polymerase chain reaction
PDE	phosphodiesterase
PE	phenylephrine
pGC	particulate guanylate cyclase
PKA	protein kinase A
PLN/PLB	phospholamban
PRKG	protein kinase G
PSTN	periostin
PTM	post-translational modification
pVASP	phosphorylated VASP
RAAS	renin angiotensin aldosterone system
RCM	restrictive cardiomyopathy
RFP WT	red fluorescent protein-tagged tubulin A 1 B WT cell line
RNA	ribonucleic acid

RNAseq	RNA sequencing
RNP	ribonucleoprotein
RP8	Rp-8-Br-PET-cGMPs
rpm	revolutions per minute
RT	room temperature
RT	relaxation time
-RT	negative control without reverse transcriptase
RT-qPCR	reverse transcription quantitative PCR
RYR2	ryanodine receptor 2
sac	sacubitrilat
sacval	sacubitrilat/valsartan
scr	scrambled
SDS	sodium dodecyl sulfate
SEM	standard error of the mean
SERCA2	sarcoplasmic reticulum calcium ATPase
sGC	soluble guanylate cyclase
SGLT2	sodium glucose cotransporter 2
siRNA	small interfering RNA
SOX2	SRY-box transcription factor 2
SSEA3	stage specific antigen 3
STAT3	signal transducer and activator of transcription 3
SVBP	small vasohibin-binding protein
TA	tranexamic acid
TAC	transverse aortic constriction
TALEN	TAL effector nucleases
TBS-T	tris-buffered saline with Tween20
TBX	T-box transcription factor
TCAP	titin cap
TGFß	transforming growth factor ß
TL	tibia length
TnC	Troponin C
TnI	Troponin I
TNNI3	troponin I 3, cardiac type
TNNT2/TnT	troponin T 2, cardiac type
TRPC6	transient potential canonical 6
TSC2	tuberous sclerosis 2
TTL	tubulin tyrosine ligase
TTN	titin
TTP	time to peak
TUBA4A	tubulin alpha 4A
Tyr-tub	tyrosinated tubulin

US	United States
V	volt
val	valsartan
VASH1/2	vasohibin 1/2
VASHi	VASH inhibitor
VASP	vasodilator-stimulated phosphoprotein
VIM	vimentin
Wnt3a	WNT family member 3A
WT	Wild-type
XAV	XAV-939
XIRP2	xin repeat protein 2
Y	Y-27632
YAP	YES-associated protein
YFP	yellow fluorescent protein
ZFN	zinc finger
ZSF1	hybrid of the zucker diabetic fatty rat and the spontaneously hypertensive heart failure rat
α-Tub	alpha tubulin
β-Tub	beta tubulin
Δ2Tub	delta2 tubulin

List of figures

List of tables

Abstract

Increased microtubule detyrosination is a hallmark of heart failure and has been consistently observed in various *in vitro* and *in vivo* models. As heart failure prevalence rises worldwide, understanding the disease mechanisms and developing new therapeutic options are needed. Previous studies showed that reducing microtubule detyrosination improved cardiomyocyte contractility (Caporizzo et al., 2020; C. Y. Chen et al., 2020; Eaton et al., 2023; Robison et al., 2016). The heart failure drug LCZ696 (sacubitril/valsartan) outperforms standard therapy, but its effect on microtubule detyrosination/re-tyrosination has not been explored.

The main aim of my PhD Thesis was therefore to evaluate the impact of LCZ696 *in vitro* and to decipher the cellular pathway involved.

We established an endothelin 1-induced hypertrophy model with human induced pluripotent stem cell-derived cardiomyocytes (hiPSC-CMs). These cells exhibited a twofold increase in cell area and volume and a >1-5-fold increase in microtubule detyrosination, alongside typical transcriptomic and proteomic alterations. Cellular hypertrophy was prevented by sacubitrilat (sac), valsartan (val) or the combination of both, but only sac alone prevented the molecular and detyrosination changes. Reduction in microtubule detyrosination was also measured in mice subjected to transverse aortic constriction treated with LCZ696.

We hypothesized that sac reduced microtubule detyrosination via the cGMP-PRKG1 signaling. PRKG1 knockdown or inhibition increased detyrosination in hiPSC-CMs, while natriuretic peptides and sac activated PRKG1, indicated by VASP phosphorylation at serine 239. In hiPSC-CMs lacking the ability to re-tyrosinate microtubules, atrial natriuretic peptide increased microtubule tyrosination, suggesting PRKG1 inhibits the detyrosinase vasohibin 1 (VASH1) by phosphorylation. A VASH inhibitor produced the same effect, supporting the mechanism. Collaborators identified seven potential PRKG1A phosphorylation sites in the VASH1 C-terminus. Mutation of these sites to mimic phosphorylation reduced enzyme activity after transduction in VASH1-deficient hiPSC-CMs.

Since hiPSC-CMs deficient in vasohibin activity still exhibited about 20% of microtubule detyrosination (Pietsch et al., 2024), the last part of this PhD thesis was to assess the role of the newly identified detyrosinase MATCAP1. We successfully established a MATCAP1-deficient hiPSC line, which passed all implied quality control steps. In hiPSC-derived 2D culture of CMs or 3D engineered heart tissues, MACAP1 knockout caused extensive proteomic changes affecting structural and metabolic pathways and reduction in microtubule detyrosination in the EHTs.

Overall, our results show that microtubule detyrosination is a key driver of cardiomyocyte hypertrophy and highlight cGMP-PRKG1 pathway as a potential therapeutic target to improve heart failure outcome.

Zusammenfassung

Die erhöhte Detyrosinierung ist ein Kennzeichen verschiedener Formen der Herzinsuffizienz. Dies wurde in verschiedenen *in vitro* und *in vivo* Modellen dieser Pathologie beschrieben. Angesichts der weltweit zunehmenden Prävalenz der Herzinsuffizienz ist ein Verständnis der zugrundeliegenden Mechanismen sowie die Entwicklung neuer therapeutischer Ansätze von großer Bedeutung. Frühere Studien zeigten, dass eine Reduktion der Detyrosinierung von Mikrotubuli die Kontraktilität von Kardiomyocaten verbessert (Caporizzo et al., 2020; C. Y. Chen et al., 2020; Eaton et al., 2023; Robison et al., 2016). Das klinisch wirksame Herzinsuffizienzmedikament LCZ696 (Sacubitril/Valsartan) zeigte sich der Standardtherapie überlegen, jedoch wurde sein Einfluss auf die Mikrotubuli Detyrosinierung und Re-Tyrosinierung bislang nicht untersucht.

Das Hauptziel dieser Dissertation war daher, die Wirkung von LCZ696 *in vitro* zu evaluieren und den zugrundeliegenden zellulären Signalweg zu verstehen.

Hierzu wurde ein Endothelin-1-basiertes Hypertrophiemodell mit humanen, aus induzierten pluripotenten Stammzellen abgeleiteten Kardiomyocyten (hiPSC-CMs) etabliert. Diese Zellen zeigten eine etwa zweifache Zunahme von Zellfläche und - volumen sowie eine 1,5-fache Zunahme der Detyrosinierung von Mikrotubuli, begleitet von typischen transkriptomischen und proteomischen Veränderungen. Die Hypertrophie wurde sowohl durch Sacubitrilat (sac), Valsartan als auch deren Kombination verhindert, jedoch konnte nur sac die molekularen Veränderungen und die erhöhte Detyrosinierung verhindern. Eine derartige Reduktion der Mikrotubuli-Detyrosinierung wurde ebenfallls in Mäusen nach transversaler Aortenkonstriktion (TAC) unter LCZ696 Behandlung beobachtet.

Wir postulieren, dass sac die Detyrosinierung der Mikrotubuli durch eine Aktivierung des cGMP-PRKG1-Signalwegs reduziert. Tatsächlich führte die hemung oder der Knockdown von PRKG1 zu einer Zunahme der Detyrosinierung, während natriuretische Peptide und sac PRKG1 aktivierten. Dies wurde durch eine erhöhte Phosphorylierung von VASP an Serin-239 belegt. In hiPSCs, denen die Fähigkeit zur Re-Tyrosinierung fehlte, erhöhte das atriale natriuretische Peptid (ANP) den

Tyrosinierungsgrad, was darauf hindeutet, dass PRKG1 die Detyrosinase Vasohibin 1 (VASH1) durch Phosphorylierung hemmt. Ein VASH-Inhibitor zeigte den selben Effekt und unterstützte somit den postulierten Mechanismus. Eine Kollaborierende Arbeitsgruppe indentifizierte sieben potenzielle PRKG1A-Phosphorylierungsstellen in der C-terminalen Domäne von VASH1. Die Mutation dieser Aminosäuren zu phosphomimetischen Varianten reuzierte die Enzymaktivität nach Transduktion in VASH1-defizienten hiPSC-CMs.

Da hiPSC-CMs mit fehlender Vasohibin-Aktivität noch etwa 20% Rest-Detyrosinierung aufwiesen (Pietsch et al., 2024), untersuchte der letzte Teil dieser Arbeit die Rolle der neu identifizierten Detyrosinase MATCAP1. Wir etablierten erfolgreich eine MATCAP1-defiziente hiPSC-Linie, die alle erforderlichen Qualitätskontrollen bestand. In 2D Kulturen und künstlichem 3D Herzmukelgewebe führte diese Defizienz zu weitreichende proteomischen Veränderungen, die sowohl strukturelle als auch metabolische Signalwege betrafen. In den 3D Geweben führte der Knockout außerdem zu einer deutlichen Reduktionn der Detyrosinierung von Mikrotubuli.

Insgesamt zeigten unsere Ergebnisse, dass die Mikrotubuli Detyrosinierung ein zentraler Treiber der Kardiomoyzytenhypertrophie ist und dass der cGMP-PRKG1-Signalweg ein vielversprechendes therapeutisches Ziel zur Verbesserung der Herzinsuffizienz darstellt.

1. Introduction

1.1 Heart failure

Heart failure (HF) represents one of the main health burdens of modern industrialized societies (Murray & Lopez, 2013). The associated direct and indirect costs impose a substantial challenge on the healthcare systems of aging societies (Luengo-Fernandez et al., 2023). It is estimated that HF accounts for economic costs of 108 billion United States (US) Dollars globally (Khan et al., 2024). The following chapter will introduce the different aspects involved and potential treatment and prevention options.

1.1.1 Prevalence, morbidity and mortality for different heart failure types

The global prevalence of heart failure is estimated to exceed 64 million (mio) cases with pronounced regional differences (James et al., 2018). Accurate assessment of the global burden is hampered by limited data availability from less developed regions (**Figure 1**). While the incidence of HF is reported to be stable or even declining, prevalence is increasing among older population groups (Roger, 2021). This trend is compounded by the increase in median age and life expectancy in industrialized countries, overall resulting in a high number of cases (Kontis et al., 2017).

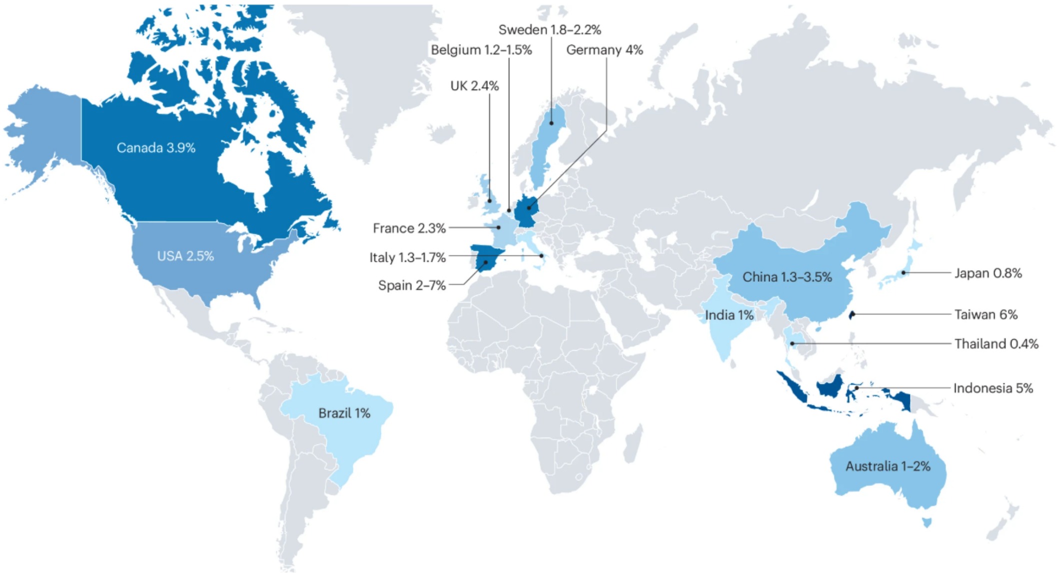

Figure 1: Global prevalence of heart failure.

Percentage of the population suffering from HF in the indicated countries. Lighter blue color represents a lower prevalence, while darker ones indicate higher values. Percentages range from 0.4% (Thailand) to 5% (Indonesia). From: (Khan et al., 2024). Abbreviations: USA, United States of America.

1.1.2 Heart failure phenotypes

HF is defined as a structural and/or functional deficit of the heart, which results in the inability to sufficiently supply the body with oxygenated blood. Ejection fraction (EF) lies at the center of most definitions and is clinically considered for treatment decisions and prognosis (Khan et al., 2022; Lund et al., 2022). Based on EF, three HF subtypes are typically distinguished: HF with reduced EF (HFrEF), HF with mildly reduced EF (HFmrEF), and HF with preserved EF (HFpEF).

HFrEF is classified by an EF of 40% or less. Approximately 23 mio of the 64 mio worldwide HF cases are classified as HFrEF. Patients often experience dyspnea and exercise intolerance. The reduction in EF is commonly accompanied by remodeling especially of the left ventricle. As symptoms are often unspecific, comprehensive diagnostic assessment is needed, including evaluation of electrocardiographic parameters and measurements of plasma natriuretic peptides (NPs; Murphy et al., 2020). Another diagnostic marker that is often employed is the measurement of cardiac troponin I (Felker et al., 2012).

HFmrEF patients, defined by an EF of 40-49%, are more likely to present with ischemic heart disease which makes them more similar to HFrEF than HFpEF (Savarese et al., 2022). Importantly, randomized and controlled trials focused on HFmrEF are lacking (Srivastava et al., 2020).

In contrast to HFrEF and HFmrEF, HFpEF represents a relatively recently defined subtype of HF. Interestingly, HFpEF patients suffer from typical HF symptoms despite an EF >50%. Obesity and diabetes are common comorbidities, explaining the inclusion of body mass index among the diagnostic parameters alongside the use of anti-hypertensive drugs, pulmonary hypertension status, left ventricular filling pressure and age. Based on these parameters, HFpEF can be further sub-divided into four different phenotypes: aging phenotype, obesity phenotype, pulmonary hypertension phenotype and coronary artery disease phenotype (Adamczak et al., 2020).

When comparing outcomes across subtypes, HFrEF has the highest mortality rates, while HFmrEF is intermediate and HFpEF generally has the lowest. Still, the risks of hospitalization and cardiovascular events are especially high in older HFrEF and HFpEF patients with comorbidities. In contrast, the event rate in HFmrEF is lower than in HFrEF but higher than in HFpEF (Yuntao Chen et al., 2021; Pocock et al., 2006; Rich et al., 2018).

Finally, the distribution of HF subtypes shows regional differences. Globally, HFpEF is slightly more prevalent than HFmrEF but in some countries, like the US or Japan, it even surpasses that of HFrEF (**Figure 2**; Khan et al., 2024).

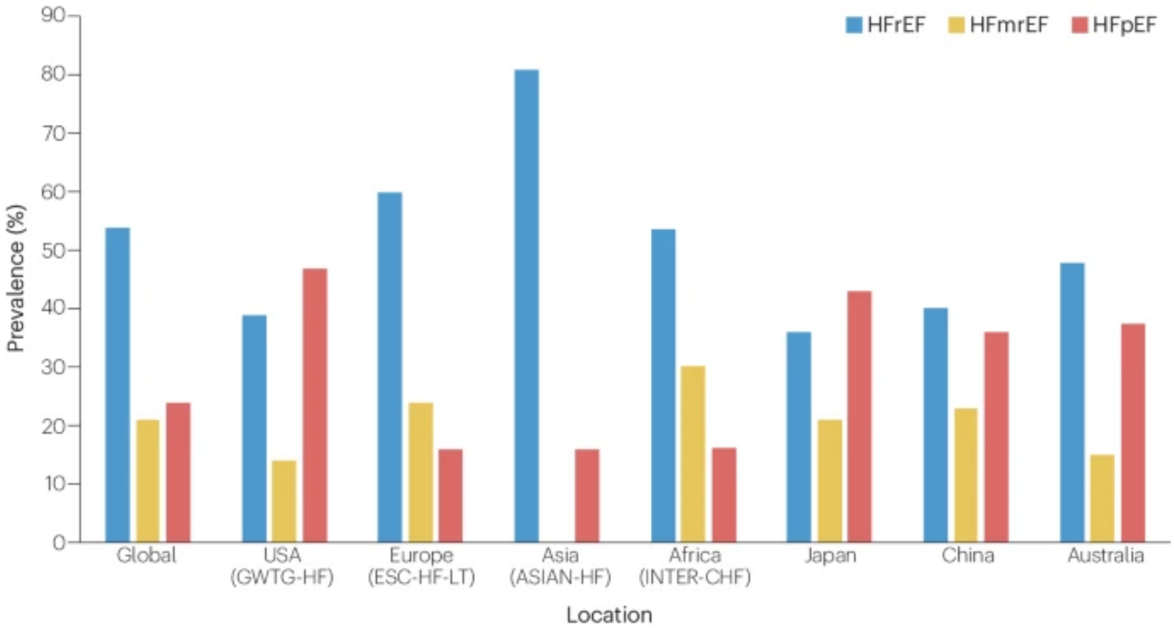

Figure 2: Regional differences in the distribution of heart failure subtypes.
Bar graph of the prevalences of HFrEF (blue), HFmrEF (yellow) and HFpEF (red) globally, in the US, Europe, Asia, Africa, Japan, China and Australia as percentage from overall HF cases. Disease etiologies grouped by geographic area. From: (Khan et al., 2024). Abbreviations: HFmrEF, heart failure with mildly reduced ejection fraction; HFpEF, heart failure with preserved ejedtion fraction; HFrEF, heart failure with reduced ejedtion fraction.

1.1.3 Causes of heart failure

The underlying causes of HF are diverse and multifactorial. A major group corresponds to ischemic factors, including myocardial infarction, chronic coronary artery disease, ischemic mitral regurgitation and microvascular dysfunction. Collectively, these myocardial injuries account for about 70% of HF cases (Del Buono et al., 2022; Grigioni et al., 2005; Heusch, 2022).

Besides that, there are non-ischemic factors like dilated cardiomyopathy (DCM), hypertrophic cardiomyopathy (HCM), restrictive cardiomyopathy (RCM) and arrhythmogenic cardiomyopathy (ACM). DCM, HCM and RCM are frequently driven by genetic variants but may also be attributed to lifestyle factors like to consumption of alcohol or exposure to other toxins like chemotherapeutic drugs, especially in the case of DCM (Seferović et al., 2019).

Pressure overload, often leading to hypertrophy, as well as inflammation and persistent infections can further predispose to HF development (Groenewegen et al., 2020; Heusch, 2022).

Ultimately different lifestyle factors are drivers of HF development and the global HF epidemic. Physical inactivity increases risk for HF, primarily through a reduction of cardiovascular fitness, and increases the likelihood of developing obesity, which promotes both hypertension and cardiac remodeling. Logically, obesity is also closely linked to suboptimal dietary patterns. Moreover, smoking severely increases the HF risk, predominantly by promoting vascular damage and increasing the risk for coronary artery disease (Del Gobbo et al., 2015; Larsson et al., 2016).

1.1.4 Treatment options for heart failure

After outlining the HF causes, it is evident that modifying lifestyle factors, including increased physical exercise and weight loss represent cost-effective strategies to prevent or manage HF in the gross population (Bozkurt, 2024).

In addition to lifestyle modifications, many HF patients receive pharmacological treatment. Classical approaches include renin-angiotensin-aldosterone (RAAS) modulators like angiotensin converting enzyme (ACE) inhibitors or β-blockers. These drugs have pronounced positive effects on survival and decrease hospitalization rates. Patients may also benefit from the use of diuretics to decrease congestion (Rossignol et al., 2019).

For the present study, a relatively novel therapeutic, sacubitril/valsartan (sacval, marketed as Entresto® by Novartis), was of particular interest. This drug combines the ACE inhibitor valsartan (val) with the neprilysin inhibitor sacubitril/sacubitrilat (sac) forming an angiotensin receptor neprilysin inhibitor (ARNI). Mechanistically, val directly blocks the angiotensin-II receptor type 1 (AT1R) which prevents the increase in blood pressure, sympathetic tone and hypertrophy. Meanwhile, sac inhibits the peptidase neprilysin (MME) which, among other proteins, degrades natriuretic peptides (NPs). As a result, sacval simultaneously augments negative effects on blood pressure and sympathetic tone via val and enhances the positive of NP effects on these factors via sac. Importantly, the hydrolysis of N-terminal prohormone brain NP (Nt-proBNP) is not catalyzed by neprilysin, still allowing the diagnostic evaluation of this parameter in HF patients. Besides NPs, MME also degrades other peptides such as endothelin 1 (ET1; Menendez, 2016). PARADIGM-HF was the landmark study demonstrating safety and effectiveness of sacval. During this study, sacval was shown to be superior in preventing hospitalization due to HF and cardiovascular death compared to the standard of care treatment enalapril. Of the included 4187 patients in the sacval group, only 21.8% died from cardiovascular causes within the observation period compared to 26.5% in the enalapril group (McMurray et al., 2014). **Figure 3** outlines the mechanism of action of sacval.

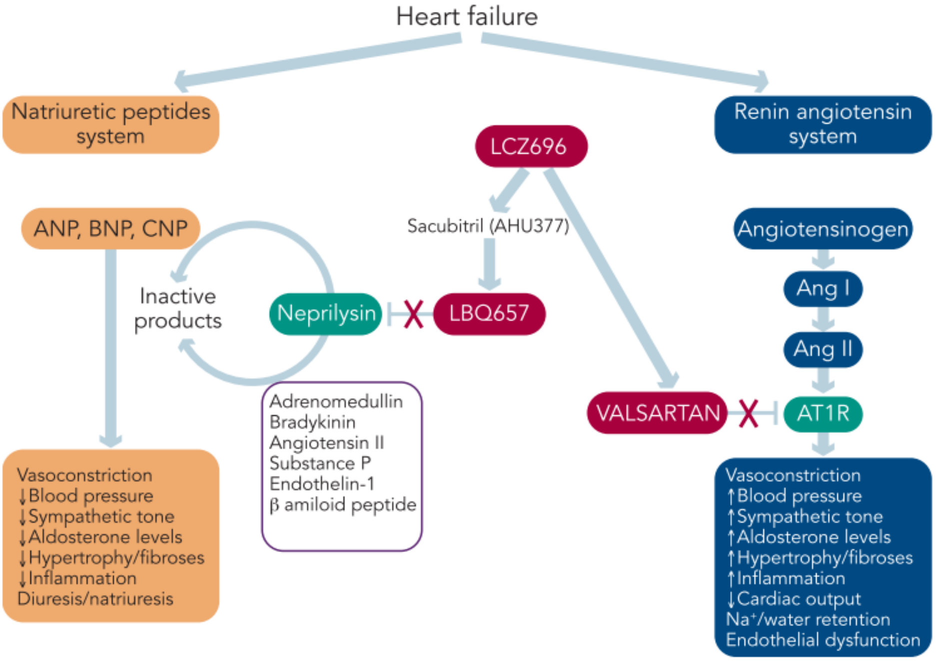

Figure 3: Mechanism of action of sacubitril(at)/valsartan.

HF is characterized by dysregulation in both the NP and RAAS system. LCZ696 (equivalent to sacval) contains two different drugs, sac and val, targeting either one. Through the dual action of sacval, the negative effects of the RAAS system are decreased while the positive effects of the NP system are enhanced. From: (Menendez, 2016). Abbreviations: Ang, angiotensin; ANP, atrial natriuretic peptide; AT1R, angiotensin receptor 1; BNP brain type natriuretic peptide; LBQ657, sacubitrilat; LCZ696, sacubitril/valsartan.

Another target for the treatment of HF, especially HFrEF, is the sodium-glucose cotransporter 2 (SGLT2). SGLT2 inhibitors have more recently gained traction as a therapeutic option for this pathology as they were shown to decrease mortality regardless of the diabetic status of patients (Murphy et al., 2020).

In addition to modification of lifestyle factors and use of pharmacotherapy, implantable devices and other advanced therapies should also be considered for HF treatment. In addition to the already high symptom load, HF patients are also more likely to experience arrhythmias (Masarone et al., 2017). Patients presenting with an EF below 35% might undergo implantation of a cardioverter-defibrillator or cardiac resynchronization therapy. Older patients (>70 years) benefit to a larger extent than younger ones (58-64 years) from the latter. There is no clear evidence for a decrease of mortality in this patient demographic with implanted cardioverter-defibrillators. In late stages of HF, where symptoms become more severe and include hypotension, progressive exercise intolerance and weight loss, positive inotropes can improve patient outcome. In cases where the remaining myocardium becomes progressively unable to supply the body with consistent blood circulation, ventricular assist devices or cardiac transplantation can be considered (E. Liu & Lampert, 2022). Both options are associated with high costs due to the high complexity of such procedures (Patel et al., 2015).

Of the mentioned therapeutic options, RAAS modulators and β-blockers are indicated for the use in HFrEF while their use in HFmrEF can be considered. They are, however, not routinely prescribed in HFpEF. Diuretics are in regular use for all three classes of HF to alleviate disease severity and symptom load. ARNIs are only used in some HFpEF cases while they belong to the recommended drugs for HFrEF and HFmrEF. SGLT2 inhibitors such as empagliflozin are in contrast recommended for all types of HF. As discussed above, implantation of assist devices or heart transplantation are usually guided by EF and therefore primarily reserved for HFrEF patients (Beghini et al., 2025; Shahim et al., 2025). This situation also paints the picture of missing therapy options for HFpEF patients.

Summarizing these points, further research is needed to improve patient care in HF prevention, management and prognosis. This is emphasized by the growing proportion of elderly people in Western societies, who often reach advanced stages of HF and require drastic measures such as heart transplantation but are considered less due to rigorous selection criteria. Therefore, a growing demand of donor organs is met by a restricted supply, creating long waiting list and possibly preventable fatalities (Immohr et al., 2022; Luengo-Fernandez et al., 2023; Ribeiro & de Oliveira, 2022).

1.2 Cardiac sarcomere and excitation contraction coupling

The cardiac sarcomere is the basic contractile subunit of striated muscle cells including in the heart. It is responsible for the contractile properties and therefore for supplying the circulation with oxygenated blood. Multiple sarcomeres aligned in series form a myofibril. Each sarcomere consists of thin (actin) and thick (myosin) filaments. Titin is also part of this structure and spans from the Z-disc, where the sarcomeres are interconnected, to the middle band (M-band). Towards each end of the sarcomere, one can find the isotropic band (I-band), which exclusively contains titin and thin filaments. This sarcomeric sub-structure is compacted during contraction. Contrary to that, the M-band does not contain thin filaments but connects the thick filaments laterally. The anisotropic band (A-band) contains both thin and thick filaments (**Figure 4**; Crocini & Gotthardt, 2021).

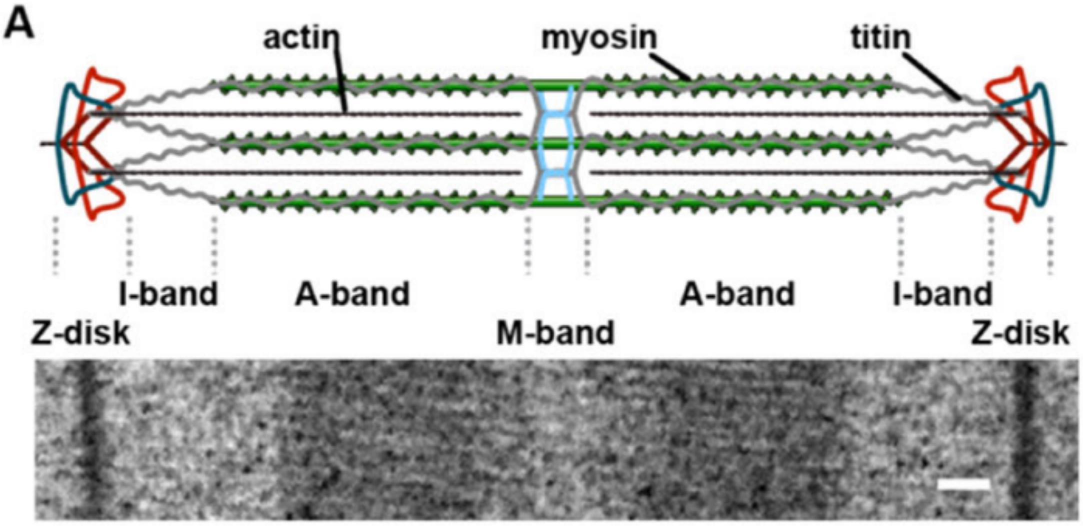

Figure 4: Structure of the cardiac sarcomere.

(Top) Schematic structure and (bottom) structure captured by electron microscopy. The cardiac sarcomere is made up of a plethora of proteins. It is the smallest functional subunit of a (contracting) muscle cell. Among the most important are the thin filament protein actin, the thick filament myosin and the titin protein, which spans half the sarcomere distance. The sarcomere is shortened during contraction. From: (Crocini & Gotthardt, 2021). Abbreviations: A-band, anisotropic band; I-band, isotropic band; M-band middle band.

Genetic variants in sarcomere components such as myosin binding protein C3 (MYBPC3) are among the most frequent causes for HCM and HF (Bonne et al., 1995; Schuldt et al., 2021; Warnecke et al., 2021).

As mentioned, the main purpose of the sarcomere is contraction. A key regulator for this funtion is calcium (Ca^{2+}). Cycling of Ca^{2+} and therefore cardiac contraction is ultimately regulated by electical signaling. The term *excitation-contraction coupling* has been coined for this phenomenon (Bers, 2002; Martin et al., 2022).

For contraction to occur, the first necessary step is depolarization of the cardiomocyte (CM) membrane during action potential propagation. This depolarization causes a Ca^{2+} influx trough voltage-dependent channels but is rather small compared to the Ca^{2+} which is subsequently released from the sarcoplasmic reticulum (SR) through calcium-induced calcium release via the ryanodine receptor 2 (RYR2). The peak concentration of cytoplasmic Ca^{2+} is thought to be around 6 µM. Subsequently, cytosolic Ca^{2+} can then bind to cardiac troponin C, a part of the thin filament (**Figure 5**; Bers, 2002; Eisner et al., 2017; Martin et al., 2022).

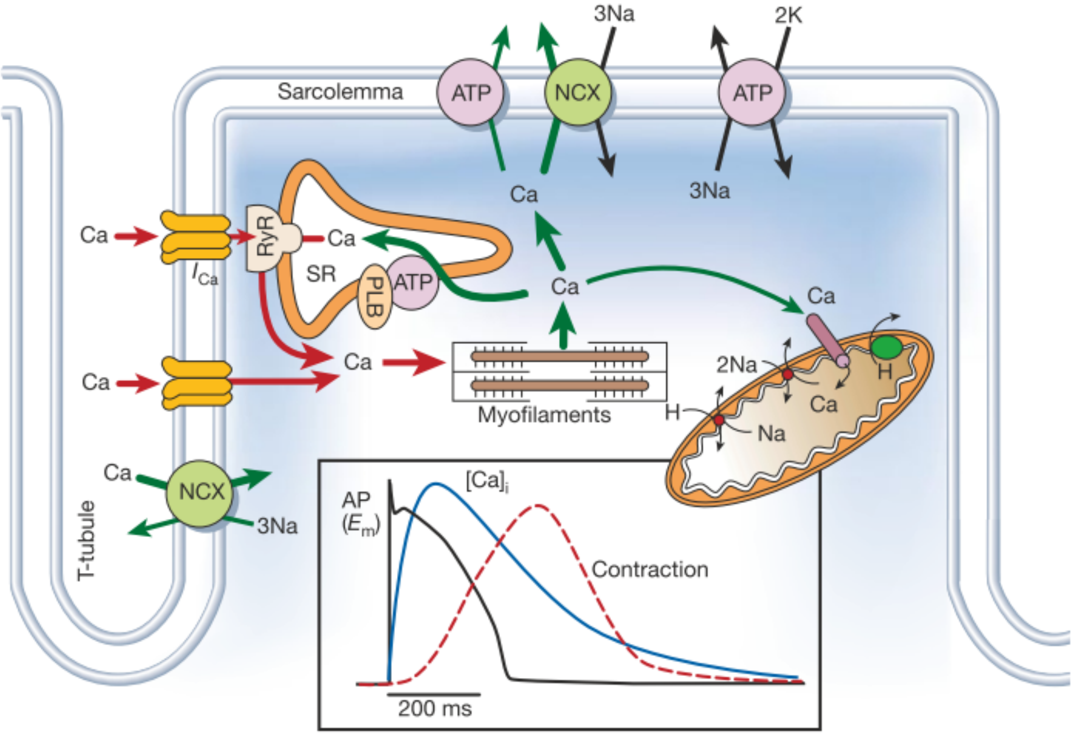

Figure 5: Calcium cycling in cardiomyocytes.

Calcium can enter the cardiomyocytes first after membrane depolarization through voltage dependent calcium channels. Calcium can then trigger further calcium release from the sarcoplasmic reticulum (SR). The elevated cytosolic calcium can then switch on contraction. For termination of contraction, calcium needs to be removed from the cytosol. This can happen via energy-dependent sarcolemmal calcium pumps, exchange of calcium and sodium ions via specialzed membrane proteinsm by transport into the mitochondria or most importantly via sarco(endo)plasmic reticulum Ca2+-ATPase 2 back into the SR. From: (Donald M. Bers, 2002). Abbreviations: AP, action potential; ATP, adenosine triphosphate; Ca, calcium; E_m, membrane potential; H, hydrogen; I_{ca}, inward calcium current; Na, sodium; NCX, sodium/calcium exchanger; PLB, phospholamban; RyR, ryanodine receptor.

Through this binding, troponin C changes its conformation which ultimately leads to the displacement of troponin I and exposition of myosin-binding sites on actin by a conformational change in tropomyosin. Therefore, the myosin heads can bind the actin filaments and contract the sarcomere by performing a pulling motion along the thin filaments (**Figure 6**; Martin et al., 2022). To terminate contraction and allow for relaxation to occur, cytoplasmic Ca^{2+} levels must return to baseline to restore resting membrane potential. In human myocardium, most of the calcium is removed via the sarco(endo)plasmic reticulum Ca^{2+}-ATPase 2 (SERCA2) which resided in the SR membrane. Its activity can be negatively modulated by phospolamban (PLN). In human myocardium, about 28% of the Ca^{2+} required for contraction is removed from the cytosol by the Na^{+}/Ca^{2+} exchanger (Bers, 2002; Eisner et al., 2017; Martin et al., 2022).

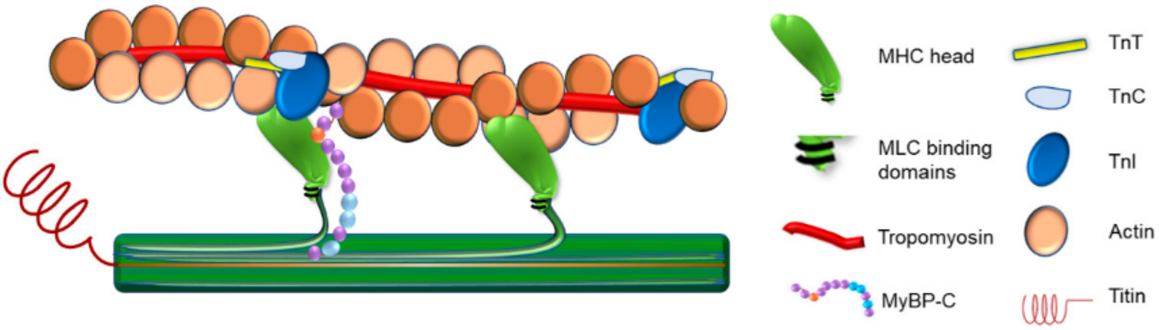

Figure 6: Contraction of the cardiac sarcomere.

Schematic illustration showing the mechanism underlying cardiac contraction. For contraction to occur, calcium needs to bin troponin C (TnC) which changes conformation and removed troponin I (TnI) from its inhibitory state towards tropomyosin. Tropomyosin can then free up myosin binding sites on actin thin filaments, which are bound by myosin heads (MHC heads). These structures then perform a pulling motion of the thick filament along the thin filament to initiate contraction. From: (Martin et al., 2022). Abbreviations: MHC head, myosin heavy chain head; MLC binding domains, myosin light chain binding domains; MyBP-C, myosin-binding protein C; TnC, troponin C; TnI, troponin I; TnT, troponin T.

1.3 Cardiac microtubules

Microtubules (MTs) are cytoskeletal structures present in all cell types independent of their mitotic status (Uchida et al., 2021). The following chapter aims to describe their specific role, their post-translational modifications (PTMs) and the respective enzymes involved.

1.3.1 Structure of cardiac microtubules

MTs are one of the three main types of cytoskeletal filaments. Besides MTs, the cytoskeleton consists of actin and intermediate filaments (Hohmann & Dehghani, 2019). Actin filaments have been found to be central in (cardiac) muscle contraction early after their initial discovery (Huxley & Hanson, 1954).

Like in other cell types, cardiac MTs are hollow, tube-like structures. These tubes most commonly consist of 13 protofilaments. The individual protofilaments are formed by α-(α-tub) and β-tubulin (β-tub) heterodimers (**Figure 7**; Manka & Moores, 2018).

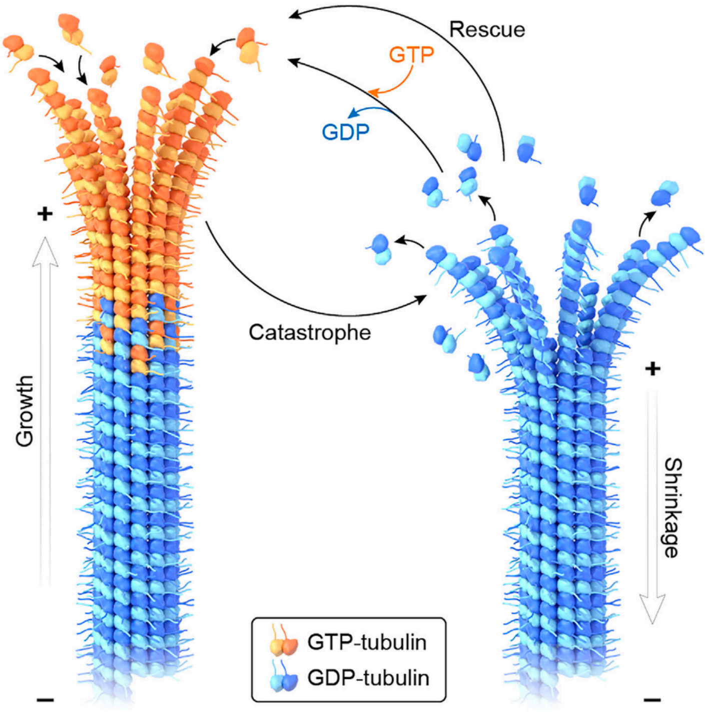

Figure 7: Dynamics of microtubules.

GDP-bound MTs (blue) are less stable and prone to shrinkage/catastrophe beginning at their plus-/cytosolic-end. This process can be rescued by the incorporation of new GTP-bound tubulin heterodimers (orange) at the + end. MTs can only be extended at the + end as the - end is attached to the MTOC. From: (Roll-Mecak, 2020). Abbreviations: GDP, guanosine diphosphate; GTP, guanosine triphosphate; MT, microtubules; MTOC, microtubule organizing center.

The human genome encodes nine isoforms of α-tub and β-tub each (Janke & Magiera, 2020). It is important to note that MTs are polarized structures with a plus and minus end. The minus end is anchored to the microtubule organizing center (MTOC) while the plus-end points away from this structure. In mitotic cells, the MTOC is localized close to the nucleus while CMs have MT with mixed polarity. Polymerization by incorporation of guanosine triphosphate (GTP) bound α-tub/β-tub dimers happens on the plus end. When the GTP bound to β-tub is hydrolyzed to guanosine diphosphate (GDP), the rapid depolarization of the MT filaments, known as *catastrophe*, may occur. This can be stopped by the incorporation of additional GTP-α-tub/β-tub heterodimers (rescue; Roll-Mecak, 2020; Uchida et al., 2021).

MTs are by most known to be the *highways of the cell.* Meaning they serve as the key structure enabling active intracellular transport by motor proteins from the kinesin and dynein families. While the smaller kinesins mostly carry out plus-end directed transport, the larger dyneins usually perform minus end directed transport (Goldstein & Yang, 2000).

MT dynamics are closely tied to post-translational modifications (PTMs) and binding of partners such as microtubule-associated proteins (MAPs). MAP inter-species conservation is much lower than tubulin isoform conservation. MAP expressions can be vastly different between cell and tissue types. Therefore, they are essential for modulating MT function according to the particular surroundings (Kitazawa et al., 2000).

In conjunction with their role in intracellular transport, MTs have recently been directly linked to the development of cardiac growth. In an elegant study, Scarborough and colleagues proved that depolymerizing cardiac MTs with nocodazole leads to perinuclear ribosome and transcript localization (Scarborough et al., 2021). This is especially important as cardiomyocytes (CMs) undergo constant mechanical stress and rely on local translation of structural (e.g. sarcomeric) proteins (Haddad et al., 2024).

1.3.2 Microtubule modifications and modifying enzymes

While being decorated with different MAPs, MTs are also heavily modified post-translationally. The most important PTMs are acetylation, polyglutamylation and detyrosination and are found on the outside of the protofilaments (**Figure 8**). On the contrary, acetylation (ac-tub) of lysine 40 (K40) of α-tub takes place within the MT lumen. The β-tub may also be acetylated. Some lesser researched PTMs include palmitoylation, sumoylation, phosphorylation, polyglycylation and ubiquitinylation (Janke & Magiera, 2020).

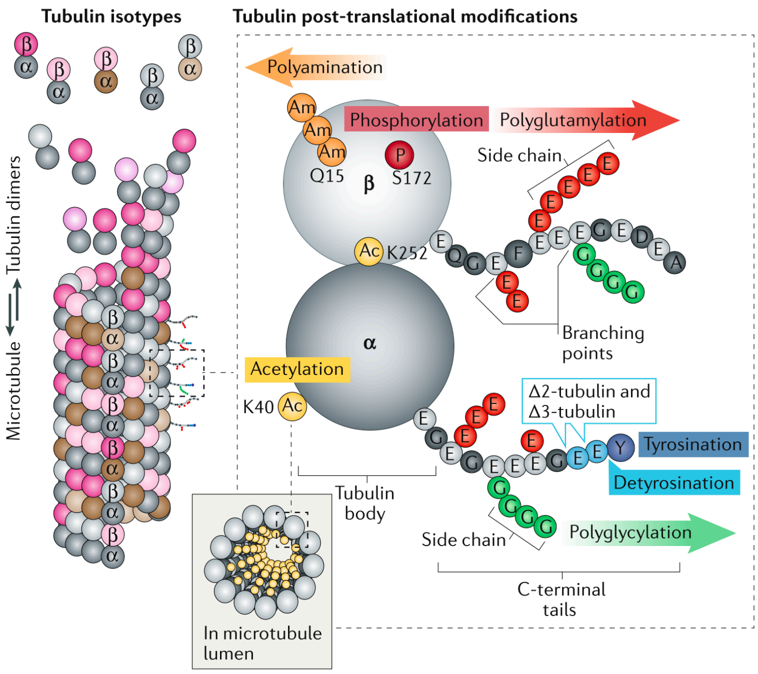

Figure 8: Overview of microtubule post-translational modifications.

Illustration showing the different known MT PTMs. The PTMs are mostly located outside the MT lumen at the C-termini of either α-tub or β-tub. Polyglutamylation and polyglycylation are added as side chains to glutamate residues and can happen on both tubulin isoforms (α/β). Tyr-tub and dTyr-tub are exclusive to the C-terminus of αTub and are both reversible. The further cleavage of dTyr-tub to Δ2tub or Δ3tub is irreversible and creates hyper-stable MT. Acetylation is the only MT PTM that can happen within the lumen. Tubulin bodies can be either acetylated or phosphorylated at different sites. The mixture of the different MT PTMs creates the *so-called* tubulin *code*. From: (Janke & Magiera, 2020). Abbreviations: Ac, acetylation; Am, amine; dTyr-tub, tubulin detyrosination; MT, microtubule; P, phosphorylation; PTM, post-translational modification; Tyr-tub, tubulin tyrosination.

In CMs, the most relevant MT PTM is the detyrosination (dTyr-tub) and re-tyrosination (Tyr-tub) of α-tub. The dTyr-tub concerns all α-tub isoforms except for tubulin alpha 4A (TUBA4A), which is translated *de novo* without the C-terminal tyrosine residue (F. Li et al., 2020). Accumulation of dTyr-tub is a stochastic process that marks rigid and stabile MTs while Tyr-tub marks the dynamic filaments (**Figure 9**; Sanyal et al., 2023). The dTyr-tub and Tyr-tub are part of a reversible cycle catalyzed by specific enzymes (Uchida et al., 2021). While the tyrosination enzyme tubulin tyrosine ligase (TTL) has been known for decades, the carboxypeptidases vasohibin 1 and vasohibin 2 (VASH1/2) and their chaperone small vasohibin-binding protein (SVBP) were described fairly recently (Aillaud et al., 2017; Nieuwenhuis et al., 2017; Wehland et al., 1986). In CMs, dTyr-tub is mainly mediated by VASH1 and SVBP (Sanyal et al., 2023).

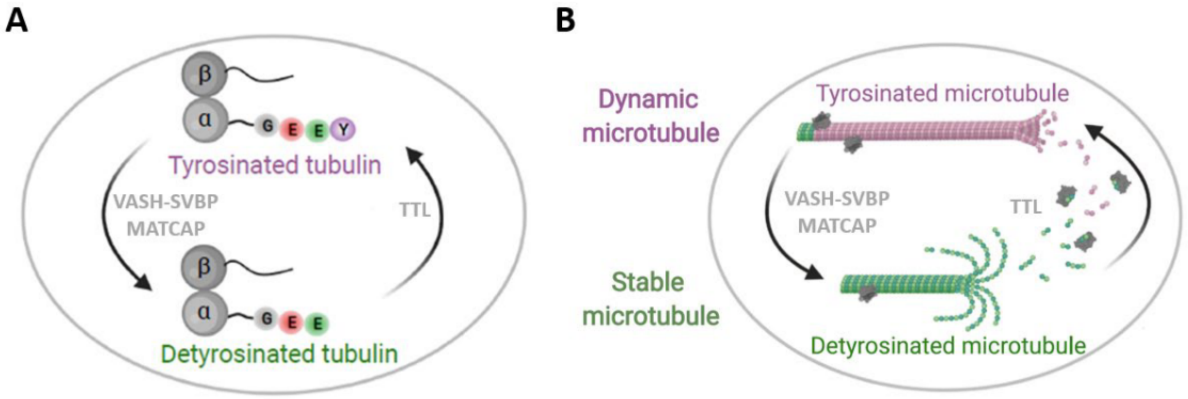

Figure 9: Tubulin detyrosination/re-tyrosination cycle.

Illustration of the detyrosination/re-tyrosination cycle of α-tub. All α-tub isoforms, except TUBA4A, are translated *de novo* carrying a C-terminal tyrosine (Y) residue. (A) This residue can be cleaved off by either a complex of VASH1/2 and SVBP or MATCAP1. The dTyr-tub may be re-tyrosinated by TTL. (B) While Tyr-tub MT (purple) are more dynamic and can be bound by the mentioned carboxypeptidases, dTyr-tub MT (green) are more stable. TTL can only bind and re-tyrosinate free tubulin heterodimers, not the polymerized MT. Adapted from: (Sanyal et al., 2023). Abbreviations: MATCAP, microtubule associated carboxypeptidase; MT, microtubule; SVBP, small vasohibin binding protein; TTL, tubulin tyrosine ligase; VASH, vasohibin.

In neurons however, another peptidase, microtubule associated tyrosine carboxypeptidase 1 (MATCAP1) has been shown to catalyze the same reaction (Landskron et al., 2022). Regarding their mechanism of action, TTL and VASH1/2 differ significantly. While TTL can bind and tyrosinate free heterodimers, VASH1/2 and SVBP exclusively bind polymerized MT (F. Li et al., 2020; Szyk et al., 2011). In contrast to VASH1/2, MATCAP1 only binds one filament (**Figure 10**; Landskron et al., 2022).

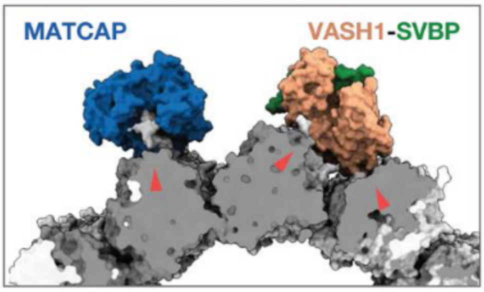

Figure 10: Microtubule binding by MATCAP1 or VASH1-SVBP.

Illustration of the binding mode of either MATCAP1 (blue) or VASH1/SVBP (orange/green) to MTs. While MATCAP1 binds a single protofilament, VASH1/SVBP requires binding of two adjacent ones. Adapted from: (Landskron et al., 2022). Abbreviations: MATCAP, microtubule associated carboxypeptidase; SVBP, small vasohibin binding protein; VASH, vasohibin.

After the cleavage of the terminal tyrosine residue of α-tub, the penultimate amino acid, glutamate, can also be cleaved. This reaction yields Δ2tub, which is increasingly accumulated on very long lived and stable MTs. Moreover, Δ2tub cannot be re-tyrosinated by TTL (Lafanechère et al., 1998; Paturle-Lafanechère et al., 1994; Pero et al., 2021). Cytosolic carboxypeptidases are responsible for Δ2tub formation (Sanyal et al., 2023).

Another key MT PTM is ac-tub. As is true for dTyr-tub, this modification is found on long lived MT. As acetylation recovers more quickly and densely after MT depolymerization, it is possible to assume that its enrichment also increases the likelihood of dTyr-tub occurrence (Tang et al., 2023). The acetylation reaction is carried out by the specific tubulin acetyltransferase ATAT1, while the reverse reaction is performed by the histone deacetylase 6 (Andreu-Carbó et al., 2024; Bance et al., 2019).

The other mentioned PTMs are not studied as deeply with regard to their presence and relevance in CMs and will therefore not be described in detail (Uchida et al., 2021).

1.3.3 Microtubule modifications in cardiomyocyte health and disease

Among the various MT PTMs, dTyr-tub and Tyr-tub play the most significant role for heart disease and HF. Stable dTyr-tub MTs accumulate in tissues of patients suffering from different forms of cardiomyopathies and in isolated failing human CMs. This accumulation goes hand in hand with an overall densification of the entire network (**Figure 11**; C. Y. Chen et al., 2018; Schuldt et al., 2021). Similar findings originate from disease models such as the ZSF1 obese rat, which has an early onset of a HFpEF-like phenotype, that display increased dTyr-tub levels (Eaton et al., 2023).

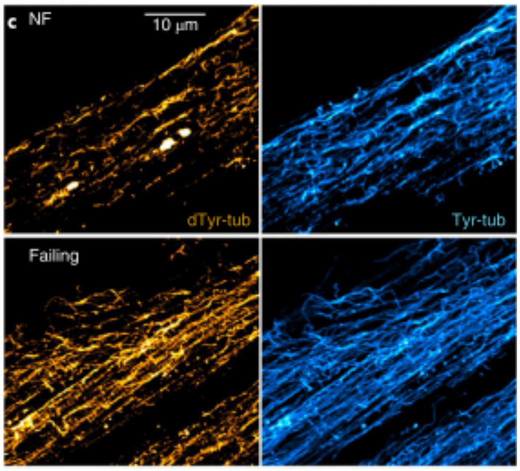

Figure 11: Microtubules in non-failing and failing human cardiomyocytes.

Microscopic images of non-failing (NF) (top) and failing (bottom) human CMs stained for dTyr-tub (orange) and Tyr-tub (blue). The MT network is visibly disorganized and increased in density in the failing CM compared to NF. From: (C. Y. Chen et al., 2018). Abbreviations: dTyr-tub, detyrosinated tubulin; NF, non-failing, Tyr-tub, tyrosinated tubulin.

In beating CMs, researchers have shown that MTs buckle during the contraction. This is due to the sarcomeric anchoring of longitudinal MTs. That way, MTs constantly transition from an elongated to a sinusoidal shape. In this respect, they can be viewed as contraction-resisting spring-like structures (**Figure 12**). The occurrence and amplitude of this phenomenon can be decreased by application of the detyrosination inhibitor parthenolide or overexpression (OE) of TTL. Similarly, TTL OE was shown to increase the maximal delta in sarcomere length in a dose-dependent manner (Robison et al., 2016).

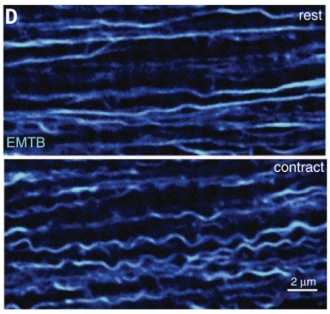

Figure 12: Buckling of microtubules during contraction.

Microscopic images of CM MTs (blue) during rest (top) and contraction (bottom). During the rest period MTs appear elongated while they form a sinusoidal shape (buckling) during contraction. From: (Robison et al., 2016). Abbreviations: EMTB, microtubule-binding protein ensconsin fused to three copies of green fluorescent protein.

Several independent studies have demonstrated that decreasing dTyr-tub and increasing Tyr-tub levels are beneficial for cardiomyocyte contractility and thereafter heart function. This holds true for adeno-associated viral vector-based OE of TTL, depletion of VASH1 by application of interfering ribonucleic acids (RNA) and most excitingly the pharmacological inhibition of VASH1 (C. Y. Chen et al., 2018, 2020; Robison et al., 2016). A 2024 study revealed that overexpressing TTL in a mouse model of HCM did not significantly alter the proteome as evaluated by mass spectrometry (MS) analysis. However, it was sufficient for improving cardiac output, which could not be attributed to an attenuation of hypertrophy but to improved compliance and end-diastolic pressure-volume relation (Pietsch et al., 2024).

Taken together, these data highlight a key role for the tubulin detyrosinatio/re-tyrosination cycle and its fine tuning for the maintenance of physiological cardiac function. A sustained tipping of the scales in favor of dTyr-tub causes functional deficits and is ultimately associated with HF (Sanyal et al., 2023; Uchida et al., 2021).

Besides dTyr-tub, ac-tub (K40) can modulate the mechanical properties of MTs. In sharp contrast to dTyr-tub, ac-tub does not increase stiffness to stabilize MTs. Instead, ac-tub is mostly thought to enhance flexibility. This allows MT to withstand mechanical stress. Xu et al. have also proposed a mechanism where MTs are specifically acetylated as a response to bending (Andreu-Carbó et al., 2024; Z. Xu et al., 2017). Importantly, the α-tub acetyltransferase 1 can only acetylate polymerized MT much like the detyrosination enzymes (Aillaud et al., 2017; Coombes et al., 2016; Nieuwenhuis et al., 2017). Similarly to the TTL enzyme, histone deacetylase 6 can only bind tubulin dimers but not the polymerized filaments (Pietsch et al., 2024; Skultetyova et al., 2017).

Further downstream from the direct effects of MT PTMs on mechanical properties of CMs, it has been revealed that they confine the localization of regulators of cell cycle. The group of James Martin investigated Yes associated protein (YAP), a cell cycle regulator, in this regard. They found that active (acetylated) YAP is confined to the cytosol by MTs, incapable to enter the nucleus to upregulate cell cycle activity (S. Liu et al., 2024). Compatible with this data, unpublished work from our group has indicated that decreasing MT stiffness by knocking out SVBP (SVBP-KO), also increases cell cycle activity (Pietsch et al., n.d.). The underlying mechanism remains elusive.

1.4 Human induced pluripotent stem cells, derived cardiomyocytes and genome editing

1.4.1 Human induced pluripotent stem cells

The reprogramming of differentiated cells like fibroblasts to pluripotent stem cells was pioneered nearly 20 years ago when Takahashi and Yamanaka evaluated a panel of different candidate factors. In that groundbreaking study, they used retroviral vectors to introduce the factors into mouse fibroblasts. Through a series of validation experiments, the *Yamanaka factors* were defined. From the tested ones, Octamere-binding transcription factor 3/4 (OCT3/4), SRY-box transcription factor 2 (SOX2), proto-oncogene c-Myc (C-MYC) and krüppel-like factor 4 (KLF4) were found to be essential. The latter two can be exchanged for other oncogenes, such as the signal transducer and activator of transcription 3 (STAT3; Takahashi & Yamanaka, 2006). Shortly after, two independent groups described protocols to create human induced pluripotent stem cells (hiPSCs) from somatic cells, pushing the envelope for disease modeling in a human context and potentially making animal models less relevant (Takahashi et al., 2007; Yu et al., 2007).

From that point on, hiPSCs have developed into a powerful tool. They are utilized for disease modeling, drug discovery and show potential for the usage in personalized medicine and cardiac repair (Jebran et al., 2025; Querdel et al., 2021; Sharma et al., 2020).

The key advantage compared to primary cell cultures is their availability and scalability. While primary cells from tissues like skin might be easily obtained, brain and heart tissues are unavailable to most researchers. Conversely, a challenge for hiPSC-derived cells is imposed by a general lack of maturity, which is thought to be caused by the lack of cues from the surrounding microenvironment (Cerneckis et al. 2024).

1.4.2 Human induced pluripotent stem cell-derived cardiomyocytes

One of the many cell types that are nowadays routinely generated from hiPSCs are CMs (hiPSC-CMs). A plethora of protocols exists for the generation of CM subtypes such as atrial, nodal-like or ventricular CMs. In this thesis, the focus will be set on ventricular CMs, which will in the following be referred to as (hiPSC-)CMs.

Generally, the existing protocols for hiPSC-CM generation can be sub-grouped into suspension cultures where embryoid bodies (EB) are generated and monolayer protocols (Di Baldassarre et al., 2018). Table 1 and Table 2 outline the respective advantages of EB-based and monolayer-based CM differentiation protocols. Comparing both basic approaches, each of them seems suited for different use cases. For individual *in vitro* studies, like the one at hand, monolayer protocols present a flexible and viable option. The particular setup used for hiPSC-CM generation here was adapted from Mosqueira et al. and is described in detail in the methods section as well as Meyer-Jens et al. (Meyer-Jens et al., 2024; Mosqueira et al., 2018).

Table 1: Pros and cons of EB-based CM differentiation protocols.

Pros	**Source**
Highly scalable up to bioreactor format	(Prondzynski et al., 2024)
High purity	(Prondzynski et al., 2024)
High yield	(Prondzynski et al., 2024)
Reduced batch to batch variability	(Kahn-Krell et al., 2021)
Possibly more physiologically relevant microenvironment	(Leitolis et al., 2019)
Cons	**Source**
Complex setup especially during scale-up	(Kahn-Krell et al., 2021)
Dissociation efficiency dependent on used agent	(Fischer et al., 2018)

Table 2: Pros and cons of monolayer CM differentiation protocols.

Pros	**Source**
High efficiency	(Batalov & Feinberg, 2015)
Simple setup and shorter differentiation time	(Burridge et al., 2014)
Dependent on protocol: low variability	(J. Zhang et al., 2012)

Cons	Source
Low scalability/missing automation	(Batalov & Feinberg, 2015; Prondzynski et al., 2024)
Significantly higher hands-on time	(F. Wang et al., 2023)

Frequently used monolayer hiPSC-CM differentiation protocols consist of a series of chemical cues that gradually cause CM specification (**Figure 13**). The switch between Wnt-pathway activation with bone morphogenic factor 4 (BMP4) and activin A and Wnt-pathway inhibition is crucial. While the activation is meant to drive mesoderm specification of the hiPSCs, the inhibition with XAV939 (XAV) and KY02111 (KY) allows the cells to form cardiac progenitor cells (Rajamohan et al., 2016). HiPSC-CMs may be further matured by performing lactate selection and other metabolic maturation approaches (Feyen et al., 2020; Horikoshi et al., 2019; Knight et al., 2021; Machiraju & Greenway, 2019; Meyer-Jens et al., 2024).

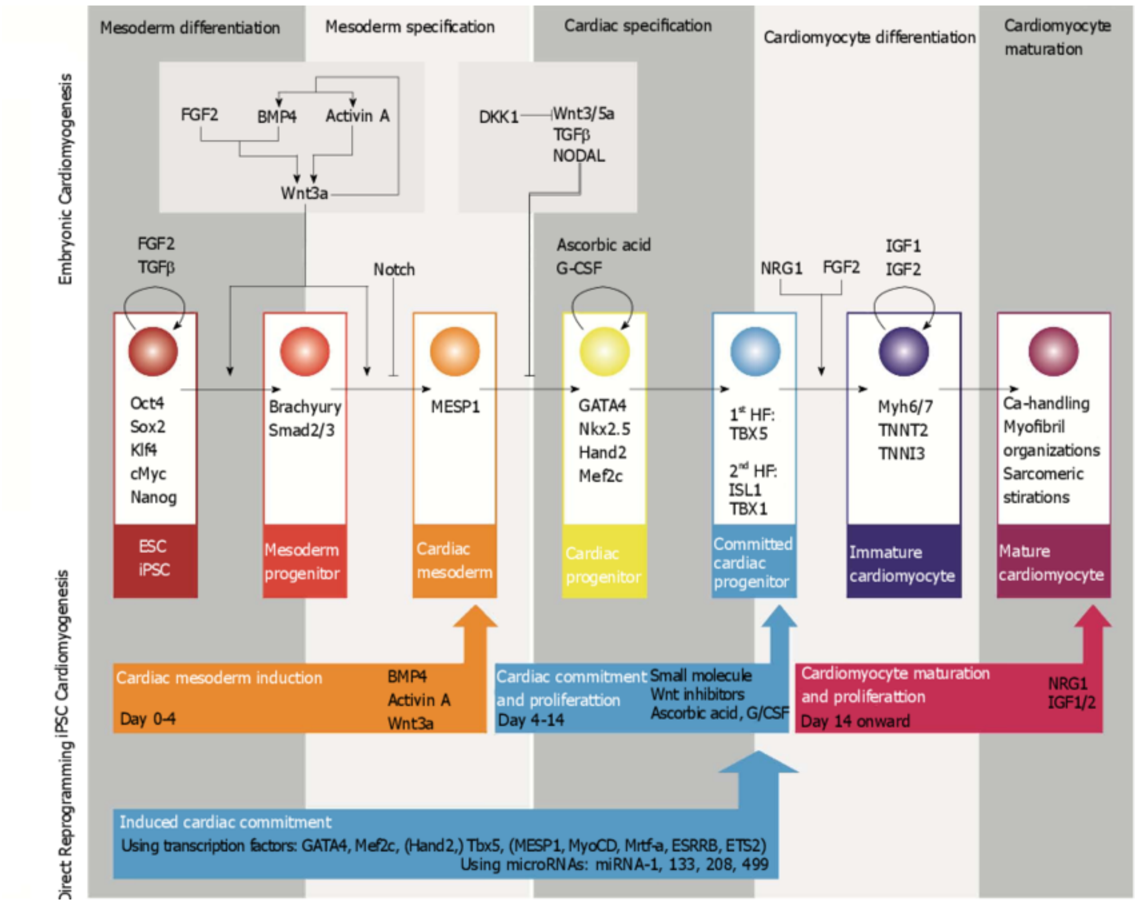

Figure 13: Factors commonly used for human induced pluripotent stem cell-derived cardiomyocyte differentiation.

The illustration outlines the factors needed for hiPSC-CM differentiation. Differentiation begins with mesoderm specification, here factors like BMP4 and activin A are key. Afterwards Wnt-signaling is modified to induce cardiac specification and finally CM differentiation. From: (Kamps, 2016). Abbreviations: Ca, calcium; CSF, colony stimulating factor; DKK1, Dickkopf WNT signaling pathway inhibitor 1; ESC, embryonic stem cell; ESRRB, estrogen related receptor beta; ETS2, ETS proto-oncogen 2 transcription factor; FGF2, fibroblast growth factor 2; GATA4, GATA binding protein 4; IGF, insulin like growth factor; ISL1, ISL LIM homeobox 1; MEF2C, myocyte enhancer factor 2C; MESP1, mesoderm posterior BHLH transcription factor 1; MRTFA, myocardin related transcription factor A; MYH6/7, myosin heavy chain 6/7; MYOCD, myocardin; NANOG, homeobox transcription factor nanog NODAL, nodal growth differentiation factor; NRG1, neuregulin 1; TBX1/5, T-box transcription factor 1/5; TGFβ, transforming growth factor β; TNNI3, troponin I3, cardiac type; TNNT2, troponin T2, cardiac type; Wnt3a, wingless-type family member 3a.

The success of hiPSC-CM differentiation is primarily evaluated by quantifying the cardiac troponin T2 (cTnT)-positive cells. Current protocols routinely reach >80% purity which allows for reliable experimental setups (Batalov & Feinberg, 2015; Meyer-Jens et al., 2024; Prondzynski et al., 2024).

1.4.3 Genome editing in human induced pluripotent stem cells

The advances in hiPSC-biology have also fostered an uptick in the application of different genome editing techniques. Besides zinc-finger nucleases (ZFN) and TAL effector nucleases (TALENs), the most widely used tool is the clustered regularly interspaced palindromic repeat (CRISPR) system that features associated nucleases (Cas; Gaj et al., 2016). Originally, the CRISPR-Cas9 system was discovered as an immune-like system in bacteria. Through molecular biology techniques, it can nowadays be adapted to target almost any genomic locus. Compared to ZFNs and TALENs, the adaptation of the CRISPR-Cas system requires less effort. Additionally, targeting multiple sites in one approach is possible (Doudna & Charpentier, 2014).

The researchers can design a CRISPR RNA (crRNA), specific to their locus of interest with readily available online tools (IDT, 2025). These crRNAs need to be complementary to the target region and contain a protospacer adjacent motive (PAM). The consensus PAM sequence is ‘N-G-G’ and key for deoxyribonucleic acid (DNA) recognition. Mechanistically, the crRNA, a trans-acivating RNA (tracrRNA) and the Cas enzyme, in most cases Cas9, form a complex and the crRNA guides the enzyme to the desired site (Karvelis et al., 2013). The DNA is partially unwound and the target recognized by Watson-Crick base pairing. Cas9 can then introduce a double-strand break (DSB). The DSB will then be recognized by cellular factors and can either be repaired with the precise homology directed repair (HDR) or the error prone non-homologous end joining (NHEJ; **Figure 17**; Ran et al., 2013).

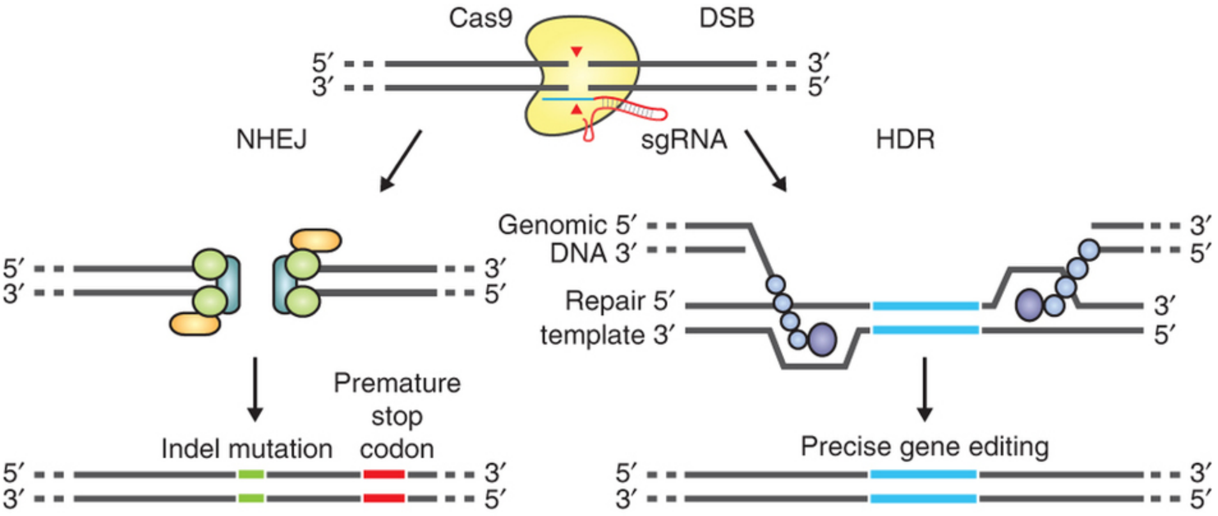

Figure 14: Mechanism of CRISPR-Cas9 genome editing.

Illustration for CRISPR/Cas9 function. The Cas9-enzyme is guided to the desired target site by a crRNA (here scrRNA). After binding, the Cas-nuclease creates a double-strand break (DSB). In the cell DSBs can be resolved via two different pathways, either the non-homologous end joining (NHEJ; left) or homology directed repair (HDR; right). NHEJ is active during all cell cycle phases. Both ends of the DSB are bound by specific protein factors, including nucleases and ligases. This repair pathway aims to re-ligate the two loose DNA ends without correction function and therefore frequently induces indel mutations and/or premature stop codons. HDR is only highly active during S/G2-phase of the cell cycle. It is a highly precise mechanism that uses a template to repair the DSB. This template can either be designed by the researcher or be the sister chromatid. From: (Ran et al., 2013). Abbreviations: Cas9, CRISPR-associated nuclease 9; DNA, deoxyribonucleic acid; DSB, double strand break; HDR, homology directed repair; NHEJ, non-homologous end joining; sgRNA, single guide RNA.

HDR can repair the DSB with the sister-chromosome or a genome-editing template. The template needs to have sufficient homology to the targeted locus upstream and downstream of the DSB but may include a sequence variant. Therefore, HDR can introduce site specific mutations matching or correcting patient variants (Liao et al., 2024; Prondzynski et al., 2019). Silent mutations of the PAM sequence can also be introduced as a label to distinguish the different genomic alleles and to prevent repeated binding and cutting of the DNA (Lobo et al., 2025).

NHEJ is the dominant DSB repair mechanism but highly error prone. The involved machinery ligates the DSB while creating random insertions and deletions (indels). These indels are likely to disrupt the reading frame and cause a premature stop codon (H. Liao et al., 2024; Ran et al., 2013). Consequently, NHEJ is used to create large genetic modifications such as knockout (KO; Pietsch et al., 2024). For the CRISPR-approach used in this study (4.4), we also relied on NHEJ. An important distinction between NHEJ and HDR is that NHEJ is active in all cells, independent of cell cycle stage while HDR activity is very low in non-dividing cells (Iyama & Wilson, 2013; H. Liao et al., 2024).

To achieve the highest possible activity of DNA repair mechanisms, especially HDR, genome editing is usually performed during the growth phase (Ferrari et al., 2022).

After the CRISPR-experiment, validation of correct editing is performed with different techniques. Most commonly, the targeted region is amplified via polymerase chain reaction (PCR), the product sequenced and compared to the unedited sequence. Additionally, the frequently used crRNA design tools also evaluate off-targets (OTs) potential (IDT, 2025). These OTs are each assigned a score, from low to high, indicating the likelihood for unintended targeting by Cas9. Often the potential OTs will be found in intronic regions, but they can also corrupt genomic loci, creating unwanted effects (Guo et al., 2023). Like other academic labs, we evaluate the ten most likely OTs for each crRNA used. Similar to the target locus, each OT must be PCR amplified and sequenced (Prondzynski et al., 2019).

Another crucial quality control step is karyotyping. This can be achieved by G-banding or methods like Nanostring nCounter analysis (Lobo et al., 2025; Pietsch et al., 2024; Prondzynski et al., 2019). Different groups have described karyotypic abnormalities after CRISPR-Cas9 genome editing including the loss of whole chromosomes (Alanis-Lobato et al., 2021; Papathanasiou et al., 2021).

For KO strategies, absence of the respective RNA and protein should be determined in the cell type used for subsequent studies to ensure success (Joung et al., 2016). Obviously, pluripotency must be confirmed for any hiPSC-line, independent of genome editing and due to cell line differences, every hiPSC-line should be compared to an isogenic control, meaning one, that shares an identical genetic background (Mosqueira et al., 2018; Pietsch et al., 2024; Prondzynski et al., 2019).

Ultimately, genome editing of hiPSCs and the derived cell types, such as CMs, can be used to create precise models for patient pathologies in relevant cell types such as hiPSC-CMs.

1.5 Disease models of heart failure and hypertrophy

The landscape of models of HF, cardiac hypertrophy and different etiologies of heart disease has expanded vastly over the past decades. State-of-the-art experimental systems range from 2D cellular models like hiPSC-CMs, adult rat or mouse ventricular myocytes (ARVMs/AMVMs) or neonatal rat ventricular myocytes (NRVMs), to 3D models like engineered heart tissues (EHTs) and organoids. Beyond cell-based models, *ex vivo* models like cardiac tissue slices and Langendorff-perfused hearts remain valuable tools. Despite the broad availability of the mentioned systems, animal models are considered the gold standard by many, but are increasingly replaced by alternative setups (Van Der Velden et al., 2022). The following chapter will elaborate on these different models and outline their key features.

1.5.1 2D models of hypertrophy and heart failure

Classical models for hypertrophy and HF commonly rely on isolated myocytes from mice or rats. NRVMs are typically isolated from pups one to three days (d) after birth. These cells are well suited for 2D culture, can be obtained in large numbers, and remain widely used models (S. R. Singh et al., 2021). Pharmacological stimulation with agents like phenylephrine (PE) or angiotensin II (AngII) can induce hypertrophic adaptations like increased cell size and transcriptional adaptations, including the upregulation of A-type and B-type natriuretic peptide (NPPA/NPPB) and modifications in cell cycle activity (Kliesow Remes et al., 2025; J. M. Li et al., 2020; R. Zhang et al., 2022). Due to their availability and robustness, NRVMs have become a standard model for high throughput approaches like small interfering RNA (siRNA) and compound library screens (S. R. Singh et al., 2021). Despite the mentioned advantages, NRVMs have several inherent shortcomings. First, the cell population can be heterogeneous, meaning a varying percentage of actual CMs in each experiment can potentially induce variability when no countermeasures (purification e.g.) are taken (D. Yang et al., 2018). Secondly, they are less mature compared to ARVMs and AMVMs which makes them less suitable for studying structures like t-tubules (Van Der Velden et al., 2022). Thirdly, NRVMs do require animal housing, mating and sacrifice, which do impose financial and ethical burdens upon the researcher. In many countries like Germany, any researcher wanting to isolate NRVMs, also needs to acquire a permission that allows for handling and sacrifice of rats.

An alternative to NRVMs is the use of adult ventricular CMs (AMVMs/ARVMs). However, the isolation of these CMs is technically more challenging than that of NRVMs. Also, they require the use of adult animals, increasing housing costs compared to NRVMs (Ackers-Johnson et al., 2016). A major limitation of AMVMs and ARVMs is their low viability as they deteriorate quickly after isolation and typically fail attach to culture dishes (B. Liu et al., 2019). Consequently, they are employed in studies that require more mature CMs but lower throughput is acceptable (Kadota et al., 2017). For example, they may be used for live cell imaging studies, studying processes like cytoskeletal dynamics (Salomon et al., 2021). AMCMs and ARCMs can also readily be isolated from genetically modified animals expressing protein variants or tools like Förster resonance electron transfer (FRET) sensors (Sprenger et al., 2016). Importantly, while their higher degree of maturity positions them closer to human ventricular CMs, they remain a rodent model and therefore retain species-specific differences in cellular physiology (Van Der Velden et al., 2022).

In recent years, hiPSC-CMs have emerged as an increasingly important model system for different characteristics of cardiac hypertrophy. Protocols for the induction of hypertrophy in hiPSC-CMs include the use of PE or endothelin 1 (ET1). These pharmacological cues have been reported to induce activation of the hypertrophic gene program, metabolic adaptations and increased cell size. Importantly, a higher degree of metabolic and structural maturation seems to be of need for appropriate responses (Knight et al., 2021; Meyer-Jens et al., 2024; Redwanz et al., 2024). They do, however, present a compelling model to evaluate signaling pathways and cellular physiology with a human background, allowing for modeling of patient-specific genetic variants and personalized medicine approaches (Loos et al., 2023; Prondzynski et al., 2019;

Warnecke et al., 2021; Zech et al., 2022). Other potential applications include drug testing, especially if the research question concerns a specific patient group and a drug with unknown therapeutic benefit (Saleem et al., 2020). Because of the theoretically unlimited supply of hiPSC-CMs due to the expansion capacity of hiPSCs, hiPSC-CMs provide an excellent platform for multi-omics approaches enabling researchers to integrate findings across different readouts (Pietsch et al., 2024). Regardless of these advantages, the culture of hiPSCs and their differentiation into CMs is a technically demanding, cost intensive process and requires substantial expertise and hands-on time (Funakoshi et al., 2021; Mosqueira et al., 2018). Variations in hiPSC quality may also greatly impact differentiation and therefore downstream experimental success making a tightly controlled quality control parameters crucial (Prondzynski et al., 2024). Other limitations of hiPSC-CMs and their use as a disease model are their immaturity and the lack of cellular complexity (Kadota et al., 2017). They are mostly considered to resemble embryonic or at best neonatal CMs especially metabolically. In contrast to adult CMs, which use fatty acids as the main energy source, hiPSC-CMs rely on glycolysis. Maturation can be enhanced with media containing increased amounts of fatty acids. Additionally, many researchers have observed improved model accuracy when they cultured hiPSC-CMs for prolonged time periods and/or on micro-patterned substrates (Feyen et al., 2020; Forsten, 2020; Knight et al., 2021; X. Yang et al., 2019).

Almost all 2D models have the inherent shortcoming that any adherent culture presents substrate stiffness that far surpass anything that would realistically be seen in an organism (Vite et al., 2022). To overcome this and other downsides, cardiac 3D models have become popular over the past decades.

1.5.2 3D models of hypertrophy and heart failure

As the heart is a highly complex three-dimensional organ, approaches to model physiological and pathological mechanisms are implied that include a 3D setup. These models have been pioneered more than 25 years ago with chick CMs and have transitioned towards neonatal rat or mouse cardiac cells to now including hiPSC-CMs (Eschenhagen et al., 1997; Hirt et al., 2012; Schaaf et al., 2011). Recently there have also been advances in bioprinting with reports on the fabrication of hydrogel-based EHTs (Juarros et al., 2024). Another approach that is gaining traction is the use of organoids, often fabricated with complex bioreactor setups. Prondzynski and colleagues were able to reveal that the forming organoids were larger than the embryoid bodies resulting from the regular differentiation and that they exhibited higher alpha actinin 2 (*ACTN2*) levels. Interestingly, these self-assembled chamber-like structures and showed a mixed cell population which is a more realistic setting for future disease modeling approaches (Prondzynski et al., 2024). Because such approaches are less controlled, research has also focused on the use of multi-cell type EHTs. The most commonly implemented cell types include fibroblasts, vascular smooth muscle cells and immune cells (e.g. macrophages). These models resemble the cellular composition of the heart more closely and therefore might be a more suitable cardiac disease model (Laskary et al., 2025; Naito et al., 2006; Wrona et al., 2022).

Complementing hiPSC-CMs with other hiPSC-derived cell types might also improve model performance when with compounds such as PE and ET1 in EHTs (Wrona et al., 2022). As most differentiation protocols focus on the mainly force generating ventricular CMs, specialized protocols to produce atrial-like CMs have been established. These atrial hiPSC-CMs have also been used in 3D EHT models. Atrial hiPSC-CM EHTs crucially differ in beating frequency, force generation and electrophysiological parameters (Banfeng, 2022; Lemme et al., 2018; Schulz et al., 2023)

3D cardiac tissue models also represent a promising option to replace lost cardiac tissue after infarction. It has been shown that transplantation of such constructs improves cardiac contractility in a dose-dependent manner (Jebran et al., 2025; Querdel et al., 2021).

1.5.3 Animal models of cardiac hypertrophy and heart failure

In HF research, animal models, especially small animals like mice, rats or guinea pigs have been essential tools for driving discovery. The induction of disease depends on the pathology of interest and can be surgical, pharmacological or genetic.

A commonly used surgical model inducing pressure overload accompanied by hypertrophy and ultimately HF is the transverse aortic constriction (TAC) often performed in rodents. In this model, the aorta is constricted with a cannula as a stabilizer for the positioning of a suture. Once the suture is positioned correctly, the cannula is removed. Through the reduction of aortic diameter, the pressure in the aorta before the suture and subsequently in the left ventricle increases (deAlmeida et al., 2010; Rockman et al., 1991). A schematic overview of the TAC procedure is depicted in **Figure 15**.

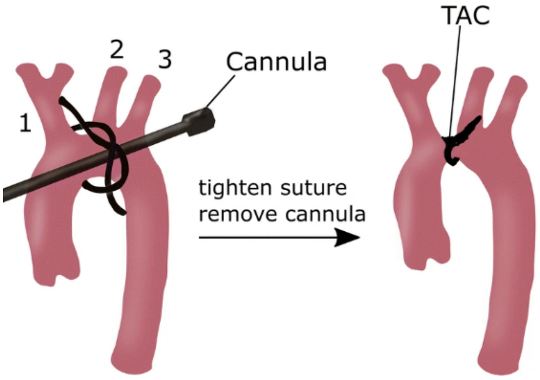

Figure 15: Schematic overview of the transverse aortic constriction procedure.
Schematic illustration for TAC (transverse aortic constriction) procedure in animals. In short, the aorta is constricted with a suture. This constriction creates a pressure overload in the left ventricle which causes structural remodeling and hypertrophy. Modified from: (Bacmeister et al., 2019). Abbreviations: TAC, transverse aortic contriction.

Alternatively, myocardial infarction (MI) can be induced by a temporary ligation of the left anterior descending (LAD) coronary artery. When the LAD ligation is permanent, it leads to a large infarcted area compared to a rather small one when reperfusion is allowed to occur. This procedure can also be used to study ischemia or regeneration when performed in neonatal animals (de Villiers & Riley, 2020; Haubner et al., 2016). Other researchers have also shown that cryo-injuries present a reproducible and feasible option to model MI in rodents (Stüdemann et al., 2022).

On the side of pharmacological models, animals, mostly mice or rats, are infused or injected with pro-hypertrophic agents such as PE, AngII or isoproterenol (Iso). These models have the advantage of relying less on individual surgical skills compared to TAC and LAD ligation models. Therefore, they represent more controlled and reproducible settings but lack structural complexity. Still, the onset of hypertrophy can be observed early on and the procedural recovery of the animals is quick (Agostinucci et al., 2022; Phyo et al., 2022; Rau et al., 2017).

One of the most prominent models for HFpEF is the hybrid of the zucker diabetic fatty rat and the spontaneously hypertensive HF rat (ZSF1 obsese). These rats develop classical HFpEF features such as elevated end-diastolic pressure, prolonged relaxation, diastolic dysfunction and increased dTyr-tub (Eaton et al., 2023).

1.6 Protein kinase G1 signaling

The cyclic guanosine monophosphate (cGMP)-protein kinase G1 (PRKG1) signaling axis has been described to modulate adverse cardiac remodeling. Also its activation has been implicated to decrease hypertrophy and blood pressure in animal models and patients (Blanton et al., 2012; Kong & Blanton, 2013). The following paragraphs will elucidate on structure and function of PRKG1 isoforms, canonical cGMP-PRKG1 signaling pathways and modulators as well as its role in the myocardium.

1.6.1 Structure and function of PRKG enzymes

There are two different PRKG isoforms, PRKG1 and PRKG2 which are encoded by two different genes. In addition, the PRKG1 gene gives rise to two different splice isoforms, PRKG1A and PRKG1B. All PRKG enzymes are cGMP-dependent serine/threonine kinases. The isoforms differ in tissue expression. Because PRKG2 is not expressed in the circulatory system to a relevant extent, the following descriptions will focus on PRKG1 isoforms. Both enzymes are organized identically, only differing in size and sequence slightly. They harbor an N-terminal regulatory domain, which consists of a Leucine zipper (LZ) domain and two cyclic nucleotide binding domains (CNB-A/B). Towards the C-terminus, the catalytic domain, made up of the small and large lobe is located. Additionally, all PRKG enzymes contain an auto inhibitory domain (AI) located in between the LZ and CNB domains (**Figure 16**). The LZ domain is crucial for enzyme activity as it mediates enzyme dimerization. Homodimer formation is essential for correct localization and association with interaction partners such as scaffolding and anchoring proteins. In its inactive state, the AI quenches the catalytic site. A conformational change takes place once cGMP binds to the CNBs, releasing the catalytic domain and rendering the enzyme active. Conversely, there is evidence for low baseline PRKG1 activity in absence of cGMP (Casteel et al., 2010; Kim & Sharma, 2021; Sharma et al., 2022).

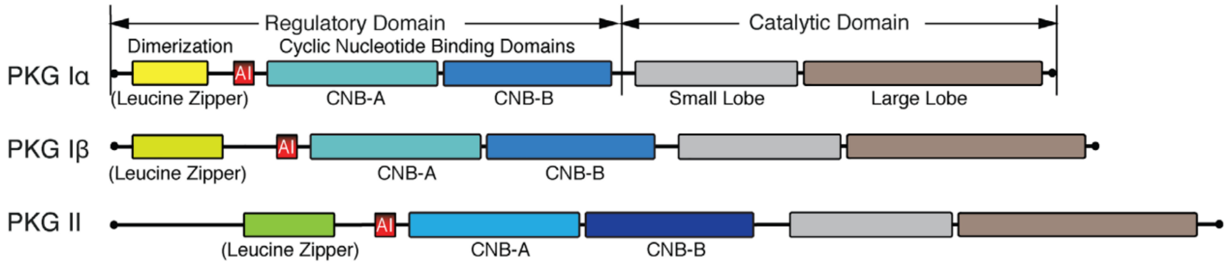

Figure 16: Domain structure of human PRKG1/2 enzymes.

Schematic illustration of PRKG1/2 domain architecture. Each isoform includes a N-terminal regulatory and C-terminal catalytic domain. The regulatory contains a dimerization (LZ) domain, AI domain and twocyclic nucleotide binding domains (CNBs). The catalytic domain consists of the small and large lobe and performs the kinase reaction. Adapted from: (Kim & Sharma, 2021). Abbreviations: AI, autoinhibitory domain; CNB-A, cyclic nucleotide binding domain A; CNB-B, cyclic nucleotide binding domain B; PKG Iα, LZ, leucine zipper; PKG Iα, protein kinase G 1α (PRKG1A); PKG Iβ, protein kinasse g 1β (PRKG1B); PKG II, protein kinase g II (PRKG2).

The two PRKG1 isoforms differ mainly in their N-termini. Through a roughly 100 amino acid difference, the LZ and AI domains are distinct for the α and β isoenzymes causing differential enzyme activation kinetics and binding partners. Differences in enzyme kinetics can be explained by deviations in cGMP sensitivity. Tissue distribution also differs with PRKG1A being the dominant isoform in heart, lung and some neuronal cell types, while PRKG1B is mostly found in smooth muscle cells and platelets. Tissue specific expression pattern underscores the differential roles of the isoenzymes (Casteel et al., 2010; R. Sharma et al., 2022; Uniprot, 2025).

1.6.2 Regulation of cGMP-PRKG1A signaling

As described above, PRKG1 is activated by the second messenger cGMP. This molecule can be generated via two distinct enzyme families. On the one hand, soluble guanylate cyclases (sGCs) represent a group of cytosolic enzymes that convert GTP to cGMP upon nitric oxide (NO) stimulation. These sGCs can reside in the cytosol as NO can freely diffuse through cell membranes (Benza et al., 2024; Faleeva et al., 2022; Stuehr et al., 2021). On the other hand, a substantial amount of cGMP in cardiomyocytes is generated by the membrane bound NP receptors (NPR1/2). NPR1 binds ANP/BNP while NPR2 exclusively binds CNP. Both receptors contain an extracellular NP binding domain, a transmembrane domain and an intracellular particulate guanylate cyclase domain (pGC). Upon NP binding, the pGC catalyzes the conversion of GTP to cGMP which can then activate PRKG1A/B (Faleeva et al., 2022; Goetze et al., 2020). Termination of cGMP signals can be caused by the activity of specific phosphodiesterases (PDEs; **Figure 18**).

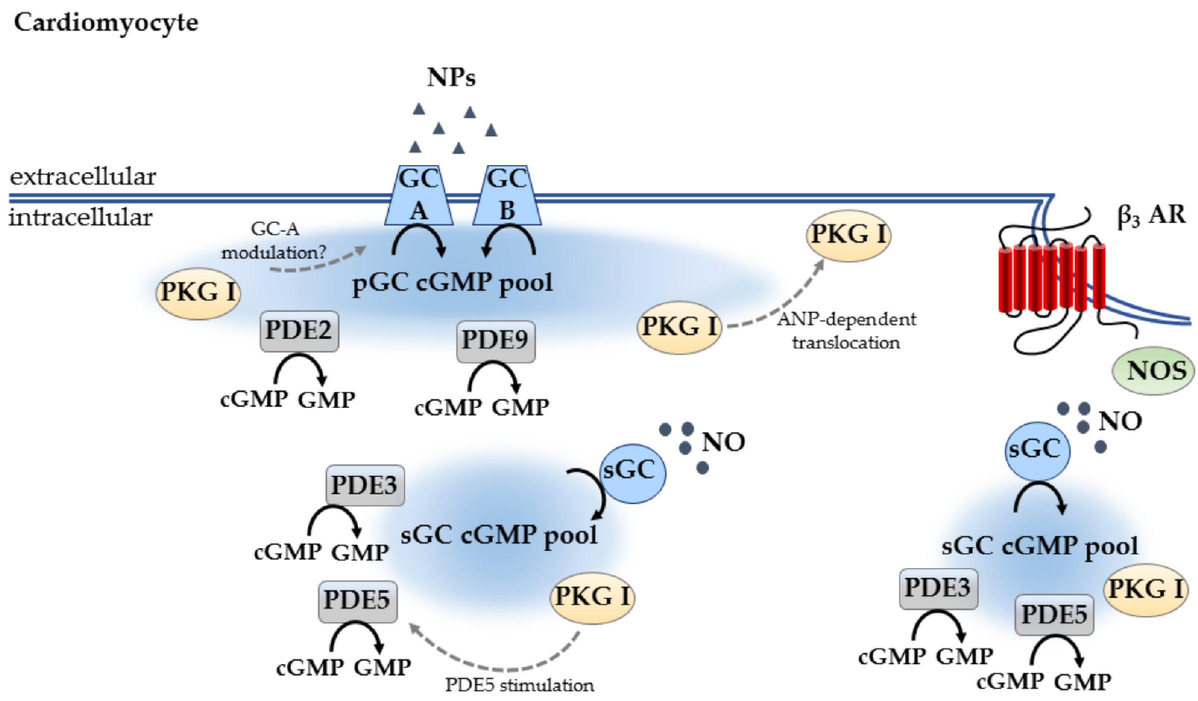

Figure 17:Schematic for the regulation and compartmentalization of cGMP-PRKG1A signling in cardiomyocytes.

Schematic illustration for the regulation of cGMP-PRKG1A signaling in cardiomyocytes (CMs). PRKG1 can be activated by cyclic guanosin monophosphate (cGMP). This second messenger is generated either upon natriuretic peptide binding to their respective receptors by the intracellular guanylate cyclase (GC) domain or by soluble guanylate cyclases (sGC) upon nitric oxide (NO) binding. These sGCs can reside in the cytosol because NO is able to diffuse through the cell membrane. Moreover, NO synthases (NOS) can generate NO downstream of β_3-adrenergic signaling. Both types of GCs generate independent pools of cGMP. The signaling can be modulated or even terminated by the hydrolyzation of cGMP to guanosine monophosphate (GMP). This reaction is catalyzed by a diverse pool of phosphodiesterases (PDEs). From: (Bork & Nikolaev, 2018). Abbreviations: ANP, atrial natriuretic peptide; cGMP, cyclic guanosine monophosphate; GC, guanylate cyclase; GMP, guanosine monophosphate; GTP, guanosine triphosphate; NO, nitric oxide; NOS, nitric oxide synthase; NP, natriuretic peptide; PDE, phosphodiesterase; PKG1, protein kinase g 1 (PRKG1); sGC, soluble guanylate cyclase; β_3 AR, β_3 adrenergic receptor.

Some PDEs (PDE1, PDE2, PDE3) can hydrolyze both cyclic adenosine monophosphate (cAMP) and cGMP while others (PDE5, PDE6, PDE9) exclusively break down cGMP. It has to be mentioned that PDE6 is not expressed in the heart (Calamera et al., 2022; Faleeva et al., 2022; Tcheudji et al., 2001). PDEs play a central role in PRKG1 signaling as they are highly compartmentalized. This compartmentalization allows for localized cGMP-level regulation and subsequent PRKG1 activity. It has been shown that PDE9 is mainly responsible for degrading cGMP arising from NP signaling but not NO/sGC signaling (Kokkonen & Kass, 2017; Lee et al., 2015; Mishra et al., 2021). This contrasts with the function of PDE5 which mostly localizes to Z-discs and degrades cGMP of the latter origin (Benza et al., 2024; Frank & Frey, 2011). PDE5 activity can also be increased via PRKG-dependent phosphorylation, creating a feedback loop, dampening cGMP-PRKG1 signaling (Castro et al., 2010).

1.6.3 Targets of cGMP-PRKG1A signaling in the heart

Cardiac cGMP-PRKG1 activity has diverse targets partaking in calcium handling, cytoskeletal processes and cellular stress response. Because the work at hand is focused on CMs, PRKG1A targets and subsequent signaling will be explored further as PRKG1B is not expressed in our experimental setting (data not shown; PRKG1 from now on equivalent to PRKG1A).

PRKG1 can modulate Ca^{2+} signaling by phosphorylating targets including calcineurin-nuclear factor of activated T-cells (NFAT), L-type calcium channels (LTCC) and transient potential canonical 6 (TRPC6). Phosphorylation of LTTC and TRPC6 attenuates Ca^{2+} entry. Moreover, PRKG1 can phosphorylate PLN, decreasing its inhibitory effect on SERCA2, which then can remove calcium from the cytosol by transporting it into the sarcoplasmic reticulum (Colyer, 1998; Nakamura & Tsujita, 2021).

By phosphorylating tuberous sclerosis 2 (TSC2), PRKG1 reduces the activity of mechanistic target of rapamycin complex-1 (mTORC1). Research has shown that mutating the PRKG1 target site on TSC2 (serine 1364) abolishes the antihypertrophic effects of cGMP-PRKG1 signaling *in vitro* and *in vivo* emphasizing the beneficial effects on physiological cardiac function (**Figure 18**; Ranek et al., 2019).

However, any negative inotropic effects of PRKG1 activity can be attributed to phosphorylation of targets such as but not limited to PLN, cardiac troponin I and titin (TTN) following NO/sGC signaling. In particular, cellular stiffness may be directly modulated by PRKG1 via the phosphorylation of the N2B domain of TTN. Phosphorylation of this domain was shown be sufficient for decreasing domain rigidity (Krüger et al., 2009; Nakamura & Tsujita, 2021). This effect on the diastolic properties of CMs might directly contribute to cGMP-PRKG1 signaling changes in HF.

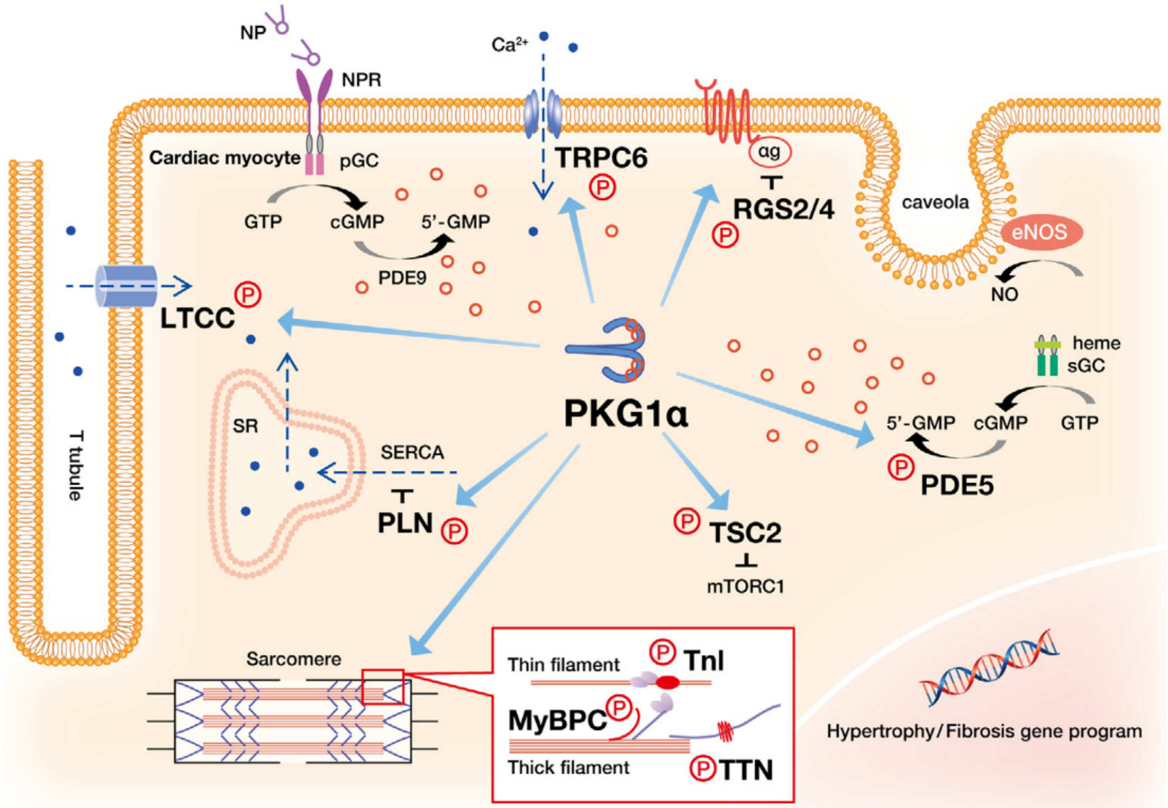

Figure 18: Overview of cGMP-PRKG1A signaling in cardiomyocytes.

Schematic illustration of PRKG1/PKG1 targets in CMs. PRKG1 can phosphorylate PLN, LTCC and TRPC6 which modifies calcium signaling and therefore contractility. Moreover, sarcomeric targets like TNNI/TnI may be phosphorylated and modulate the interaction between the thin and thick filament. PRKG1 can also phosphorylate TSC2, ultimately modulating mTORC1 activity and cellular anabolism. Via targets not illustrated in detail, hypertrophy and fibrosis are also modulated. From: (Nakamura & Tsujita, 2021). Abbreviation: 5'-GMP, guanosine monophosphate; αg, activating G-protein-coupled receptor; Ca^{2+}, calcium; cGMP, cyclic guanosine monophosphate; eNOS, endothelial nitric oxide synthase; GTP, guanosine triphosphate; LTCC, L-type calcium channel; mTORC1, mechanistic target of rapamycin complex-1; MyBPC, myosin binding protein C; NO, nitric oxide; NP, natriuretic peptide; NPR, natriuretic peptide receptor; P, phosphate; PDE5, phosphodiesterase 5; PKG1α, protein kinase g

1α (PRKG1A); PLN, phospholamban ; RGS2/4, regulator of G-protein signaling 2/4; SERCA, sarco(endo)plasmic reticulum calcium ATPase 2; sGC, soluble guanylate cyclase; SR, sarcoplasmic reticulum; TnI, troponin I; TRPC6, transient potential canonical 6; TSC2, tuberous sclerosis 2; TTN, titin.

1.6.4 cGMP-PRKG1A signaling in heart failure and disease

It has been known for long that PRKG1 activity has a protective effect on the cardiovascular system. Past studies have outlined lower activity of cGMP-PRKG1 signaling in samples derived from HF patient myocardium (Krüger et al., 2009; Michel et al., 2020). This also holds true for animal models of these pathologies. The activity levels of the PRKG1 signaling network components drive CM stiffness and hypertrophy (Fiedler et al., 2002; Krüger et al., 2009; Michel et al., 2020; Perera et al., 2015). An interesting example are NPR1 KO mice which developed overt hypertrophy and HF (Ellmers et al., 2007). Similar findings stem from a study performed in PRKG1 KO mouse that was subjected to TAC (Frantz et al., 2013). A possible reason for decreased cGMP-PRKG1 signaling activity in HF might be an increase in oxidative stress. This oxidative stress can cause oxidation of cysteine 42 which is located in the regulatory domain of PRKG1 and crucial in the dimerization and therefore enzymatic activity (Oeing et al., 2020; Takimoto & Kass, 2007). As already mentioned above, a physiological target of PRKG1 is the N2B domain of TTN. Logically, a reduction in PRKG1 activity also causes a hypophosphorylation of TTN favoring development of diastolic dysfunction (Hamdani et al., 2013; Michel et al., 2020).

Because of the broad involvement of cGMP-PRKG1 signaling in both physiology and pathology, drugs targeting this pathway are regularly used. Especially HFrEF patients can benefit from the application of the widely known PDE5 inhibitor sildenafil which was originally intended to be used as a male potency medication (Nakamura & Tsujita, 2021; Numata & Takimoto, 2022). More recently, inhibitors of the neprilysin (MME) enzyme have gained traction. These drugs (e.g. sac) aim at decreasing the degradation of NPs which can then drive PRKG1 activation via increased cGMP synthesis (1.1.4.; McMurray et al., 2014; Solomon et al., 2012, 2020).

Recent research has also uncovered that TSC2 phosphorylation at serine 1365 causes a shift in metabolic substrate utilization towards glycolysis which is protective towards ischemic reperfusion (Oeing et al., 2021). Conversely, another group evaluated the effects of long-term activation of the pathway. Schwaerzer and colleagues exposed knock-in mice expressing a constitutively active PRKG1 to either TAC surgery or AngII infusion. These mice reacted with pronounced hypertrophy and fibrosis accompanied by CM apoptosis compared to wildtype (WT) littermates. These pathological changes ultimately lead to dilation and cardiac dysfunction (Schwaerzer et al., 2021).

Summarizing, one can clearly state that cGMP-PRKG1 signaling is a finely tuned system in CMs and the overall cardiovascular system. Either a depletion or an overt activation can lead to pathological adaptations, underlining the need for careful evaluation of any therapeutic approach targeting this pathway.

2. Aims of this study

Previous research has positioned LCZ696 (sacval) as a drug superior to previous state of the art treatment enalapril for heart failure (McMurray et al., 2014). As different etiologies of heart disease and HF show significant accumulation of dTyr-tub and an overall densification of the MT network (C. Y. Chen et al., 2018; Schuldt et al., 2021), we first set out to with the following aims:

1) To develop a 2D hiPSC-CM model for CM hypertrophy that displays classical hypertrophy as well as higher levels of dTyr-tub,
2) To evaluate the effect of sacval and its two components, sac and val, on different parameters of the *in vitro* hypertrophy model.

As we were able to show significant upregulation of hypertrophic gene expression, cellular hypertrophy (2-fold higher) and dTyr-tub in ET1-treated hiPSC-CMs compared to control, which were impressively augmented by sac but not val application, we aimed at the following points:

3) Dissect differentially expressed proteins to identify potential pathways downstream of the canonical action of sac that could potentially regulate dTyr-tub.

Through our unbiased MS proteomic analyses, we were able to identify cGMP-PRKG1A signaling as a potential downstream target of sac that could also modify the activity of the main microtubule detyrosinase in hiPSC-CMs, VASH1. We therefore extended our research to:

4) Evaluating the impact of direct and indirect modulations of PRKG1A and VASH1 activity.

As we were able to locate a potential phosphorylation site of PRKG1A on the C-terminus of VASH1, we aimed to:

5) Evaluate the effect of the overexpression of phosphomimetic and non-phosphorylatable forms of VASH1 in VASH1-KO hiPSC-CMs.

Furthermore, as during the course of this study a third detyrosinase, MATCAP1, was discovered in neurons (Landskron et al., 2022). This was especially interesting as mice and hiPSC-CMs lacking VASH-SVBP activity still have remaining dTyr-tub (Pagnamenta et al., 2019; Pietsch et al., 2024). Therefore, we wanted to:

6) Create a hiPSC-line deficient in MATCAP1 (MATCAP1-KO) and evaluate molecular and functional consequences of MATCAP1-KO in hiPSC-CMs and hiPSC-CM EHTs.

3. Materials and Methods

All procedures were conducted in accordance with the Declaration of Helsinki. Animal procedures were conducted at the University of Greifswald. The cloning of VASH1 constructs and the experiments with isolated MTs were performed by the group of Marie-Jo Moutin (Grenoble, France).

3.1 Materials

The materials used to generate the presented data e.g. antibodies, chemicals, assays, cell lines etc. are listed in the appendix.

3.1.1 Human induced pluripotent stem cell lines

This study was conducted in the commercial hiPSC-line mTagRFP-TUBA1B (RFP WT) (AICS-0031-035, Corriell Institute). This line was also used to generate KO lines for *SVBP* and *TTL* (Pietsch et al., 2024), *VASH1* (Pietsch et al., n.d.) and *MATCAP1*. The latter was created during this study and the specific methodology and strategy are outlined in the results of this thesis.

3.1.2 Plasmid construction and lentivirus production

Plasmids encoding VASH1 were cloned by the lab of Marie-Jo Moutin (Grenoble Institute of Neurosciences, France). During this thesis, pLV-YFP-VASH1-IRES-SVBP, pLV-YFP-VASH1-7E-IRES-SVBP and pLV-YFP-VASH1-7A-IRES-SVBP were used (IRES, internal ribosome entry site). The 7E variant contains glutamate residues instead of serine residues that could potentially be targeted by PRKG1A, mimicking the phosphorylated state. For the 7A variant those serine residues were mutated to alanine residues, rendering them non-phosphorylatable. In short, the mutated VASH1 constructs (7E or 7A) for immunofluorescence studies were generated by PCR amplification of the VASH1-WT construct with primers including the repective substitutions. The backbone and WT as well as expression and purification of the respective proteins were described by our collaborators (Ramirez-Rios et al., 2023). For the generation of plasmids to produce lentiviruses, all components were individually amplified via PCR (YFP, VASH1, IRES, SVBP) and cloned into the lentiviral production vector with the In-Fusion HD kit (Clonetech). In order to induce the 7A and 7E mutation, the forward primer for the amplification of the VASH1 coding sequence was altered to include the variant. All cloned plasmid constructs were verified by sequencing.

The lentiviruses used during study were generated from plasmids we received as kind gifts from Marie-Jo Moutin and produced by Dr. Ingke Braren of the Vector Facility at the UKE.

3.2 Methods

All experiments were conducted in accordance with the standard operating procedures that are in place at the Institute for Experimental Pharmacology and Toxicology at the University Medical Center Hamburg-Eppendorf.

3.2.1 Human induced pluripotent stem cell culture

3.2.1.1 Coating of culture vessels

Geltrex or matrigel aliquots were stored at -20 °C and -80 °C, respectively. Before usage, they were removed from the freezer, placed in a styrofoam box on wet ice. Once thawed geltrex was diluted 1:100 and matrigel 1:60 in cold RPMI medium. One ml/10 cm^2 culture vessel surface of the coating solution was added (48-, 24-, 12, 6-well plates or T75-flasks) and incubated for 30 to 60 min at room temperature (RT). For immediate use, vessels were incubated at 37 °C for at least 30 min, for storage, cell culture plates were wrapped with parafilm and stored at 4 °C for up to two weeks. The coating solution was removed just before the cells were plated in the intended culture medium.

3.2.1.2 Thawing of hiPSC

Cryovials containing 1-2 mio hiPSCs were collected from the -150 °C freezer and transferred to the cell culture lab on dry ice. For thawing the vials were placed in a

37 °C water bath for 2-3 min until only 20-30% of the contents remained frozen. The tube was then removed from the water bath, sprayed with 70% ethanol and placed under the sterile work bench. Afterwards, 5 ml of FTDA (DMEM-F12, 2 mM L-glutamine, 5 mg/ml transferrin, 5 µg/ml selenium, 0.1% human serum albumin, 1x lipid mix, 5 mg/ml insulin, 50 mM dorsomorphin, 2.5 ng/ml activin A, 0.5 ng/µl TGFβ, 30 ng/ml FGF2; in house) supplemented with 10 µM Y-27632 (Y) (FTDA++) were drawn up in a 5-ml serological pipette. The full pipette was used to draw up the cell solution from the cryovial and the mixture transferred to a 50-ml falcon tube. Next, cells were centrifuged at 200 x g for 3 min, the supernatant was aspirated and the tube scratched lightly to loosen the cell pellet. Finally, the cell pellet was resuspended in 2 ml FTDA++ per 1 mio and plated on 1-2 wells of a geltrex-coated 6-well plate. Culture conditions were 37 °C, 5% CO_2, 98% humidity and hypoxia (5% O_2).

3.2.1.3 Passaging of hiPSC

For passaging, hiPSCs were collected from the hypoxia incubator and placed under the sterile work bench. The culture medium was removed, and each well/flask was rinsed with warm PBS. Afterwards, accutase solution was added (1 ml/well of a 6-well plate; 5 ml/T75 flask). After 5-10 min at 37 °C, the cells were checked microscopically for detachment. The culture vessels were tapped lightly and the accutase reaction was stopped with equal amount of FTDA++. This cell suspension was transferred to a 15-ml or 50-ml falcon tube and centrifuged at 200 x g for 5 min. Following the centrifugation, the supernatant was aspirated, tubes were scratched lightly on the sterile bench, and the pellet was resuspended in FTDA++ (1 ml/well or 5 ml/T75). Cells were then counted with an automated CASY-cell counter according to manufacturer's instructions. Finally, cells were seeded at 5×10^5 cells/well for 6-well plates and 4.5×10^6/T75 onto Geltrex coated culture dishes and placed in the hypoxia incubator.

3.2.1.4 Feeding of hiPSC

HiPSCs were fed daily with FTDA without Y-27632 (FTDA+) with 2 ml/well for 6-well plates or 20 ml/T75. This schedule was kept until they reached a confluency of 80-90% and needed to be passaged.

3.2.1.5 Freezing of hiPSC/Creation of cell banks

The appropriate amount of freezing medium (90% fetal calf serum (FCS), 10% dimethylsulfoxide (DMSO), 10 µM Y) was prepared and kept cold until needed. Per cryovial 1–2 x 10^6 cells were resuspended in freezing medium (1 ml/vial) and distributed evenly in a maximum of 18 vials per cell line. The cryovials were placed in a Mr. Frosty freezing container which was then stored at -80 °C for 24 h. Lastly, the cells were transferred to ultra-low freezers for long-term storage. For the analysis of pluripotency, 5 x 10^5 hiPSCs were kept in FCS at 4 °C until further processing.

3.2.1.6 SSEA3 staining

The hiPSCs collected before freezing or during routine passaging were split into two fluorescence activated cell sorting (FACS) tubes and centrifuged for 2 min at 100 g and 4 °C. Next, the supernatant was discarded, and the cells were stained with either a stage specific antigen 3 (SSEA3)-specific antibody or an isotype control for 30 min on ice, protected from light exposure. Antibodies were diluted in SSEA3 staining buffer (phosphate-buffered saline (PBS), 5% FCS). After the staining, samples were washed with staining buffer twice and finally resuspended in PBS. FACS measurements were carried out at the FACS core facility of the UKE.

3.2.1.7 Mycoplasma testing

Mycoplasma testing was performed according to the standard operating procedures at place at the Institute for Experimental Pharmacology and Toxicology in a weekly to bi-weekly routine with cell culture supernatant or genomic gDNA. Samples were subjected to PCR testing that included a positive control and internal amplification control. Tests were conducted by Silke Reischmann-Düsener, Lisa Krämer, Grit Höppner or Ellen Orthey.

3.2.2 CRISPR-Cas9 genome editing of hiPSCs

HiPSCs were thawed and cultured as described (3.2.1.1; 3.2.1.2; 3.2.1.3; 3.2.1.4) but instead of FTDA, commercial mTesR plus was used. Prior to nucleofection, the hiPSCs needed to be at a density between 50% and 80%. The Cas9 electroporation enhancer was resuspended in the IDT duplex buffer to reach a concentration of 100µM, while the crRNA and tracrRNA were mixed at an equimolar ratio (50 µM each), incubated at 95 °C for 5 min and then cooled down to RT. HiPSCs medium was changed to mTesR plus supplemented with 10 µM Y, and a 12-well plate was coated as described before (3.2.1.1). To assemble the ribonucleoprotein complex (RNP), 2 µl of annealed crRNA and tracrRNA and 1.6 µl of Cas9 enzyme were mixed per reaction and incubated for 10 min at RT. Then the hiPSCs were passaged (3.2.1.3) and 8 x 10^5 cells/reaction were aliquoted into fresh 1.5-ml tubes. The tubes were centrifuged again at 200 x g for 2 min, and the supernatant was removed. Then, the cells were resuspended in 100 µl nucleofector solution, mixed gently with the RNP and transferred into a nucleofection cuvette. Immediately, the nucleofection was performed with an Amaxa 4D Nucleofector and placed in the hypoxia incubator for 10 min. Finally, 500 µl of mTesR plus, supplemented with 1:10 CloneR, were added to the cuvette, and the cell solution was transferred to a 12-well plate. The next day, 1 ml mTesR plus with CloneR was added per well, and after 48 h the cells were passaged (3.2.1.3) and seeded at a density of 200, 400 or 600 cells/well onto a geltrex-coated 6-well plate. The same day, the medium was used to perform a Phire Tissue Direct PCR according to the supplied protocol to check for successful genome editing.

After five to seven days, clones from the single cell seeding plate were picked with a P100 pipette and cultured in individual wells of a 48-well plate. Each clone was split once 1:2 onto copy plates, of which one was used for freezing (3.2.1.5), while the other was used for genomic DNA extraction and PCR analysis.

Clones positive for the desired genomic edit were thawed, expanded and cell banked (3.2.1.2; 3.2.1.3; 3.2.1.5). Afterwards normal karyotype was determined with the Nanostring nCounter system and performed by Lisa Krämer of the respective Core Facility at the UKE. Also, SSEA3 staining (3.2.1.6) was performed to confirm pluripotency and hiPSCs. Finally, OT analysis was performed for the ten most likely OTs for each used crRNA.

Edited cells were also differentiated into hiPSC-CMs and their transcriptome was analyzed with specific primers to confirm the genomic KO of *MATCAP1* via RT-qPCR (3.2.6.4; 3.2.6.5; 3.2.6.6).

Materials used for CRISPR-Cas9 genome editing were purchased from IDT (crRNAs; tracrRNA, Cas9, buffer) while cuvettes and nucleofector were from Amaxa/Lonza. The Specific crRNAs were designed for the targeted genomic locus with the respective online tool of IDT (IDT, 2025). This tool also calculated the OT scores and sites. A detailed layout of the genome editing strategy can be found in the results of this thesis.

3.2.3 Cardiac monolayer differentiation

3.2.3.1 Cheese protocol

HiPSCs were passaged at least three times before they were used for differentiation into hiPSC-CMs. At the start of the differentiation, cells were seeded at a density of 5-6 x 10^5 cells/well onto matrigel-coated 6-well plates. The next day, FTDA++ was exchanged for FTDA+ in the morning before Stage 0 medium (StemPro-34-SFM, StemPro Supplement 2.6%, 1 ng/ml BMP4, 2 mM L-glutamine, 1% matrigel) was added in the evening. After 14-16 h stage 0 was replaced with stage 1 medium (StemPro-34-SFM, StemPro Supplement 2.6%, 10 ng/ml BMP4, 2 mM L-glutamine, 8 ng/ml activin A), containing factors that induce specification of cardiac progenitor cells. After two subsequent 48 h incubation times, stages 2.1 (RPMI 1640, 2% B27, 10 µM KY, 10 µM XAV) and 2.2 (RPMI 1640, 2% B27, 10 µM KY, 10 µM XAV, 3.21 µg/ml insulin) were used. Both contained Wnt-inhibitors, for 2.2 also insulin was used. Finally, two days after 2.2, the feeding medium (RPMI 1640, 2% B27, 3.21 µg/ml insulin) was added every other day until cells started contracting and were ready for dissociation. Differentiations were carried out under normoxic conditions.

3.2.3.2 Dissociation of differentiated hiPSC-CMs

Dissociation of differentiated hiPSC-CMs was initiated once the culture started beating homogenously. First, the culture medium was removed, and the cells were washed twice with 1 ml warm hank’s buffered saline solution (HBSS). Afterwards, 1 ml collagenase II solution, supplemented with 10 µM Y and 30 µM N-Benzyl-Toluensulfonamide (BTS), was added per well and the cells incubated for 90-120 min at 37 °C under normoxic conditions. The cells were monitored microscopically for detachment. Once sufficient detachment was reached, the hiPSC-CMs were washed off the wells with a 1-ml pipette by triturating 3-5 times and transferred to a 50-ml falcon tube. Then equal amount of blocking medium (DMEM, 1% penicillin/streptomycin (P/S), 6 µl/ml DNase) was added and the cells centrifuged for 10 min at 100 x g. Thereafter, the supernatant was aspirated, the cell pellet was resuspended in basic medium (DMEM, 1 % P/S) and the cells were counted with a Neubauer counting chamber according to the following calculations:

Number of cells per array = sum of counted cells/number of counted arrays
Number of cells per ml = number of cells per array x 10^4 x dilution factor

In order to evaluate cTnT-positive hiPSC-CMs, a sample of 5 x 10^5 cells was taken in a FACS tube and processed as described in 3.2.3.4. The rest of the obtained hiPSC-CMs were either frozen (3.2.3.3), plated (3.2.4.2) or used for EHT casting (3.2.5.1).

3.2.3.3 Freezing of hiPSC-CMs

For freezing, the desired number of hiPSC-CMs was resuspended in freezing medium and distributed equally into cryotubes. The cryotubes were placed in a Mr. Frosty freezing container at -80 °C for 24 h and then transferred to -150 °C for long-term storage.

3.2.3.4 Analysis of cTnT-positive cells

After performing the dissociation and sampling (3.2.3.2), the hiPSC-CMs were washed once with 2 ml PBS at 200 x g for 3 min. The supernatant was discarded, 500 µl of ROTI Histofix were added and the tube was briefly vortexed. Then the sample was incubated for 20 min on ice which was followed by two washing steps with the above-mentioned parameters. When FASC analysis was intended, 500 µl of permeabilization buffer (PBS, 5% FCS, 0.5% saponin, 0.05% sodium azide) were used for another wash before the sample was split into two different tubes and either stained with a specific cTnT antibody or isotype control, both labelled with FITC for 1 h at 4 °C in the dark. Finally, samples were washed twice with 1 ml permeabilization buffer and PBS subsequently, before being resuspended in 200 µl PBS. Samples were measured with the BD FACS Canto II at the FACS Core Facility of the UKE.

Alternatively, fixed hiPSC-CMs were stained with either cTnT-AF647 antibody and DAPI or DAPI only (as isotype control) for analysis with a Chemometec Nucleocounter. Incubation time was 30 min at RT in the dark, followed by two washing steps with PBS and resuspension in 100 µl PBS.

3.2.4 2D culture of hiPSC-CMs

3.2.4.1 Thawing of hiPSC-CMs

Cryovials were collected from the -150 °C freezer and transferred to the cell culture lab on dry ice. Vials were placed in a 37 °C water bath until only 20-30% of the contents remained frozen. Afterwards, the cryovial was placed under the sterile workbench and the contents transferred to a 50-ml falcon tube. Next, the cell vial was washed with 1 ml thawing medium (RPMI16040, 10% B27, 1% P/S), followed by 8 ml that were added to the cell falcon dropwise over 60 s while continuously swirling it. The falcon was inverted twice, and a sample was taken for counting. Counting was done in a Neubauer counting chamber according to the following calculation:

Number of cells per array = sum of counted cells/number of counted array
Number of cells per ml = number of cells per array x 10^4 x dilution factor
Total amount of cells needed = number of wells x desired number of cells per well
Volume of cells = total amount of cells needed/number of cells per well
Total volume needed = (number of wells + 1) x desired volume per well
Volume of medium needed for dilution = total volume needed - volume of cells

The hiPSC-CMs were centrifuged 10 min at 100 x g, the supernatant was removed, and the cells were centrifuged again with 10 ml fresh thawing medium to wash remaining collagenase II from the dissociation away. After the second centrifugation, the cells were resuspended in the appropriate volume of medium and seeded (3.2.4.2).

3.2.4.2 Seeding of hiPSC-CMs

HiPSC-CMs were plated on geltrex-coated culture 6-, 12-, 24- or 96-well plates (see also 3.2.1.1.) in complete EHT medium (DMEM, 1% P/S, 10% horse serum (HS), 10 µg/ml insulin, 33 µg/ml aprotinin) at the following densities:

Table 3: Used culture formats and seeding densities for hiPSC-CMs.

Culture format	Seeded amount of cell
6 well	$6\text{-}8 \times 10^5$
12 well	$0.7\text{-}2.5 \times 10^5$
24 well	1×10^5
96 well	$5 \times 10^3 – 2 \times 10^4$

The exact densities used are indicated in the respective figure legends. Culture conditions were 37 °C, 7% CO_2, 98% humidity and normoxia.

3.2.4.3 Compound treatment of hiPSC-CMs

HiPSC-CMs were treated with PE, ET1, val, sac, ANP, CNP, Rp-8-Br-PET-cGMPs (RP8), DT3 or alkaline EpoY (VASHi) at various concentrations (as indicated) in serum free medium. If applicable concentrations were adapted from plasma levels in patients (sac, val; McMurray et al., 2014; Ponikowski et al., 2016) or determined experimentally by the researcher. Treatment times varied and are indicated for the respective experiments.

3.2.4.4 Transfection of human induced pluripotent stem cell-derived cardiomyocytes

Transfections of small interfering RNAs (siRNAs) into hiPSC-CMs were performed in 12-well format. First, culture medium was exchanged for 500 µl OptiMEM and the cells were placed back in the incubator for 30 min. During that time, Lipofectamine3000 was added to OptiMEM medium (4 µl/ml). The siRNAs were diluted in OptiMEM and mixed at a ratio of 1:1 with OptiMEM/Lipofectamine-mix. This mixture was then incubated for 15 min before being added to the hiPSC-CMs. After 4 h equal amount of double concentrated medium was added to the cells which were then cultured for 5 d until harvest. The used concentrations of siRNAs were as indicated and each experiment included appropriate scrambled (scr) control transfections.

3.2.4.5 Transduction of hiPSC-CMs

For lentivirus transduction, polybrene was diluted in OptiMEM 1:1250. This mixture was added to the 12- or 6-well plates with the hiPSC-CMs. Cells were then incubated for 30 min. Afterwards, the appropriate amount of lentivirus (dilution) was added to the cells and they were centrifuged 30 min at 30 °C and 2500 revolutions per minute (rpm). This was followed by a 4 h incubation time and the addition of double concentrated culture medium. Transduced cells were kept for up to 5 d.

3.2.5 Engineered heart tissue culture

3.2.5.1 Casting of EHTs

EHTs were cast either from fresh hiPSC-CMs right after dissociation (3.2.3.2) or frozen hiPSC after thawing (3.2.4.1). The mastermix for casting was prepared in 15-ml round bottom tubes containing:

Table 4: Mastermix components for casting of ten EHTs from hiPSC-CMs.

Component	amount
hiPSC-CMs	10 x 10^6
2X DMEM	56 µl
Y	1 µl
Fibrinogen	25 µl
Non-cardiomyocyte medium (NKM)	ad 1 ml

The mastermix was resuspended with a 5-ml serological pipette and put on ice. Simultaneously, 1.5 ml 2%-agarose was added to each well of a 24-well plate and a teflon spacer was placed in each row, creating casting molds for the EHTs. After 10 min, the spacers were removed and replaced with silicone racks. For casting the EHTs, 100 µl of the mastermix was mixed with 3 µl thrombin in individual 0.2-ml tubes for each EHT and immediately pipetted into a casting mold without introducing bubbles. When the mastermix was used up or the plate was full, it was transferred to the hyperoxia incubator (37 °C, 7% CO_2, 40% O_2, 98% humidity) for 1.5-2 h. Afterwards, 500 µl of warm DMEM were added to each individual EHT and the plate was incubated again for 15 min. Before collecting the EHT plate from the incubator again, another plate with 1.5 ml complete EHT medium per well was prepared. Then the EHT plate was placed under the sterile hood, tapped firmly once and the silicone racks were pulled from their agarose molds in a swift and smooth manner before being transferred to the media plate. For the experiments presented in this thesis, yellow silicone racks with a stiffness of 0.8 mN/mm were used.

3.2.5.2 Feeding and measurement of EHTs

EHTs were fed with 1.5 ml complete EHT culture medium supplemented with 200 µM tranexamic acid (TA) on Monday, Wednesday and Friday at least 90 min before being measured. Functional measurements of EHTs were performed in the White-Box systems of the IEPT. Each EHT was measured for an amount of time that guaranteed to produce a measurement of at least five individual contractions.

3.2.5.3 Pacing of EHTs

EHTs were paced either at day 30 or day 60 with custom graphene electrodes. The electrodes were placed in the 24-well plate filled with 2 ml complete medium per well instead of the usual 1.5 ml. Afterwards the EHTs were carefully inserted in the electrodes. After 2 h in the incubator, the plates were placed in a White-Box system and the electrodes were connected with the pacing leads. The parameters for electrical pacing were set to 2 volts (V), biphasic pulses, 4 ms per direction with frequency ranging from 1 – 2 Hz in 0.5-Hz steps.

3.2.6 Analysis of nucleic acids

3.2.6.1 DNA extraction

DNA extraction was performed from frozen cell pellets with the Quiagen DNeasy Blood & Tissue Kit (69506) according to manufacturer's instructions.

3.2.6.2 Polymerase chain reaction

PCR was performed with the Applied Biosystems AmpliTaq Gold DNA Polymerase kit (4311806) according to manufacturer's instructions. Touchdown PCR was performed as following:

Table 5: Touchdown PCR conditions.

PCR Stage	Temperature	Duration	Cycles
Pre-denaturation	95 °C	3 min	1
Denaturation	95 °C	30 seconds (s)	11
Annealing	68-63 °C (0.5 °C reduction per cycle)	30 s	
Extension	72 °C	60 s/kilobase (kb)	
Denaturation	95 °C	30 s	24
Annealing	63 °C	30 s	
Extension	72 °C	60 s/kb	
Final extension	72 °C	2 min	1
Hold	4 °C	10 min	1

Extension times and annealing temperatures were adapted to the desired amplicon size and specific primers. PCR products were analyzed on 1% agarose gels for correct fragment size with ethidium bromide. Agarose gels were imaged with a BioRad Chemidoc imaging system.

3.2.6.3 hiPSC-CMs harvesting for RNA extraction

For RNA extraction, medium of cell cultures was removed and 500 µl TRIzol reagent were used per well to detach the hiPSC-CMs. Afterwards, TRIzol-cell mixture was transferred to 1.5-ml Eppendorf tubes and frozen immediately.

3.2.6.4 RNA extraction

RNA extraction was performed with the ThermoFisher 15596026 TRIzol reagent according to manufacturer's instructions.

3.2.6.5 Complementary DNA synthesis

Synthesis of complementary DNA (cDNA) was performed with the BioRad 1708891 iScript according to manufacturer's instructions in 100-200 ng of total RNA per reaction and a negative control without reverse transcriptase (-RT).

3.2.6.6 Reverse transcription quantitative PCR reaction

RT-qPCR was performed with the Thermo Fisher K0222 SYBR-Green/ROX Master Mix according to manufacturer's instructions. Reaction volume was reduced to 10 µl and cycle count was increased to 45. Dilutions of 1:2, 1:5 or 1:10 of the cDNAs and specific primers were used.

3.2.6.7 Determination of nucleic acid concentrations

Purity and quantity of nucleic acids (RNA/DNA) were assessed with the NanoDrop Spectrophotometer ND-1000.

3.2.6.8 Nanostring nCounter analysis

Nanostring nCounter analysis was performed with 40 ng of total RNA per sample and custom tag sets. Experiments were carried out by Lisa Krämer of the Nanostring Core Facility of the UKE.

3.2.6.9 RNAseq analysis

For RNAseq analysis, cells were washed once with warm PBS and then detached with TrypLE 10x or Accutase solution. Detached hiPSC-CMs were scraped, centrifuged for 2 min at 500 x g in a tabletop centrifuge and washed again with warm PBS. Afterwards supernatant was discarded and the cell pellets were snap frozen in liquid nitrogen. RNA isolation for RNAseq analysis was performed with the Direct-zol RNA Microprep Kit. Resulting material was subjected to a DNase digestion step. Messenger RNAs were enrtiched with a NEBNext Poly(A) magnetic module. Libraries were prepped with the NEBNext Ultra II RNA Directional Library Prep Kit. Sequencing was performed with an Illumina NextSeq 2000 sytstem. RNAseq analysis was performed by Dr. Annika Witten and Dr. Marisol Herrera at the Core Facility Genomics of Münster University. The methods were in detail described by our group in a recent manuscript (Pietsch et al., 2024).

3.2.7 Protein analysis

3.2.7.1 2D hiPSC-CMs harvesting for protein analysis

For protein analysis via Western blot (3.2.7.3) hiPSC-CMs were washed once with warm PBS before 50-80 µl lysis buffer (ddH$_2$O, 1.5 M Tris pH 8.8, 5 mM EDTA, 30 mM sodium floride (NaF), 3% sodium dodecyl sulfate (SDS), 10% glycerol, 1 µM dithiothreitol (DTT) were added depending on culture format and cell number. Finally, cells were scraped with a cell scraper, transferred to a 1.5-ml Eppendorf tube and frozen at -80 °C.

3.2.7.2 Protein isolation from hiPSC-CMs EHTs

HiPSC-CM EHTs were washed once with PBS, removed from the silicone posts and placed in individual 2-ml Eppendorf tubes. Afterwards they were snap frozen in liquid nitrogen and stored at -80 °C until further processing. For protein isolation, 100 µl of lysis buffer supplemented with 1 µM DTT were added to each EHT. Tissues were subjected to three subsequent freeze thaw cycles with liquid nitrogen. Next, steel balls were placed in the tubes, and the samples were homogenized with a Quigen

TissueLyser twice for 30 s and 20 Hz. The steel balls were removed from the tubes and the samples were centrifuged for 30 min at 13200 rpm and RT. The supernatant was used for subsequent analysis.

3.2.7.3 Western blotting

For Western blot analysis of proteins, samples were mixed with 6x ThermoFisher Laemmli buffer and boiled for 5 min at 95 °C with shaking. Afterwards, samples were briefly spun down in a tabletop centrifuge and loaded onto BioRad 10- or 15-well 4-15% SDS-acrylamide gels. BioRad DualColor or Kaleidoscope markers were used to determine molecular weights of the analyzed proteins. Gels were run for 10 min at 80 V and at 150 V until sufficient separation was achieved in 1x electrophoresis buffer (ddH_2O, 25 mM Tris base, 192 mM glycine, 0.1% SDS) in the BioRad MiniProtean chambers. blotting was either performed for 75 min at 350 mA on ice with a wet blot setup (ddH_2O, 25 mM Tris base, 190 mM glycine, 20% methanol) or with the preset mixed molecular weight protocol and BioRad Trans-blot Turbo ready-to-assemble system and a BioRad Transblot Turbo semi-dry blotter onto 0.22-µm nitrocellulose membranes. After protein transfer, membranes were stained with Ponceau S for whole protein, washed with 0.1% Tris-buffered saline with Tween 20 (TBS-T; 0.1 molar (M) Tris base, 0.15 M sodium chloride (NaCl), 0.1% Tween 20, pH 7.5) (TBS-T) and blocked in 5% milk powder or 5% bovine serum albumin (BSA) solution (5% milk powder or BSA in TBS-T) for 90 min at RT. This was followed by washing in TBS-T and primary antibody incubation over night at 4 °C. The next day, membranes were washed and incubated with secondary antibodies for 90-120 min at RT before being imaged with the BioRad Chemidoc or Vilber imager. Horseradish peroxidase (HRP)-coupled secondary antibodies were imaged with the BioRad Western Clarity ECL solution 1705061. Dilutions of antibodies and respective diluents can be found in the appendix (I.IV Antibodies). Quantifications of protein signals were performed with the software provided by the manufacturers of the respective devices.

3.2.7.4 Immunofluorescence analysis of hiPSC-CMs

For immunofluorescence analysis (IF) of hiPSC-CMs, cells were cultured on glass bottom 96-well plates with black edges. After the respectively indicated culture period, the culture medium was removed and all wells were washed with warm PBS. Then, 50 µl Roti Histofix were added per well and the cells were fixed at 4 °C for 20 min. This was followed by two washing steps with PBS. Afterwards, primary antibodies were diluted in permeabilization buffer (PBS, 3% milk powder, 0.1% Triton X100) as detailed in the appendix (I.IV Antibodies) and incubated over night at 4 °C with gentle shaking. The next day, the wells were washed with PBS and incubated with the matching secondary antibodies in permeabilization buffer for 2 h at RT. HiPSC-CMs were washed again with PBS and then stained with 1:2000 Hoechst33342 for 20 min at RT in PBS. Imaging was performed with a Zeiss LSM800 microscope with the respective software. Cell size, volume and other metrics were assessed with Fiji and its built-in tools. For cell area, the ACTN2 (for single cells) or N-cadherin (for multiple adjacent cells) signal were quantified, this was combined with z-stack imaging for cell volume quantification.

3.2.7.5 Mass spectrometry analysis of hiPSC-CMs and hiPSC-CMs EHTs

MS was performed at the MS Core facility of the UKE from frozen hiPSC-CMs or EHTs by Dr. Hannah Voss, Bente Siebels, Ali Biabani, Kilian Müller and Prof. Hartmut Schlüter. EHTs were detached from silicone racks after washing with warm PBS. Tissues were transferred to 1.5-ml Eppendorf tubes and snap frozen in liquid nitrogen. All samples were stored at -80 °C until further processing. In short, EHTs were then dissolved in 100 mM triethyl ammonium bicarbonate supplemented with 1% SDS, cooked for 5 min at 95 °C and sonicated. Sample concentrations were evaluated with the Pierce bicinchoninic acid assay. Twenty µg were used per EHT sample. Prior to the analysis, all samples were reduced for 30 min at 60 °C with 10 mM DTT and cysteines were alkylated with 20 mM iodoacetamide for 30 min at 37 °C in the dark. This was followed by trypsin digestion at a ratio of 100:1 O/N at 37 °C. The enzymatic digestion was stopped the next morning with sodium deoxycholate and 1% formic acid. Afterwards, samples were centrifuged at 16000 x g for 5 min and the pellets dried with a vacuum centrifuge. Chromatography was performed with. Nano-UPLC system and peptides were analyzed with a quadrupole-orbitrap ion trap tribid mass spectrometer. Further details can be found in a recent publication (Pietsch et al., 2024).

3.2.7.6 Analysis of natriuretic peptides in medium

ANP levels in cell culture medium were determined using a specific ELISA kit (ThermoFischer) according to the instructions of the manufacturer. At the indicated time points, the medium was collected in 1.5-ml tubes and frozen immediately at -80 °C. The ELISA assays were performed by Prof. Dr. Maike Frye and Danny Schreier (UKE).

3.2.7.7 PRKG1A in vitro kinase assay

The underlying method for the in vitro kinase assay performed by our colleagues in Grenoble, France has been described before (Banko et al., 2011). Two µM of the respective VASH1 enzymes were incubated with or without 10 nM purified PRKG1A for 60 min at 30 °C (40 mM Tris-HCl pH 7.5, 100 mM NaCl, 10 mM MgCl2, 5% glycerol, 1 mM DTT and 60 µM ATPγS). Reaction was stopped with 20 mM EDTA and p-nitrobenzyl mesylate was used for alkylation for 60 min at RT. Samples were mixed with Laemmli buffer and Western blot was performed with an anti-thiophosphate ester antibody to detect phosphorylation sites.

3.2.7.8 Taxol-stabilized microtubule preparation

Our collegues in Grenoble, France performed the purification of HeLa-cell α-tub used for the assays according to a previously described (Souphron et al., 2024).

3.2.7.9 Immunofluorescence analysis of in vitro detyrosination activity

The specific activity of VASH1 was measured by our colleagues in Grenoble, France as described before (Ramirez-Rios et al., 2023). For microscopy, isolated MTs were incubated with 50 pM purified VASH1-SVBP for 30 min at 37 °C. MT PTMs were detected with specific antibodies and imaging was performed thereafter with a Leica DMI600/ROPER microscope. Data acquired was analyzed in Fiji with a custom plugin as described before (Ramirez-Rios et al., 2023).

3.2.7.10 Total internal reflection fluorescence micropcopy

Total internal reflection fluorescence micropcopy was performed by our colleagues in Grenoble, France as described before (Ramirez-Rios et al., 2023). In short, taxol-stabilized MTs were transferred to the imaging chambers and incubated at RT for 5 min. Unbound MTs were washed out and 30 µl of a 50 pM VASH1-construct solution were added. Imaging was performed during the first 30 min with an inverted Nikon Eclipse Ti and a 100x oil immersion lens. The frame rate was set to 50 ms per frame and the temperatue during the experiments was 35 °C. Data acquired was analyzed in Fiji with a custom plugin as described before (Ramirez-Rios et al., 2023).

3.2.8 Presentation of omics data

For RNA-seq and MS analyses, data are expressed as log2 ratio, which represents the difference in log2 mean value between the test and reference groups (=log2[test]−log2[reference]) where the mean of log2[reference] was set to 0. Dot plots were created with the clusterProfiler R package in Rstudio, version 2023.12.1,41 with adjusted *P* values (*P*adj) obtained with the Benjamini-Hochberg method for multiple comparisons.

3.2.9 Statistical analysis

The data obtained were expressed as mean ± standard error of the mean (mean±SEM) and analyzed with the GraphPad Prism 8 software. Data were tested for normality with the Shapiro-Wilk test and the Kolmogorov-Smirnov test if the first did not yield normality. If the normal distributions were not met with both tests, we performed a robust regression and outlier removal (ROUT) analysis at 1% to detect potential outliers that were removed from the analysis. When normal distributions were not met or when the sample size was insufficient to test normality (eg, n<6), a nonparametric test was applied. Unpaired Student’s t-tests were used for comparing two groups, while one-way ANOVA with Tukey’s or Dunnett’s multiple comparisons tests were used for comparing more than two groups. When two groups were divided into sub-groups by treatment, two-way ANOVA and Holm-Sidak’s multiple comparisons tests were used. Mann-Whitney U-test was used for comparing two groups with n<6 or when the values were not normal-distributed. The non-parametric Kruskal-Wallis test was employed otherwise with Dunn’s multiple comparisons test and the Brown-Forsythe & Welch ANOVA and Dunnett’s T3 multiple comparisons test used for unequal SDs. If two groups divided into subgroup had $n<6$ or were not normal-distributed, a Mixed-Effect model with Tukey’s multiple comparisons test was used. Statistical tests used are indicated in the respective figure legends. Significance levels are indicated in the figures, a p-value less than 0.05 was considered significant.

4. Results

4.1 Development of a hiPSC-CM-based *in vitro* hypertrophy model

In a study published by our group (Meyer-Jens et al., 2024) sham or TAC surgery was performed in mice by our collaborators Kristin Wenzel and Stephanie Könnemann in Greifswald. Two weeks post-surgery, a treatment with solvent or sacval via oral gavage was started and resumed for six weeks (**Figure 19A**). During that period, the mice were monitored functionally via non-invasive echocardiography (day 0, 14, 35 and 56; **Figure 19C**). After the final echocardiographic assessment (day 56), mice were sacrificed, and the level of dTyr-tub was quantified. Sham animals that received sacval did not show any changes in either dTyr-tub levels or ejection fraction (EF) over time (**Figure 19B,C**) compared to the solvent group. TAC/Solvent animals displayed a 2-fold increase in dTyr-tub levels compared to Sham/Solvent and Sham/sacval. The application of sacval in the TAC animals fully rescued the dTyr-tub levels (**Figure 19B**). Functionally TAC-operated animals showed a marked decline in ejection fraction (EF) by about 10% over the first two weeks. The application of sacval stabilized the EF of TAC mice at 40%, while TAC/Solvent animals gradually declined to below 30% (**Figure 19C**). When we plotted EF and dTyr-tub fold changes (over mean Sham/Solvent) against each other, an inverse correlation was seen between dTyr-tub levels and EF (**Figure 19D**). We also investigated fibrosis content (**Figure 19E**), which showed a pattern comparable to dTyr-tub levels. In this case, fibrosis was 4.5-fold higher in TAC/Solvent animals than in both sham groups and 3-fold higher than TAC/sacval animals. As no groups were included in this mouse study that only received the individual components of sacval, sac or val, we could not determine which of the two was responsible for the beneficial effects on dTyr-tub, EF and fibrosis. Therefore, we aimed to develop a model for cellular hypertrophy in 2D hiPSC-CMs.

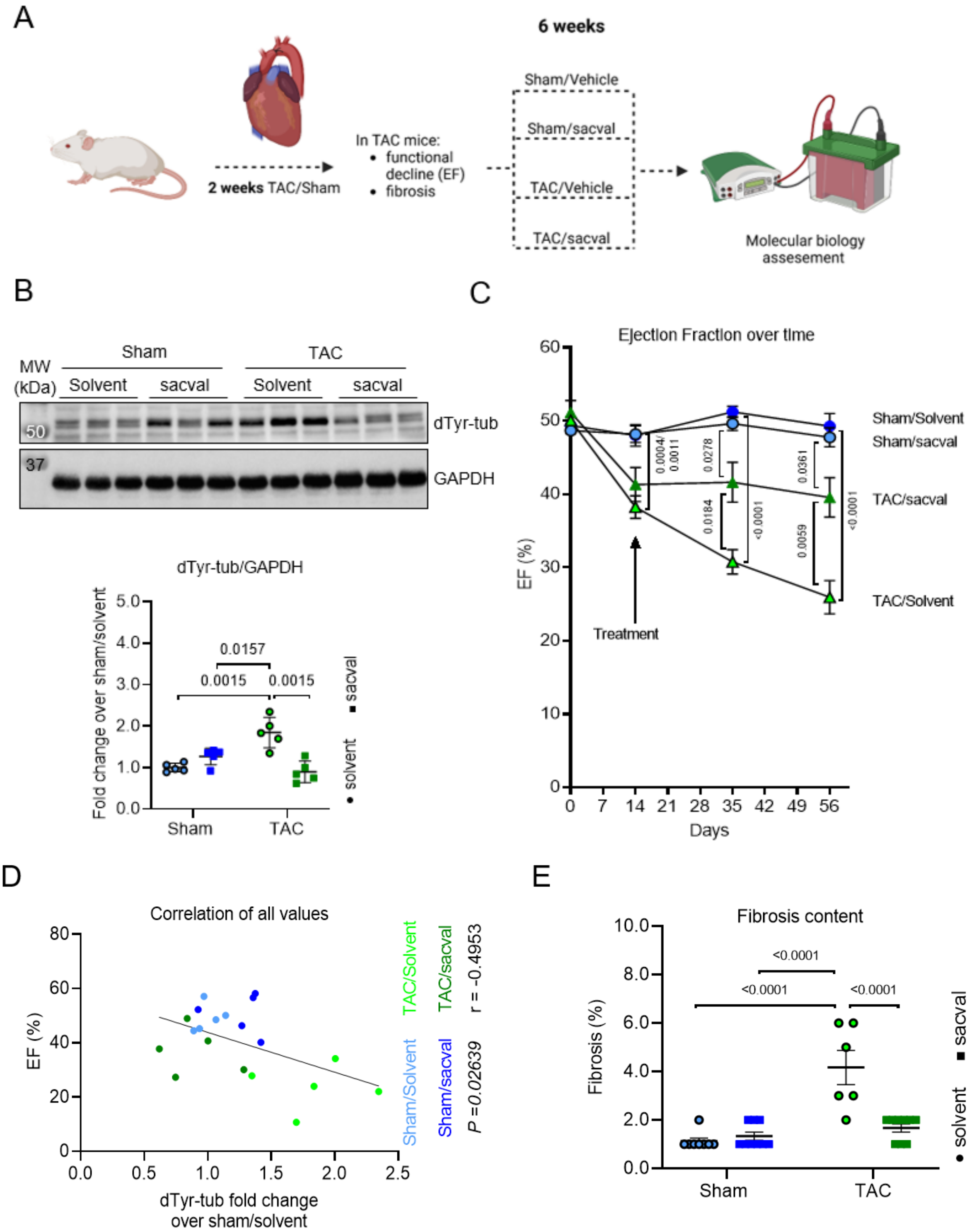

Figure 19: Previous experiments in sham/transverse aortic contriction operated mice. Mice were subjected to either sham or TAC surgery and treated with either solvent or sacval after 14 d for a total duration of 6 weeks via oral gavage. (A) Protocol (created with Biorender.com). (B) Representative Western blot and quantification of dTyr-tub-levels, normalized to glyceraldehyde-3-phosphade dehydrogenase (GAPDH) (n = 5 per group). (C) EF over time (n = 10 per group). (D) Correlation between EF and dTyr-tub content (n = 5 per group). (E) Fibrosis content (n = 6-10 per group). Data are presented as mean±SEM (A), (C) and (E). P-values were obtained with a Mixed-Effects's model test with Tukey's multiple comparisons test (B; n = 5-6), a two-way ANOVA with Tukey's multiple

comparisons test (C, E; n = 6-10) or linear regression for (D). Part of these data (echo and fibrosis content) were published in (Meyer-Jens et al., 2024).

4.1.1 Endothelin 1 causes cellular hypertrophy and transcriptional adaptations in hiPSC-CMs

First, we evaluated the mRNA levels of the *MME*, encoding the neprilysin enzyme that is inhibited by sac. We observed an almost 5-fold higher levels in septal myectomies of HCM patients (HCM+) than in non-failing tissue samples (**Figure 20A**). This suggests that *MME* is up-regulated in conditions of hypertrophy. Then, we tested different compounds to induce a hypertrophic response in RFP WT hiPSC-CMs. RFP WT hiPSC-CMs were treated with either solvent (control; H_2O), ET1 (100 nM), PE (50 µM) or a combination of ET1 and PE for 24 h. Similar to HCM septal myectomies, the *MME* levels were were about 6-fold, but not significantly, higher after 24 h of ET1, whereas PE or PE/ET1 did not affect it (**Figure 20B**). We also evaluated the level of the hypertrophic marker xin repeat protein 2 (*XIRP2*). *XIRP2* mRNA level was 2.8-fold higher in ET1-treated group than in any other groups, while PE treatment did not have an effect besides possibly masking the ET1 effect (**Figure 20C**). We performed a Nanostring analysis which did not reveal major alterations in gene expression levels between the different groups. For example, the classical hypertrophic markers *NPPA* and *NPPB* were not upregulated (**Figure 20D**). Overall, these experiments showed a presence of the *MME* transcript in the intended setting (hiPSC-CMs) making the experimental approach of modeling 2D hypertrophy viable. However, we were not in the correct conditions to induce the markers of hypertrophy in 2D hiPSC-CMs.

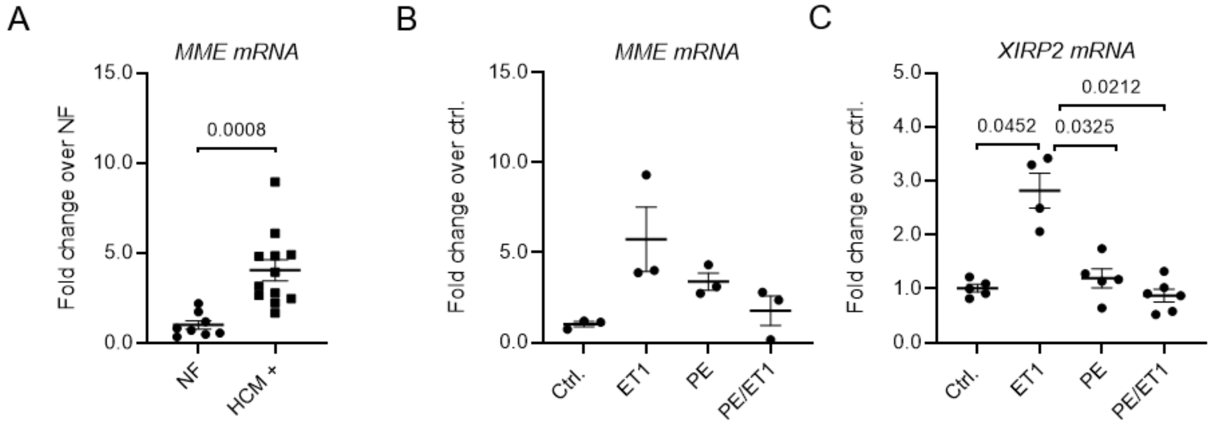

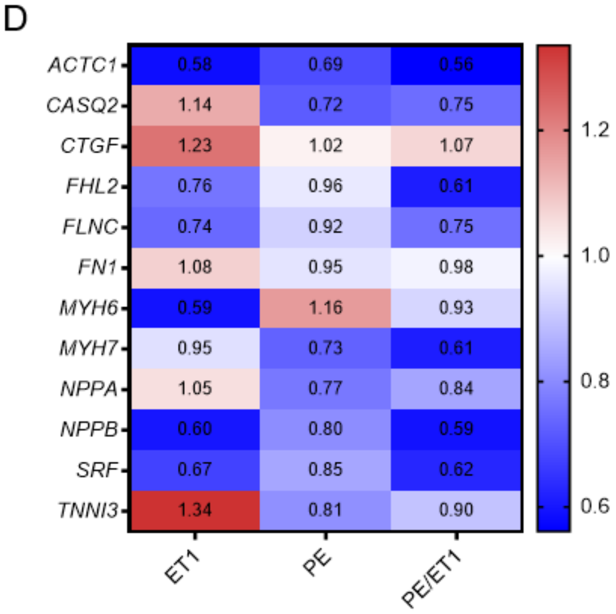

	ET1	PE	PE/ET1
ACTC1	0.58	0.69	0.56
CASQ2	1.14	0.72	0.75
CTGF	1.23	1.02	1.07
FHL2	0.76	0.96	0.61
FLNC	0.74	0.92	0.75
FN1	1.08	0.95	0.98
MYH6	0.59	1.16	0.93
MYH7	0.95	0.73	0.61
NPPA	1.05	0.77	0.84
NPPB	0.60	0.80	0.59
SRF	0.67	0.85	0.62
TNNI3	1.34	0.81	0.90

Figure 20: Gene expression analysis in different experimental settings.

Gene expression analysis analyzed by RT-qPCR with RNAs isolated from human heart tissue samples (A) or 2D hiPSC-CMs (B, C) or Nanostring nCounter anaylsis with RNA isolated from 2D hiPSC-CMs (D). (A) RT-qPCR analysis of *MME* mRNA levels in NF donor hearts (n = 8) and HCM + patient samples (n = 13). (B) RT-qPCR analysis of *MME* (n = 3) or (C) *XIRP2* (n = 4) mRNA levels in RFP WT hiPSC-CMs (RFP WT) treated with H_2O (Ctrl.), 100 nM ET1, 50 µM PE or a combination of both for 24 h. (D) Nanostring nCounter analysis of indicated transcripts in RFP WT hiPSC-CMs. Cells were treated as indicated for (B) and (C) (n = 3; data are expressed as fold-change over control, set to 1, not shown). Data are presented as mean±SEM. P-values were obtained with an unpaired Student's t-test (A) or a Brown-Forsythe & Welch ANOVA with Dunnett's T3 multiple comparisons test (B, C).

We then evaluated the level of XIRP2, α-tub and dTyr-tub by Western blot. XIRP2 level was 4-fold higher in ET1 group than in control group, 1.5-fold and 2-fold higher than in PE and PE/ET1 groups, respectively (**Figure 21A,B**). The level of α-tub did not significantly differ from control in the treatment groups (**Figure 21C**). The level of dTyr-tub did not differ between the groups (**Figure 21D**). Due to the promising effects, we continued the model development with ET1.

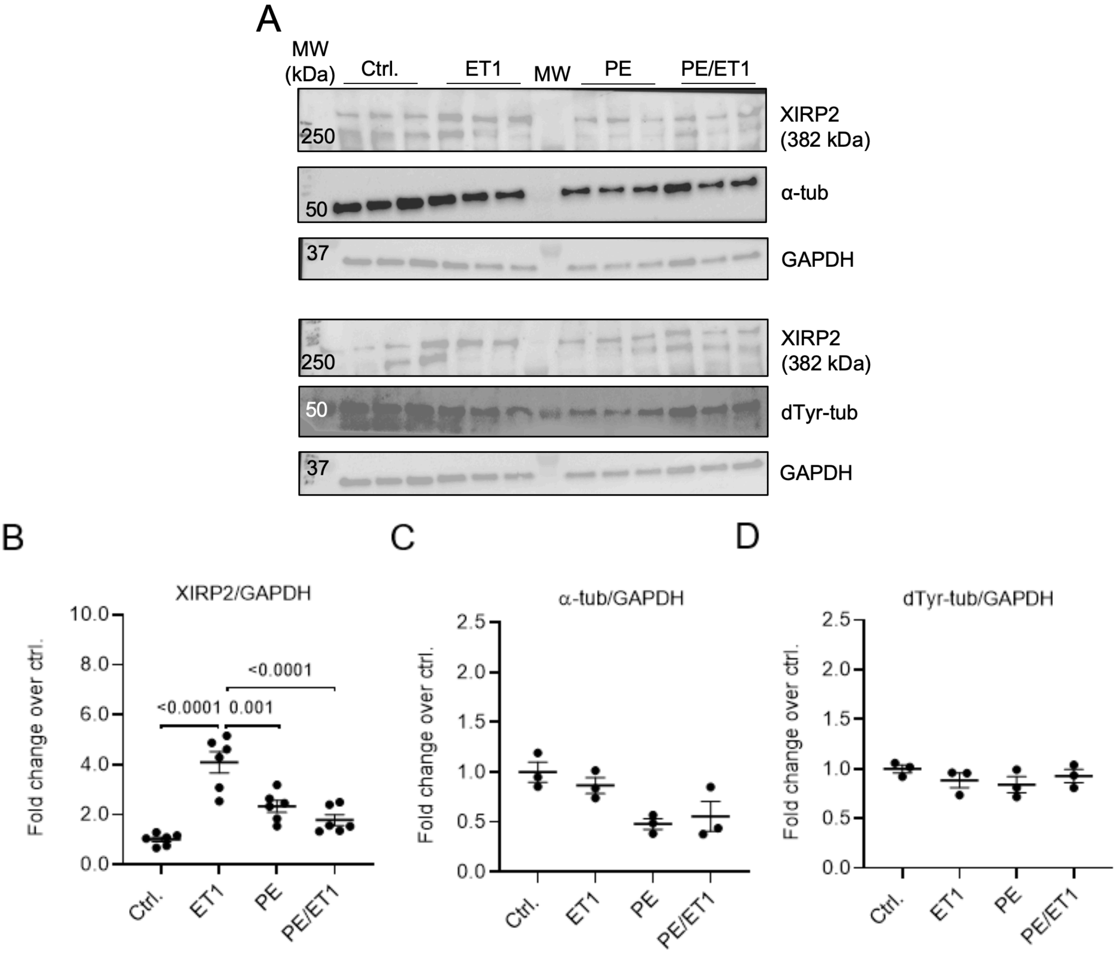

Figure 21: Western blot evaluation of XIRP2, α-tub and dTyr-tub after ctrl., ET11, PE or a combined treatment.

RFP WT hiPSC-CMs were treated with H_2O (Ctrl.), 100 nM ET1, 50 µM PE or a combination of both for 24 h. (A) Respresentative Western blot images stained for XIRP2, α-tub, dTyr-tub or GAPDH (loading control) and (B-D) show the respective quantifications. Data are presented as mean±SEM. P-values were obtained with one-way ANOVA with Tukey's post-hoc test (B; n = 6)) or a Brown-Forsythe & Welch ANOVA with Dunnett's T3 multiple comparisons test (C, D; n = 3).

We then tested the time-dependency of 100 nM ET1 on cellular hypertrophy in RFP WT hiPSC-CMs. The concentration of ET1 was tested before in our institute in 2D hiPSC-CMs. Those hiPSC-CMs were cultured in maturation medium (MM) at low density (7,500 cells/well) to allow for single cell imaging. HiPSC-CMs were treated with 100 nM ET1 over 24, 48 or 72 h in 96-well plates. At the different time points ET1-treated and time-matched control cells were fixed and stained for ACTN2 for sarcomeres and Hoechst33342 for nuclei. Afterwards, z-stack confocal images of single cells were recorded with a slice thickness of 0.29 µm. Cell volume (**Figure 22A**), cell area (**Figure 22B**) and cell height (**Figure 22C**) were evaluated with a custom Fiji macro which calculated the area based of the α-actinin 2 (ACTN2) signal and height and volume considering the z-stack slices. ET1 induced a time-dependent increase in cell volume and cell area, which were both 1.5-2.5-fold higher than control after 72 h. Interestingly, cell height did not significantly differ from control after ET1 treatment. The number of nuclei per cell also did not differ between the groups (**Figure 22D**).

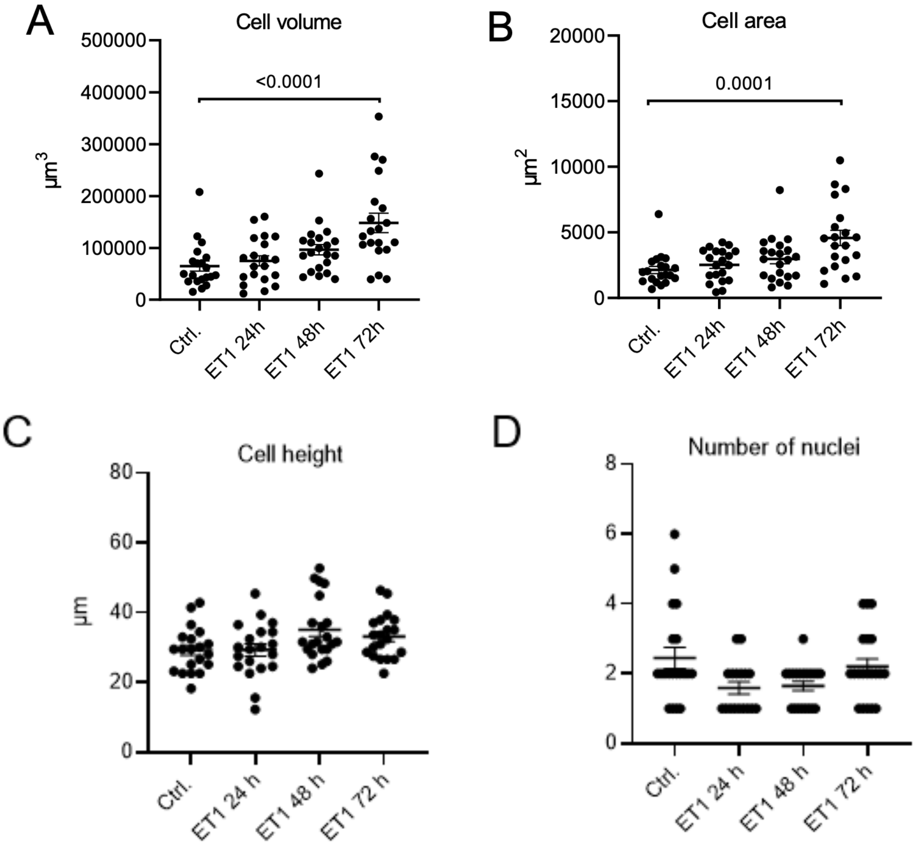

Figure 22: Assessment of time-dependent effect of control or ET1 on cellular hypertrophy of RFP WT hiPSC-CMs.

HiPSC-CMs were plated in black-edge 96-well plates at a density of 7.5 x10^3 cells/well for two weeks in maturation medium (MM) and afterwards exposed to ctrl. (H_2O) or ET1 (100 nM) treatment for 24-72 h. Medium and compounds were exchanged every 24 h. (A - D) Quantification of the indicated parameters at the indicated time points (n = 20). Data are presented as mean±SEM (B-E). P-values were obtained with a one-way ANOVA with Tukey’s multiple compariosns test (A, B; n = 20-21), a non-parametric Kruskal-Wallis test with Dunn’s multiple comparisons test (C, n = 20-21) or a Brown-Forsythe & Welch ANOVA with Dunnett’s T3 multiple comparisons test (D; n = 17-20; 3 outliers removed in ET1 24 h, 1 outlier removed in ET1 48). Some of the data were published in (Meyer-Jens et al., 2024).

Simultaneously, we evaluated the transcriptomic adaptations to ET1 treatment overtime with the Nanostring nCounter system (**Figure 23A**). The mRNA levels of several markers of hypertrophy increased with ET1 in a time-dependent manner. *NPPB* (2.81-fold), *MYH7* (1.61-fold), connective tissue growth factor (*CTGF*; 1.41-fold), calsequestrin 2 (*CASQ2*; 1.34-fold), and *NPPA* (1.32-fold) were progressively upregulated with ET1 exposure, while *TNNI3* (0.91-fold), *TTN* (0.86-fold), obscurin (*OBSCN*) (0.78-fold), four and a half LIM domains protein 2 (*FHL2*; 0.76-fold), *RYR2* (0.71-fold), *MYH6* (0.71-fold) and titin-cap (*TCAP*; 0.67-fold) were progressively downregulated. The downregulation of *MYH6* with simultaneous upregulation of *MYH7*, the downregulation of *FHL2*, and the marked upregulation of *NPPA* and *NPPB* represented clear signs of the hypertrophic gene program. This indicated that our 2D hiPSC-CM model recapitulated different aspects of this pathology. We also evaluated the levels of *XIRP2* and *MME* via RT-qPCR and revealed an upregulation of *XIRP2* at 2 by 2.7-fold (24 h), 2-fold (48 h) and 3.8-fold (72 h, non-significant; **Figure 23B**), while *MME* was only upregulated at 24 h (4.4-fold) and 72 h (2-fold; **Figure 23C**).

We considered the establishment of a 2D model for hypertrophy in hiPSC-CMs to be successful at cellular and transcriptomic level.

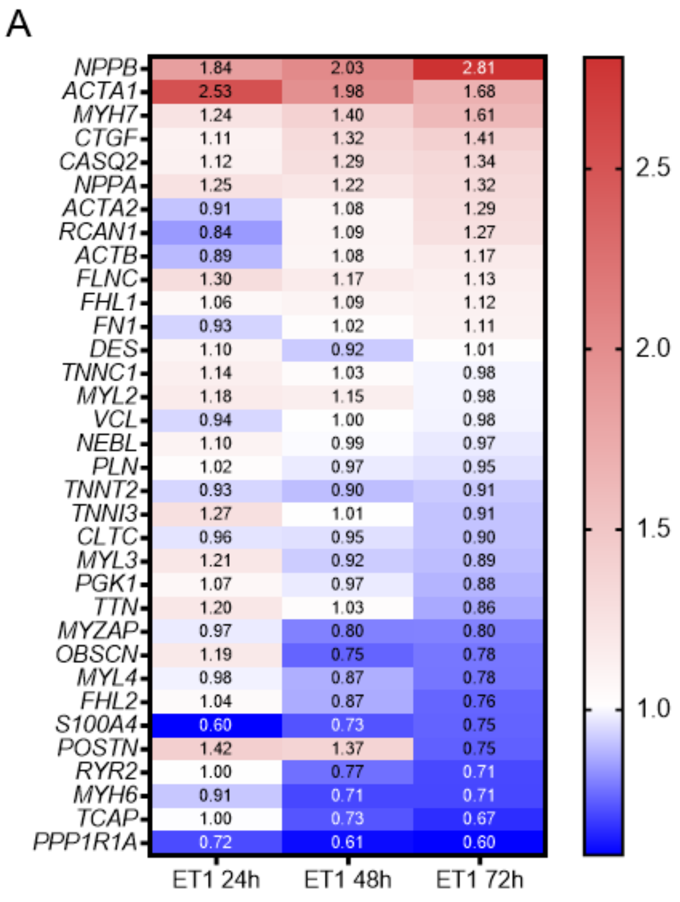

	ET1 24h	ET1 48h	ET1 72h
NPPB	1.84	2.03	2.81
ACTA1	2.53	1.98	1.68
MYH7	1.24	1.40	1.61
CTGF	1.11	1.32	1.41
CASQ2	1.12	1.29	1.34
NPPA	1.25	1.22	1.32
ACTA2	0.91	1.08	1.29
RCAN1	0.84	1.09	1.27
ACTB	0.89	1.08	1.17
FLNC	1.30	1.17	1.13
FHL1	1.06	1.09	1.12
FN1	0.93	1.02	1.11
DES	1.10	0.92	1.01
TNNC1	1.14	1.03	0.98
MYL2	1.18	1.15	0.98
VCL	0.94	1.00	0.98
NEBL	1.10	0.99	0.97
PLN	1.02	0.97	0.95
TNNT2	0.93	0.90	0.91
TNNI3	1.27	1.01	0.91
CLTC	0.96	0.95	0.90
MYL3	1.21	0.92	0.89
PGK1	1.07	0.97	0.88
TTN	1.20	1.03	0.86
MYZAP	0.97	0.80	0.80
OBSCN	1.19	0.75	0.78
MYL4	0.98	0.87	0.78
FHL2	1.04	0.87	0.76
S100A4	0.60	0.73	0.75
POSTN	1.42	1.37	0.75
RYR2	1.00	0.77	0.71
MYH6	0.91	0.71	0.71
TCAP	1.00	0.73	0.67
PPP1R1A	0.72	0.61	0.60

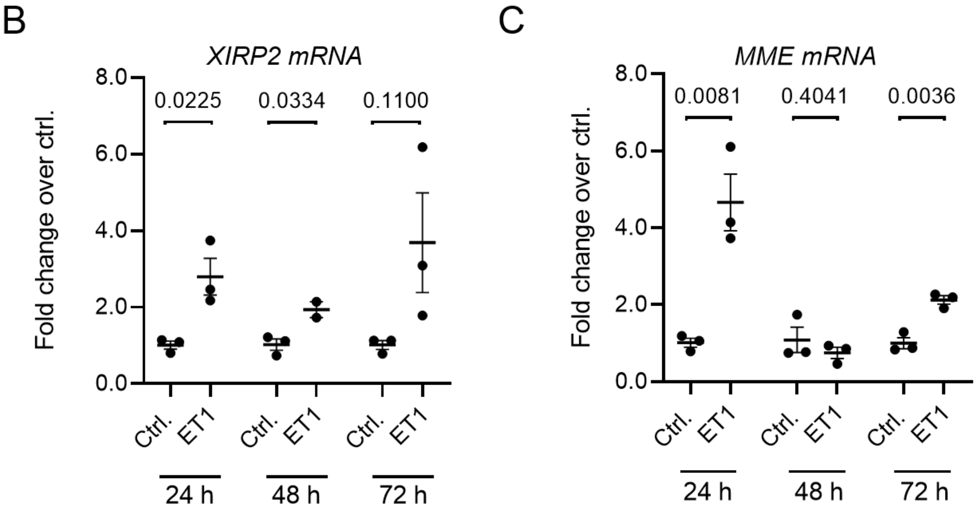

Figure 23: Transcriptional alterations after 24-72 h of control or ET1 treatment.
HiPSC-CMs were plated in 12-well plates at a density of 7 x10^4 cells/well for 2 weeks in maturation medium (MM) and afterwards exposed to ctrl. (H_2O) or ET1 (100 nM) treatment for 24-72h. Medium and compounds were exchanged every 24 h. (A) Nanostring nCounter analysis of indicated transcripts after 24-72 h of 100 nM ET1 treatment. Transcript levels are compared to time-matched ctrl. (n = 3; data are expressed as fold-change over control, set to 1, not shown). RT-qPCR analysis of (B) XIRP2 and (C) MME transcript levels after 24-72 h of ET1 treatment. Data are presented as mean±SEM (B, C). P-values were obtaind with an unpaired Student's t-test for each individual time point (B, C; n = 3).

4.1.2 Sacubitrilat prevents transcriptomic alterations, cellular hypertrophy and pathological changes in α-tubulin post-translational modifications

As a next step, we evaluated the effect of sac (40 µM), val (13 µM) or the combination of both (sacval) on the ET1 treatment for 72 h. We confirmed that ET1 for 72 h caused a drastic upregulation of *MYH7* (15.6-fold), *NPPA* (1.84-fold), *NPPB* (8.58-fold) and *CTGF* (2.73-fold), but also skeletal alpha actin 1 (*ACTA1*; 3.21-fold), *FHL1* (2.14-fold) and desmin (*DES*; 2.08-fold) while only *FHL2* (0.54-fold) and *MYH6* (0.45-fold) were downregulated. *FHL2* was the only target normalized by all treatments. More strikingly, both sac and sacval, but not val alone prevented, at least partially, the effect of ET1 on the expression of markers of hypertrophy: *MYH7* levels were at least 3-fold lower in ET1sac and ET1sacval than in ET1 alone, *NPPB*, *CTGF* and *FHL1* were at about 2-fold lower and *ACTA1* was about 40% lower in these prevention groups. Sac and sacval also prevented the ET1-induced decrease in *MYH6* mRNA level (**Figure 24A**). The changes observed in *XIRP2* and *MME* mRNA level were not significant. Still, *XIRP2* mRNA tended to be higher in ET1 compared to ctrl., which was completely prevented by the application of sac alone, but not by val alone or sacval. Furthermore, *MME* was almost 5-fold higher in ET1 than in ctrl., and sacval and sac, but not val tended to prevent the this increase (**Figure 24B**,**C**).

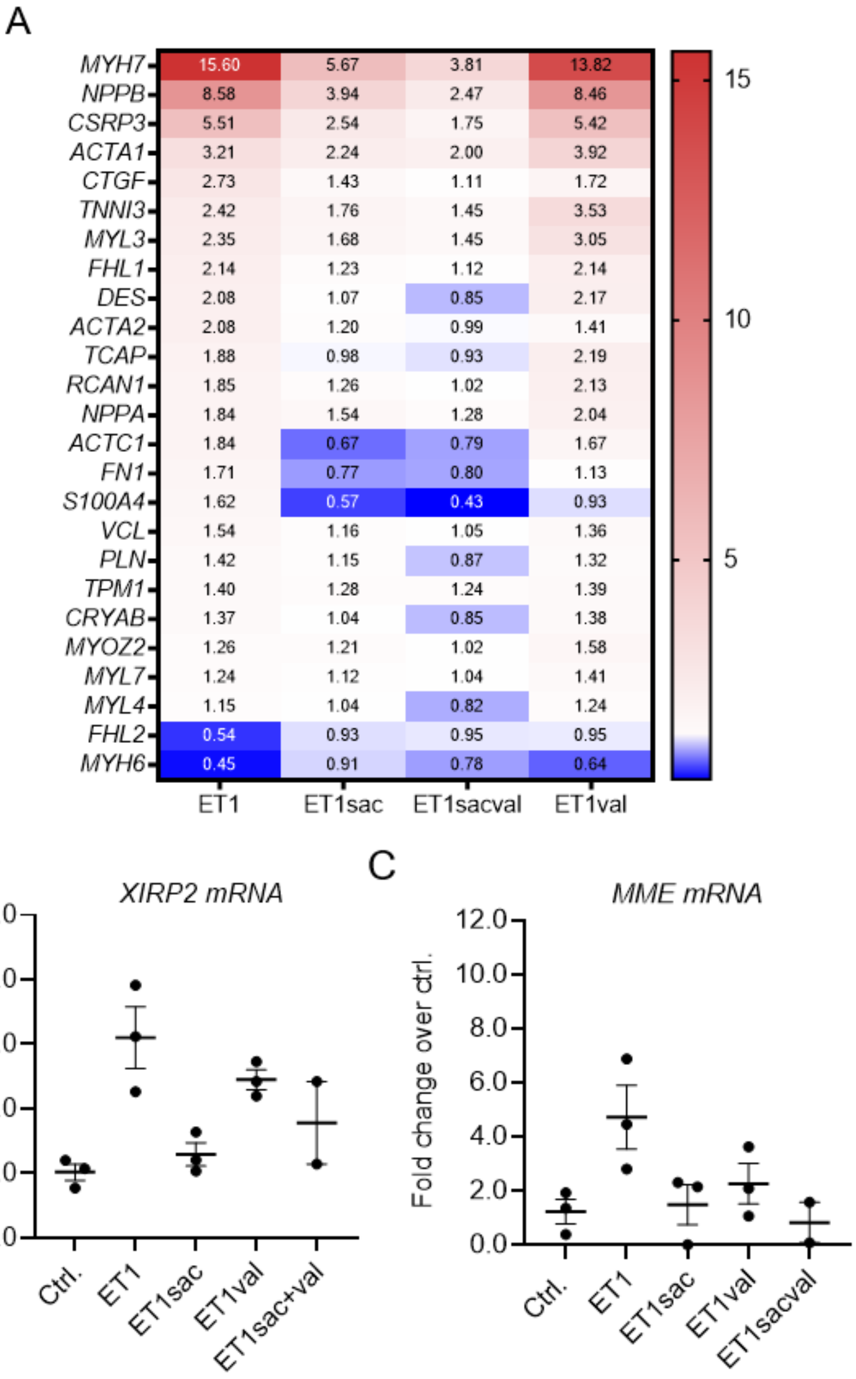

	ET1	ET1sac	ET1sacval	ET1val
MYH7	15.60	5.67	3.81	13.82
NPPB	8.58	3.94	2.47	8.46
CSRP3	5.51	2.54	1.75	5.42
ACTA1	3.21	2.24	2.00	3.92
CTGF	2.73	1.43	1.11	1.72
TNNI3	2.42	1.76	1.45	3.53
MYL3	2.35	1.68	1.45	3.05
FHL1	2.14	1.23	1.12	2.14
DES	2.08	1.07	0.85	2.17
ACTA2	2.08	1.20	0.99	1.41
TCAP	1.88	0.98	0.93	2.19
RCAN1	1.85	1.26	1.02	2.13
NPPA	1.84	1.54	1.28	2.04
ACTC1	1.84	0.67	0.79	1.67
FN1	1.71	0.77	0.80	1.13
S100A4	1.62	0.57	0.43	0.93
VCL	1.54	1.16	1.05	1.36
PLN	1.42	1.15	0.87	1.32
TPM1	1.40	1.28	1.24	1.39
CRYAB	1.37	1.04	0.85	1.38
MYOZ2	1.26	1.21	1.02	1.58
MYL7	1.24	1.12	1.04	1.41
MYL4	1.15	1.04	0.82	1.24
FHL2	0.54	0.93	0.95	0.95
MYH6	0.45	0.91	0.78	0.64

Figure 24: Transcriptional alterations after 72 h of ctrl., ET1, ET1sac, ET1val or ET1sacval treatment.

HiPSC-CMs were plated in 12-well plates at a density of 7 x10^4 cells/well for 2 weeks in maturation medium (MM) and afterwards exposed to ctrl. (0.08% DMSO), ET1 (100 nM), ET1sac (40 µM), ET1val (13 µM) or a combination of both for 72h. Medium and compounds were exchanged every 24 h. (A) Nanostring nCounter analysis of indicated transcripts after 72 h of indicated treatments. Transcript levels are compared to ctrl. (pools with n = 3; data are expressed as fold-change over control, set to 1, not shown). RT-qPCR analysis of (B) *XIRP2* and (C) *MME* transcript levels after 72 h of ET1, ET1sac, ET1val or ET1sacval treatment. Data are expressed as mean±SEM (B, C). Statistical testing was performed using a Brown-Forsythe & Welch ANOVA with Dunnett’s T3 multiple comparisons test (B, C). Data in (A) was published in (Meyer-Jens et al., 2024).

Naturally, we also investigated the influence of ET1sac, ET1val and ET1sacval on cellular hypertrophy after 72 h (**Figure 25**). As expected, cell volume and cell area were significantly higher in ET1 than in ctrl. (**Figure 25B,C**). All treatments prevented the effect of ET1 on cell volume and area, whereas only sacval prevented the ET1 effect on cell height. The number of nuclei did not differ between the groups (**Figure 25E**).

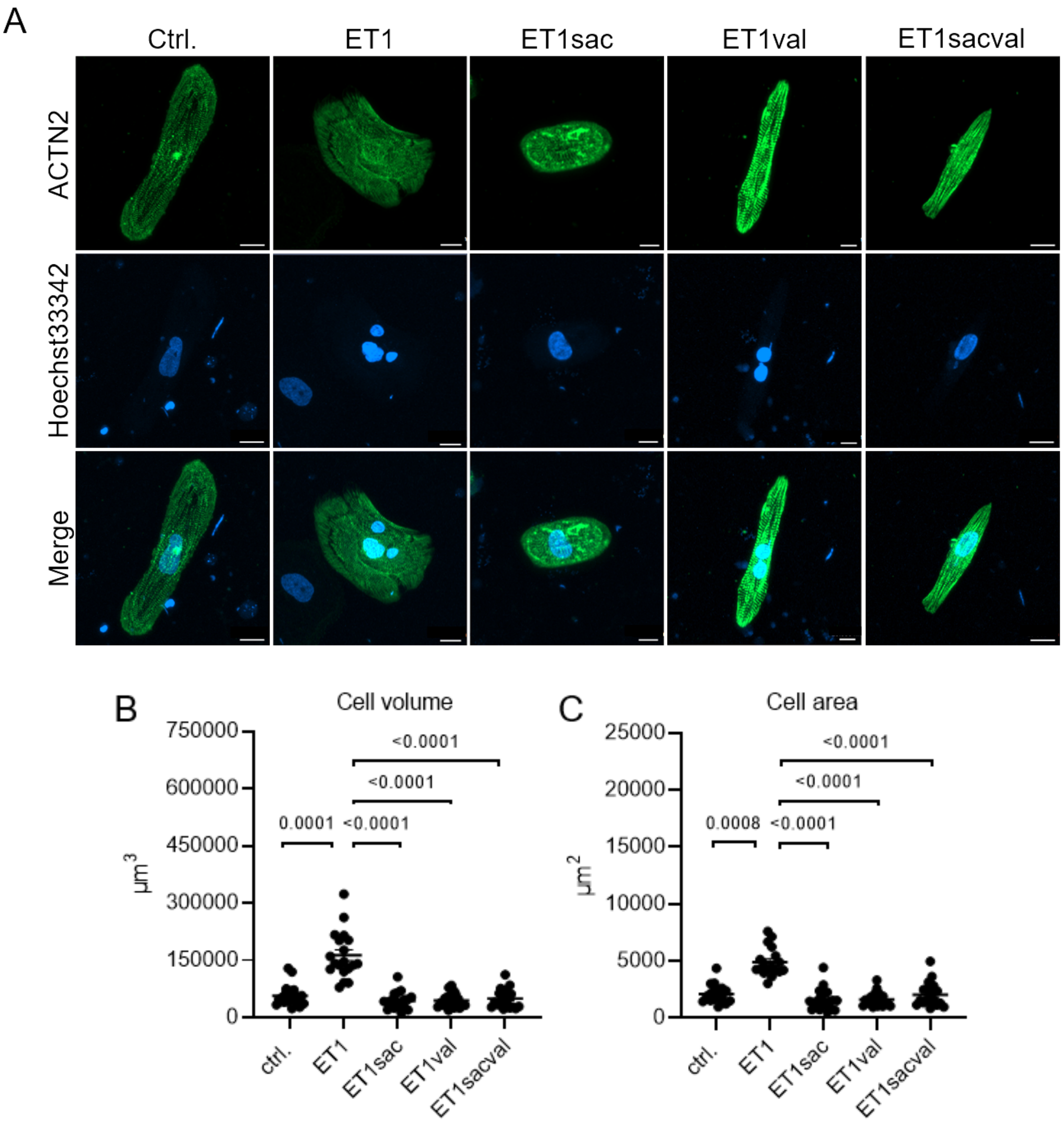

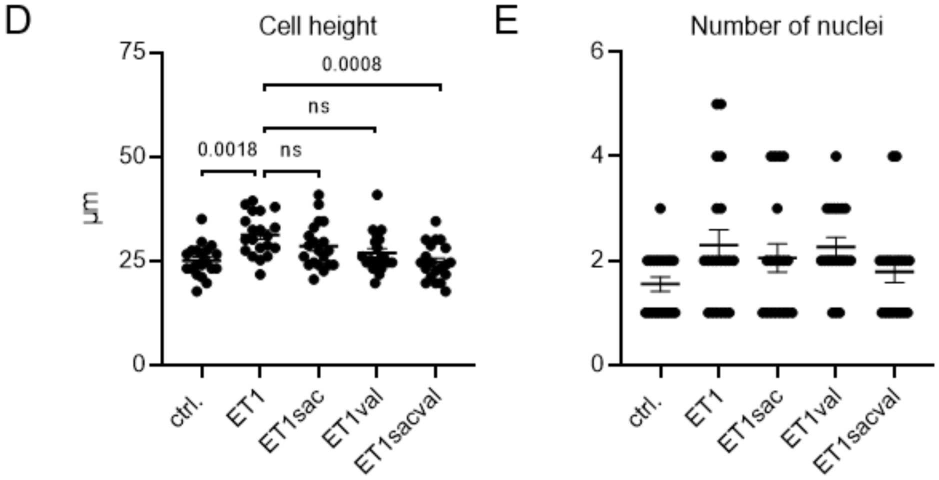

Figure 25: Assessment of the effect of ctrl., ET1, ET1sac, ET1val or ET1sacval treatment on cellular hypertrophy of RFP WT hiPSC-CMs.

HiPSC-CMs were plated in black-edge 96-well plates at a density of 7.5 x 10^3 cells/well for 2 weeks in maturation medium (MM) and afterwards exposed to ctrl. (0.08% DMSO), ET1 100 nM, ET1sac (40 µM), ET1val (13 µM) or a combination of both for 72h. Medium and compounds were exchanged every 24 h. (A) Microscopic images of RFP WT hiPSC-CMs with the indicated treatments and ACTN2 (green) for the assessment of cell area and volume and Hoeachst33342 (blue) for the DNA/nuclei staining. Scale bar represents 20 µm for ctrl., ET1 and ET1sacval and 10 µm for ET1sac and ET1val. (B-E) show the quantification of the indicated parameters at the indicated time points. Data are presented as mean±SEM. P-values were obtained wit a non-parametric Kruskal-Wallis test with Dunn's multiple comparisons test (B, C, D, E; n = 19-20; (B) 1 outlier removed in ET1; (C) outlier removed in ctrl. and ET1; (E) outlier removed in ET1sac and ET1val). Data was published in (Meyer-Jens et al., 2024).

As described before, TAC induced accumulation of dTyr-tub, which was normalized by application of sacval (**Figure 19B**). We evaluated the level of dTyr-tub after 72 h of ET1, ET1sac, ET1val or ET1sacval treatment (**Figure 26**). The level of dTyr-tub was 1.5-2-fold higher in ET1-treated than vehicle-treated RFP WT hiPSC-CMs, which was fully prevented by the co-application of sac. ET1val and ET1sacval did not significantly modify dTyr-tub-level compared to ET1.

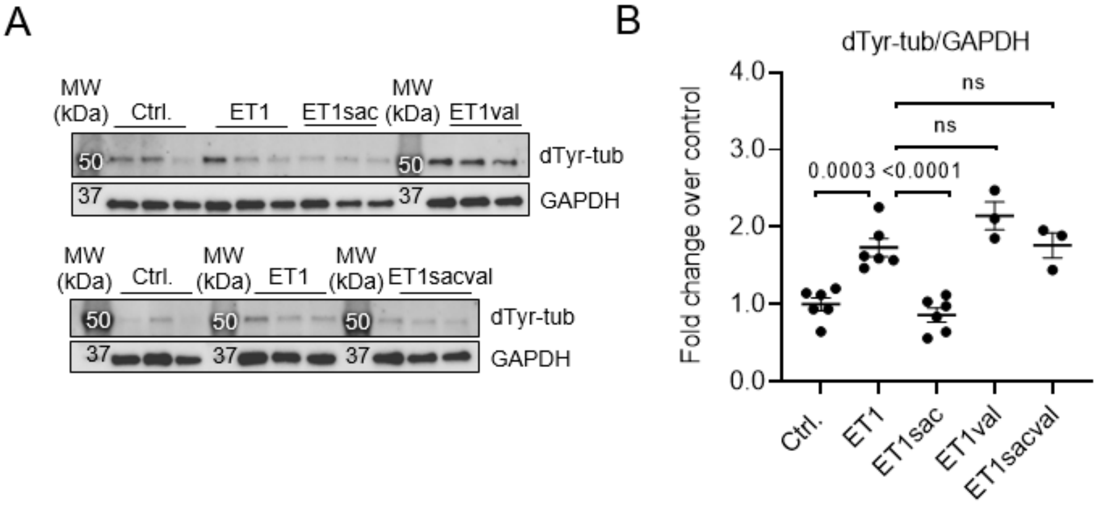

Figure 26: Western blot evaluation of dTyr-tub level after ctrl., ET1, ET1sac, ET1val or ET1sacval treatment.

HiPSC-CMs were plated in 12-well plates at a density of 7 x 10^4 cells/well for 2 weeks in maturation mediumand afterwards exposed to ctrl. (0.08% DMSO), ET1 (100 nM), ET1sac (sac 40 µM), ET1val (val 13 µM) or a combination of both (ET1sacval) for 72 h. Medium and compounds were renewed every 24 h. (A) Representative Western blots stained for dTyr-tub or GAPDH (loading control). (B) quantification of dTyr-tub level normalized to GAPDH. Data are presented as mean±SEM. P-values were obtained with a one-way ANOVA Dunnett's multiple comparisons test (B; n = 3-6).

We also evaluated the level of the PTM ac-tub, which is known to also be present on long lived MTs (Salomon et al., 2021). We observed tendencies for higher ac-tub in ET1 (2-fold) than ctrl. and prevention by sac but these were not significant (**Figure 27**).

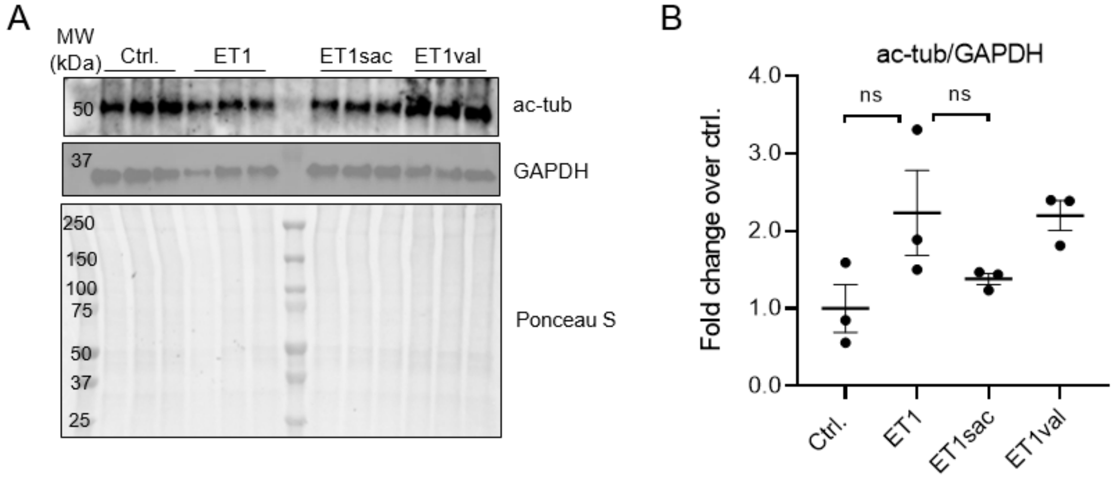

Figure 27: Western blot evaluation of ac-tub after ctrl., ET1, ET1sac or ET1val treatment.

HiPSC-CMs were plated in 12-well plates at a density of 7 x 10^4 cells/well for 2 weeks in maturation mediumand afterwards exposed to or ctrl. (0.08% DMSO), ET1 (100 nM), ET1sac (40 µM), ET1val (13 µM) for 72 h. Medium and compounds were renewed every 24 h. (A) Western blot images stained for ac-tub (acetylated tubulin) or GAPDH (loading control) and (B) the respective quantification. Data are presented as mean±SEM. P-values were obtained with a Brown-Forsythe & Welch ANOVA with Dunnett's T3 multiple comparisons test (B; n = 3).

4.1.3 Mass spectrometry analysis reveals potential pathways modulating hypertrophy in endothelin 1-treated hiPSC-CMs

To closely dissect the pathways and mechanisms at play in RFP WT hiPSC-CMs treated with ET1, ET1sac, ET1val or ET1sacval, we performed unbiased mass spectrometry analysis (MS). We found significantly higher levels of several relevant targets after 72 h of ET1 treatment compared to ctrl (FHL1, FHL2, TNNI3, TNNT2, NPPA and microtubule associated protein 1B (MAP1B; **Figure 28A**). Sac treatment normalized levels of FHL1, TNNI3 and MAP1B but not TNNT2, FHL2 and NPPA (**Figure 28B**). The application of ET1val only significantly modulated the level of FHL2 (**Figure 28C**), while ET1sacval prevented the ET1-induced increase in FHL1, FHL2, TNNI3, TNNT2 and MAP1B (**Figure 28D**).

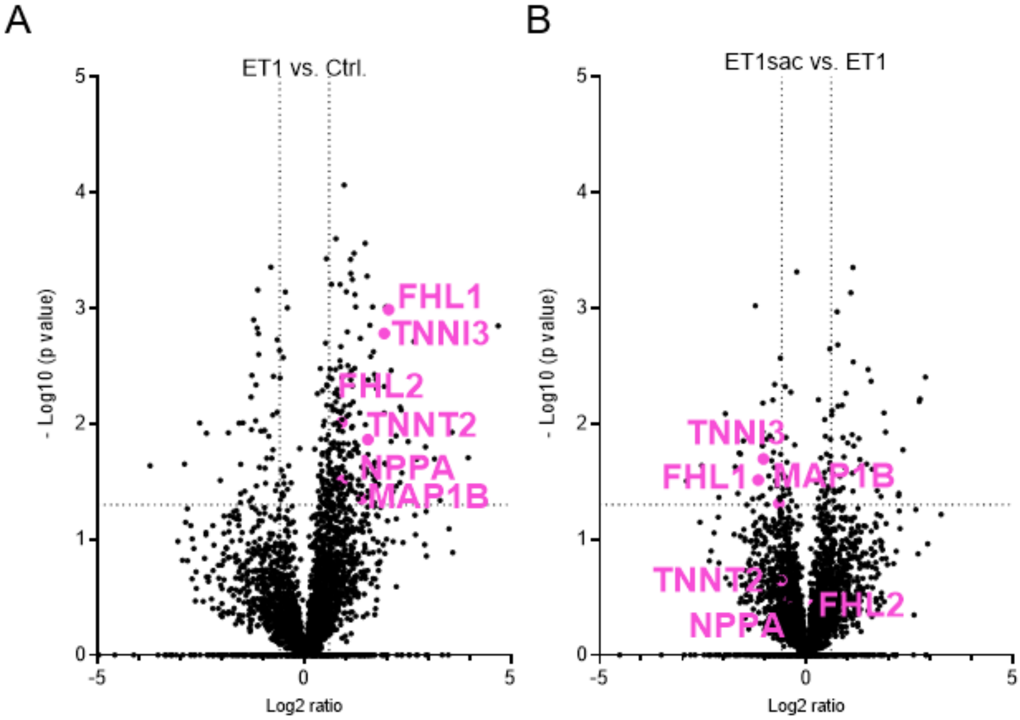

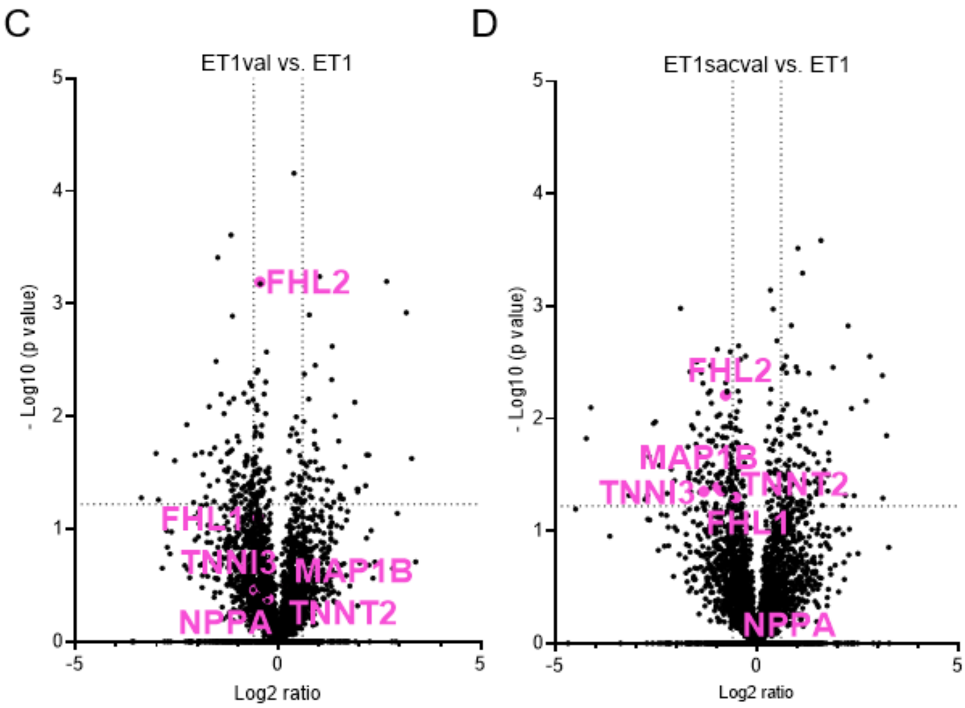

Figure 28: Volcano plot of mass spectrometry analysis of RFP WT hiPSC-CMs treated with ctrl., ET1, ET1sac, ET1val or ET1sacval.

HiPSC-CMs were plated in 12-well plates at a density of 7 x 10^4 cells/well for 2 weeks in maturation mediumand afterwards exposed to ctrl. (0.08% DMSO), ET1 (100 nM), ET1sac (40 µM), ET1val (13 µM), or a combination of both for 72 h. Medium and compounds were exchanged every 24 h. Afterwards, cells were washed with PBS and snap frozen in liquid nitrogen, before being subjected to unbiased mass spectrometry. Data are plotted as Log2 ratio (x-axis) and -Log10 (*p value*) (y-axis). (A) to (D) display the comparisons as indicated (n = 3).

After evaluating the previous experiments, we decided to separately plot the MS data of ET1-treated hiPSC-CMs compared to either ctrl (**Figure 29A**) or ET1sac (**Figure 29B**). This way we were able to interpret the changes in the ET1 group that were attenuated by ET1sac more closely. When comparing ET1 to ctrl., we found 197 proteins to be significantly higher and 43 to be significantly lower. In contrast, ET1sac resulted in 44 significantly accumulated proteins and 40 that were less abundant. Among the proteins that were enriched in ET1 compared to the ctrl. were vimentin (VIM), beta actinin (ACTB), actinin alpha 4 (ACTN4), filamin A (FLNA), filamin B (FLNB), filamin C (FLNC), FHL1, TNNI3, TNNT2, ACTA1, NPPA, MAP1B, ACTN2, actinin alpha 1 (ACTN1) and αB-Crystallin (CRYAB) (**Figure 29A**). Out of these targets, the increases in FLNA, FLNB, VIM, TNNI3, FHL1 and MAP1B were prevented by sac (**Figure 29B**).

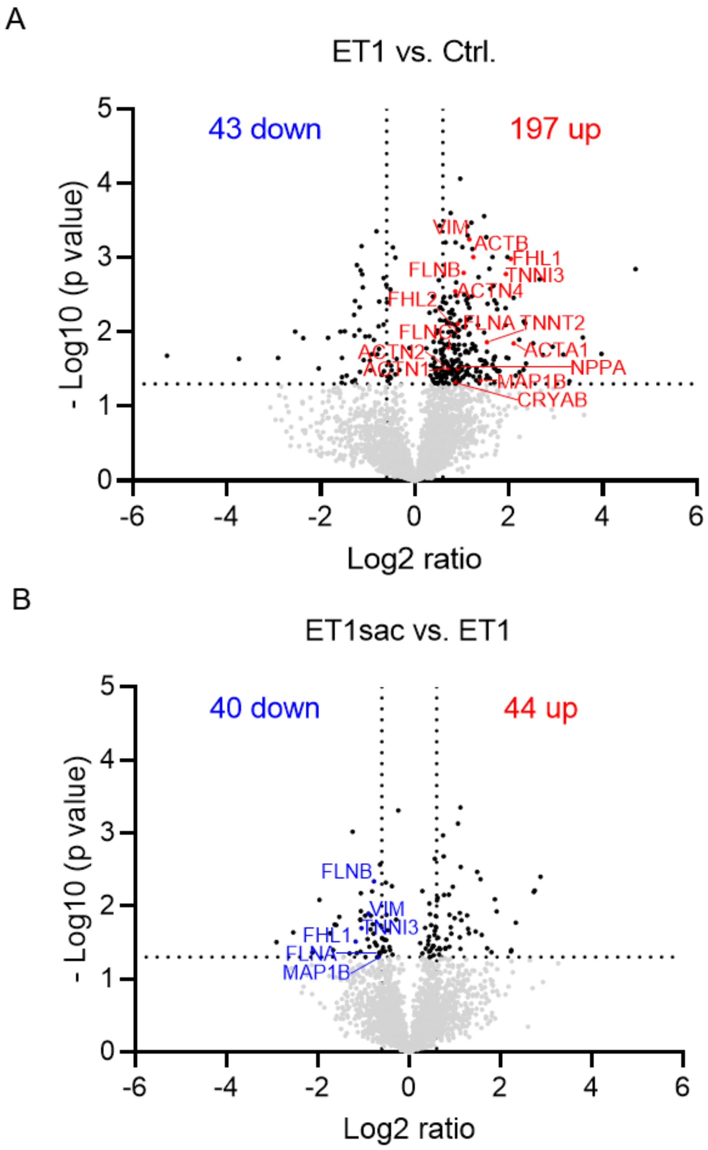

Figure 29: Volcano plot of mass spectrometry analysis of RFP WT hiPSC-CMs treated with control, ET1 or ET1sac.

HiPSC-CMs were plated in 12-well plates at a density of 7 x 10^4 cells/well for 2 weeks in maturation medium and afterwards exposed to ctrl. (0.08% DMSO), ET1 (100 nM) or ET1sac (40 µM) for 72 h. Medium and compounds were exchanged every 24 h. Afterwards, cells were washed with PBS and snap frozen in liquid nitrogen, before being subjected to unbiased mass spectrometry analysis. Data are plotted as Log2 ratio (x-axis) and -Log10 (p value) (y-axis). (A) and (B) show the comparisons as indicated (n = 3). Data was published in (Meyer-Jens et al., 2024).

4.1.4 Bulk RNA sequencing reveals broad transcriptional changes in endothelin 1-treated hiPSC-CMs

To further deepen our insights into the differentially expressed genes in RFP WT hiPSC-CMs treated with ET1 or ET1sac, we performed bulk RNAseq analysis. In ET1-

treated hiPSC-CMs, ankyrin D1 (*ANKRD1*), cysteine and glycine rich protein 3 (*CSRP3*), nebulin-related anchoring protein (*NRAP*), bone morphogenic protein 10 (*BMP10*), ATPase Na+/K+ Transporting Family Member Beta 4 (*ATP1B4*), *MYH7*, *NPPB*, *NPPA*, *DES*, *XIRP2* and *MME* were significantly upregulated while aurora kinase B (*AURKB*), kinesin family member 20A (*KIF20A*), kinesin family member 18A (*KIF18A*), kinesin family member 14 (*KIF14*), centromere protein U (*CENPU*) and centromere protein M (*CENPM*) were significantly downregulated compared to ctrl. (**Figure 30A**). When comparing ET1sac to ET1 treated RFP WT hiPSC-CMs, *KIF20A*, kinesin family member 1C (*KIF1C*), kinesin family member 4A (*KIF4A*), centromere protein F (*CENPF*) and *CENPU* were upregulated while *ACE2*, periostin (*PSTN*), NP receptor 3 (*NPR3*), *XIRP2*, *MME* and *BMP10* were downregulated (**Figure 30B**).

We then analyzed the enrichment of gene ontology (GO) terms in the 2-fold up- or downregulated transcripts in both comparisons. The genes that were significantly changed and at least 2-fold higher expressed in ET1 compared to ctrl. were matched to terms like muscle contraction, extracellular matrix organization, actin cytoskeleton organization, supramolecular fiber organization, heart development, anatomical structure development and response to stimulus (**Figure 30B**). When examining the transcripts that were at least 2-fold downregulated in the ET1 group compared to the ctrl., GO terms like kinetochore organization, sister chromatid segregation, chromosome segregation, cell cycle checkpoint signaling, mitotic cell cycle, cell division, DNA replication, microtubule cytoskeleton organization and cytoskeleton organization were found (**Figure 30C**). We carried out the analogous analysis for the comparison of the ET1sac with the ET1 group. Through this, we uncovered that GO terms matching the regulation of chromosome segregation, mitotic spindle organization, G2/M transition of mitotic cell cycle, microtubule cytoskeleton organization involved in mitosis, regulation of nuclear division (among others) were deducted from the at least 2-fold upregulated (**Figure 30E**), while the terms muscle tissue development, cell adhesion, heart development and extracellular region (e.g.) were matched to the at least 2-fold downregulated transcripts (**Figure 30F**).

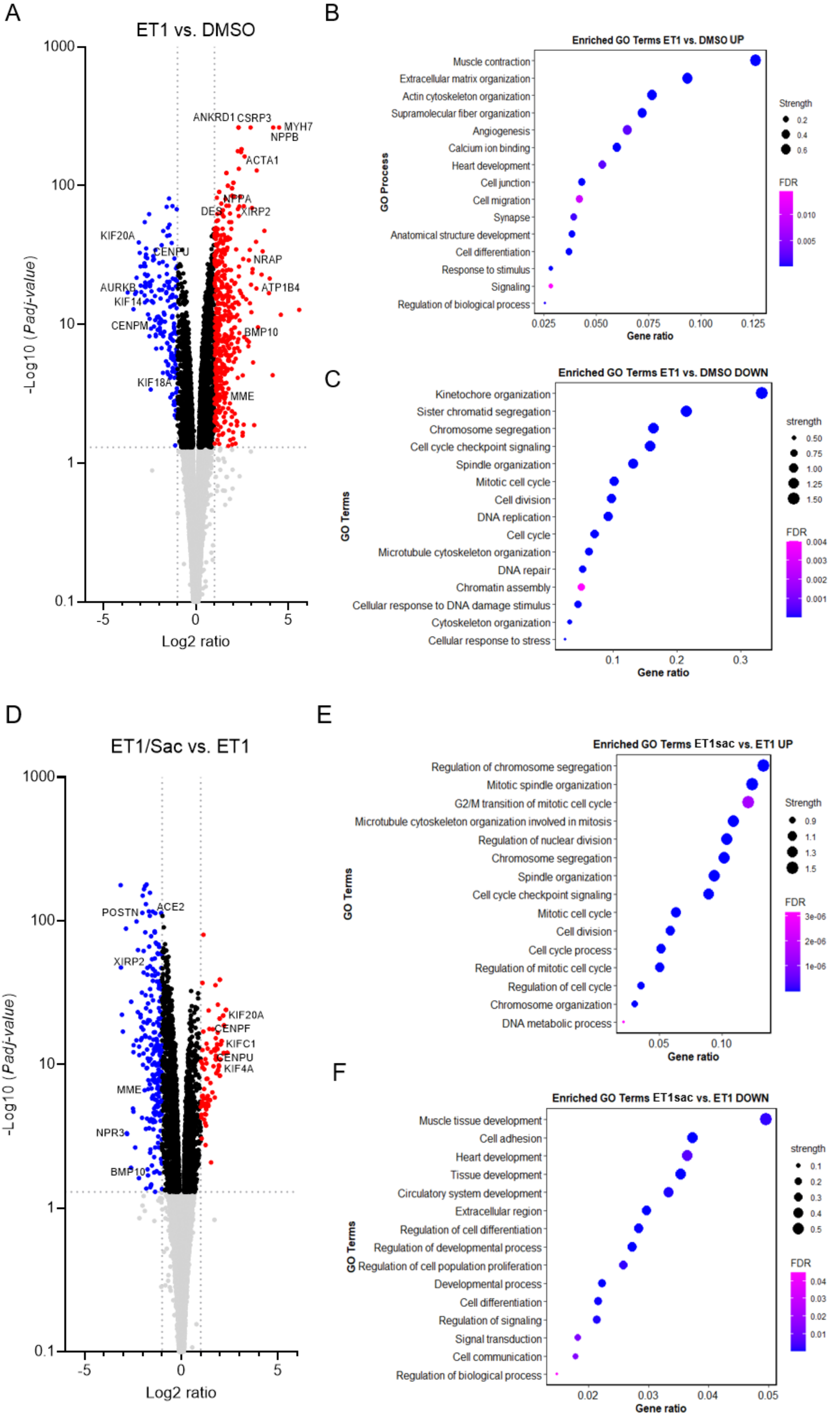

Figure 30: RNAseq analysis of RFP WT hiPSC-CMs treated with ET1 or ET1sac compared to ctrl.

HiPSC-CMs were plated in 12-well plates at a density of 7 x10^4 cells/well for 2 weeks in maturation mediumand afterwards exposed to ctrl. (0.08% DMSO), ET1 (100 nM) or ET1sac (40 µM) for 72 h. Medium and compounds were exchanged every 24 h. Afterwards, cells were snap washed with PBS and snap frozen in liquid nitrogen, before being subjected to bulk RNAseq analysis. Volcano plots of (A) ET1-treated hiPSC-CMs compared to ctr. and (D) ET1sac-treated hiPSC-CMs compared to ET1. Adjusted p-value (padj) depicted on y-axis and Log2 ratio on x-axis. Dot plots of enriched GO terms of transcripts that are either (B, E) 2-fold higher or (C, F) 2-fold lower and significantly changed with regard to padj in the respectively indicated comparisons (n = 3).

From the same data set we also extracted the number of commonly dysregulated genes. While ET1 caused the dysregulation of 1547 transcripts compared to ctrl. (DMSO), ET1sac dysregulated only 1001 transcripts (**Figure 31**). In the overlap, 774 transcripts were found.

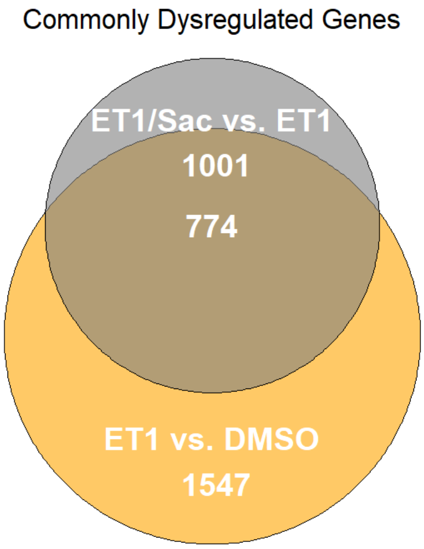

Figure 31: Number of commonly dysregulated genes in ET1 vs. DMSO and ET1sac vs. ET1. Samples were treated as described before (Figure 30). For the analysis, transcripts that were changed with a Log2 ratio of >1 or < -1 and padj-value of < 0.05 were considered.

We used the overlapping genes to generate **Figure 32** to show the counteracting effect of ET1sac compared to ET1 only. This underlines the tendencies that were already observed with the analysis in **Figure 30A,D**. The expression pattern of the cell cycle marker *Ki67* (*MKI67*) was inversed when comparing ET1 with ctrl. (Log2 ratio -2.95) and ET1sac with ET1 (Log2 ratio 1.90). Other cell transcripts involved in cell cycle regulation such as cyclin dependent kinase inhibitor 2C (*CDKN2C*) and cyclin dependent kinase 1 (CDK1) displayed a similarly inverse expression pattern. As we had observed in the Nanostring data before (**Figure 24**), *NPPB* was prominently more abundant in ET1 compared to ctrl. (Log2 ratio 4.18) but not fully prevented by ET1sac compared to ET1 (Log2 ratio -1.69; **Figure 32**).

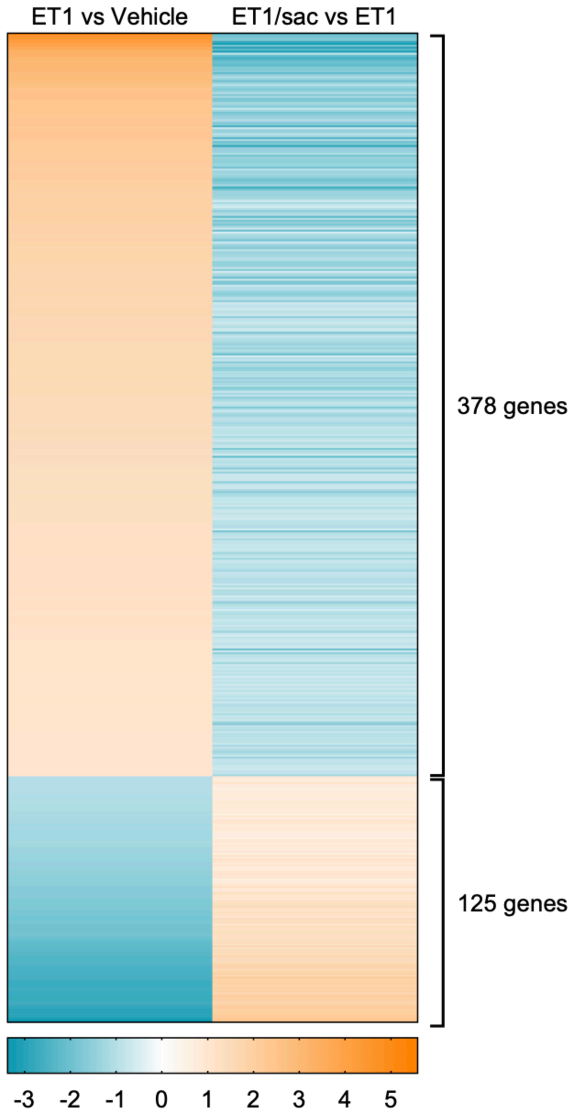

Figure 32: Normalized genes from RNAseq analysis.

Samples were treated as described before (Figure 30). For the analysis, transcripts that were changed with a Log2 ratio of >1 or < -1 and padj-value of < 0.05 were considered.

4.1.5 Endothelin 1 and sacubitrilat treatment modulate proteasomal activities

As during the development of HCM and HF cellular pathways such as the proteasomal degradation are commonly dysregulated (Schlossarek & Carrier, 2011), we aimed at evaluating the chymotrypsin-like activity, which serves as a surrogate for the proteolytic activity of the ubiquitin-proteasome system. Samples from ventricular tissue of the mouse study and those generated from the hiPSC-CMs were analyzed with this regard. In mice, the chymotrypsin-like activity was 2-fold higher in the TAC/solvent group than in all other groups (**Figure 33A**). In 2D hiPSC-CMs, the chymotrypsin-like activity was 1.5-fold higher after 72 h of ET1 exposure than of vehicle. Sac partially prevented this effect, but it was not significant.

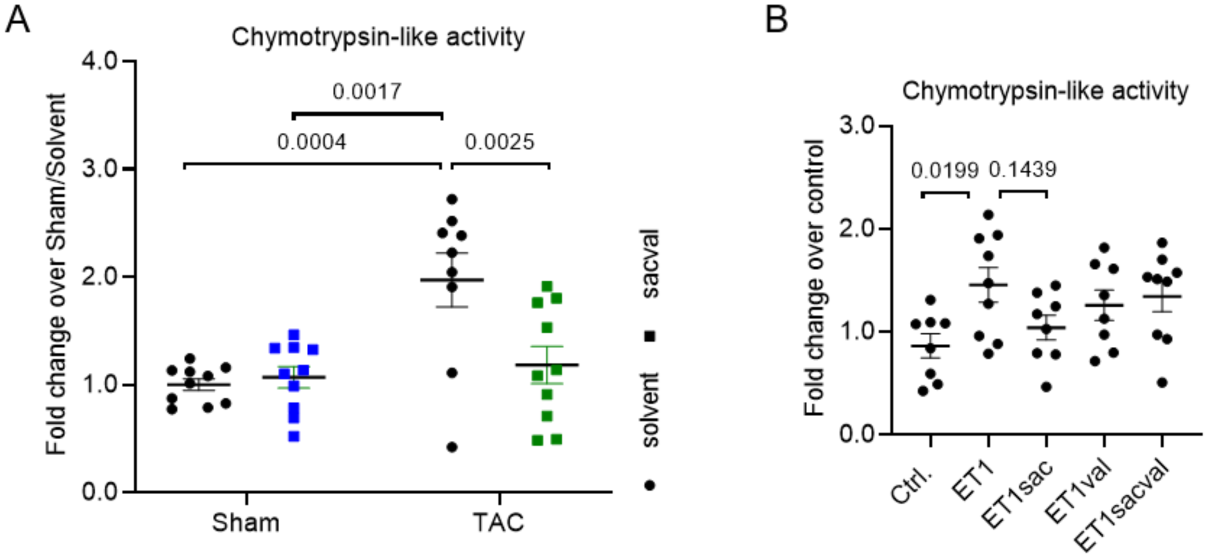

Figure 33: Evaluation of chymotrypsin-like activity in mouse heart tissue and hiPSC-CMs.
Mice were treated as described before (Figure 19). RFP WT hiPSC-CMs were as before treated for 72 h with daily medium changes with either ctrl. (0.08% DMSO), ET1 (100 nM), ET1sac (40 µM), ET1val (13 µM) or ET1sacval. Afterwards cells were snap-frozen, and the cytosolic fraction was used for the assay. (A) Chymotrypsin-like activity in ventricular tissue of sham/TAC mice treated with solvent or sacval and (B) chymotrypsin-like activity in RFP WT hiPSC-CMs treated as outlined. Data are presented as mean±SEM. P-values were obtained with a Mixed-Effect Model with Tukey's multiple comparisons test (A; n = 9-10) or a one-way ANOVA with Tukey's multiple comparisons test (B; n = 8-9 in 3 batches) (B). Data was published in (Meyer-Jens et al., 2024).

4.1.6 Summary of the endothelin 1-based hiPSC-CM hypertrophy model

To summarize, we have first described the heart function and dTyr-tub levels in TAC operated mice to be significantly impaired and higher respectively. A six-week treatment with sacval was sufficient to stabilize heart function and fully normalize dTyr-tub levels. To understand the underlying molecular mechanisms, a hiPSC-CM-based *in vitro* model for CM hypertrophy with the use of ET1 was developed. This model showed typical transcriptomic dysregulations and cellular hypertrophy. Both effects were time dependent. Interestingly, treatment with sacval and the individual components revealed that only sac was able to prevent the 1.5-2-fold increase in dTyr-tub otherwise observed with ET1-treatment. Sac was also able to prevent key transcriptomic and proteomic alterations as well as normalize chymotrypsin-like proteasome activity. These results suggested a superior role of sac in the above-described mouse model compared to val.

4.1.7 Hypothetical pathway for the mechanism of action of sacubitrilat downstream of the inhibition of neprilysin

After synthesizing all our data obtained in the 2D hiPSC-CM hypertrophy model, we developed the hypothesis illustrated in **Figure 34**. We hypothesize that the inhibition of MME causes an increase of the A-, B- and C-type NPs. Their receptors, NPRA/B have a pGC that converts GTP to cGMP upon substrate binding (Mezzasoma et al. , 2021; Pandey, 2014). The increasing levels of intracellular cGMP then cause an activation of PRKG1A which can phosphorylate multiple downstream targets. Glycogen synthase kinase 3B (GSK3B) is one of the classical targets that is inactivated by a phosphorylation of serine 9 (Das et al., 2008). In neurons, it was shown that active GSK3B can phosphorylate MAP1B, a target that was significantly upregulated by ET1 and normalized by ET1sac. This particular phosphorylation would also be inhibitory. In this context, MAP1B has also been implicated as a regulator for MT dynamics, especially in neuronal growth cones (Leibinger et al., 2023). Moreover, GSK3B is also known to phosphorylate and inactivate collapsin response mediator protein 2 (CRMP2) (Xia et al., 2013) and microtubule associated protein 4 (MAP4), which are both associated with tubulin tyrosination and microtubule dynamicsy (Kitazawa et al., 2000). Lastly, we also hypothesize that VASH1, the key detyrosinating enzyme in CMs, could possess a phosphorylation site that is recognized by PRKG1A. In this case, the phosphorylation would be inhibitory. In short, we propose that sac increases natriuretic peptide levels and therefore PRKG1A activity via intracellular cGMP elevation. This active PRKG1A then inactivates multiple targets, including VASH1, that critically modulate microtubule PTM levels.

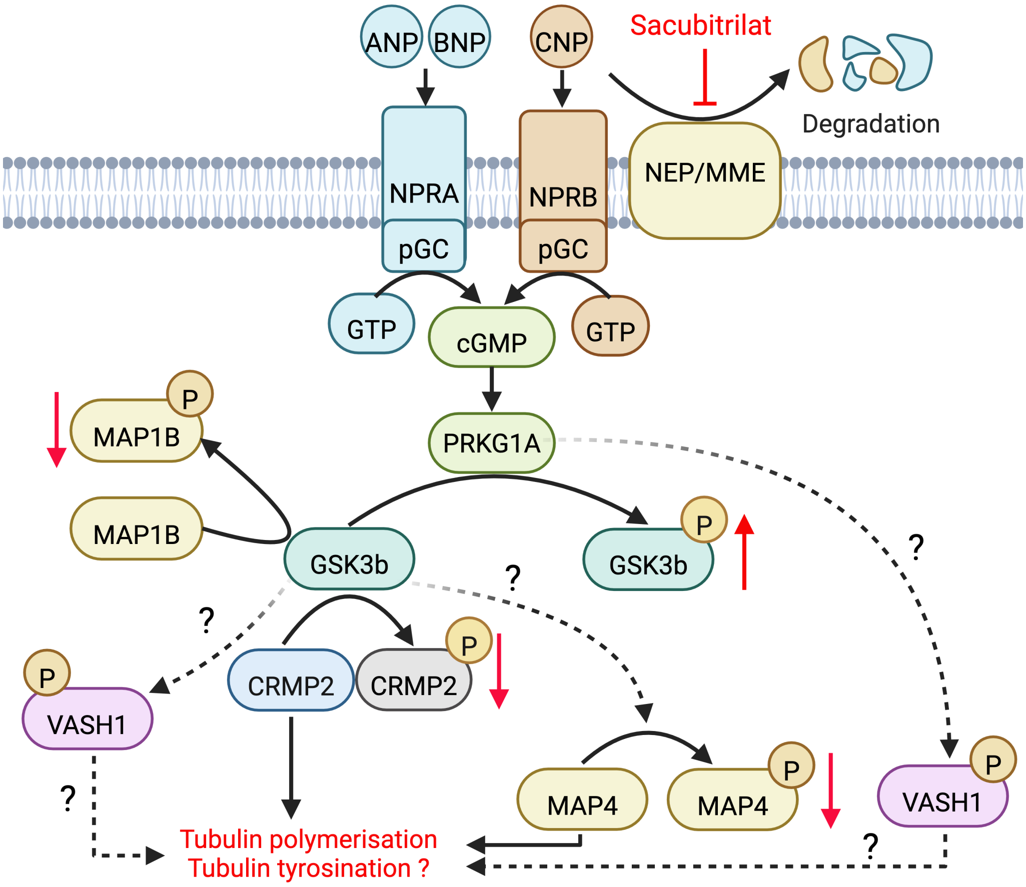

Figure 34: Hypothetical pathway for the downstream influence of sacubitrilat on cGMP-PRKG1A signaling and microtubule post-translational modifications.

Abbreviations: ANP, atrial natriuretic peptide; BNP, brain type natriuretic peptide; CNP, C-type natriuretic peptide; cGMP, cyclic guaniosine monophosphate; CRMP2, collapsing response mediator protein-2; GSK3b, Glycogen synthase kinase-3 beta; GTP, guanosine triphosphate; MAP1B, microtubule associated protein 1B; MAP4, microtubule associated protein 4; MME/NEP, neprilysin; NPRA, natriuretic peptide receptor A; NPRB, natriuretic peptide receptor B; P, phosphorylation/phosphate group; pGC, particulate guanylate cyclase; PRKG1A, protein kinase G 1A; VASH1, vasohibin 1.

4.2 Modulation of PRKG1A signaling in hiPSC-CMs

As outlined in the previous chapters, we had justified reasons to believe that the modulation of PRKG1A activity can directly modulate dTyr-tub levels via phosphorylation of the main detyrosinase in hiPSC-CMs, VASH1. In the following chapter, we investigated the different levels of this hypothesis.

4.2.1 Inhibition of PRKG1A by Rp-8-Br-PET-cGMPs directly increases microtubule detyrosination in hiPSC-CMs

We first tested the small molecule PRKG1A inhibitor Rp-8-Br-PET-cGMPs (RP8). Because there was no available data for the appropriate concentration, we performed a concentration response experiment in RFP WT hiPSC-CMs. Therefore, we incubated the cells with an increasing concentration of RP8 ranging from 0 to 10 µM for 45 min and evaluated the cell lysates for dTyr-tub content (**Figure 35A,B**). RP8 induced an increase in dTyr-tub level to about 1.5-fold with a concentration of 0.01 µM, but we did not observe a concentration-dependency on dTyr-tub levels. To support the data from the concentration-response study, we repeated the experiment with only 0.01 µM RP8 for 45 min in a few more samples. We confirmed that dTyr-tub level was 1.5-fold higher in the inhibitor group than in ctrl. (**Figure 35C**). These results suggest that PRKG1 can regulate the dTyr-tub levels in RFP WT hiPSC-CMs after only a short exposure time.

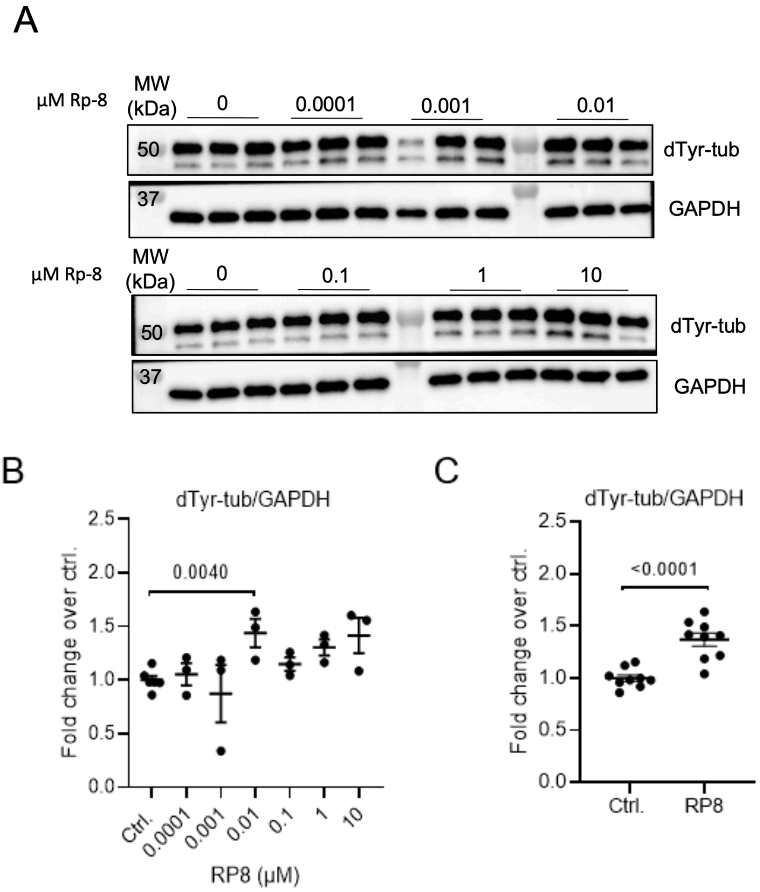

Figure 35: Western blot analysis of dTyr-tub level after a concentration-response experiment with the PRKG1A inhibitor RP8.

RFP WT hiPSC-CMs were cultured at a density of 2 x 10^5 cells/well in a 12-well plate. The cells were kept in maturation mediumfor 14 days with medium changes every five days. (A) Western blot for dTyr-tub and GAPDH (loading control) and (B) analysis of dTyr-tub levels after 45 min concentration-response experiment for RP8 exposure and (C) analysis of dTyr-tub levels after 45 min treatment with 0.01 µM RP8. H_2O was used as a solvent for RP8. Data are presented as mean±SEM. P-values were obtained with an unpaired Student's t-test. For (B) only the two indicated groups were compared with each other (B, n = 3; C, n = 9 in 3 batches).

4.2.2 *PRKG1A* knockdown in hiPSC-CMs increases stabilizing microtubule post-translational modifications

To add a second line of argumentation and because of the possibility for PRKG1A inhibitors to be considered unspecific, we supplemented this approach with a siRNA-based knockdown (KD). The experimental setup is presented in **Figure 36A**. We used two different commercially available siRNAs targeting PRKG1A (*si1/si2; siPRKG1A 1/2*) as well as a scrambled (*scr*) negative control. RFP WT hiPSC-CMs were transfected with different concentrations and combinations of both siRNAs. After five days of transfection, the CMs were harvested for protein and RNA analysis. The first and primary readout was the Western blot evaluation of dTyr-tub levels (**Figure 36B**). The corresponding quantification (**Figure 36C**) revealed a 1.4-fold higher dTyr-tub level with 150 nM of *si1* than with *scr*. Conversely, *si2* did not impact the level of dTyr-tub. The combination of both siRNAs at a concentration of 100 nM each resulted in a 1.6-fold increase in dTyr-tub over *scr*. A further increase of both siRNA concentrations to 150 nM each did not yield a more pronounced increase of dTyr-tub. In this group the dTyr-tub levels were 1.3-fold higher than in *scr* (**Figure 36C**). Because the combination of the two siRNAs at 100 nM seemed to be the most promising condition, we also tested the KD efficiency of the targeted *PRKG1A* via RT-qPCR. *PRKG1A* mRNA transcript levels were 75% lower in the KD group than in the *scr* control (**Figure 36D**). The level of PRKG1A protein level after KD was about 40% lower (**Figure 36E,F**). Due to the low n-numbers, we cannot conclusively evaluate the significance of the results here, which needed to be tested with the non-parametric Mann-Whitney U-test.

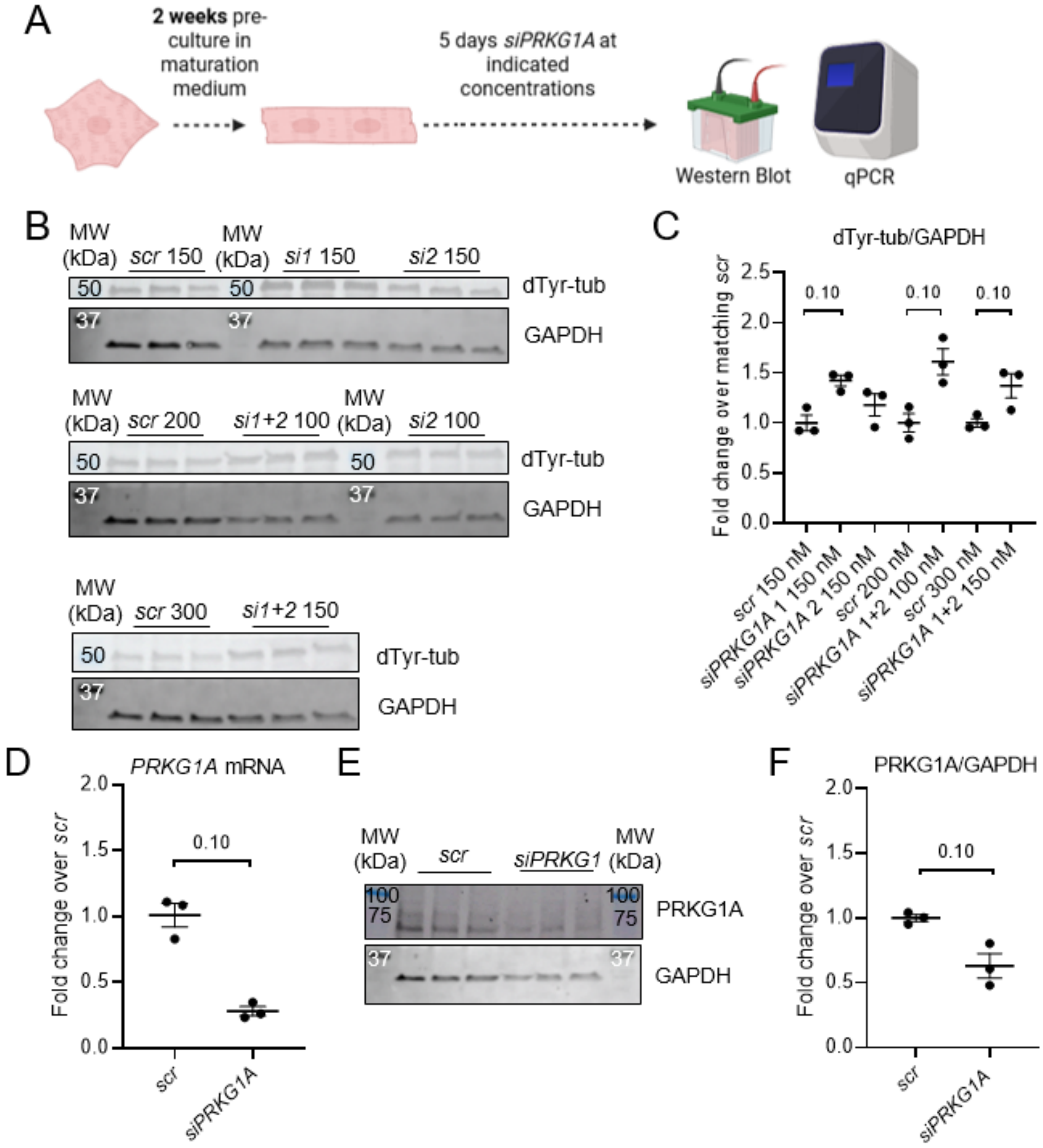

Figure 36: Evaluation of siRNA-based knockdown of PRKG1A.

RFP WT hiPSC-CMs were cultured at a density of 2 x 10^5 cells/well in a 12-well plate. The cells were kept in maturation medium for 14 days with medium changes every five days. Cells were then transfected with *scr* or specific *PRKG1A* siRNAs at the given concentrations for five days. (A) Schematic layout for the experimental setup (created with Biorender.com), (B) Western blot analysis for dTyr-tub and GAPDH (loading control) after *scr* or *siPRKG1A* treatment with (C) corresponding quantification. (D) RT-qPCR analysis of *PRKG1A* mRNA after knockdown with 100 nM siRNA 1 and 2. (E) Western blot analysis of PRKG1A and GAPDH (loading control) after knockdown with 100 nM siRNA 1 and 2 and (F) respective quantifications. SiRNAs were dissolved in H_2O. Data are presented as mean±SEM. P-values were obtained with a Mann-Whitney U-test as indicated (C, D, F; n = 3).

We repeated the experiments with the combination of both siRNAs at a concentration of 100 nM (siPRKG1) and evaluated different microtubule PTMs (dTyr-tub, Tyr-tub, α-tub, Δ2-tub, ac-tub; **Figure 37**). Quantification of the Western blots revealed a 1.2-fold increase in dTyr-tub, which was lower than before (1.6-fold; **Figure 36B,C**) but still highly significant (**Figure 37C**). The level of Tyr-tub and α-tub did not differ between *PRKG1A* KD and *scr* (**Figure 37D,E**). In contrast to that, Δ2-tub level was 1.4-fold higher, even more than dTyr-tub, than in scr-treated cells (**Figure 37G**). Similarly, ac-tub levels were 1.3-fold higher after *PRKG1A* KD (**Figure 37H**). Neiter Δ2-tub or ac-tub were significantly regulated.

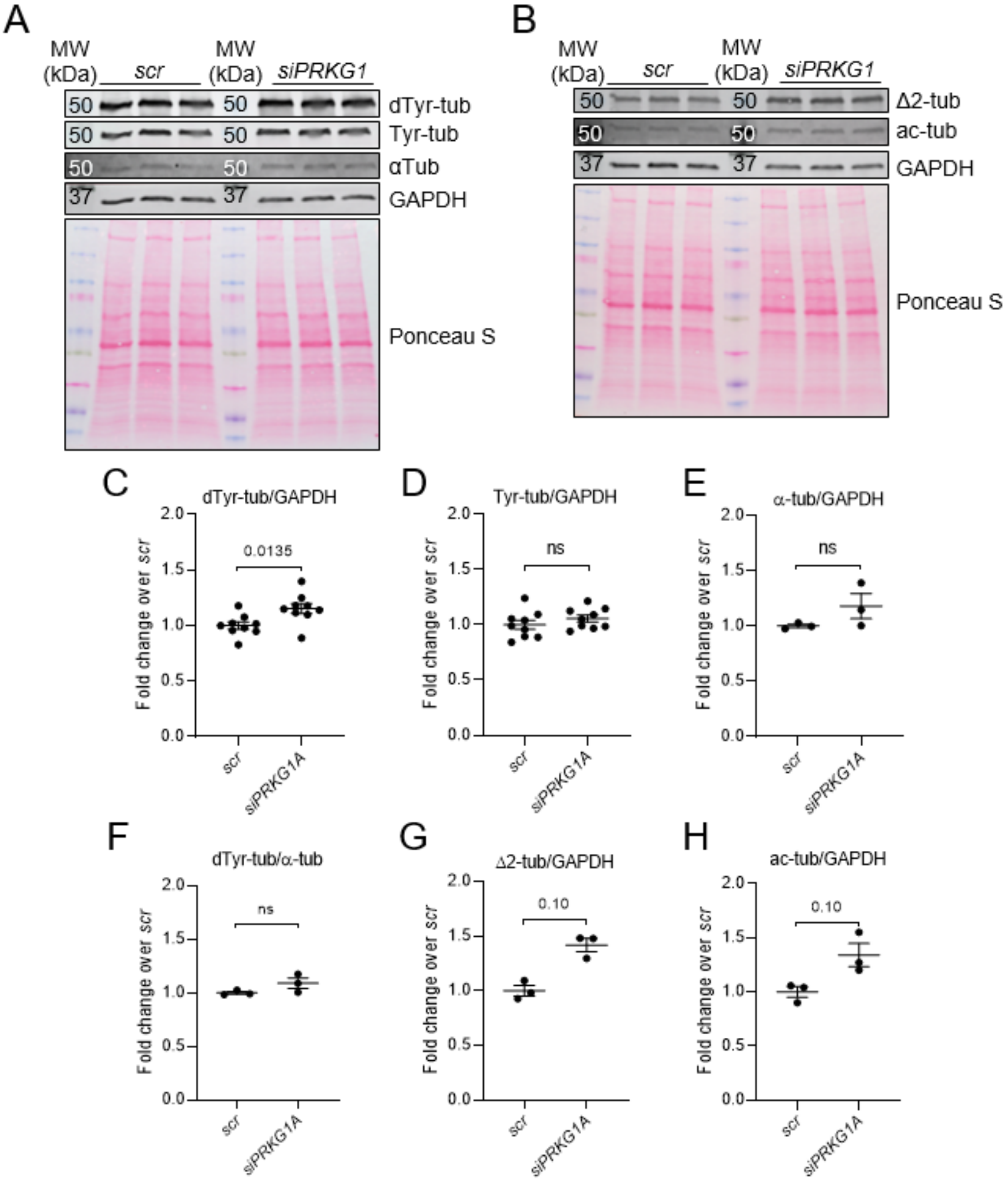

Figure 37: Western blot analysis of microtubule post-translational modifications after siPRKG1A. RFP WT hiPSC-CMs were cultured at a density of 2 x 10^5 cells/well in a 12-well plate. The cells were kept in maturation medium for 14 days with medium changes every five days. Cells were then transfected with *scr* or specific *PRKG1A* siRNAs at the given concentrations for five days. (A) Western blot analysis for dTyr-tub, Tyr-tub, α-tub and GAPDH (loading control) or (B) Δ2-tub, ac-tub and GAPDH (loading control) after knockdown with 100 nM siRNA 1 and 2. (C) Quantification of dTyr-tub, (D) Tyr-tub , (E) ac-tub, (F) Δ2-tub, (G) αTub and (H) the normalized ratio between dTyr-tub and αTub. SiRNAs

were dissolved in H_2O. P-values were obtained with an unpaired Student's t-test (C, D; n = 9 in 2 batched) or the Mann-Whitney U-test (n = 3).

4.2.3 PRKG1A stimulation by natriuretic peptides and VASH1 inhibition enhance tubulin tyrosination

As we had already built a hypothesis (**Figure 34**) for the downstream action of sac on microtubule PTMs and dissected the effect of PRKG1A activity modulation via both inhibition and KD (0, 0), we aimed at evaluating the effects of natriuretic peptides (NPs) on microtubules and their PTMs. At first, we tested if ET1/CNP could rescue the increase in dTyr-tub that is otherwise expected with ET1 only. The RFP WT hiPSC-CMs were incubated with 100 nM ET1 for the first 48 h and in the ET1/CNP group, 100 nM CNP were added for the final 24 h of the experiment. The Western blot analysis and matching quantification did not show significantly higher levels of dTyr-tub in the ET1-only group, but the observed tendency (1.3-fold) was blunted in the ET1/CNP group (**Figure 38A,B**). Interestingly, ANP levels as determined with an ELISA assay witht the cell culture supernatant, were elevated in both ET1- and ET1/CNP-treated RFP WT hiPSC-CMs. Contrary to that, there was no difference observed between the ANP levels in the medium of hiPSC-CMs treated with ET1 compared to those also incubated with CNP (**Figure 38C**).

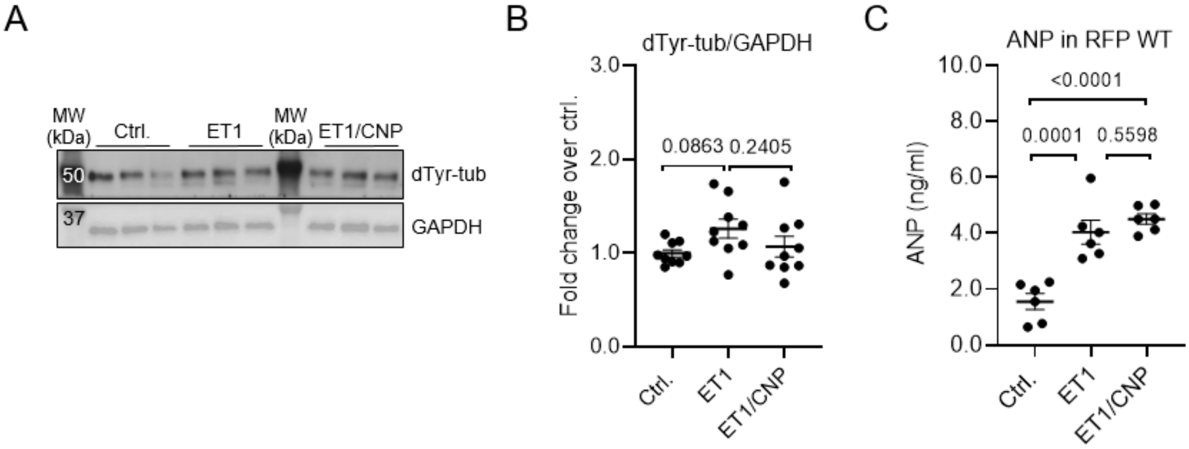

Figure 38: Western blot and ANP ELISA assay analysis of dTyr-tub levels after ET1 or ET1/CNP treatment.

RFP WT hiPSC-CMs were cultured at a density of 2 x10^5 cells/well in a 12-well plate. The cells were kept in maturation medium for 14 days with medium changes every five days. Afterwards cells were treated with ctrl. (H_2O), 100 nM ET1 for 72 h or 100 nM ET1 with the final 24 h including 100 nM CNP. (A) Western blot analysis for dTyr-tub or GAPDH (loading control) and (B) respective quantification. ET1 and CNP were dissolved in H_2O. Data are presented as mean ± SEM. P-values were obtained with one-way ANOVA with Dunnett's multiple comparisons test (B, n = 9 in 2 batches; C, n = 6).

We then evaluated whether PRKG1A activity is directly modulated by the application of either CNP (100 nM) or the previously tested inhibitor RP8 (10 nM) for 45 min to 1 h. We tested the two phosphorylation sites of the vasodilator-stimulated phosphoprotein (VASP), namely serine 239 (pVASP S239) and serine 157 (pVASP S157). While pVASP S239 is known to be the site favored by PRKG1A (Das et al., 2008), pVASP S157 served as a control, as this is favored by protein kinase A (PKA) (Eckert & Jones, 2007). The level of pVASP S239 was markedly higher after ET1, and RP8 had no effect (**Figure 39A**). On the other hand, whereas pVASP S157 level was slightly higher with ET1, it was even more in the presence of RP8, but both were not significant. We therefore decided to use the pVASP S239-specific antibody for further analyses.

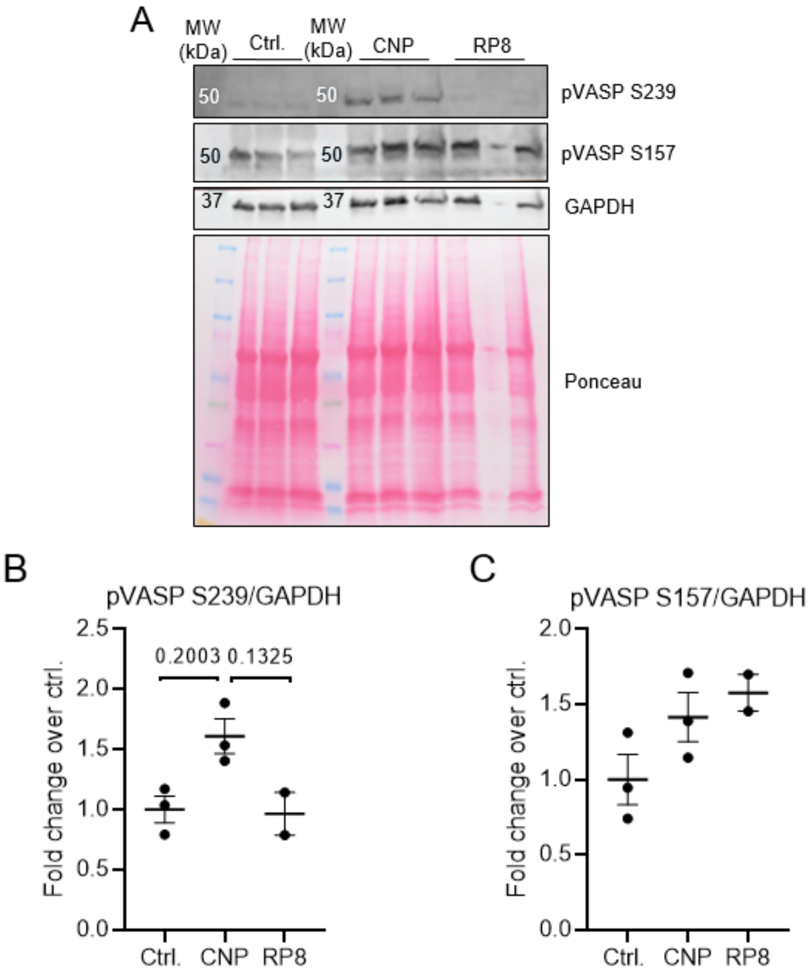

Figure 39: Western blot analysis of pVASP S239 and S157 after CNP or RP8 treatment.

RFP WT hiPSC-CMs were cultured at a density of 2 x 10^5 cells/well in a 12-well plate. The cells were kept in maturation medium for 14 days with medium changes every five days. Afterwards cells were treated with ctrl. (H_2O), 100 nM CNP for 1 h or 0.01 µM RP8 for 45 min. (A) Western blot analysis for pVASP S239/157 or GAPDH (loading control) and (B, C) respective quantifications. CNP and RP8 were dissolved in H_2O. Data are presented as mean±SEM. P-values were obtained with a non-parametric Kruskal-Wallis test with Dunn's multiple comparisons test (B, C; n = 2-3; 1 outlier was removed in both due to uneven loading).

Because the effect of sac on cGMP-PRKG1 signaling is indirect via the accumulation of NPs, we treated RFP WT hiPSC-CMs overnight (O/N) with the compound (**Figure 40A**). Surprisingly, in this experiment, sac alone, without previous stimulation via ET1, lowered the dTyr-tub level by 15% (**Figure 40B**). Furthermore, the level of Tyr-tub were 10% higher, though non-significant (**Figure 40C**). The level of pVASP S239 was about 15% higher in sac-treated cells than in the ctrl. group.

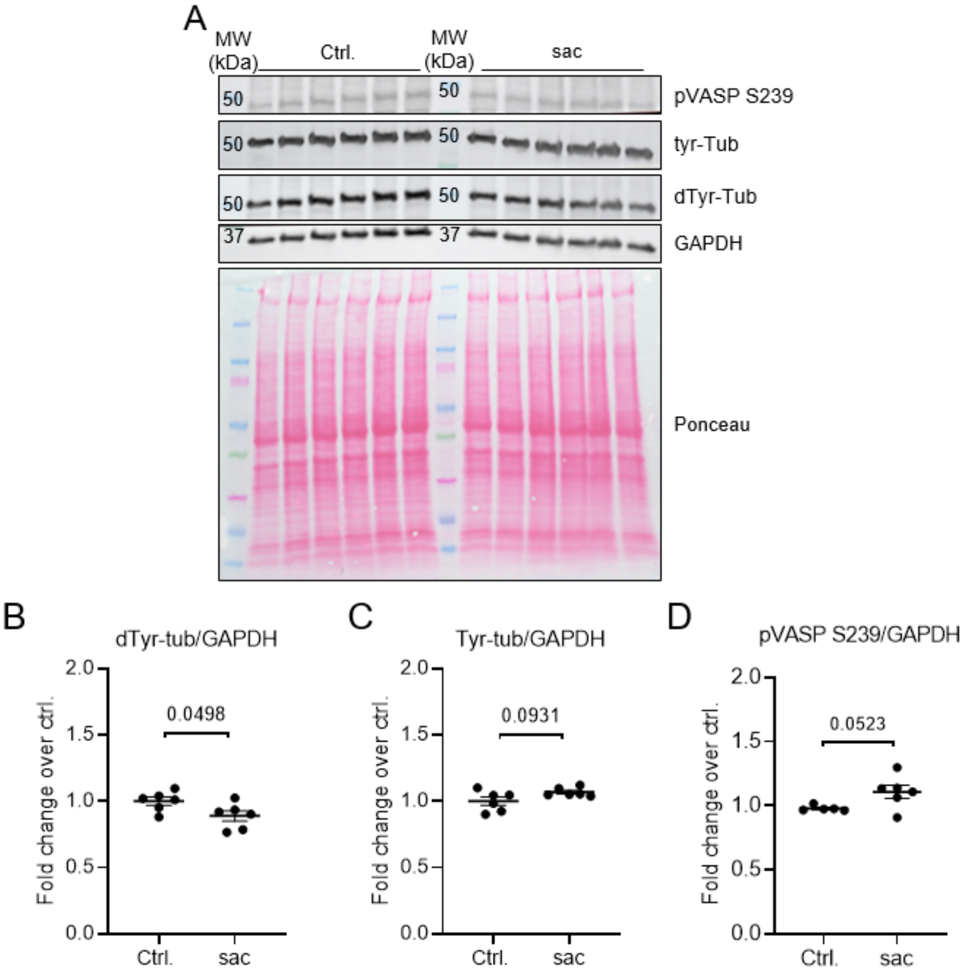

Figure 40: Western blot analysis of dTyr-tub, Tyr-tub and pVASP S239 and Tyr-tub after overnight sac exposure.

RFPtub hiPSC-CMs were cultured at a density of 2 x10^5 cells/well in a 12-well plate. The cells were kept in maturation medium for 14 days with medium changes every five days. Afterwards cells were treated with ctrl. (0.08% DMSO) or 40 µM sac O/N. (A) Western blot analysis for pVASP S239, Tyr-tub or

GAPDH (loading control) and (B, C, D) respective quantification. Data presented as mean±SEM. P-values were obtained with an unpaired Student's t-test (B, D; n = 5-6; (D) 1 outlier removed in Ctrl.) or Mann-Whitney U-test (C n = 6).

We have now established that the NP-cGMP-PRKG1A signaling axis is active in hiPSC-CMs, we then used A-type natriuretic peptide (ANP) as a stimulator of this pathway. We performed a concentration-response experiment on the pVASP Ser239 level.

While we used RFP WT hiPSC-CMs before, we now used TTL-KO hiPSC-CMs (Pietsch et al., 2024), which would afterwards also allow us to capture the newly synthesized Tyr-tub due to the genetic KO of the respective enzyme. Indeed, as all tubulin isoforms, except for TUBA4A, are synthesized carrying a C-terminal tyrosine (Nieuwenhuis & Brummelkamp, 2019), the TTL-KO hiPSC-CMs allowed us to indirectly estimate the activity of the detyrosinating enzymes (VASH1/2, MATCAP1) via Tyr-tub, which therefore captures newly synthesized tubulin. Conversely, changes in dTyr-tub would not be seen in TTL-KO hiPSC-CMs as the level of this PTM is about 30- to 35-fold higher than in RFP WT hiPSC-CMs (Pietsch et al., 2024).

We first tested concentrations of ANP ranged from 0 to 500 nM on the level of pVASP Ser239 for 20 min. The level of pVASP Ser 239 was already about 2-fold higher with 10 nM of ANP and remained higher with higher concentrations, except with 30 nM, which we could not explain (**Figure 41**).

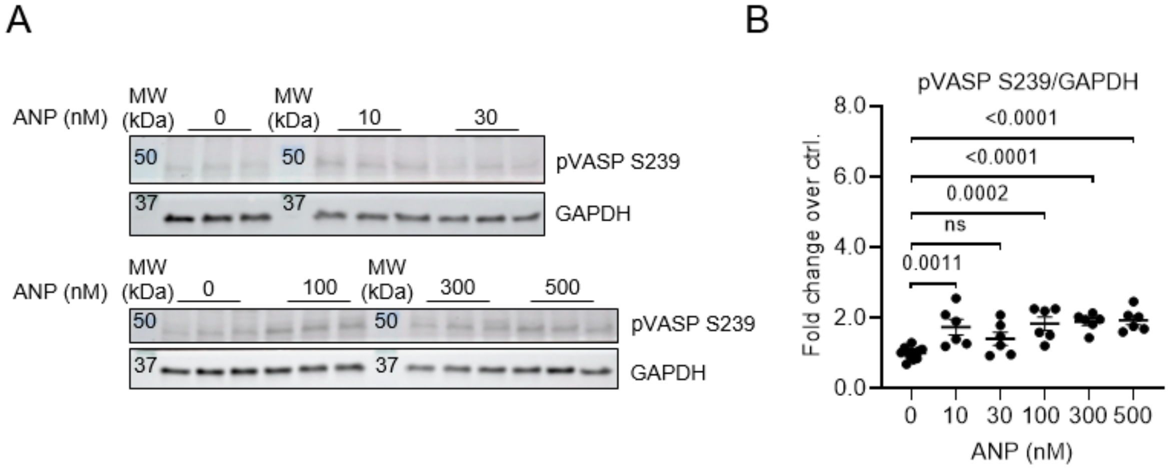

Figure 41: Western blot analysis of pVASP S239 after concentration response experiment with ANP.

TTL-KO hiPSC-CMs were cultured at a density of 2 x 10^5 cells/well in a 12-well plate. Initial plating was performed in complete medium, which was replaced with maturation medium after three days. The cells were kept in maturation medium for 14 d with medium changes every five days. Afterwards cells were treated with 0-500 nM ANP for 20 min. (A) Western blot analysis for pVASP S239 or GAPDH (loading control) and (B) respective quantification. ANP was dissolved in H_2O. Data are presented as mean±SEM. P-values were obtaines with a one-way ANOVA with Dunnett's multiple comparisons test (B; n = 6).

Despite the absence of significant effect on pVASP with 30 nM ANP, we evaluated the impact of this concentration on the level of Tyr-tub. The level of Tyr-tub was 1.25-fold higher after only a 20-min stimulation with ANP (**Figure 42**).

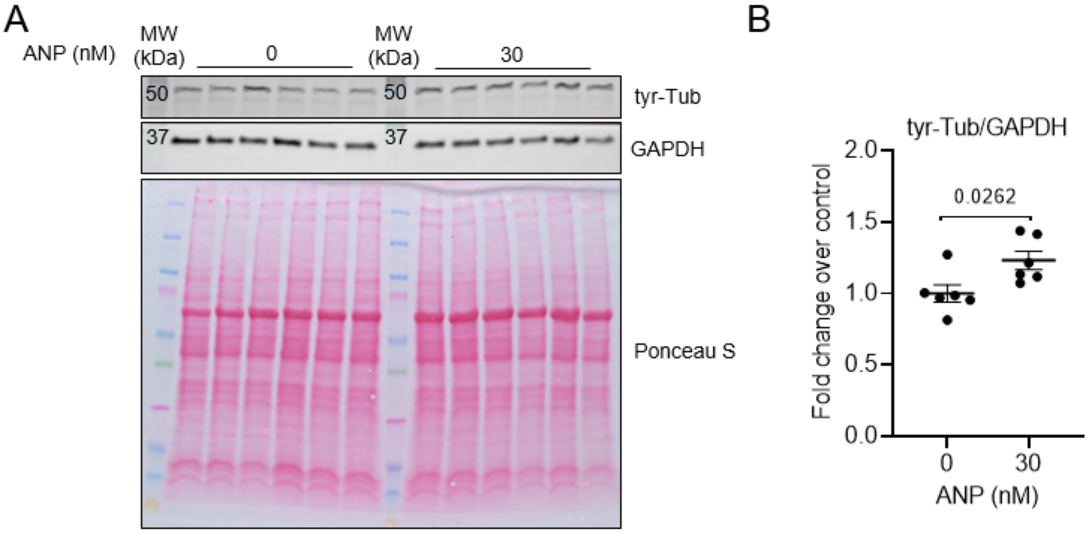

Figure 42: Western blot analysis of Tyr-tub after treatment with 30 nM ANP.

TTL-KO hiPSC-CMs were cultured at a density of 2 x 10^5 cells/well in a 12-well plate. The cells were kept in maturation medium for 14 days with medium changes every five days. Afterwards cells were treated with H_2O (= 0 nM ANP) or 30 nM ANP for 20 min. (A) Western blot analysis for Tyr-tub or GAPDH (loading control) and (B) respective quantification. Data presented as mean±SEM. P-value was obtained with an unpaired Student's t-test (B; n = 6).

To validate the ANP effect on Tyr-tub, we performed a concentration-response experiment with the VASH1/2 inhibitor alkaline EpoY (alk. EpoY), which we received as a gift from Marie-Jo Moutin (Grenoble, France). Here the concentrations ranged from 0-100 µM in an overnight setting. The level of Tyr-tub increased 1.25-fold with 10 and 100 µM of the inhibitor, whereas the dTyr-tub level slightly decreased (**Figure 43A,B**).

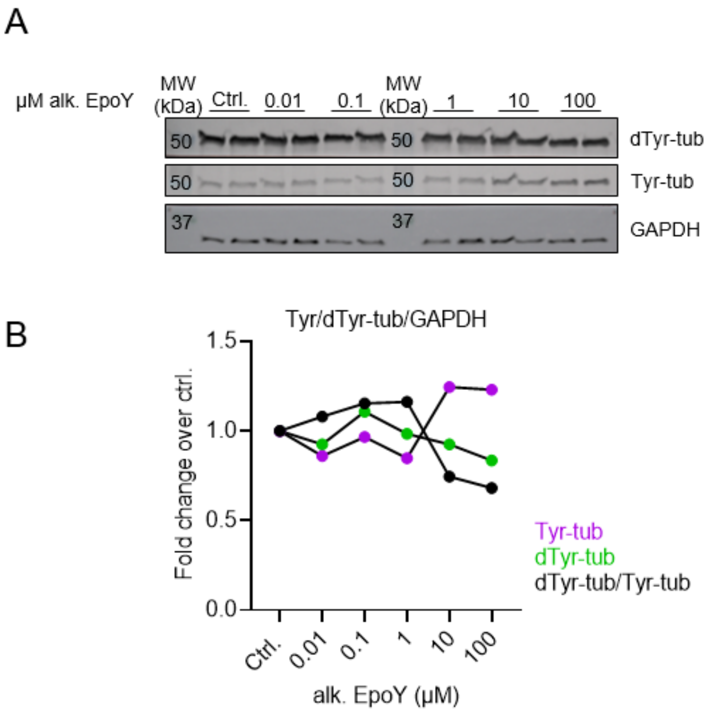

Figure 43: Western blot analysis of dTyr-tub and Tyr-tub after concentration response experiment with alkaline EpoY.

TTL-KO hiPSC-CMs were cultured at a density of 2 x 10^5 cells/well in a 12-well plate. The cells were kept in maturation medium for 14 days with medium changes every five days. Afterwards cells were treated with 0-100 µM alk. EpoY overnight. (A) Western blot analysis for dTyr-tub, Tyr-tub or GAPDH (loading control) and (B) respective quantification. Alk. EpoY was dissolved in DMSO (ctrl.). Data are presented as mean±SEM (B; n = 2).

Considering the low n-number in the concentration response experiment (n = 2) we repeated the experiment, only with 10 µM alk. EpoY overnight. In this conditions, the level of Tyr-Tub was 1.35-fold higher with the VASH inhibitor than with vehicle (**Figure 44**), which was comparable to the change after 30 nM ANP treatment (**Figure 42B**).

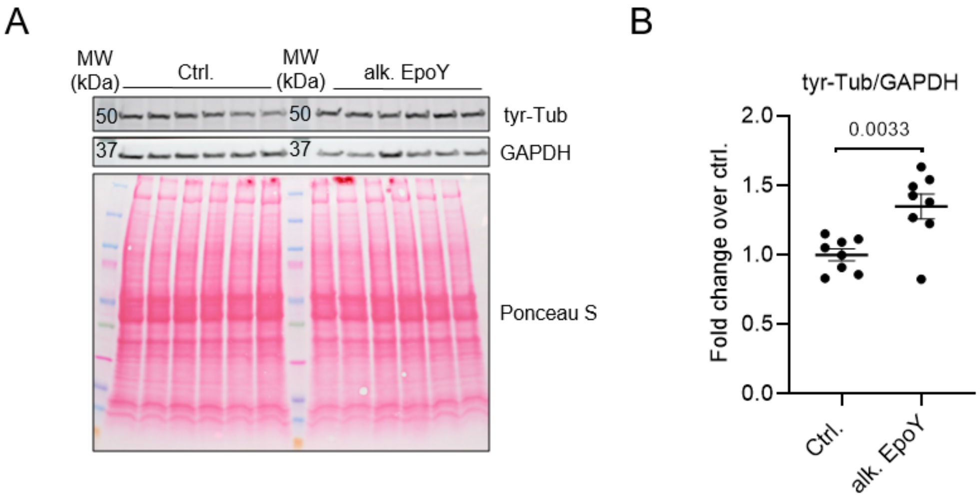

Figure 44: Western blot analysis for Tyr-tub after 10 µM alkaline EpoY treatment.
TTL-KO hiPSC-CMs were cultured at a density of 2 x 10^5 cells/well in a 12-well plate. The cells were kept in maturation medium for 14 days with medium changes every five days. Afterwards cells were treated with ctrl. (0.1% DMSO) or 10 µM alk. EpoY overnight. (A) Western blot analysis for Tyr-tub or GAPDH (loading control) and (B) respective quantification. Alk. EpoY was dissolved in DMSO. Data presented as mean±SEM. P-value was obtained with an unpaired Student's t-test (B; n = 8).

4.2.4 Sacubitrilat and CNP peptide stimulate intracellular cGMP production and sacubitrilat inhibits ANP degradation

Finally, we also wanted to validate that application of sac to CMs can directly increase intracellular cGMP levels. We therefore performed an ELISA assay for cGMP. In this assay, each group contained three replicates each consisting of two pooled wells from a 6 well plate. The treatments (40 µM sac, 100 nM CNP) yielded a 2-fold and 8-fold increase in cGMP levels respectively (**Figure 45A**).

As the manufacturer of the ELISA kit could not deliver further units during the data acquisition phase of this study, we aimed at testing intracellular cGMP levels with a FRET sensor. The cGi500 was encoded in an adenoviral vector (Adv-cGi500). In this sensor consists of a cyan fluorescent protein (CFP) as well as a yellow fluorescent protein (YFP) which are both coupled to a cGMP binding domain. With no cGMP bound, both fluorophores are in proximity, and the CFP can stimulate the YFP. This means that with the excitation of CFP with a 445-nm laser light, mainly the 535 nm light from the YFP is emitted, because the emission wavelength of CFP (480 nm) is the excitation wavelength of YFP. Once cGMP binds to the coupled cGMP binding domains, they change their confirmation and the distance between the fluorophores increases. Now YFP is excited less by the emission wavelength of CFP and the ratio between CFP and YFP signal (FRET) increases (**Figure 45B;** Thunemann et al., 2014). After the sac treatment, each experiment was concluded by adding a mixture of 100 nM CNP and 100 µM 3-Isobutyl-1-methylxanthin (IBMX; phosphodiesterase inhibitor) to reach the maximal possible response.

Out of all FRET traces captured, about 65% showed a response to either sac or CNP/IBMX exposure, while the others did not react to the stimuli. Out of the ones that reacted, three example traces are shown in **Figure 45C**. It proved to be difficult to reach a clear and stable baseline in the measurements, which makes the data difficult to interpret. Nevertheless, upon the addition of sac the left and middle trace showed an increase in FRET signal, which could only be increased upon by CNP/IBMX in the middle trace. The right trace did not convincingly react to sac application but showed a clear increase in FRET after the addition of CNP/IBMX.

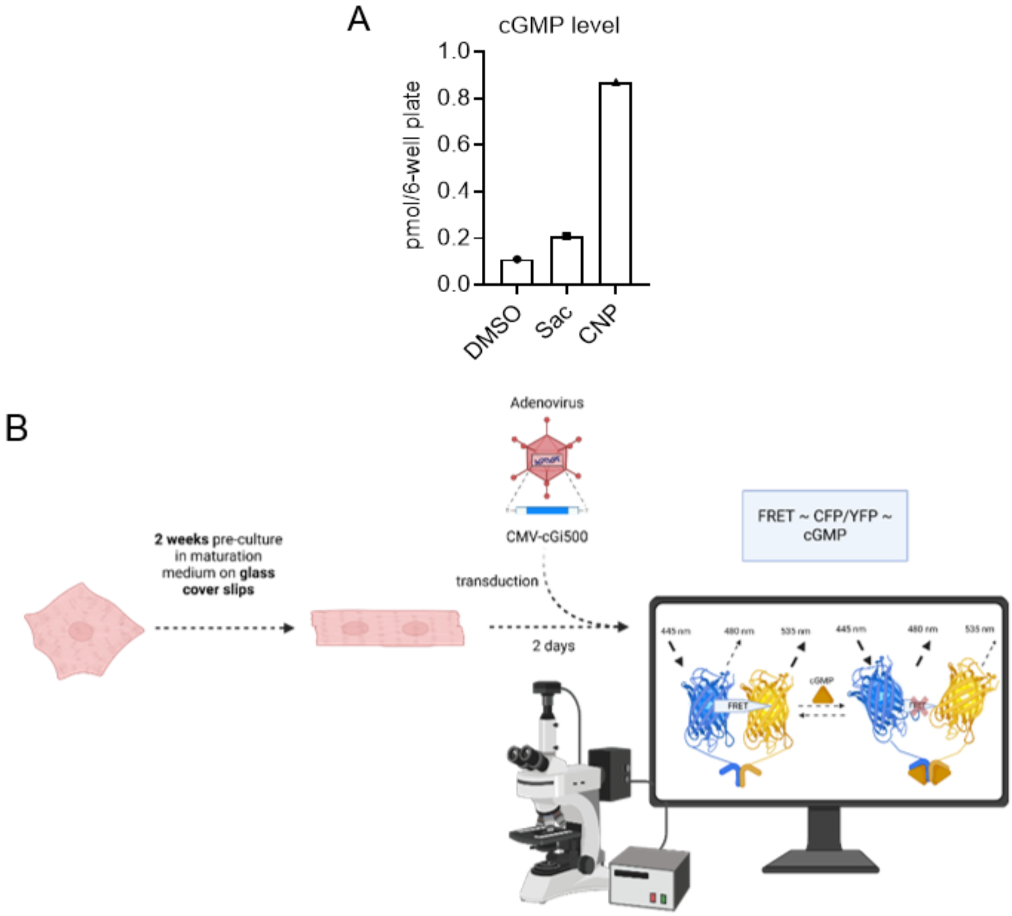

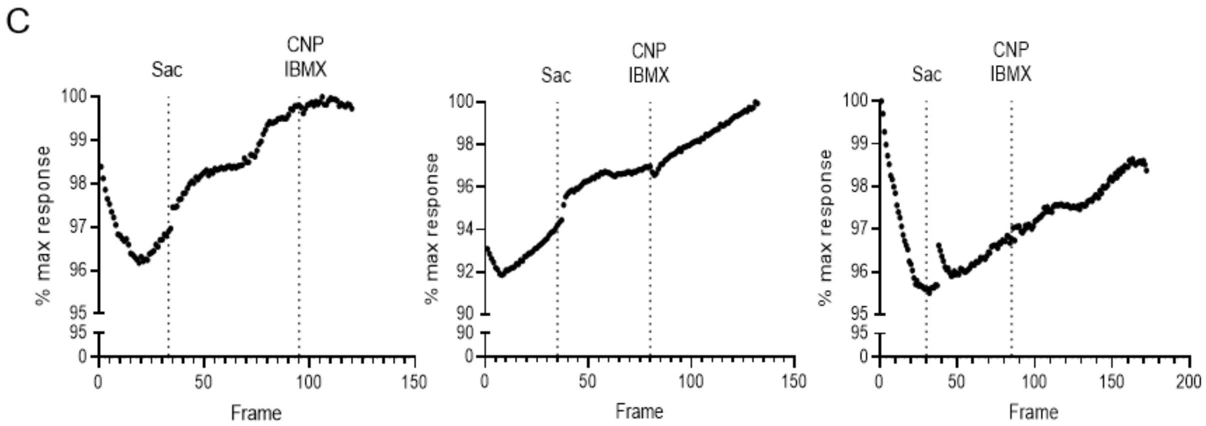

Figure 45: Direct assessment of intracellular cGMP changes after sac or CNP exposure.

RFP WT hiPSC-CMs were cultured at a density of 8 x 10^5 cells/well in a 6-well plate. The cells were kept in maturation medium for 14 days with medium changes every five days. Transductions were performed with an adenovirus encoding the cGMP FRET sensor cGi500 (multiplicity of infection of 30). (A) Elisa Assay for direct assessment of intercellular cGMP levels after 20 min of sac or CNP treatment (3 x 2 wells per condition). (B) Schematic illustration for RFP WT hiPSC-CM transduction and subsequent FRET measurement (created with Biorender.com). (C) Three exemplary FRET traces displaying the maximal response in the CFP/YFP ratio on the y-axis and the measurement frame on the x-axis (1 frame = 10 s). RFP WT hiPSC-CMs were acutely stimulated with 40 µM sac or 100 nM CNP and 100 µM IBMX as indicated.

Since we analyzed the effects of sac on hiPSC-CMs with regard to pVASP S239, dTyr-tub and Tyr-tub, we also aimed to evaluate the inhibitory effect of sac on MME. According to the mechanism of action of sac, ANP protein in the medium should be increased. In fact, O/N incubation of TTL-KO hiPSC-CMs with sac caused an almost 50% increase in ANP levels in the supernatant (**Figure 46**). We could therefore deduct that sac had the expected effect.

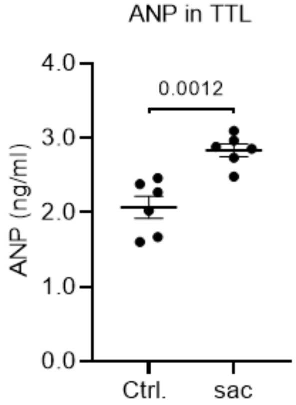

Figure 46: Atrial natriuretic peptide levels in supernatant of TTL-hiPSC-CMs treated with ctrl. or sac overnight.

TTK-KO hiPSC-CMs were plated at a density of 2 x 10^5 in a 12-well plate and kept in culture for two weeks in maturation medium with medium changes every five days. HiPSC-CMs were then treated with either ctrl. (0.08% DMSO) or 40 µM sac O/N. The supernatant was collected and frozen at -80 °C until being analyzed with a specific ANP ELISA kit. Data presented as mean±SEM. P-value was obtained with an unpaired Student's t-test (n = 6).

4.2.5 Summary of PRKG1A signaling modulation by natriuretic peptides, sacubitrilat and VASH1 inhibition

We observed significantly higher levels of dTyr-tub in RFP WT hiPSC-CMs treated with the PRKG1 inhibitor RP8 or transfected with siRNAs targeting the kinase. Moreover, ET1 and CNP both increased ANP secretion into cell culture media by RFP WT hiPSC-CMs during a 72 h treatment. We confirmed that CNP increases the phosphorylation of VASP at S239 which is PRKG-specific. This effect was also almost significantly mimicked by sac application. Additionally, ANP and VASH1 inhibition resulted in higher levels of Tyr-tub in TTL-KO hiPSC-CMs indicating the inhibitory effect downstream of ANP on VASH1 activity. Lastly, ANP levels were significantly higher in the medium of TTL-KO hiPSC-CMs treated with sac, and both sac and CNP increased intracellular cGMP levels.

4.3 Impact of mutant VASH1 on microtubule modifications

4.3.1 Discovery of the PRKG1A target site on VASH1

It was previously shown by the Moutin's lab in Grenoble that the VASH1-SVBP complex binds to microtubules via the C-terminal (Ct) domain of VASH1 and promotes detyrosination of microtubules *in vitro* (Ramirez-Rios et al., 2023). We therefore hypothesized that PRKG1A might directly phosphorylate VASH1 and therefore inhibit its detyrosination activity. KinasePhos 2.0 revealed seven putative serine residues in the Ct domain (S313, S323, S324, S330, S331, S337, and S344) that may be phosphorylated by PRKG1. The experiment was performed by our colleagues in Grenoble. They used their previously generated sfGFP-VASH1-SVBP complex (VASH1-WT) and the truncated version of VASH1 containing the CD and Ct domain, consisting of residues 57-365 (VASH1-CD+Ct; Ramirez-Rios et al., 2023). In addition, they constructed a phosphomimetic VASH1 where all 7 serines in the Ct domain were mutated to glutamates (VASH1 7E; **Figure 47A**). They incubated the VASH1 recombinant proteins (2 µM) with 10 nM of recombinant PRKG1A for 1 h in the presence of the slowly hydrolyzed adenosine triphosphate (ATP) analogue ATP-γ-S. The kinase substrate is therefore labelled with this analogue and the incubation with p-nitrobenzyl mesylate results in thiophosphate ester formation. Afterwards the resulting samples were loaded on an SDS-PAGE and phosphorylation was detected with a thiophosphate ester-specific antibody. This strategy allows for the detection of phosphorylation sites without the need for specific antibodies but lacks the capability to distinguish between sites. The SDS-PAGE confirmed equal loading across conditions for all three recombinant proteins. In contrast, the thiophosphate ester Western blot exhibited prominent signals for VASH1-WT and VASH1-CD+Ct, but only a faint signal for VASH1 7E (data not shown). Together, these data suggest that PRKG1A targets serine residues for phosphorylation within the Ct domain of VASH1.

We then hypothesized that the activation of the cGMP/PRKG1 pathway by sac also induces phosphorylation of VASH1, its inactivation and therefore reduction of dTyr-tub levels in hiPSC-CMs. Our colleagues in Grenoble generated plasmids encoding mouse YFP-VASH1-WT-IRES-SVBP (VASH1-WT), phosphomimetic YFP-VASH1 7E-IRES-SVBP (VASH1 7E) and non-phosphorylatable VASH1, where all 7 serines were mutated to alanine (VASH1 7A). With these different constructs, lentiviruses were generated by Dr. Ingke Braren from the Vector Facility of the UKE. These lentiviruses were then used to transduce VASH1-KO hiPSC-CMs to determine the specific effects of the mutant constructs in a relevant cellular model (**Figure 47B**).

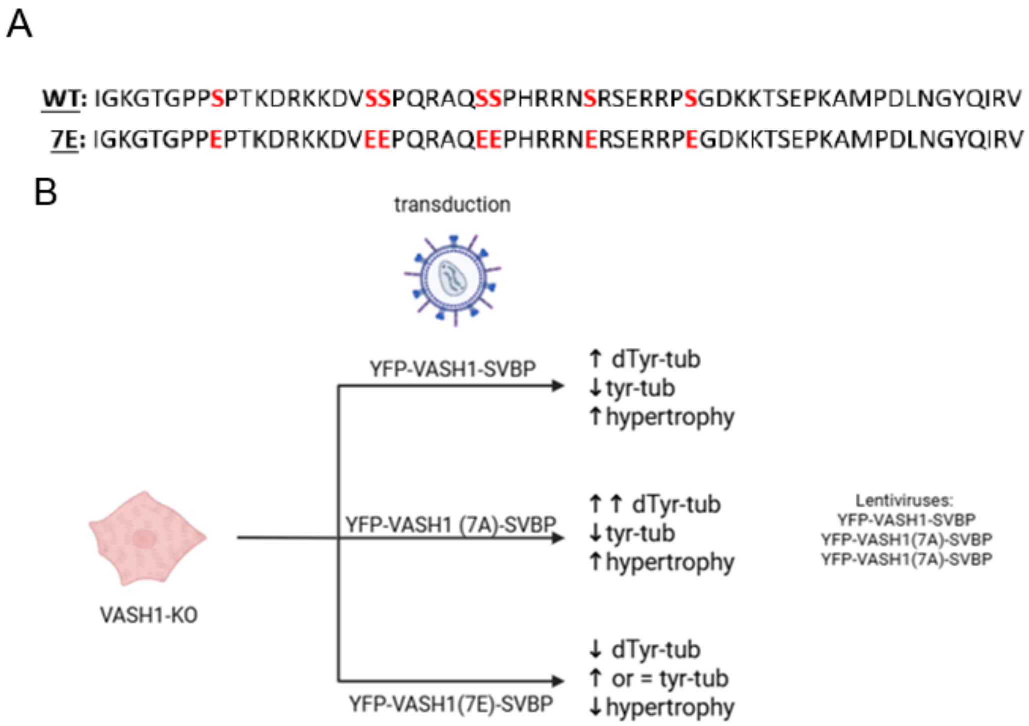

Figure 47: Discovery of the target site for PRKG1A on VASH1.

(A) C-termini of VASH1-WT and VASH1 7E with the potential PRKG1-targeted serine residues highlighted in red (WT). These serine residues were mutated to glutamate residues in the VASH1 7E. (B) Protocol for the transduction of VASH1-KO hiPSC-CMs with mutant VASH1 lentivirus constructs (created with Biorender.com). (A) provided by Chadni Sanyal, Sacnite Ramirez-Rios and Marie-Jo Moutin.

4.3.2 Consequences of mutant VASH1 overexpression in VASH1-defiecient hiPSC-CMs

To determine the effects of exogenous VASH1 7E and VASH1 7A on dTyr-tub and Tyr-tub levels, we performed a lentivirus volume-concentration response of either lentivirus in VASH1-KO hiPSC-CMs for 72 h (**Figure 48A**). All VASH1 constructs carried a Nt YFP-tag. Exogenous YFP-VASH1 7E and -7A proteins accumulated in a a volume-dependent manner and were >40-fold higher with the highest volume of lentivirus transduction (10 µl) than with the lowest volume (0.03 µl; **Figure 48B**). The level of dTyr-tub was higher was 5-fold higher with 10 µL for both VASH1 7E and VASH1 7A; however, it was already 3-fold higher with 1 µL of VASH1 7A, but not 7E (**Figure 48C**). Interestingly, Tyr-tub levels were about 50% lower with 0.3 µL lentivirus in both groups (**Figure 48D**). To evaluate the catalytic activity of VASH1, we plotted the ratio of dTyr-tub/VASH1, which was the highest with 0.1-0.3 µL and much higher with VASH1 7A than 7E, though non-significant (**Figure 48E**). These data suggest that the enzymatic activity of the tubulin carboxypeptidase complex is higher with VASH1 7A-SVBP than with VASH1 7E-SVBP.

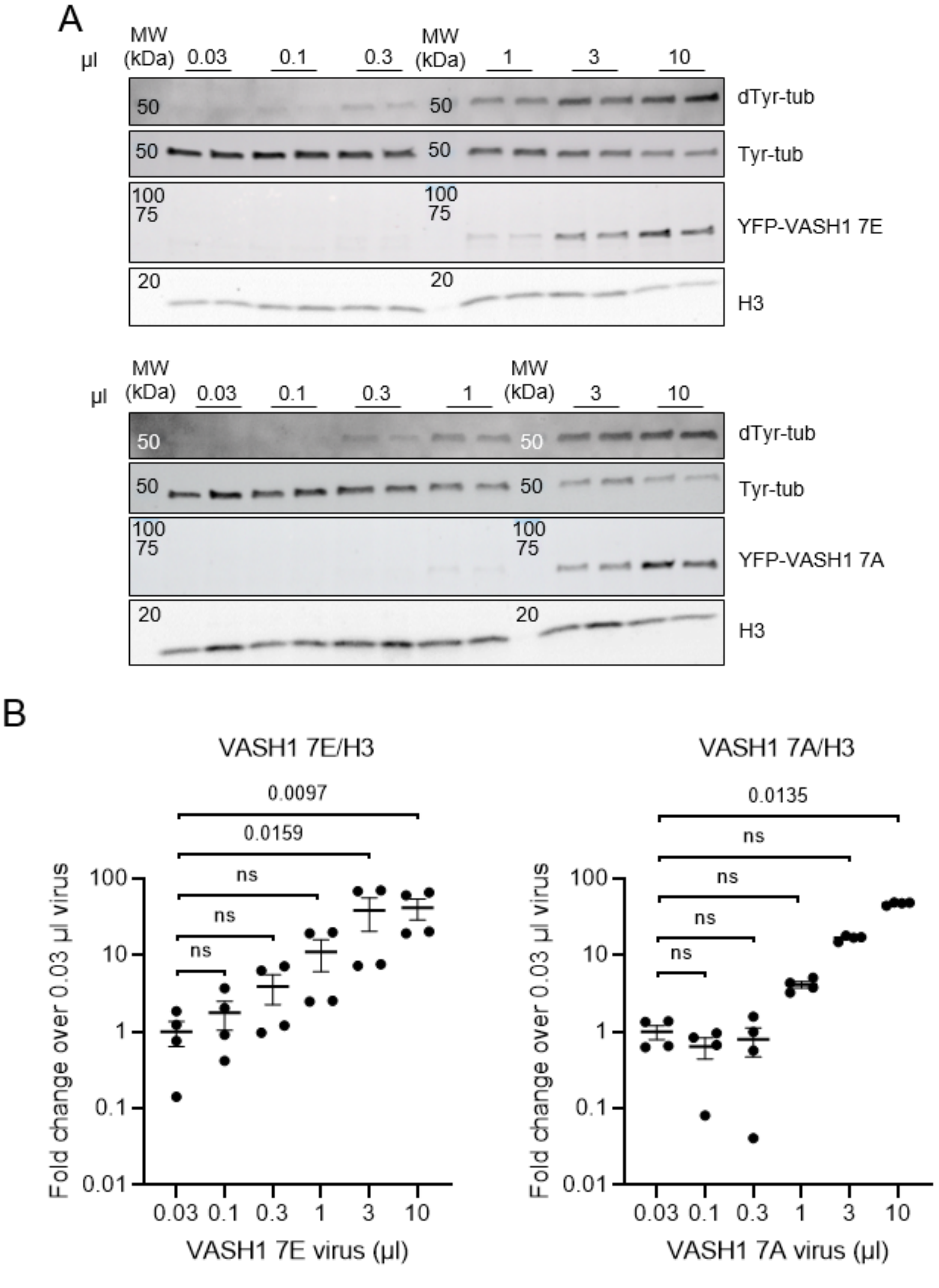

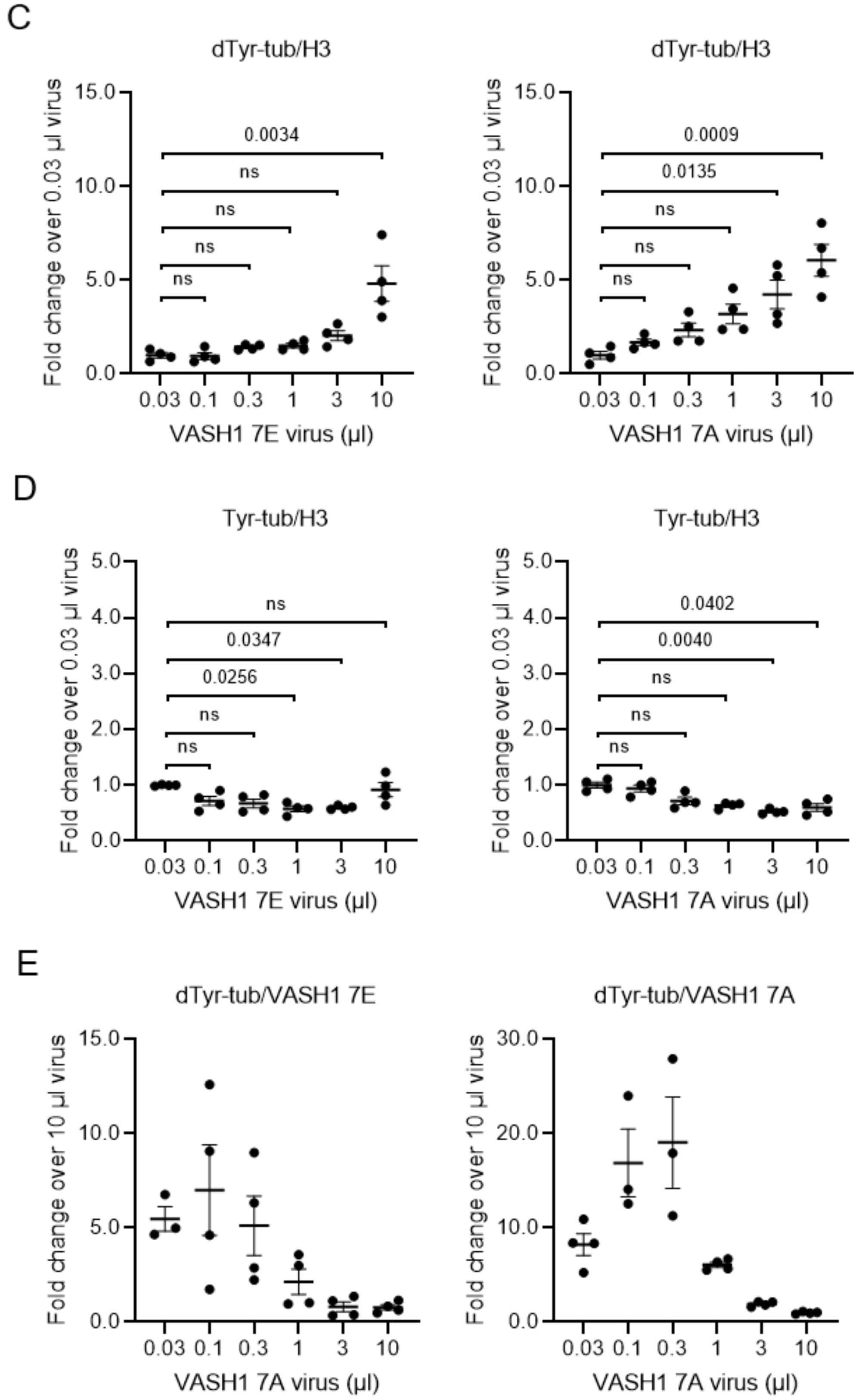

Figure 48: Transduction and consequences of VASH1 7E/7A and WT in VASH1-KO hiPSC-CMs. VASH1-KO hiPSC-CMs were seeded at a density of 1 x 10^5 per well into 12-well plates and cultured in complete medium for one week prior to transduction with increasing volumes of either VASH1 mutant construct (0.03-10 µl) or VASH1 WT with an MOI of 1.5. (A) Representative western blot images for dTyr-tub, Tyr-tub, YFP-VASH1 and H3 (loading control) after increasing volumes of VASH1 7E

transduction (B, C, D, E) and indicated quantifications. Cells were harvested after 72 h of transduction. Data are presented as mean±SEM. P-values were obtained with the non-parametric Kruskal-Wallis test with Dunn’s multiple comparisons test (B, C, D, E; n = 4).

We then compared the impact of 10-µL transduction of VASH1-KO with VASH1-WT, -7E and -7A for 72 h on the levels of dTyr-tub and Tyr-tub. The microscopic images revealed a lower number of YFP-positive cells with the VASH1 7E and VASH1 7A than for the VASH1-WT, suggesting a lower titer for the mutant lentivirus (**Figure 49A**). Western blot analysis was performed to evaluate the impact of the different constructs on the levels of YFP-VASH1, dTyr-tub and Tyr-tub (**Figure 49B**). The level of exogenous YFP-VASH1 was about 60-70% lower in VASH1-KO hiPSC-CMs transduced with VASH1 7E or VASH1 7A than transduced with VASH1-WT (**Figure 49B,C**), reflecting the lower titer of the lentivirus encoding the mutant VASH1. No significant difference in dTyr-tub level was quantified between VASH1 7E and VASH1 7A. In the absence of endogenous VASH1 in VASH1-KO hiPSC-CMs, the low, basal level of dTyr-tub is mediated by other enzymes, such as the VASH2-SVBP complex or MATCAP1 or by TUBA4A, which is synthesized as detyrosinated tubulin. The level of dTyr-tub was higher in all conditions than in untreated VASH1-KO cells (**Figure 49B,D**), suggesting that all exogenous VASH1 can induce microtubule detyrosination. However, the level of dTyr-tub was lower in VASH1 7E-transduced cells than in VASH1-WT- and VASH1 7A-transduced cells, suggesting that the presence of the phosphomimetic VASH1 partly prevents the attachment of the VASH-SVBP complex to promote detyrosination. Of note, the level of Tyr-tub did not markedly differ between the groups, except in cells transduced with VASH1 7A where it was lower than those transduced with VASH1 7E (**Figure 49B,E**).

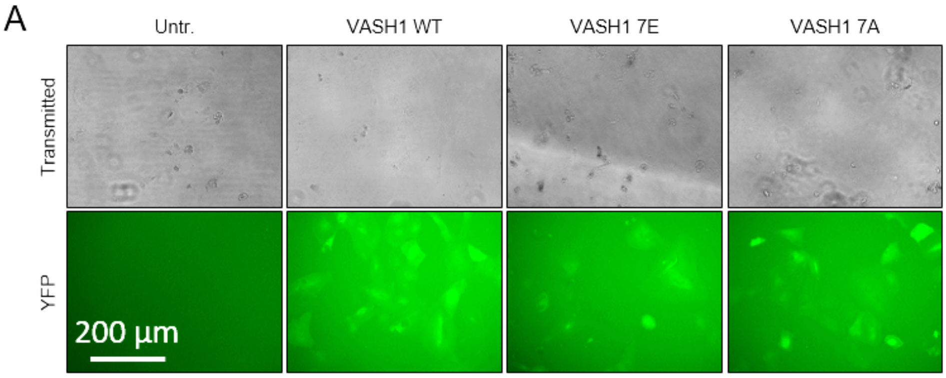

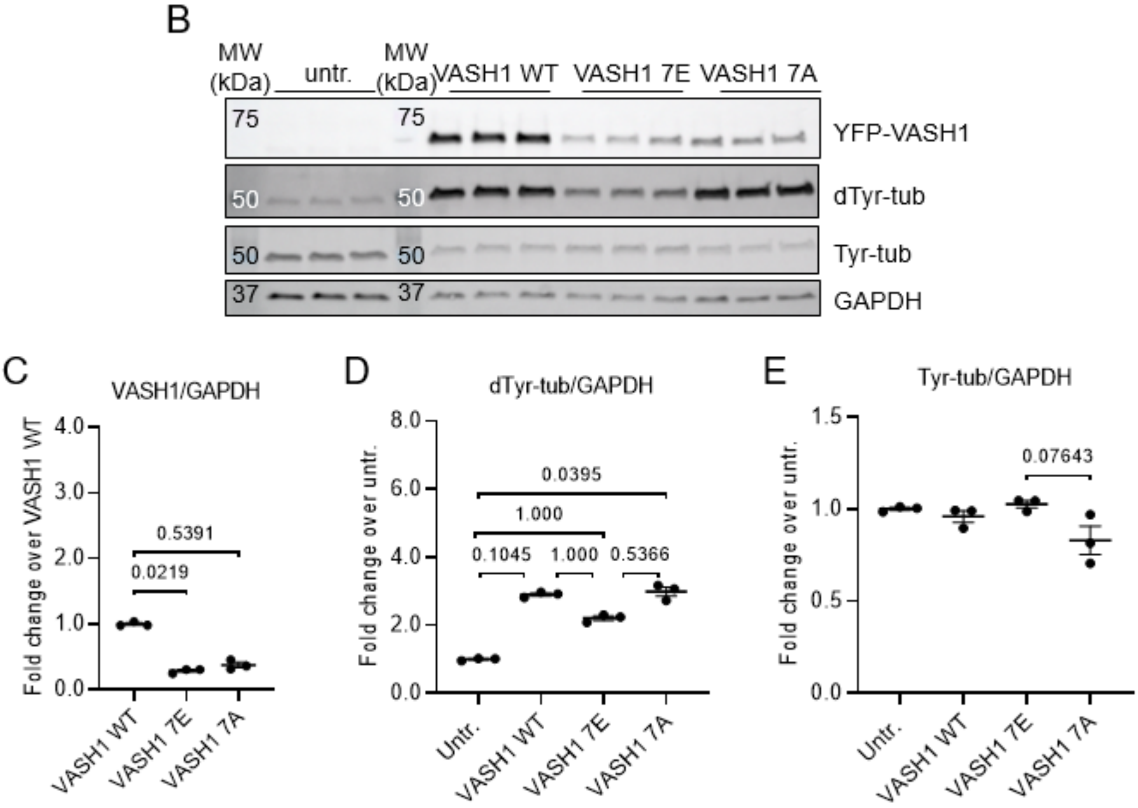

Figure 49: Transduction and consequences of VASH1 WT and VASH1 7E/7A in VASH1-hiPSC-CMs.

VASH1-KO hiPSC-CMs were seeded at a density of 2 x10^5 per well into 12-well plates and cultured in complete medium for one week prior to transduction with increasing volumes of either VASH1 mutant construct or VASH1 WT with an MOI of 1.5. Cells were harvested after 72 h of transduction. (A) Representative microscopic images of untransduced (untr.) VASH1-KO hiPSC-CMs or those transduced with 10 µl VASH1 7E/7A lentivirus or MOI of 1.5 of the VASH1 WT lentivirus under transmitted light or showing the GFP/YFP channel. (B) Western blot images for YFP-VASH1, dTyr-tub, Tyr-tub and GAPDH (loading control) and (C, D, E) matching quantifications. Data presented as mean±SEM. P-values were obtained with a non-parametric Kruskal-Wallis test with Tukey’s multiple comparisons test (C, D, E; n = 3).

4.3.3 Summary of the effects of mutant VASH1 overexpression in VASH1-deficient hiPSC-CMs

Our collaborators provided eveidence in cell-free systems that PRKG1 targets a serine residue in the Cter of VASH1. A database search conducted by them revealed seven such residues which they subsequently mutated to either glutamate (VASH1 7E) ot alanine (VASH1 7A) in a plasmid vector encoding YFP-VASH1 alsongside SVBP. Glutamate should mimick a phosphorylation of VASH1 while alanine cannot be phosphorylated anymore. We overexpressed these constructs in VASH1-KO hiPSC-

CMs with lentiviruses and revealed efficient expression of all by fluorescence microscopy and Western blot analysis. Both VASH1 7E and 7A increased dTyr-tub and decreased Tyr-tub. The ratio between dTyr-tub and VASH1 revealed that 7A is more effective at detyrosinating MTs than 7E. This suggests that PRKG1-induced phosphorylation of VASH1 inhibits, at least in part, its detyrosinae activity.

4.4 Creating a hiPSC-line deficient in *MATCAP1*

The main microtubule detyrosinating enzymes VASH1/2 and their chaperone SVBP have been described almost a decade ago by two different groups independently of each other (Aillaud et al., 2017; Nieuwenhuis et al., 2017). Still, hiPSC-CMs and mice lacking the enzymatic VASH activity were shown to still possess dTyr-tub which can likely not be accounted for merely through the expression of the *de novo* detyrosinated isoform TUBA4A. The relative activity of either VASH1 and VASH2 is thought to be tissue specific (Pagnamenta et al., 2019; Pietsch et al., 2024; Sanyal et al., 2023). This suggested the presence of additional tubulin carboxypeptidases. In 2022, such an enzyme, MATCAP1, was first described in neurons. In contrast to the VASH/SVBP complex, MATCAP1 does not bind at the interface of two laterally aligned MT protofilaments but instead a single protofilament. However, so far its relevance has only been initially described in neurons while its role in other cell types, like CMs, remains elusive (Landskron et al., 2022).

4.4.1 CRISPR-Cas9 genome editing strategy for creation of a *MATCAP1*-knockout hiPSC-line

As the consequences of a loss of MATCAP1 for CMs were unknown, we wanted to perform CRISPR-Cas9 genome editing to create KO hiPSC-cell line (MATCAP1-KO). As a basis for this cell line we used the RFP WT hiPSCs as these also served as an isogenic control for SVBP-KO, TTL-KO, VASH1-KO (Pietsch et al., 2024). The genomic locus of *MATCAP1* is 8442 base pairs (bp) long and consists of six coding exons. The resulting protein consists of 472 amino acids (MATCAP1 Gene Card, n.d). In our database search, no long non-coding RNAs or other genes were found in that region. The gene is flanked by the genes *EXOC3L1* upstream and *NOL3* downstream. *NOL3* and *MATCAP1* share a small overlap in their 3’ regions (NCBI, 2025). Our strategy aimed at removing a 2783-bp fragment between the two indicated crRNAs. Within this fragment the two functional domains of MATCAP1 are also encoded. This approach would leave the overlap with NOL3 unaffected and still ensure a full KO of *MATCAP1*. **Figure 50** depicts the described locus. The hereafter described editing strategy was to be conducted in both RFP WT and SVBP-KO hiPSC lines to create MATCAP1-KO and SVBP/MATCAP1-double-KO. The latter line would have been deficient in any known functioning detyrosinating enzyme.

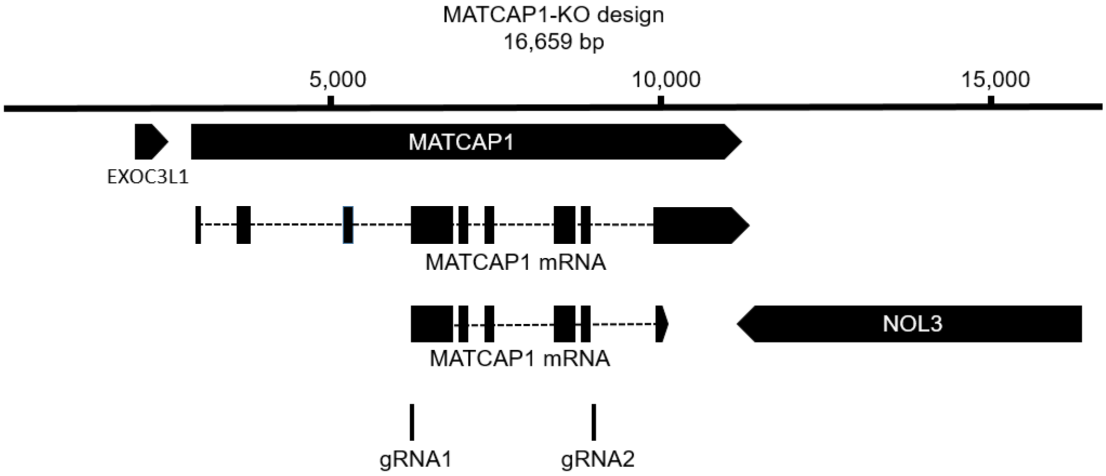

Figure 50: MATCAP1 genomic locus with transcripts.

Genomic locus of MATCAP1 on chromosome 16 with the exon-structure. Also indicated are the two crRNAs and flanking genes EXOC3L1 and NOL3. Below the genomic locus, unspliced and spliced MATCAP1 mRNA are shown. Whole genomic locus has a size of 16,659 bp. From: (IDT, 2025; NCBI, 2025).

Next, we planned the validation strategy for the edited hiPSC clones. We first validated the sequences around the intended target sites for crRNA1 and crRNA2 of our RFP WT hiPSCs, which matched the reference genome (data not shown). We then tested the internal primer set and external primer set which are indicated in **Figure 51**. Both reactions worked as intended (data not shown). These two latter PCR reactions also served as genotype tools. A homozygous KO clone would only show the external fragment without the internal fragment. If a short external (771 bp instead of 2783 bp) and internal fragment could be amplified the clone would be heterozygous KO.

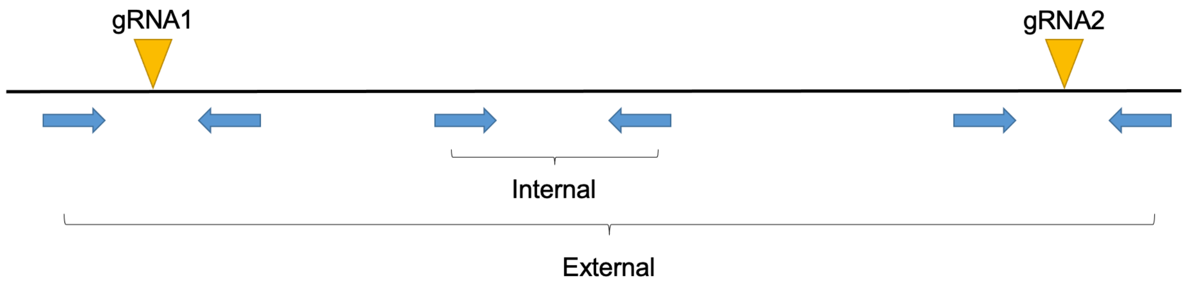

Figure 51: Schematic depiction of intended crRNA and primer location for MATCAP1-KO creation and validation primer sets (blue arrows).

Afterwards, we designed our crRNAs with the online tool of IDT (IDT, 2025). For each locus we provided the intended target site to the tool and the depicted matrices (**Figure 52**) were generated. The crRNAs should be selected from the upper right quadrant of the results matrix as those have the highest on-target (x-axis) and lowest OT (y-axis) potential. The sequences in the lower part of each panel show the sequence of the crRNAs as well as their PAM, on-target and OT score. On one hand, the crRNA for the 5' editing site (crRNA1) had a high score for both on- and OT of 80 and 82, respectively. On the other hand, the one for the 3' editing site only scored 64 for its on-target potential, while having a superior OT score of 92.

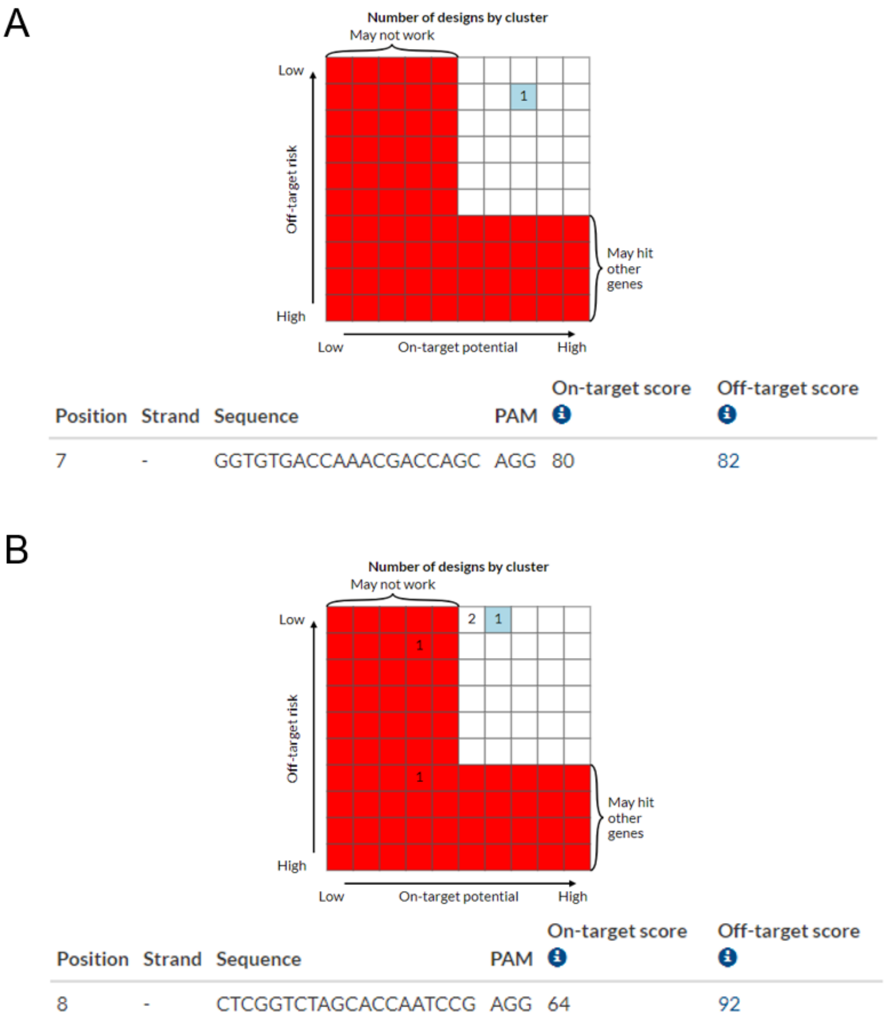

Position	Strand	Sequence	PAM	On-target score	Off-target score
7	-	GGTGTGACCAAACGACCAGC	AGG	80	82

Position	Strand	Sequence	PAM	On-target score	Off-target score
8	-	CTCGGTCTAGCACCAATCCG	AGG	64	92

Figure 52: Selection of crRNA for 5'- and 3' editing site.

Matrices outlining the selection of the (A) 5'- and (B) 3'-crRNA. The matrices are divided into four quadrants with the y-axis showing off-target risk from high to low and the x-axis showing the on-target potential from low to high. This results in the upper right quadrant representing crRNAs that combine low off-target risk and high on-target potential. Below the matrices the sequences of the highlighted (light blue) crRNAs are shown with PAM sequence, on-target score and OT score. Abbreviations: crRNA, guide RNA; OT, off-target; PAM, protospacer adjacent motif.

For improved clarity, **Figure 53** illustrates the workflow for a CRISPR-Cas9 genome editing approach. First hiPSCs were taken at the earliest available passage and cultured until number was available. Then, the RNP (1.4) is assembled and the cells are nucleofected via electroporation. It is crucial that the density of hiPSCs before nucleofection is between 50 and 80% of confluence. At this density, the hiPSCs are still in the exponential growth phase. It has been shown that hiPSCs, besides being more proliferative in this phase, show improved viability, more efficient DNA repair, enhanced maintenance of pluripotency as well as better clonal expansion (Lobo et al., 2025). After two days, the cells are assessed microscopically for intracellular fluorescence of the ATTO555-coupled tracrRNA, which is part of the RNP and the cells are seeded as single clones. These clones are picked after 5-7 days and cultured until they can be frozen for gDNA extraction and cryo-conservation (3.2.1.5, 3.2.1.2). After genotyping, positive clones can be cultured again and the quality controls performed.

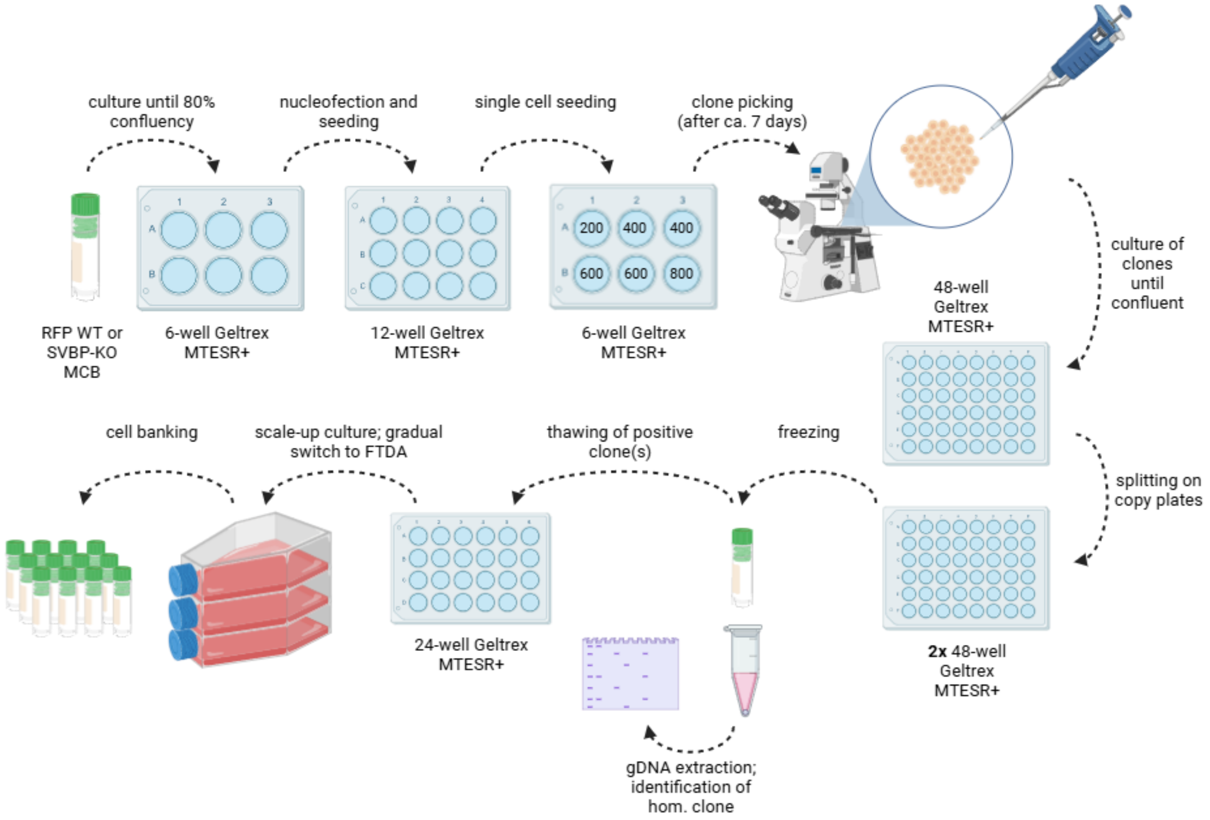

Figure 53: Workflow for CRISPR/Cas9 genome editing in hiPSCs for the creation of MATCAP1-knockout.

Schematic for the workflow of CRISPR/Cas9 genome editing in hiPSCs. HiPSCs need to be in the growth phase when they are transfected with the CRISPR/Cas9 genome editing components. After transfection, the cells are seeded at single cell density to enable clone picking after about seven days. The clones are then cultured and their genotype analyzed. Cells harboring the desired edit are then cultured further and subjected to quality control steps. Once passed, the newly created cell line(s) may be used for funcntional and molecular studies. Created with Biorender.com. Abbreviations: hom., homozygous; gDNA, genomic DNA; MCB, master cell bank.

As the approach to create a double KO for SVBP and MATCAP1 from the existing SVBP-KO hiPSC line only produced 23 heterozygous KO clones and no homozygous KO out of 144 analyzed, I decided to present only the data obtained for the single MATCAP1-KO hiPSC line. The genome editing strategy and quality measures would have been identical.

Figure 54 shows a microscopic image of RFP WT hiPSCs two days after the nucleofection with the RNP. A cytoplasmic localization of the ATTO555 signal can be appreciated, indicating a successful entry of the genome editing components into the hiPSCs. Therefore, we could continue with further analysis of the generated CRISPR pool.

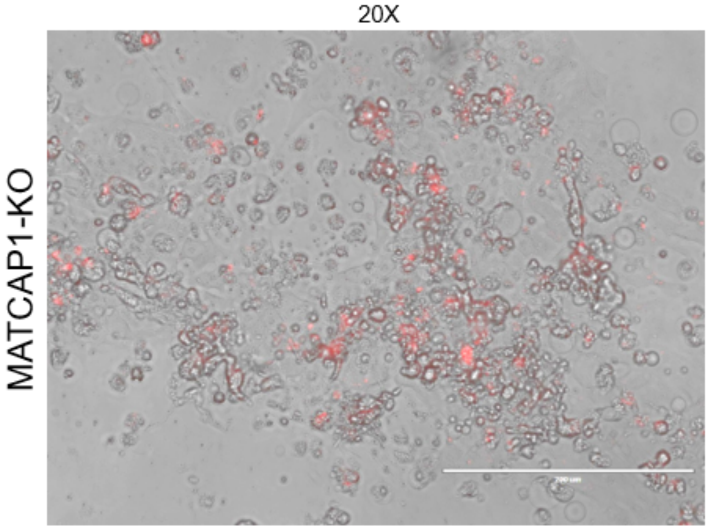

Figure 54: Microscopic image of RFP WT hiPSCs two days after nucleofection with ribonucleic acid protein complex to induce MATCAP1-knockout.

RFP WT hiPSCs were nucleofected with the CRISPR-Cas9 genome editing RNP. Red dots indicate ATTO555 labelled tracrRNA. Scale bar represents 200 µm.

For this pool analysis, the supernatant of both non-nucleofected RFP WT hiPSCs and RNP-nucleofected (potential) MATCAP1-KO hiPSCs were collected and subjected to a PCR with the Phire Tissue Direct PCR Master Mix and primers for either the site around crRNA1 (1), crRNA2 (2) or amplification of the external fragment around both cutting sites (3). Reactions 1 and 2 showed clear bands for both RFP WT and MATCAP1-KO at the expected sizes. Reaction 3, which was intended to amplify the external fragment, did not amplify a fragment for the RFP WT supernatant, which was due to the amplification time only being 1 min. The fragment without the intended deletion of 2783 bp could not be amplified in this time frame. In contrast to that, the MATCAP1-KO pool showed several bands in reaction 3: one around 450 bp, one around 550-600 bp, one above 1 kb and one at the expected size (771 bp) as indicated by the red arrow in **Figure 55**.

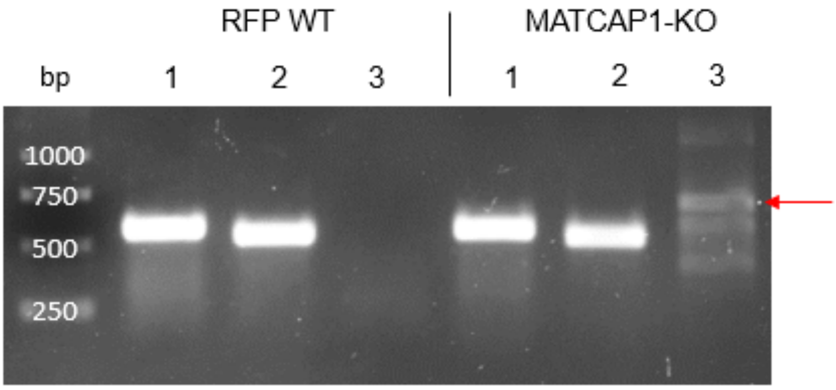

Figure 55: PCR validation of CRISPR pool after ribonucleic acid protein complex nucleofection.

Reaction 1: site around crRNA1 (582 bp), reaction 2: site around crRNA2 (549 bp), reaction 3: amplification of external fragment (771 bp) as outlined in before (**Figure 51**). Red arrow indicates the desired external fragment. 1% agarose-TBS gel stained with Midori Green.

After the genotyping of 37 surviving clones of the initially picked 48, three were determined to be heterozygous, while only one was a homozygous KO. The remaining clones appeared to still be WT. **Figure 56** depicts examples of all three described outcomes. From clone B6 only the internal fragment (reaction 2) was amplified, while both internal and external fragments were amplified from gDNA of clone B8. Finally, the PCRs for clone B7 only yielded a product for reaction 1 (external) but not reaction two. Therefore, clone B7 was determined to be the top candidate to be a homozygous KO of MATCAP1. Clone B6 remained WT and B8 was either a heterozygous KO or a mixed clone.

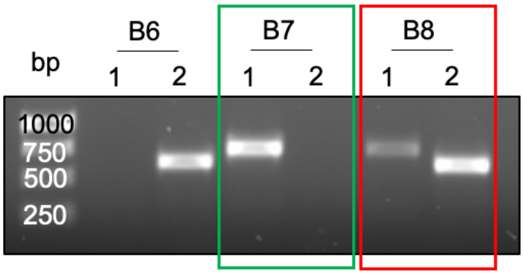

Figure 56: PCR genotyping of clones B6-B8 for MATCAP1-knockout.

Reaction 1: internal fragment (643 bp), reaction 2: external fragment (771 bp). 1% agarose-TBS gel stained with Midori Green. Green box indicated homozygous clone, red box indicates heterozygous or mixed clone.

4.4.2 Validation and quality control of a homozygous MATCAP1-knockout clone

In the previous paragraphs, we have outlined the generation of a potential MATCAP1-KO hiPSC-clone. After the initial genotyping (**Figure 56**) we started to validate this clone and perform all quality control measures at place at the Institute of Experimental Pharmacology and Toxicology. The first important quality assurance was the analysis of the karyotype. Karyotypic integrity was analyzed with a custom Nanostring nCounter panel that contained probes for frequently aberrant chromosomal sites including all autosomes and gonosomes. The signal that should be observed is a copy number of two (depicted on the y-axis of **Figure 57A**) for each site, except for the X- and Y-chromosome as the original RFP WT hiPSC-line stems from a male patient (Allen Institute, n.d.), which therefore should only display a copy number of one. No abnormalities were seen for any locus, only one probe did not give a signal on the Y-chromosome, but this is a technical issue present in all of our analyses. Additionally, we evaluated the *MATCAP1* mRNA levels in MATCAP1-KO hiPSC-CMs differentiated from clone B7. By RT-qPCR analysis, the transcript was not detectable while it was present in RFP WT hiPSC-CMs (**Figure 57B**).

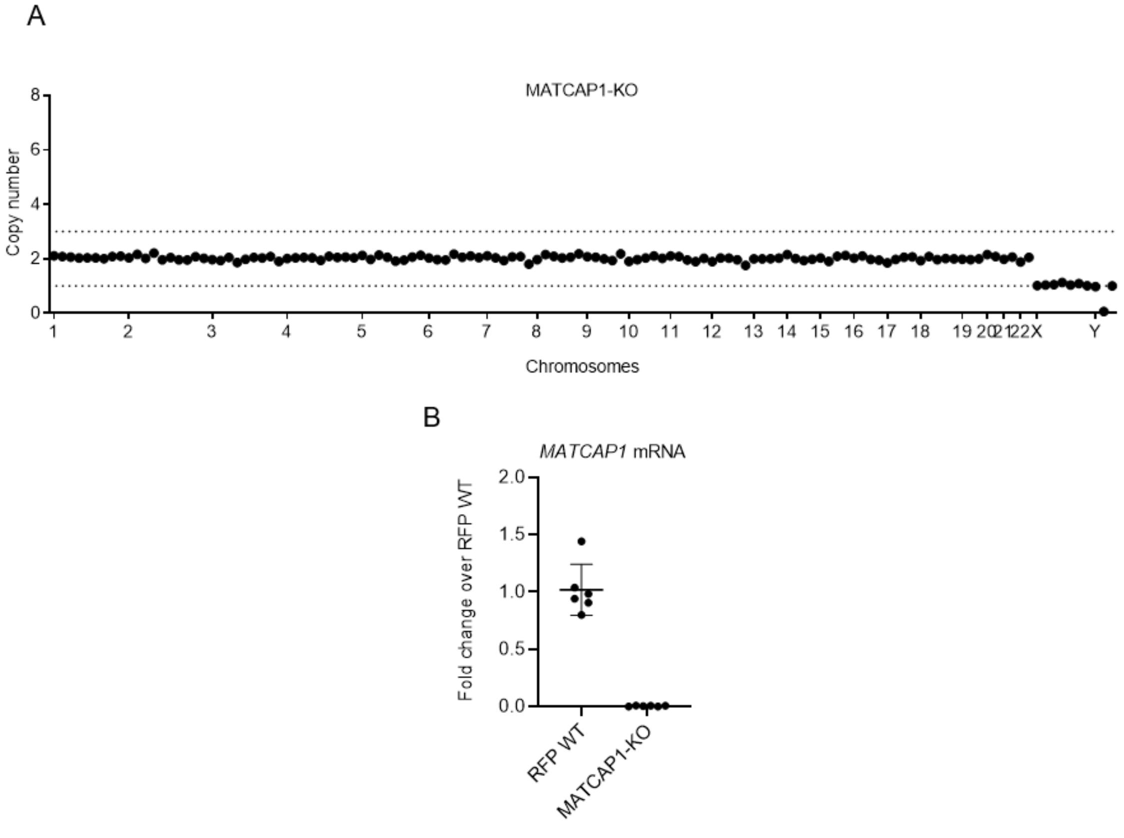

Figure 57: Karyotype assessment and MATCAP1 transcript levels in MATCAP1-KO hiPSCs and hiPSC-CMs.

(A) Confirmation of normal karyotype of MATCAP1-KO with a custom Nanostring nCounter analysis panel analyszing genomic DNA isolated from hiPSCs and (B) confirmation of the absence of MATCAP1 mRNA compared to RFP WT hiPSC-CMs by RT-qPCR.

Next, we investigated the OTs for the crRNAs used. According to our quality measures, the ten most likely OTs for each crRNA should be investigated via sequencing. All OT sites were amplified with specific PCR primers and the products sequenced. **Figure 58** displays the alignments of MATCAP1-KO sequences with RFP WT sequences for the top the OTs for crRNA1 (A) and crRNA2 (B). No OT edits were found in any of the sequenced OTs.

Figure 58: OT sequencing results comparing MATCAP1-KO with the RFP WT (isogenic control) hiPSCs.

Genomic DNA was isolated from hiPSCs. Specific primers were designed for each OT, used to amplify the region around the potential Cas9 binding site and then the forward primer was used for sequencing. Sequences for the top ten OTs for (A) crRNA1 and (B) crRNA2. MATCAP1-KO sequences are displayed on top, RFP WT sequences below.

The final quality control step was the determination of pluripotency via FACS. The marker used in our case was SSEA3 which is a cell surface protein commonly used for this purpose (Andrews & Gokhale, 2024). The analysis of MATCAP1-KO hiPSCs from the master cell bank revealed that 100% of the cells were SSEA3+ and consequently considered pluripotent (**Figure 59**). Testing for mycoplasma contamination via PCR was negative (data not shown).

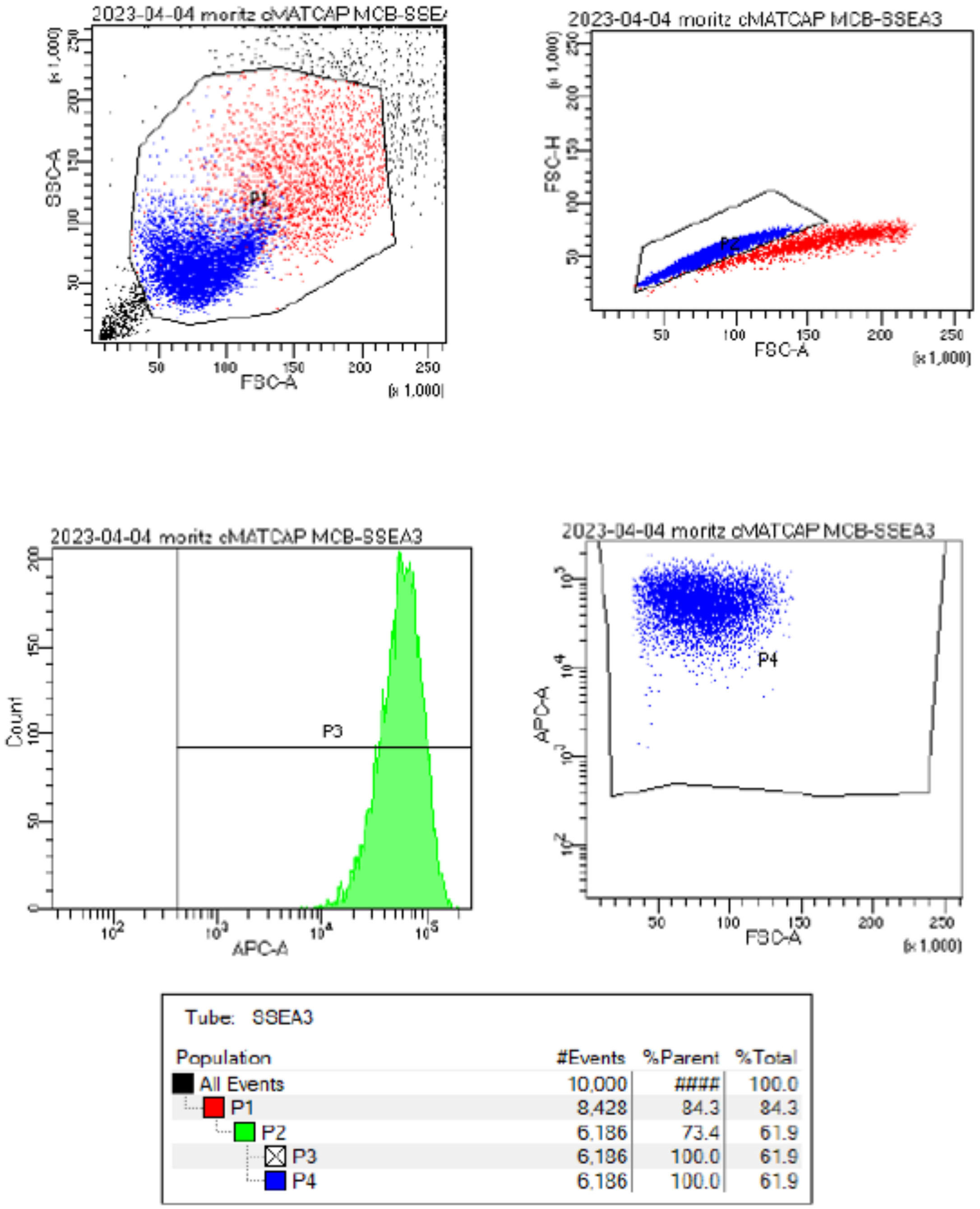

Tube: SSEA3

Population	#Events	%Parent	%Total
⬛ All Events	10,000	####	100.0
🟥 P1	8,428	84.3	84.3
🟩 P2	6,186	73.4	61.9
☒ P3	6,186	100.0	61.9
🟦 P4	6,186	100.0	61.9

Figure 59: Determination of pluripotency of MATCAP1-KO hiPSCs via FACS.

FACS analysis and gating of MATCAP1-KO hiPSCs after staining for the pluripotency marker SSEA3. As the table on the bottom of the figure indicates, 100% of the analyzed cells were SSEA3 positive and can therefore be considered pluripotent.

Taken together, we have created and validated the quality of a MATCAP1-KO hiPSC line. Accordingly, this line could be used in the generation of hiPSC-derived cell types, such as CMs, for the analysis of molecular and functional consequences of the KO.

4.4.3 MATCAP1 deficiency causes altered microtubule post-translational modifications in hiPSC-CMs and hiPSC-CM EHTs

As MATCAP1 is a microtubule modifying enzyme capable of detyrosinating α-tub, we then evaluated the levels of microtubule PTMs after KO of this enzyme. For this analysis we used matured 12-week-old EHTs derived from both RFP WT and MATCAP1-KO hiPSC-CMs. We evaluated the levels of dTyr-tub, Tyr-tub, ac-tub and total α-tub (**Figure 60A**). The level of dTyr-tub was 40% lower in MATCAP1-KO than in isogenic control EHTs (**Figure 60B**). Interestingly, the level of total α-tub was 1.5-fold higher in the KO EHTs (**Figure 60C**) and Tyr-tub level was 25% lower than in WT (**Figure 60D**). The lower level of dTyr-tub was accompanied by a lower level of ac-tub (**Figure 60E**). The lower levels of dTyr-tub and ac-tub which are both associated with more stable and longer-lived MTs could here be compensated for by an increase in total α-tub (Phyo et al., 2022).

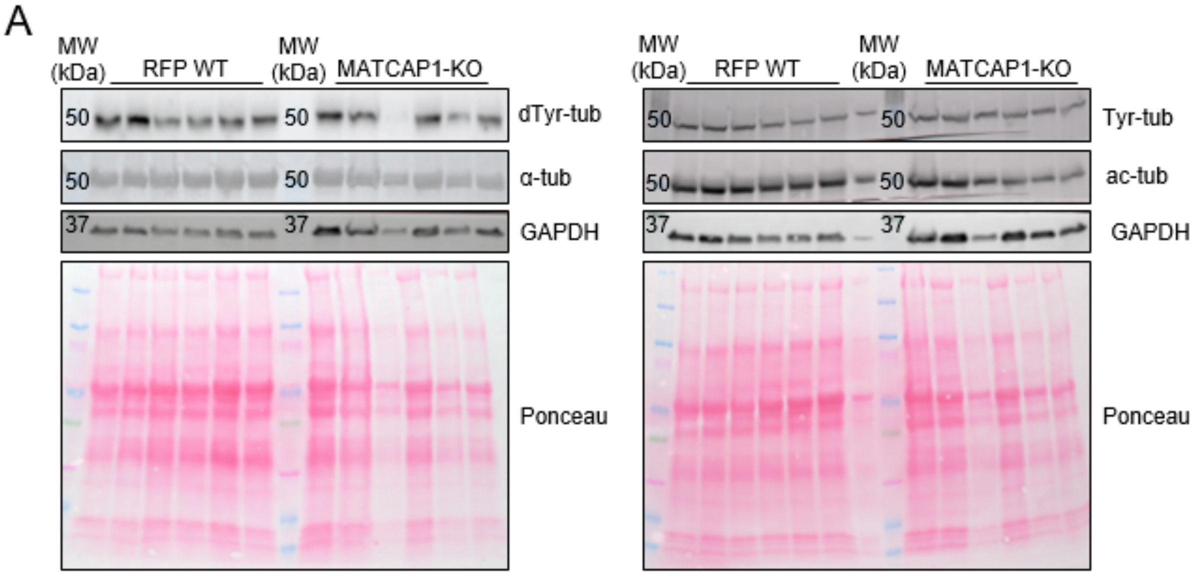

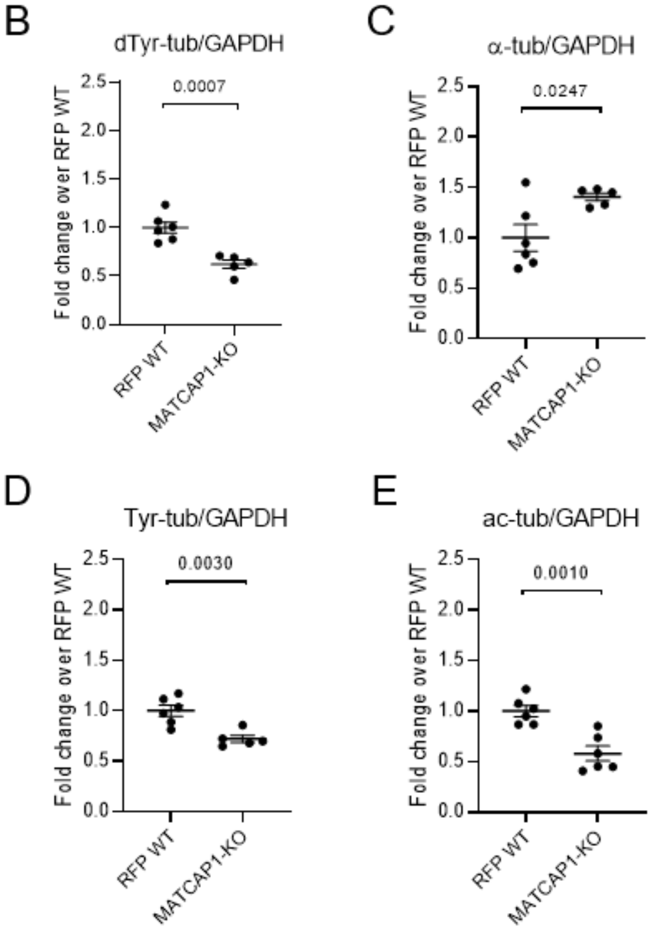

Figure 60: Western blot analysis of dTyr-tub, Tyr-tub, ac-tub and α-tub in hiPSC-CM EHTs.
RFP WT or MATCAP1-KO hiPSC-CMs were cast into EHTs and cultured for twelve weeks on yellow posts. (A) Western blot analysis for dTyr-tub, α-tub, Tyr-tub, ac-tub or GAPDH (loading control) and (B,C,D,E) respective quantification. Data are presented as mean±SEM. P-values were obtained with an unpaired Student’s t-test (B, C, D, E; n = 5-6; (B) and (C) 1 outlier removed in MATCAP1 due to uneven loading).

We then evaluated the level of dTyr-tub in 2D hiPSC-CMs after two weeks of culture in MM. We compared RFP WT, SVBP-KO and MATCAP1-KO (**Figure 61A**). The level of dTyr-tub was 80% lower in SVBP-KO than in WT, due to the missing activity of both VASH1 and VASH2. This result was compatible with data previously published by our group (Pietsch et al., 2024). Due to variability in the samples, this was not significant in the presented data set. In contrast, the dTyr-tub level was 15-fold higher in MATCAP1-KO hiPSC-CMs than in RFP WT and SVBP-KO cells, respectively (**Figure 61**). This result exhibited a stark contrast to the findings in the matured EHTs. The underlying mechanisms for these differences remain elusive though it has to be said that the 2D and 3D hiPSC-CM models present vastly different circumstances.

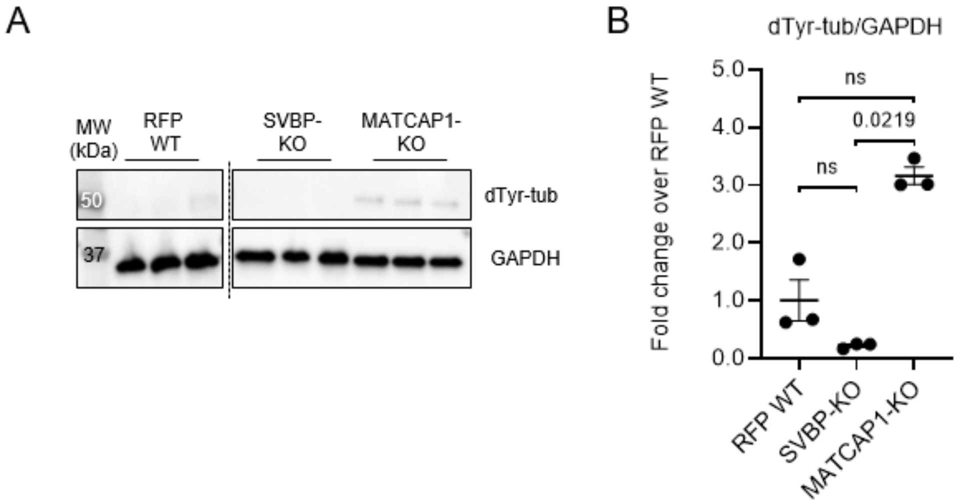

Figure 61: Western blot analysis of dTyr-tub in 2D hiPSC-CMs.

RFP WT, SVBP-KO or MATCAP1-KO hiPSC-CMs were cultured at a density of 2 x 10^5 cells/well in a 12-well plate. The cells were kept in maturation medium for 14 days with medium changes every five days. (A) Western blot analysis for dTyr-tub or GAPDH (loading control) and (B) respective quantification. Data are expressed as mean±SEM. P-values were obtained with the non-parametric Kruskal-Wallis test and Dunn’s multiple comparisons test (n = 3).

4.4.4 MATCAP1 deficiency markedly alters the proteome of EHTs

To evaluate the molecular changes in MATCAP1-KO EHTs beyond the microtubule PTMs, we subjected KO and RFP WT EHTs to unbiased MS analysis. This analysis revealed 265 proteins to be significantly accumulated in MATCAP1-KO, while 97 proteins were significantly decreased (**Figure 62**). Among the accumulated proteins, NRAP, CSRP3, CRYAB myosin heavy chain 11 (MYH11), myomesin 3 (MYOM3), TNNI3 and VIM were found. MYH6, calpain 2 (CAPN2) and calmodulin 1 (CALM1) were among the lower number of downregulated proteins in MATCAP1-KO hiPSC EHTs. These data suggest that MATCAP-KO is more mature than RFP WT.

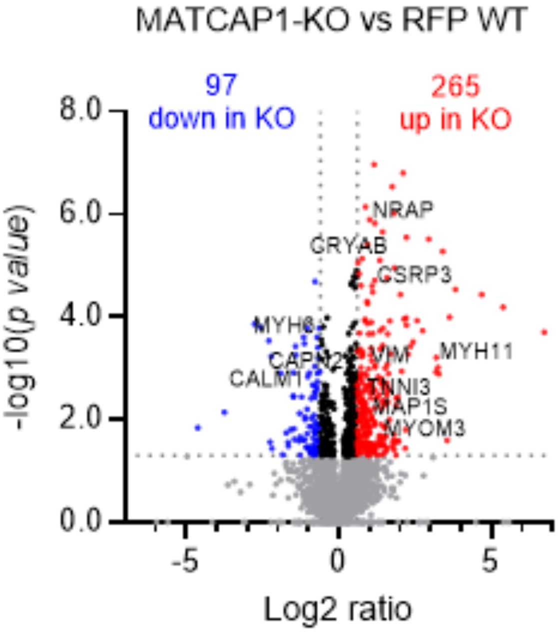

Figure 62: Volcano plot of mass spectrometry analysis of MATCAP1-knockout vs RFP WT hiPSC-CM EHTs.

RFP WT or MATCAP1-KO hiPSC-CMs were cast into EHTs and cultured for twelve weeks. Afterwards, EHTs were washed with PBS and snap frozen in liquid nitrogen, before being subjected to unbiased MS analysis. Dare are plotted as Log2 ratio (x-axis) and -Log10 (*p value*) (y-axis) (n = 6).

To understand the broad proteome dysregulations better, we performed GO pathway analysis with the String database (Swiss Institute of Bioinformatics et al., n.d.). In the RFP WT EHTs, a plethora of keywords indicating the negative regulation of metabolic pathways were enriched, including negative regulation of endopeptidase activity, negative regulation of proteolysis, negative regulation of metabolic process, negative regulation of nitrogen compound metabolic process, negative regulation of metabolic process and negative regulation of macromolecule metabolic process. Unexpectedly, we also found the terms negative regulation of complement activation and acute phase response which would classically be more associated with immune cells than CMs. Also, the term female pregnancy came up, with no direct connection to our used cell type (**Figure 63**).

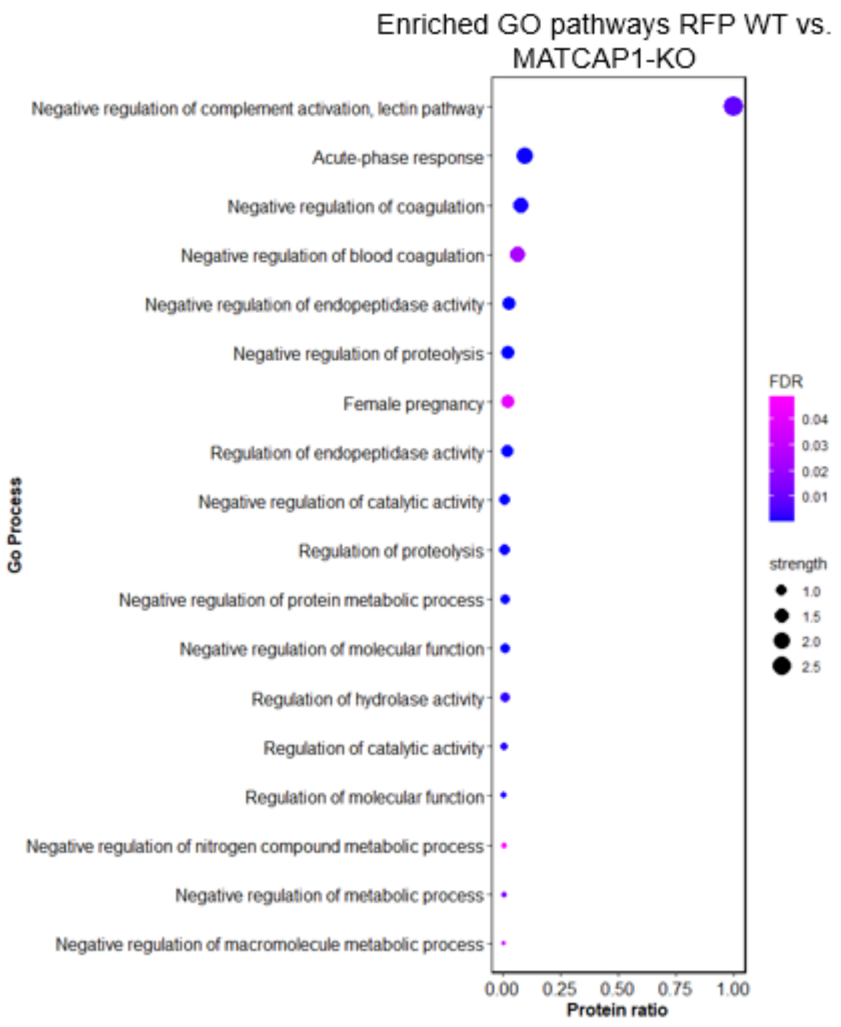

Figure 63: Enriched GO pathways in RFP WT hiPSC-CM EHTs compared to MATCAP1-KO hiPSC-CM EHTs.

RFP WT or MATCAP1-KO hiPSC-CMs were cast into EHTs and cultured for twelve weeks. Afterwards, EHTs were washed with PBS and snap frozen in liquid nitrogen, before being subjected to unbiased MS analysis. Resulting data was subjected to pathway analysis. Cutoff values were a *q-value* <0.05 and a fold change of ≥1.5 (n = 6).

In contrast to that, in the MATCAP1-KO EHTs, many developmental and cytoskeletal terms were enriched. The analysis for example uncovered the terms muscle cell differentiation, connective tissue development, muscle structure development, anatomical structure formation involved in morphogenesis, tissue development, animal organ development, cell differentiation and multicellular organism development. In addition to that, we found unexpected terms including regulation of chondrocyte differentiation, regulation of cartilage development, cartilage development. Enriched cytoskeletal terms included actin filament bundle assembly, actin cytoskeletal organization, supramolecular fiber organization, cytoskeleton organization and cell adhesion. Lastly, energy metabolism and nucleoside metabolism pathways such as nucleoside diphosphate phosphorylation, adenosine diphosphate (ADP) metabolic process, glycolytic process, carbohydrate catabolic process, ATP metabolic process and small molecule metabolic process were enriched (**Figure 64**).

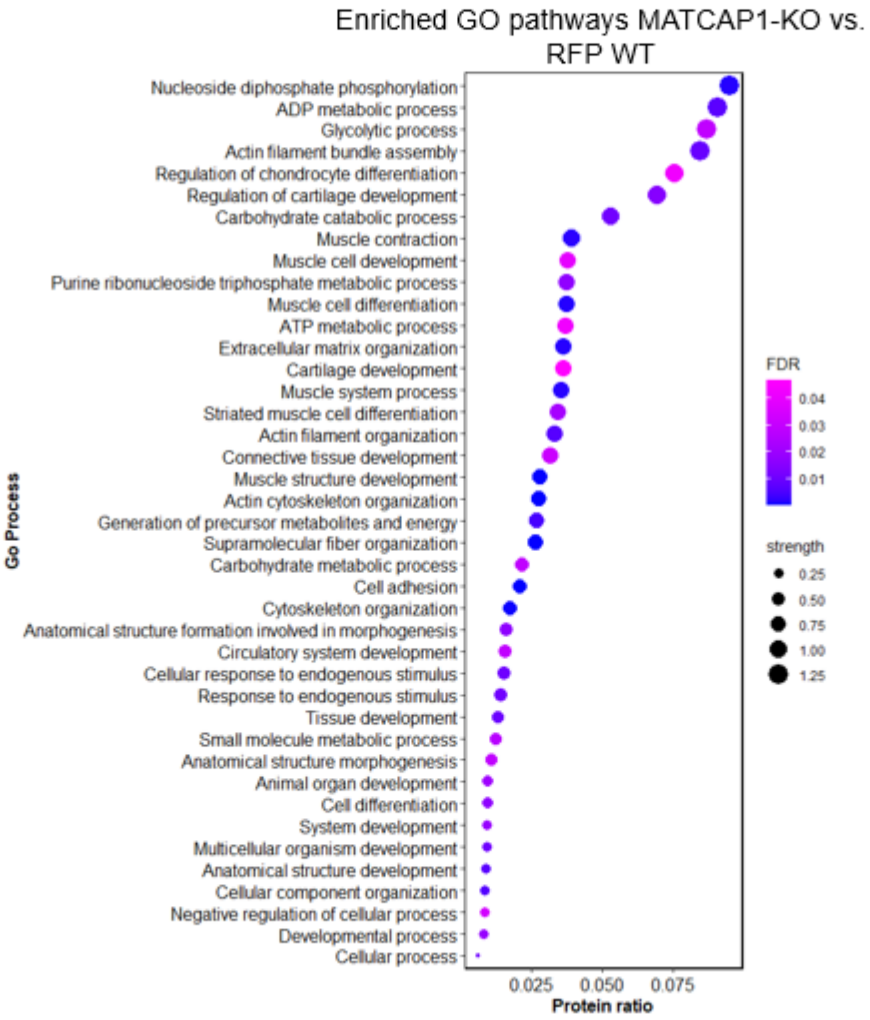

Figure 64: Enriched GO pathways in MATCAP1-knockout hiPSC-CM EHTs compared to RFP WT hiPSC-CM EHTs.

RFP WT or MATCAP1-KO hiPSC-CMs were cast into EHTs and cultured for twelve weeks. Afterwards, EHTs were washed with PBS and snap frozen in liquid nitrogen, before being subjected to unbiased MS analysis. Resulting data was subjected to pathway analysis. Cutoff values were a *q-value* <0.05 and a fold change of ≥1.5 (n = 6).

Summarizing the findings from the MS analysis conducted in RFP WT and MATCAP1-KO EHTs it can be concluded that a deficiency in the MATCAP1 gene causes extensive proteomic alterations. In total 362 proteins were significantly dysregulated.

The dysregulated proteins were largely associated with structural and metabolic pathways (**Figure 63**, **Figure 64**).

4.4.5 MATCAP1 deficiency alters the contractility of EHTs

Logically, after evaluating the molecular consequences of MATCAP1-KO, we aimed at evaluating whether those also implicate functional alterations. Therefore, we recorded force and frequency of contraction of MATCAP1-KO and RFP WT hiPSC-CM EHTs with our proprietary White-Box measurement system. In this setup, contractions are captured by a camera system and the parameters are calculated by an automated software. Measurements were performed according to 3.2.5.2. Both cell lines developed similar amplitude of force overall but MATCAP1-KO was slightly stronger in the beginning of the culture and after d 35 slightly lower in force (**Figure 65A**). The force plateau was reached in both cell lines around d 60 with around 0.6 millinewton (mN). In contrast to that, frequency of MATCAP1-KO EHTs was higher than that of RFP WT EHTs after d 32. Both cell lines peaked around day 10 at 75 beats per minute (BPM) and declined over time. RFP WT reached a plateau at around 18 BPM while MATCAP1-KO EHTs only declined to a mean of 31 BPM at day 84. The BPM plateau was reached after day 35 in both cell lines (**Figure 65B**).

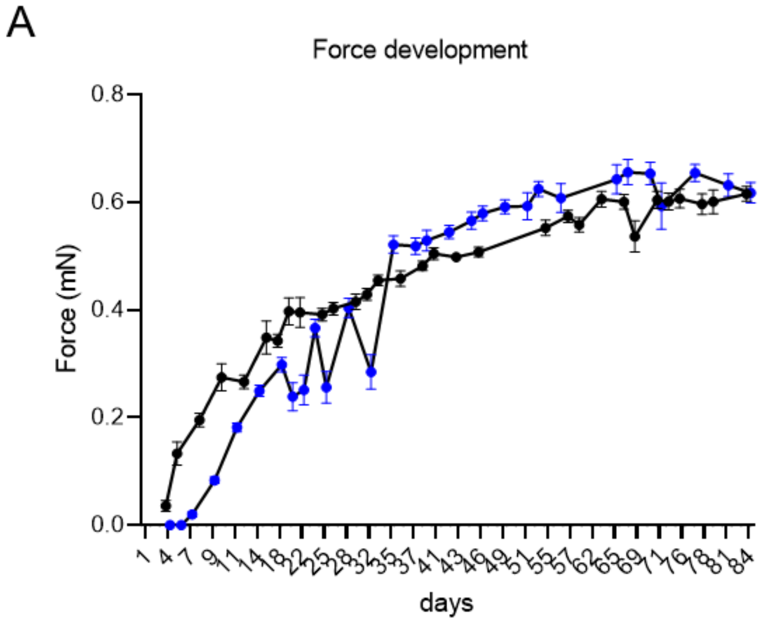

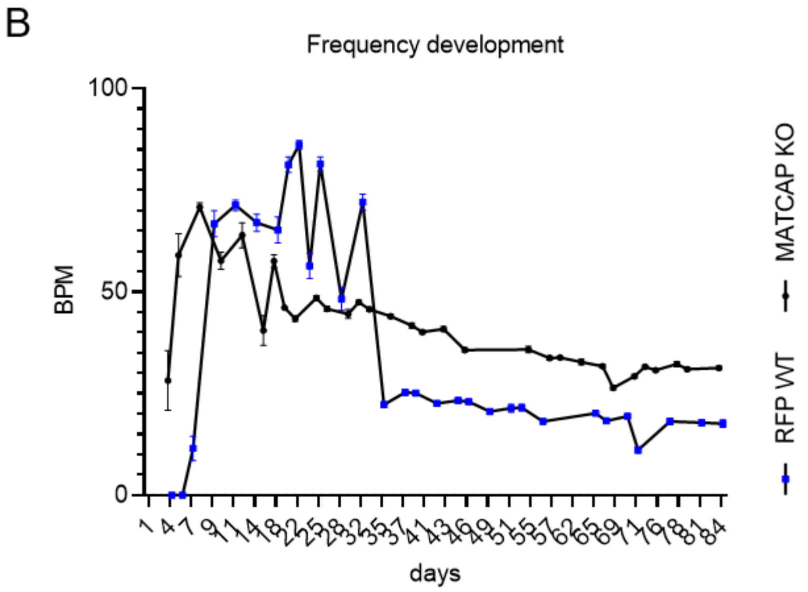

Figure 65: Force and frequency development of RFP WT and MATCAP1-knockout hiPSC-CM EHTs.

One x 10^6 RFP WT or MATCAP1-KO hiPSC-CMs were cast per EHT. Tissues were cultured on yellow posts with a stiffness of 0.8 mN/mm as described before and measured at the indicated time points. (A) Force (mN; y-axis) development over time (d; x-axis) and (B) frequency (bpm; y-axis) development over time (d; x-axis). Blue = RFP WT; black = MATCAP1-KO. (For data until d 32: MATCAP n = 80 in 4 batches and RFP WT n = 69 in 3 batches; for data until d 84: MATCAP1KO n = 24 and RFP WT n = 21). Data are expressed as mean±SEM.

The contraction parameters of EHTs can only be fully evaluated with electrical synchronization (pacing). The resulting data is then normalized and the time to peak (TTP) and relaxation time (RT) can be determined at different fractions (e.g. TTP20 = TTP 20%) of the respective contraction phase. EHTs were paced at day 30 (**Figure 66**) and day 60 (**Figure 67**) with a frequency of 1, 1.5 and 2 Hz. In this study we only display the data resulting from the 2-Hz stimulation. When analyzing the normalized contraction of RFP WT and MATCAP1-KO EHTs at day 30, a clear right shift was visible for the latter (**Figure 66A**). Accordingly, TTP20 and TTP80 were higher in MATCAP1-KO than in RFP WT (**Figure 66B,D**). RT was only higher at 20% in MATCAP1-KO than in RFP WT, while RT80 did not differ between the groups (**Figure 66C,E**).

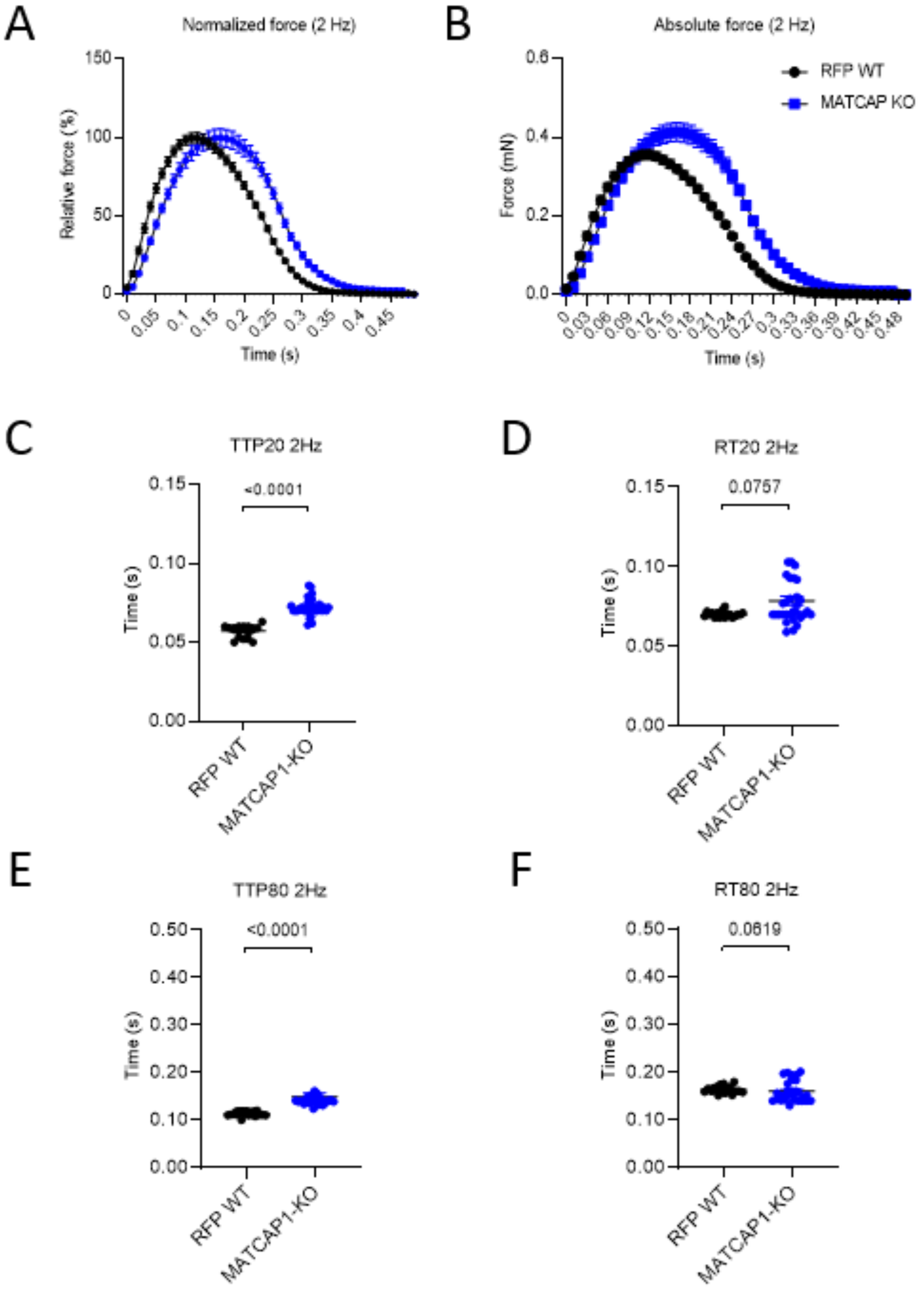

Figure 66: Contraction parameters of RFP WT and MATCAP1-knockout hiPSC-CM EHTs with electrical pacing at d 30.

One x 10^6 RFP WT or MATCAP1-KO hiPSC-CMs were cast per EHT. Tissues were cultured on yellow posts with a stiffness of 0.8 mN/mm with electrical pacing at 2 Hz. (A) Normalized force, (B) absolute, (C) TTP20, (D) RT20, (E) TTP80 and (F) RT80. Data are presented as mean±SEM. P-values were obtained with the Mann-Whitney U-test (RFP WT with n = 19, 1 batch; MATCAP1-KO with n = 31, 2 batches).

Interestingly, the differences between MATCAP1-KO and RFP WT were smaller at day 60 than at day 30. The shape of the normalized force curve at a pacing frequency of 2 Hz was only marginally shifted in MATCAP1-KO (**Figure 67A**). Still TTP20 and TTP80 were significantly higher in the KO ($p = 0.0089$; $p = 0.0023$) but RT20 and RT80 were not different between KO and isogenic control.

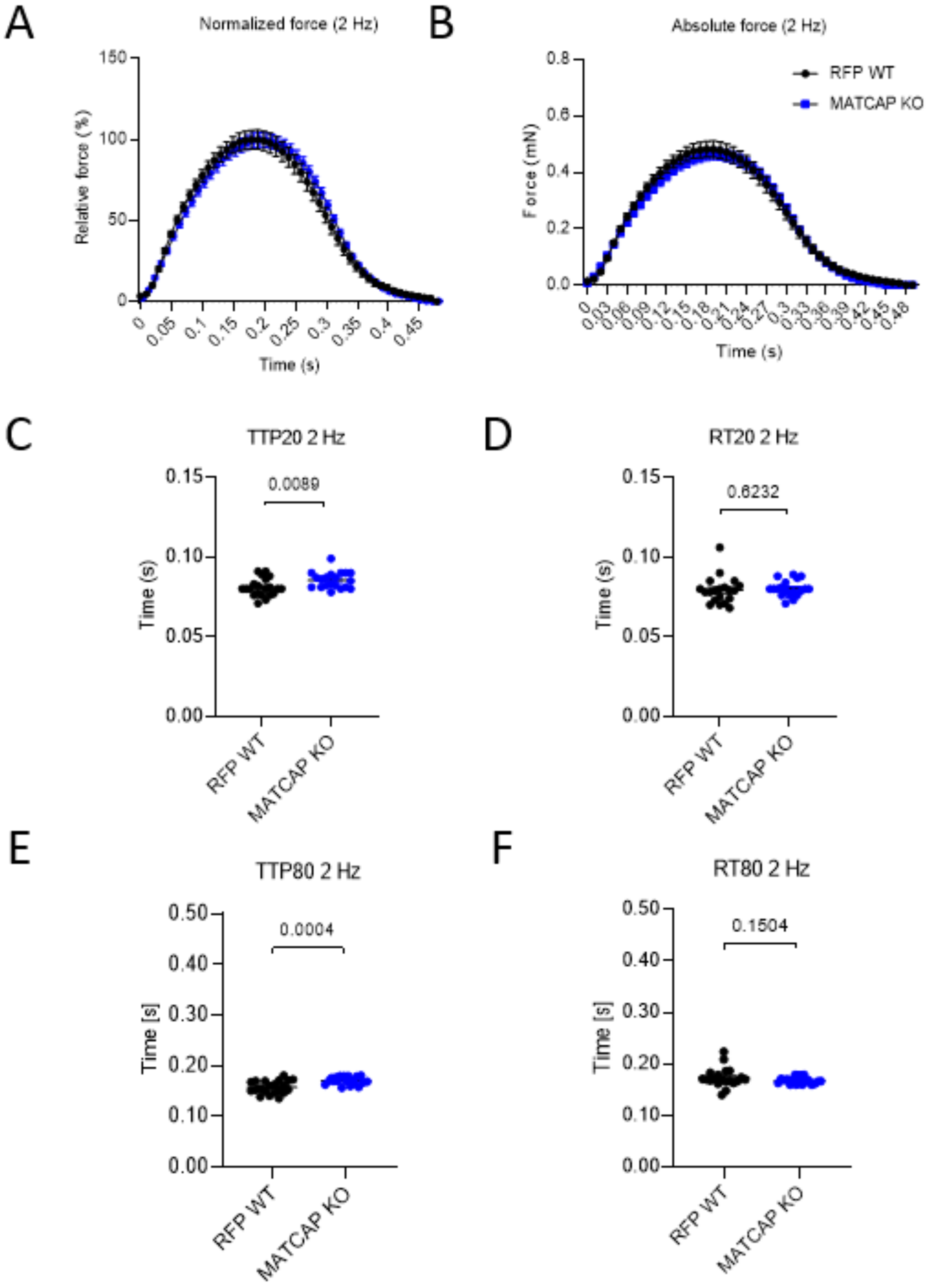

Figure 67: Contraction parameters of RFP WT and MATCAP1-knockout hiPSC-CM EHTs with electrical pacing at d 60.

One x 10^6 RFP WT or MATCAP1-KO hiPSC-CMs were cast per EHT. Tissues were cultured on yellow posts with a stiffness of 0.8 mN/mm with electrical pacing at 2 Hz. (A) Normalized force, (B) absolute force, (C) TTP20, (D) RT20, (E) TTP80 and (F) RT80. Data are presented as mean±SEM. P-values were obtained with the Mann-Whitney U-test (C, D, F) or unpaired Student's t-test (E) (RFP with n = 21, 1 batch; MATCAP1-KO with n = 20, 1 batch).

4.4.6 Summary of the creation and characteristics of a MATCAP1-deficient hiPSC-line

In summary, we successfully produced a homozygous MATCAP1-KO hiPSC-line which passed all mandatory quality control steps at place in our institute. We showed that the KO resulted in lower levels of dTyr-tub in MATCAP1-KO EHTs but higher levels in 2D hiPSC-CMs compared to RFP WT tissues and CMs. The result from the 2D hiPSC-CMs might be compounded by the low n-number and should be reevaluated. Furthermore, the KO of MATCAP1 significantly altered the proteome of 12-week-old EHTs compared to the isogenic control. The resulting signature was enriched in mainly developmental and cytosolic terms. Moreover, RFP WT and MATCAP1-KO EHTs developed similar force, but the KO showed higher beating frequency after prolonged culture. Lastly, under 2-Hz electrical pacing, 30-day-old MATCAP1-KO tissues showed higher force and longer TTP. At day 60 the force of paced MATCAP1-KO and RFP WT EHTs was similar, but TTP remained higher.

4.5 Is detyrosination of microtubules necessary for the development of hypertrophy?

We then assessed whether dTyr-tub is necessary for the development of cellular hypertrophy. We used our different KO hiPSC lines. We exposed 2D culture of RFP WT, MATCAP1-KO, TTL-KO and SVBP-KO hiPSC-CMs to either DMSO, ET1 or ET1sac as described before but used N-cadherin (NCAD) to distinguish neighboring cells. This allowed us to circumvent single cell seeding and allowed for higher n-numbers without increasing experiment and analysis time (**Figure 68A**; **Figure 25**).

It was shown previously that TTL-KO hiPSC-CMs contain supraphysiological levels of dTyr-tub (up to 40-fold), while SVBP-KO lacks enzymatic detyrosination from the main tubulin carboxypeptidase in CMs, VASH1, and of VASH2, which results in only 20% of remaining dTyr-tub (Pietsch et al., 2024). Therefore, we expected SVBP-KO to not develop hypertrophy under ET1 stimulation, while TTL-KO should be able to do so. On the other hand, whether the enzymatic activity of MATCAP1 in hiPSC-CMs is impactful enough to have an influence on cellular hypertrophy development after ET1-treatment was not known.

Visually there were differences observed, especially between the cell lines and in part their reaction to the ET1 or ET1sac treatment (**Figure 68A**). At baseline (DMSO), TTL-KO hiPSC-CMs seemed larger and less compact compared to the other three cell lines. Interestingly, RFP WT and MATCAP1-KO hiPSC-CMs reacted with decompaction and especially in the case of the former, clear structural (ACTN2) disorganization to ET1-treatment. In contrast to that, there was no clear observable difference between the DMSO and ET1 groups for TTL-KO and SVBP-KO. These visual differences also manifested when we compared the baseline cell area of DMSO-treated CMs of all four cell lines and observed that both MATCAP1-KO and TTL-KO CMs were significantly larger than either RFP WT or SVBP-KO CMs. TTL-KO hiPSC-CMs were also larger than MATCAP1-KO hiPSC-CMs (**Figure 68B**).

Accordingly, these cell lines also were not visually impacted by ET1sac compared to either DMSO or ET1 only. In RFP WT and MATCAP1-KO hiPSC-CMs, ET1sac lead to a compaction of the monolayer CMs (**Figure 68A**).

We have previously established that for the assessment of cellular hypertrophy, the use of cell volume and cell area are interchangeable (**Figure 25**). As expected, ET1 induced cellular hypertrophy in RFP WT hiPSC-CMs and sac prevented this effect to even lower cell area than with DMSO (**Figure 68C**). Similarly, ET1 induced higher cell area in MATCAP1-KO CMs and ET1sac induced lower cell area than even DMSO (**Figure 68D**). In TTL-KO, ET1-treatment had no effect, whereas cell area was lower in ET1sac than in DMSO (**Figure 68E**). ET1 did not induce hypertrophy, whereas ET1sac markedly reduced cell area in SVBP-KO cells (**Figure 68F**).

Summarizing the gathered data, we showed can suggest that a deficiency in SVBP but not MATCAP1 prevents ET1-induced cellular hypertrophy while both MATCAP1-KO and TTL-KO cause a baseline level of hypertrophy. These data merit further analyses.

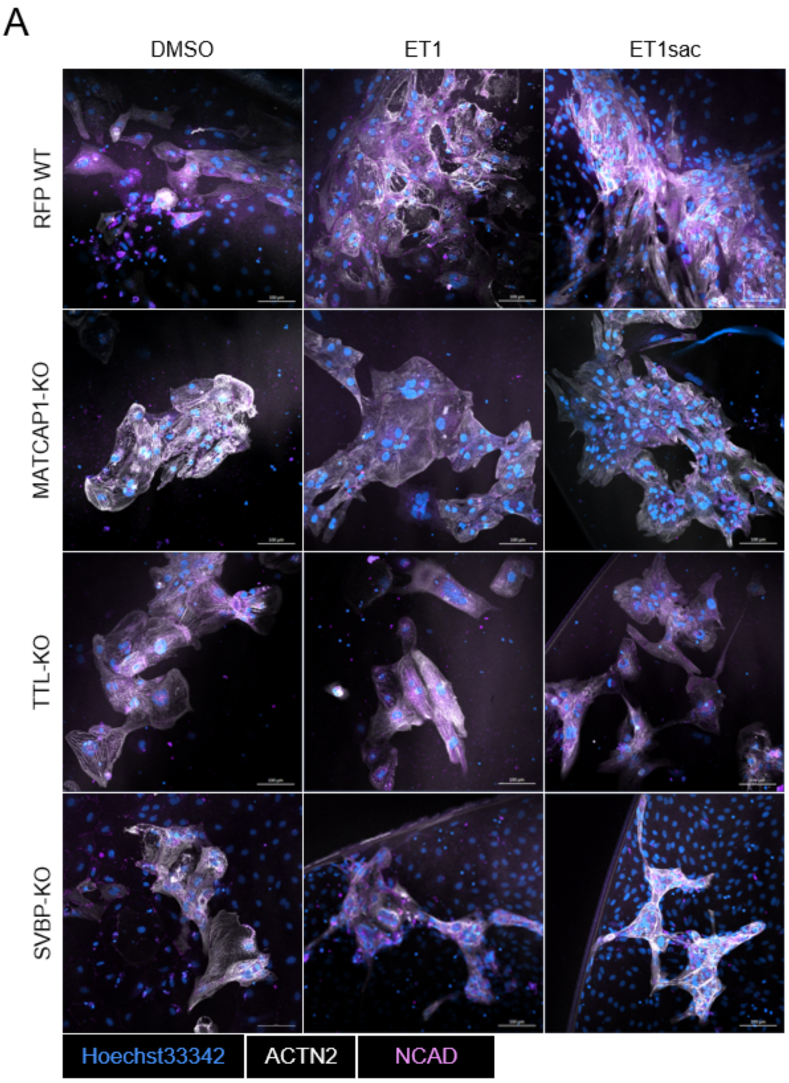
A
DMSO
ET1
ET1sac
RFP WT
MATCAP1-KO
TTL-KO
SVBP-KO
Hoechst33342
ACTN2
NCAD

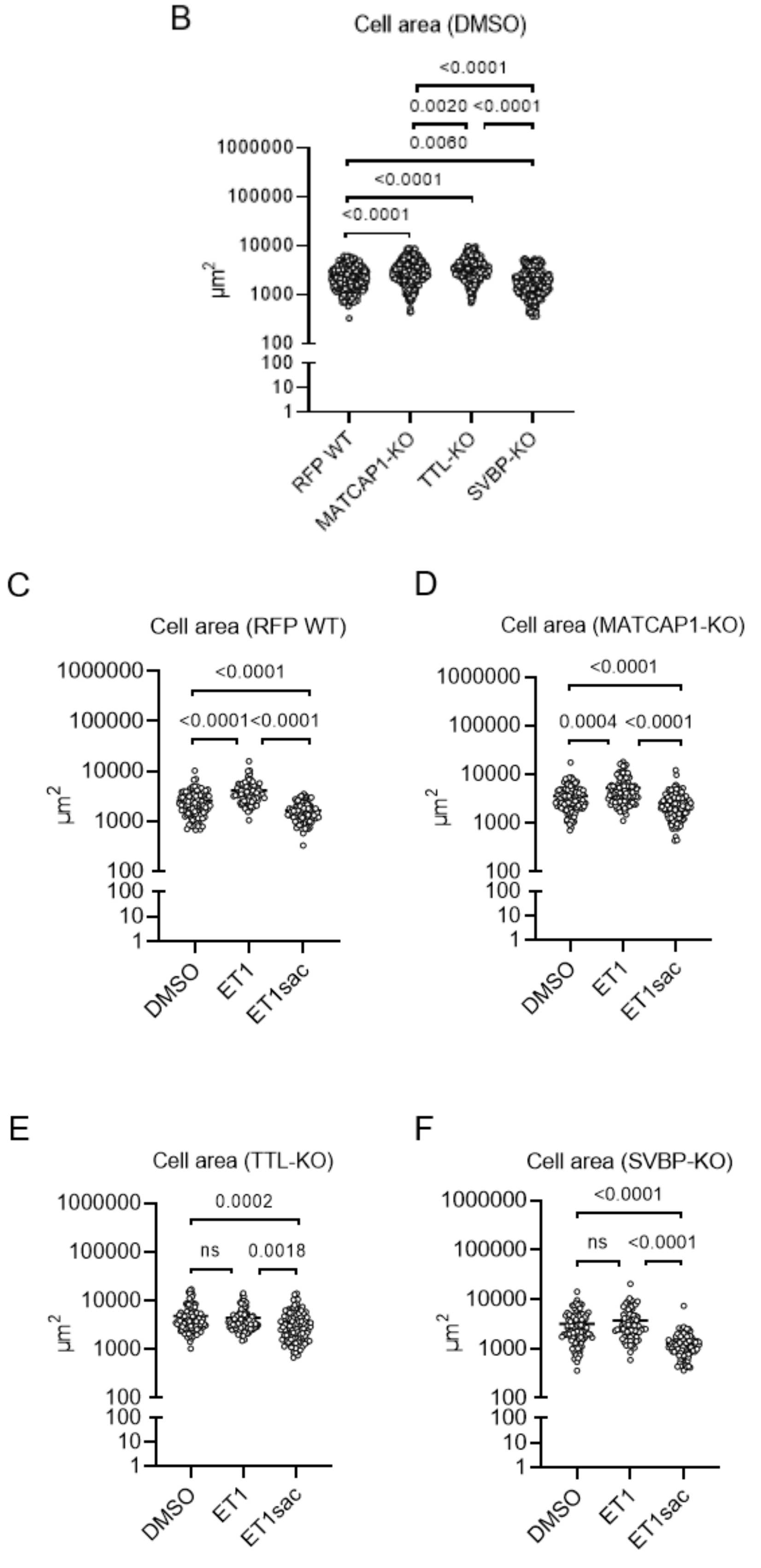

Figure 68: Cell size analysis in RFP WT, MATCAP1-KO, TTL-KO and SVBP-KO after DMSO, ET1 or ET1sac treatment for 72 h.

HiPSC-CMs were plated in black-edge 96-well plates at a density of 2 x 10^4 cells/well for 2 weeks in maturation medium and afterwards exposed to ET1 100 nM, ET1sac (40 µM) or ctrl. (0.08% DMSO) treatment for 72 h. Medium and compounds were changed every 24 h. (A) Microscopic images of RFP WT, MATCAP1-KO, TTL-KO and SVBP-KO hiPSC-CMs with the indicated treatments and ACTN2 (white) and NCAD (pink) for the assessment of cell area and Hoeachst33342 (blue) for the DNA/nuclei staining. Scale bar represents 100 µm. (B, C, D, E, F) Quantification of the cell area in the indicated cell lines (5 micrographs each of 3 well per condition. Data presented as mean±SEM (B-F). P-values were obtained with the non-parametric Kruskal-Wallis test with Dunn's multiple comparisons test (RFP WT DMSO n = 93, ET1 n = 74, ET1sac n = 93; MATCAP1-KO DMSO n = 124, ET1 n = 118, ET1sac n = 135; TTL-KO DMSO n = 112, ET1 n = 101, ET1sac n = 105; SVBP-KO DMSO n = 97, ET1 n = 77, ET1sac n= 99).

5. Discussion

Tubulin detyrosination is accumulated in HF and different forms of heart disease such as HCM (Algül et al., 2023; C. Y. Chen et al., 2018; Schuldt et al., 2021). Evidence that a modulation of the pathway and involved enzymes can positively influence the pathology has emerged in recent years (Caporizzo et al., 2020; C. Y. Chen et al., 2020; Pietsch et al., 2024; Schuldt et al., 2021). It thus far remains unclear how this phenomenon can be targeted in patients and if it is influenced by currently available therapeutic interventions such as sacval. However, there is a push for the evaluation of VASH1 inhibitors which were tested *in vivo* (Eaton et al., 2023).

Prior to our work in hiPSC-CMs, we evaluated TAC-induced hypertrophy and HF in mice. These mice presented with a 10% drop in EF two weeks after surgery. At this time point the treatment with sacval or solvent was started. Although the drug application could normalize dTyr-tub, which was1.5-2-fold higher in TAC/solvent, and fibrosis content (**Figure 19**) as well as normalize proteasome function (**Figure 33**), EF was not rescued but only stabilized. In the TAC/Solvent group, EF declined progressively until the termination of the experiment to a mean of ~26% (Meyer-Jens et al., 2024). This effect can likely be explained by the loss of myocytes which cannot be compensated for due to the low proliferation rates reported in adult hearts (Malliaras et al., 2013; Okada et al., 2004). Contrary to that, preliminary data from our group showed an increase in proliferation rate of SVBP-KO hiPSC-CMs which are low in dTyr-tub (Pietsch et al., n.d.). However, these CMs have dTyr-tub levels of only 20% of the isogenic control while the sacval treatment in TAC mice did not decrease but only normalize dTyr-tub (**Figure 19**; Pietsch et al., 2024). Therefore, sub-physiological, but not physiological, levels of dTyr-tub could be conducive to an increase in cell cycle activity. Regardless of the experimental group, the EF was inversely correlated with dTyr-tub, meaning higher dTyr-tub resulted in lower EF and vice versa. This is in line with previous data showing that MT buckle during contraction and increase passive stiffness of CMs (C. Y. Chen et al., 2018, 2020; Robison et al., 2016). Thus decreasing dTyr-tub fraction improves contractility (C. Y. Chen et al., 2018, 2020; Robison et al., 2016). The prevention of fibrosis by sacval was to be expected as well as multiple groups have reported this effect previously (Jia et al., 2021; Miyoshi et al., 2019; Vaskova et al., 2020).

5.1 Endothelin 1-based hypertrophy model

5.1.1 Successful establishment of a model of hypertrophy in hiPSC-CMs

We have presented evidence for increased dTyr-tub in TAC mice which was fully rescued by sacval application (**Figure 19**). Because no model based on hiPSC-CMs was available that displayed similar characteristics (hypertrophy, increase dTyr-tub, gene expression adaptations), we developed one. This model used 100 nM ET1 over a period of 72 h. A 2-fold increase in cell area, 1.5-2-fold increase in dTyr-tub, hypertrophic gene expression pattern and altered proteome were observed. The dTyr-tub levels were comparable between the 2D hiPSC-CM model and the TAC mice (**Figure 19**, **Figure 26**). In HCM patients though, especially those carrying a sarcomeric gene variant, dTyr-tub was up to 10-fold increased, with a mean of around 4-fold (Schuldt et al., 2021). The 1.5-2-fold increase more closely resembles levels found in patients not carrying a sarcomeric gene variant (Schuldt et al., 2021). A direct comparison of our ET1-based model with a model carrying a patient specific sarcomeric gene variant could be insightful. It could shed light on the question, if those variants can also influence dTyr-tub through thus far unknown mechanisms. Studies have already shown that dTyr-tub can promote interaction with intermediate filaments and the sarcomere. If the increased stiffness observed in tissues with sarcomeric genetic variants is causal for the increase in dTyr-tub or vice versa is not fully understood (Salomon et al., 2021).

Regarding the cell volume, we observed values of around 40,000 µm^3 in single hiPSC-CMs (**Figure 25**). This is considerably larger than what was reported in the literature for CMs isolated from different species. For example, Bensley et al. evaluated the volume of CMs from weanling mice (3-4-wks of age) to be about 5,500-6,500 µm^3, while those from adult sheep reached close to 20,000 µm^3 (Bensley et al., 2016). As hiPSC-CMs are mostly thought to resemble the former rather than the latter (Feyen et al., 2020; Knight et al., 2021), one has to critically assess our experimental procedure. CMs generated from a homozygous ACTN2 variant hiPSC line only reached values close to 20,000 µm^3 (Zech et al., 2022). This difference could be attributed to the fact that during the establishment of the model we used single hiPSC-CMs, which therefore had more space to expand compared to the other studies. Also, we used a maturation medium to metabolically mature the hiPSC-CMs (Feyen et al., 2020), which could in this setting also contribute to a larger cell size. Still the fold-change difference between control and hypertrophied cells was comparable at about 2-fold (**Figure 22**). Moreover, the cell area that we report here (**Figure 25**, **Figure 68**) is comparable to previously reported values (2,000-5,000 µm^2; Prondzynski et al., 2024; Zech et al., 2022).

5.1.2 Molecular and functional consequences of endothelin 1 stimulation in hiPSC-CMs

The development of ET1-induced hiPSC-CM hypertrophy is likely to occur first via transcriptomic alterations as they precede the cellular changes. Indeed, the first major transcriptomic alterations were already observed after 24 h with increased levels of *NPPA*, *NPPB*, *ACTA1* and *MYH7*, while the change in cell area only became significant after 72 h (**Figure 22**, **Figure 23**). Mechanistically, the pathological change in cell size is likely induced via a combination of structural dysregulations as the magnitude in *XIRP2*, *ACTA1* and *MYH6/7* change progressively increased over time. Especially the decrease in *MYH6* (0.71-fold after 72 h) combined with an increase in *MYH7* (1.61-fold after 72 h; **Figure 23**) marks a key transcriptomic adaptation that is also frequently observed in HF and hypertrophy patients (Kyselovic et al., 2024; Mosqueira et al., 2018). Other structural transcripts such as *ACTA2* (1.29-fold), myocardial zona adherens protein (*MYZAP*; 0.80-fold), *FHL2* (0.76-fold), *POSTN* (0.75-fold) and *TCAP* (0.67-fold) were also dysregulated upon prolonged ET1 exposure (**Figure 23**). This further underscores the hypothesized mechanism for the development of cellular hypertrophy (Friedrich et al., 2014; Hu et al., 2025; Kubin et al., 2020; Oka et al., 2007; Rangrez et al., 2016). Conversely, *TTN* mRNA levels were 0.14-fold lower after 72 h of ET1 treatment (**Figure 23**). In healthy CMs, TTN is the major contributor to passive cellular stiffness (Crocini & Gotthardt, 2021). We did not evaluate the stiffness of CMs in our ET1-based protocol, but due to the increase in dTyr-tub, it is reasonable to assume that it is increased as these parameters were reported to correlate (Caporizzo et al., 2020). Accordingly, the decrease in *TTN* might serve as a mechanistic counter towards the increased stiffness arising from increased dTyr-tub. Evaluation of TTN isoform composition and phosphorylation levels could shed light on this. However,

previous data did not reveal differences in TTN isoform composition in a HCM mouse model with or without the overexpression of human TTL (Pietsch et al., 2024).
A secondary mechanism might involve the mishandling of intracellular calcium as *RYR2* is almost 30% lower after 72 h of ET1-stimulation compared to baseline. RYR2 serves as one of the key regulators of intracellular calcium handling and especially calcium-induced calcium release from the sarcoplasmic reticulum (Bers, 2002).

Another transcriptomic adaptation we observed in our ET1-treated WT hiPSC-CMs was the increase in *MME* expression especially at the 24 h and 72 h time points (**Figure 23**). The 4-fold increase observed after 24 h of ET1 was comparable to the increase measured in HCM septal myectomies when compared to NF human heart samples (**Figure 20**). In our model, this higher transcript levels might be due to ET1 being one of the peptides that can be degraded by MME Therefore, *MME* upregulation could serve as a stress response to decrease ET1-stimulation (Thakur et al., 2024). An increase in *MME* was on the other hand not seen when we previously stimulated hiPSC-CMs with PE, which is a small molecule and not degraded by the peptidase (**Figure 20**; Assaf et al., 2024).The concomitant increase in both *XIRP2* mRNA and XIRP2 protein (**Figure 20**, **Figure 21**, **Figure 23**) is likely part of the hypertrophic response program of the CMs as gene expression has been shown to be upregulated during physiological and pathological hypertrophy likewise resulting in altered transcript and protein levels (Yuanjian Chen et al., 2020; Q. Wang et al., 2012, 2014).

5.1.3 Which downstream pathways result from inhibition of neprilysin?

We have shown that ET1-treated hiPSC-CM displayed 1.5-2-fold increased dTyr-tub levels comparable to TAC mice six weeks after surgery. This was prevented by the application of the MME inhibitor sac but by neither val nor sacval (**Figure 26**). On the other hand, all treatments prevented the increase in cell size that we had observed prior after 72 h incubation with the hypertrophic stimulus ET1 (**Figure 22**, **Figure 25**). For valsartan, evidence showing an anti-hypertrophic effect has been around for decades. In 1998, Thürmann et al. showed that a 8-month treatment with valsartan caused a significant regression of hypertrophy compared to atenolol in naïve hypertensive patients (Thürmann et al., 1998). Similar findings have since been shown by others in hypertensive pigs where only val, but not triple therapy with reserpine, hydralazine and hydrochlorothiazide decreased hypertrophy. The authors attributed this positive effect to val to a stimulating effect on mitochondrial biogenesis and therefore cardiac energetics and autophagy (X. Zhang et al., 2014). We did not evaluate autophagy in our hiPSC-CM model because we did not detect major difference in autophagic markers between TAC and sham mice previously (Meyer-Jens et al., 2024). On the other hand, we evaluated chymotrypsin-like activity in both mice and hiPSC-CMs and found a higher activity in both the TAC/solvent and ET1 groups. These defects were corrected with sacval in mice and only with sac in hiPSC-CMs, pointing to sac being the regulator (**Figure 33**). However, we did not find altered levels of ubiquitinated proteins (data not shown). The ubiquitin-proteasome system and autophagy lysosomal pathways represent two of the many pathways that are commonly dysregulated in cardiac disease (Schlossarek & Carrier, 2011; Zech et al., 2022). This also lead to concentrated efforts aiming at the identification of specific modulators (S. R. Singh et al., 2021). Along with such approaches, sac could be considered with this regard in the future. More recently, Ho et al. substantiated the anti-hypertrophic effect of val in a large, double-blinded study and found a markedly improved cardiac function and structure without overt adverse effects. This study presents a dataset that is well suited for comparison with our data as they only included early-stage hypertrophy patients and our treatment regimen with val was preventive (Ho et al., 2021).

Preliminary data that we acquired in ARVMs showed an increase in lysosomal movement speed and distance when incubated with a VASH1 inhibitor and the opposite effect when MTs were depolymerized with nocodazole (data not shown). This implies that lysosomal movement is not only confined to and dependent on MT but also crucially regulated by dTyr-tub. When considering that other groups have shown that MTs are required for productive hypertrophy and that an increase in dTyr-tub precedes it, one could conclude that dTyr-tub is required for hypertrophy (Phyo et al., 2022; Scarborough et al., 2021). This would argue that sac, in contrast to val, prevents hypertrophy in our model primarily through the prevention of dTyr-tub accumulation (**Figure 26**). This notion is also strongly supported by the fact that ET1 did not induce cellular hypertrophy in SVBP-KO hiPSC-CMs and that TTL-KO hiPSC-CMs displayed a baseline 2-fold increase in cell area while also having supra-physiological levels of dTyr-tub (**Figure 68**; Pietsch et al., 2024).

Because multiple studies have shown that ac-tub and dTyr-tub occur on the same subset of stable MT (Cambray-Deakin & Burgoyne, 1987; Moutin et al., 2020), we also investigated this PTM. After 72 h of ET1 stimulation, we found 2.2-fold higher level of ac-tub, which remained high with val and slightly but non-significantly prevented by sac (**Figure 27**). Accordingly, the pathways active upon MME inhibition by sac regulate dTyr-tub but likely not ac-tub. This is coherent with literature showing that the regulation of both PTMs differs. Researchers have also shown that after depolymerization of the MT network, ac-tub recovers before dTyr-tub (Tang et al., 2023). Therefore, it can be determined that both PTMs have differential kinetics, which could also partly account for the differences in effect size of sac. It must also be said that ac-tub was only assessed in a small number of samples, which makes the results difficult to interpret.

We also described that the transcriptomic alterations induced by ET1 were mostly prevented by sac or sacval but not val (**Figure 24**). The magnitude of changes after ET1 treatment was larger than in the first analysis (**Figure 23**), which could be related to batch differences. However, the changes were the same with an altered *MYH6*/*7* ratio through increased *MYH7* (about 16-fold) and decreased *MYH6* (0.45-fold) and increases in *NPPA*/*B* as well as *ACTA1/2* e.g. Integrating these findings with the influence of the interventions (sac, val, sacval; **Figure 25**) and the findings from the establishment of the hypertrophy model, it is likely that sac and val prevent cellular hypertrophy via different pathways. This conclusion is supported by the dTyr-tub level modifications. While sac prevented the 1.5-2-fold higher dTyr-tub induced by ET1, val did not and was even higher than in the presence of ET1 only.

In addition to Nanostring nCounter analysis, we also performed RNAseq analysis on 2D hiPSC-CMs treated with either ctrl. (DMSO), ET1, ET1sac, ET1val or ET1sacval. As we found sac to be the more influential compound for our interests, we focused on the first three groups mentioned. Overall, the number of dysregulated genes between ET1 and DMSO was 1547 while ET1sac only changed the expression of 1001 transcripts. Interestingly, 774 of the transcripts were found in both comparisons to be differentially expressed. Many transcripts found to be upregulated after ET1 treatment (compared to DMSO) matched the proteome data we gathered. Among those were *ACTA1*, *MYH7*, *NPPA*, *NPPB*, *CSRP3*, *XIRP2* and *DES* (**Figure 28**, **Figure 21**).

ET1sac treatment prevented the ET1-induced accumulation of *MME*, *XIRP2*, *POSTN* and *ACE2* mRNAs. This aligned with our expectation, previous data and literature showing that *MME* and *XIRP2*/XIRP2 are elevated during hypertrophy (**Figure 20**, **Figure 21**, **Figure 23**; Q. Wang et al., 2012), and that *POSTN* and *ACE2* represent important modulators in adverse cardiac remodeling (Oka et al., 2007; Zhong et al., 2010). Unexpectedly, the levels of some MT-associated transcripts such as the kinesins *KIF20A*, *KIF14*, *KIF18A* and the centromere transcripts *CENPU* and *CENPM* were repressed after ET1 treatment. Similar genes were higher expressed in ET1sac than in ET1 (*KIF20A*, *CENPF*, *KIF1C*, *KIF4A* and *CENPU*; **Figure 30**; X. Chen et al., 2025; Hirokawa & Tanaka, 2015; X. Liu & Liu, 2022; Lou et al., 2022). With String database search (Swiss Institute of Bioinformatics et al., n.d.), we evaluated GO terms associated with the changed transcriptomes. Surprisingly, the GO terms we found pointed to opposite processes in both comparisons. Overall, they indicated hypertrophy and suppressed cell cycle activity in the ET1-treated hiPSC-CMs, whereas the analysis revealed a decrease in structural transcripts along with a stark increase in those associated with cell proliferation in ET1sac-treated CMs. This is notable because CMs only possess a very limited proliferative capacity, which compounds the issues arising from events such as myocardial infarction (Malliaras et al., 2013). Importantly, unpublished work from our group suggests that decreasing dTyr-tub below physiological levels might be sufficient to induce CM proliferation. These findings, generated in hiPSC-CMs deficient in SVBP and therefore very low dTyr-tub level, showed a higher level of cell cycle activity than WT CMs, especially in the early stage after differentiation from hiPSCs (Pietsch et al., n.d.). As we did not suppress dTyr-tub below baseline levels (**Figure 26**), which is the case in the SVBP-KO model, the mechanism inducing this fingerprint might be different or be in an earlier stage that has not manifested fully in proteomic changes. Of the transcripts that were enriched in ET1sac compared to ET1, *KIF20A*, *KIF4A* and *CENPF* were highly expressed in different tumors. *KIF20A* was found to directly promote cell proliferation and inhibition of apoptosis in tumor cells (Zhao et al., 2018). Similarly, *KIF4A* has been reported to positively regulate cell cycle progression by induction of p21-signaling. Notably, in patients suffering from colorectal cancer, higher levels of *KIF4A* corresponded to poorer prognosis (Hou et al., 2018). Likewise, *CENPF* was reported to increase G2/M-phase transition and to suppress p53-signaling (X. Chen et al., 2025). It has to be mentioned that none of these findings were generated in cardiac tissues. In contrast, the group of James Martin found that MT impedes nuclear localization of the transcription regulator YAP, which is involved in regulating CM cell cycle activity. They uncovered that acetylation and therefore cytoplasmic localization of YAP is increased after MI. Importantly, they also showed co-immunoprecipitation of acetylated YAP with the detyrosinated TUBA4A. Their work directly links densification and concomitant increased dTyr-tub in CMs to cytoplasmic YAP accumulation and lower proliferation (S. Liu et al., 2024). A common mechanism between the genetic model (SVBP-KO) and sac treatment of hiPSC-CMs might be a decrease in (MT-associated) CM stiffness and therefore mechanical load. Other researchers have reported sarcomere disassembly and increased proliferation rates upon inhibition of contraction (Shehata et al., 2025). We did not observe sarcomere disassembly in our 2D hiPSC-CMs, but compared to a loss of contraction, our intervention is far less drastic.

These differential mechanisms are also supported by the MS analysis (**Figure 34**). To find the regulators involved, we investigated the significantly changed proteins comparing ET1sac to ET1 and ET1sacval to ET1. Following in-depth literature research, MAP1B was identified as being involved in dTyr-tub modulation. This protein was significantly more abundant after ET1, and the higher levels were prevented by sac. MAP1B and its phosphorylation have been reported to increase the fraction of unstable MT. The canonical kinase targeting multiple residues of MAP1B is GSK3B (Trivedi et al., 2005). GSK3B in turn is known to be phosphorylated at serine 9 by PRKG1A which inhibits the kinase (Y. T. Kim et al., 2011). Through the application of sac, the cGMP-PRKG1A signaling pathway is activated and logically should increase GSK3B phosphorylation by PRKG1A (Menendez, 2016). This in turn would cause decrease levels of phosphorylated MAP1B. In our experimental settings, the increase in MAP1B level was prevented by sac, but we did not evaluate phosphorylation levels for this protein. Phosphorylated MAP1B was shown to be responsible for the increased MT dynamics in neuronal axons and growth cones (Trivedi et al., 2005). On the one hand, this initially seems to present a contradiction because we observed less MAP1B in the ET1sac group, which should possess more dynamic Tyr-tub MTs compared to the ET1 group. On the other hand, this might also indicate a defense mechanism to reduce the increase in MT stability and cellular stiffness through a MAP1B-dependent mechanism. Following this line of argumentation, there would simply be no need for higher MAP1B levels in the ET1sac group because MT dynamics is already normalized via the fine tuning of dTyr-tub. Supporting this argument, Barnat et al. reported that inhibition of GSK3B increased branch formation in isolated adult dorsal root ganglion neurons. They also mentioned that MAP1B stabilizes Tyr-tub but not dTyr-tub (Barnat et al., 2016). Another interesting finding from the MS dataset was the significantly higher level of VIM in ET1 than in DMSO, which was also prevented by sac (**Figure 29**). VIM was shown to be mostly absent from mature CMs and increased in remodeling tissues of ischemic HF patients and an animal model of MI (Dewing et al., 2021; Kondo et al., 2022). These factors underline the relevance of our ET1-based 2D hiPSC-CM model. Higher levels of VIM could also indicate increased interaction between intermediate filaments and dTyr-tub as this connection has been shown for DES before (Salomon et al., 2021). Evaluating the broader picture, the proteomic changes augmented by sac were much less than those initially caused by ET1. ET1 changed the levels of 240 proteins compared to the control while sac only changed 84 compared to ET1 (**Figure 29**). This rather low number of significant preventions, which does not include key structural CM proteins like ACTN2, ACTA1, TNNT2 and TNNI3, argues for other structural components like MTs and PTM differences to be involved.

In the neuroscience field, scientists provided evidence for a connection between axon bifurcation, which is highly dependent on MT dynamics, and cGMP-PRKG1A signaling. In addition, it is known for decades that the growth cones of neurons are enriched in Tyr-tub (Brown et al., 1992). This suggests that the enzymes regulating the detyrosination/re-tyrosination cycle are target candidates downstream of NP signaling. One group has proposed a target of PRKG1A to modulate axon bifurcation (Dumoulin et al., 2018). Integrating this with the high proportion of Tyr-tub in neuronal growth cones, the implied target is likely regulating the cycle (**Figure 69**; Brown et al., 1992).

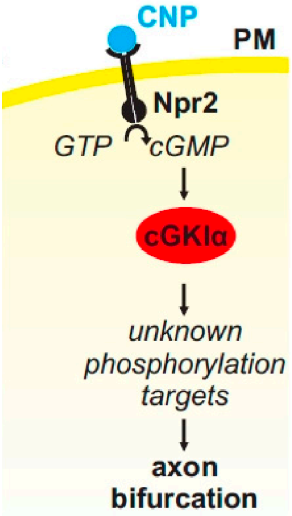

Figure 69: Signaling pathway downstream of CNP/NPR2 increasing axon bifurcation in dorsal root ganglion neurons.

Schematic depiction of CNP binding its receptor (NPR2), which converts GTP to cGMP in the cytosol. The generated cGMP can activate PRKG1A (cGKIα) which can in turn phosphorylate unknown targets that modulate axon bifurcation. PM = plasma membrane. Adapted from: (Dumoulin et al., 2018). Abbreviations: CNP, C-type natriuretic peptide; cGKIα, protein kinase g 1A; cGMP, cyclic nucleotide monophosphate; GTP, guanosine triphosphate; Npr2, natriuretic peptide receptor 2; PM, plasma membrane.

A database search conducted by our French collaborators (Marie-Jo Moutin, Sacnite Ramirez-Rios, Chadni Sanyal) resulted in the identification of seven potential PRKG1A target sites (serine residues) in the Ct of VASH1 (**Figure 47**). These phosphorylation sites could critically influence the binding to the MT by transferring one or multiple negative charges to the enzyme. The outside of the polymerized MT carries negatively charged residues, while the Ct of VASH1 carries positively charged ones. These electrostatic differences play a central role in the productive binding of MTs by VASH1 leading to dTyr-tub (Ramirez-Rios et al., 2023). Importantly, mutating all seven serine residues identified to glutamate, essentially mimicking phosphorylation, resulted in diminished dTyr-tub in isolated MTs. This lack of dTyr-tub was also shown by our collaborators to be caused by a lack of MT binding.

Summarizing our data, the findings of our collaborators and the literature it is likely that the downstream effector of NP-cGMP-PRKG1A signaling is VASH1. Hence, sac is likely causing an increase in VASH1 phosphorylation by PRKG1A, reducing its activity.

To evaluate this hypothesis in CMs, we did a preliminary experiment. We used VASH1-KO hiPSC-CMs and transduced them with lentiviral constructs encoding either VASH1 7A or -7E and SVBP. Those mutant enzymes should either be non-phosphorylatable (7A) or phosphomimetic (7E) as all potential PRKG1A-targeted serine residues of the Ct domain were changed to alanine or glutamate respectively (**Figure 47**). Our expectation was that transduction of VASH1 7A would result in higher levels of dTyr-tub compared to VASH1 7E. Our data show that VASH1 levels increased in a volume-dependent manner for both variants. Because the virus titer was not known, we normalized dTyr-tub to VASH1 levels relative to the highest used volume (10 µl). The highest ratio of dTyr-tub/VASH1 was obtained with a 0.1-0.3 µL of lentivirus/well and was much higher (20-fold) with VASH1 7A than with VASH1 7E (7.5-fold). This suggests that VASH1 7A is more active than the phosphomimetic VASH1 7E (**Figure 48**). Still, we saw substantial dTyr-tub in the presence of VASH1 7E, variant possesses substantial catalytic activity. As shown by our collaborators, VASH1 7E fully prevents binding of the enzyme to MTs. Still when overexpressed in hiPSC-CMs, western blot analysis revealed a substantial increase in dTyr-tub (**Figure 48**; Sanyal, 2024). We did not evaluate levels of VASH2 or MATCAP1 in this setting. Both of these α-tub carboxypeptidases could compensate for the lack of enzymatic activity of VASH1 7E. Moreover, *de novo* detyrosinated TUBA4A could contribute to the increased proportion of dTyr-tub (Sanyal et al., 2023).

The overexpressed VASH1 constructs did not reduce Tyr-tub below 50% in VASH1-KO hiPSC-CMs (**Figure 48**). This fact argues in favor of a high turnover of MTs overall and high levels of TTL activity. It could also indicate that the higher amount of dTyr-tub sequesters α/β-tub dimers in the polymerized MT population due to increased MT stability. This depletion of the free α/β-tub dimers might be sufficient to shift tubulin-autoregulation towards autoactivation. Autoregulation is a concept suggesting that α/β-tub dimers can directly regulate translation of α/β-tub RNAs. It has been directly shown that during phases of an increasing proportion of dTyr-tub, this is interconnected with higher transcription levels (Gasic et al., 2019; Phyo et al., 2022). Accordingly, the consistent translation of new α-tub would stabilize the proportion of Tyr-tub as only TUBA4A is translated in the dTyr-tub form (Sanyal et al., 2023). Conversely, depleting VASH1 activity in TTL-KO hiPSC-CMs via ANP or VASHi application did not increase

Tyr-tub by more than 2-fold (**Figure 42**, **Figure 44**).This outlines that TTL, VASH1 and tub neosynthesis orchestrate Tyr-tub levels tightly.

5.1.4 Direct and indirect modulation of PRKG1A signaling influences microtubule post-translational modifications

As outlined, we believe that cGMP-PRKG1A signaling can be targeted to modulate dTyr-tub and Tyr-tub. To test whether inhibition of PRKG1A can increase dTyr-tub, we applied the inhibitor RP8. In contrast to this small molecule inhibitor, which caused 1.5-fold higher levels of dTyr-tub in RFP WT hiPSC-CMs (**Figure 35**), the peptide inhibitor DT3 did not cause a significant change in dTyr-tub levels (data not shown). DT3 however was able to prevent the CNP-caused increase in growth cone area and induce dTyr-tub in isolated neurons (Sanyal, 2024). The difference in inhibitor effectiveness might be attributed to the different cell types. Otherwise, it could be due to the overall experimental setting. While the neurons were isolated and then treated with DT3, our hiPSC-CMs present a more heterogeneous, less controlled environment. Therefore, it is plausible to assume the presence of factors that sequester or degrade DT3 before it can enter the hiPSC-CMs and act on PRKG1A. It was shown that hiPSC-CMs secrete various factors that could bind peptides supplemented into the medium (Cui et al., 2024). Regarding the specificity of RP8, other researchers have found that it can also act as an activator for PRKG1A. In contrast to our study, they used RP8 at a concentration of 100 µM, which is 10,000-fold higher (Valtcheva et al., 2009). Moreover, it is unlikely that RP8 exerts an activating effect in our experimentally settings because a KD of *PRKG1A* had the same effect (higher dTyr-tub) as the inhibition of PRKG1A (**Figure 36**).

When further analyzing the effects of *PRKG1A* KD, we also found increased levels of both ac-tub and Δ2-tub. These PTMs were even more increased than dTyr-tub (~1.4-fold vs. ~1.2-fold). Generally both ac-tub and Δ2-tub are accumulated on more stable MT (Howes et al., 2014; Janke & Magiera, 2020; Wloga et al., 2017). Therefore, these PTMs could already be more abundant through stochastic mechanisms. As dTyr-tub increases stability and lifetime of MTs, this also increases the likelihood for other MT modifying enzymes to bind.

5.1.5 Natriuretic peptide signaling and VASH1 inhibition modulate microtubule post-translational modifications

We presented evidence outlining the function of NP signaling in our hiPSC-CMs. Both ANP and CNP application resulted in significantly higher levels of pVASP S239, indicating higher PRKG1A activity (Das et al., 2008). This finding also proved the presence of PRKG1A in 2D culture of hiPSC-CMs, although Western blot detection was limited and no PRKG1A was detected in our MS data set (**Figure 36**; data not shown). Both NPs increased pVASP S239 by 1.5-2-fold, which was similar to the change in dTyr-tub level after 72 h of ET1 application (**Figure 39**; **Figure 41**). Judging by the concentration response experiment we performed for ANP (**Figure 41**), 2-fold higher pVASP S239 levels might represent the maximum response. Levels could not be increased further even with up to 500 nM ANP. Correspondingly, our experimental settings represent close to optimal settings for the investigation of NP signaling in hiPSC-CMs.

As we propose an inhibitory effect of cGMP-PRKG1A signaling on VASH1 downstream of NPR1/2 activation, we naturally also investigated the effect of VASH1 inhibition as a complement. Overnight VASHi application in TTL-KO hiPSC-CMs allowed us to capture newly synthesized α-tub in its Tyr-tub form. Strikingly, VASH inhibition resulted in a ~1-3-1.4-fold higher level of Tyr-tub (**Figure 44**) associated with a decreased level of dTyr-tub (0.8-fold; **Figure 43**, **Figure 44**). Similar alterations in Tyr-tub were observed when with 30 nM ANP for as short as 20 min (**Figure 42**). This rapid kinetic emphasizes the dynamics of the MT cytoskeleton in our hiPSC-CMs. Previous studies showed that washout after depolymerization of MTs with nocodazole resulted in a regrowth of the entire network within 120 min (Tang et al., 2023). Because we did not depolymerize the network but only modulated PTMs, a shorter time frame for significant alterations is realistic. It is also likely that we would observe a more significant change in RFP WT hiPSC-CMs as they possess endogenous TTL activity in contrast to the KO. It could be a promising approach to combine VASHi and ANP treatment of hiPSC-CMs to investigate if the two have an additive effect. Critically, the VASHi we used (alk. EpoY) is thought to work as a suicide ligand mimicking Tub in the binding pocket of VASH1 (Hotta et al., 2021). Therefore, a high concentration of VASHi could result in very low VASH1 levels, meaning that an additional incubation with NPs might not have a greater effect size than VASHi only.

Crucial to our hypothesis was to prove a direct effect of sac on cGMP-PRKG1A signaling. We showed that the prevention of ET1-induced increased dTyr-tub levels by sac was possible and reproducible (**Figure 26**). This supports the findings obtained in TAC mice treated with LCZ696, which normalized the dTyr-tub levels (**Figure 19**).

Finally, we showed 2-fold higher intracellular cGMP levels in RFP WT hiPSC-CMs via FRET after acute sac application (**Figure 45**) as well as 40% higher ANP levels in medium supernatant from TTL-KO hiPSC-CMs after O/N sac treatment (**Figure 46**). In patients a multiple week follow up after initial sacval titration also revealed increased levels in ANP as tested in multiple assays. The effect size in patients was greater (>100%) than in 2D hiPSC-CMs. As the name suggests, ANP is mainly secreted by atrial CMs. However, our hiPSC-differentiation protocol induces ventricular CMs which likely secrete less of this factor. This likely explains the lower extent of ANP accumulation in medium from sac treated hiPSC-CMs compared to patient plasma (Essandoh et al., 2023; Potter et al., 2009).

5.1.6 Summary of the findings for the regulation of microtubule detyrosination

To summarize, broad cellular, transcriptomic and proteomic changes were observed using ET1. As we did not aim at understanding how the ET1-based hiPSC-CM hypertrophy model works, we cannot fully conclude. Still the presented and discussed data points towards cytoskeletal dysregulation on proteomic and transcriptomic level. Moreover, direct inhibition of VASH1 or application of ANP in TTL-KO hiPSC-CMs increased Tyr-tub, and CNP or ANP caused higher levels of pVASP S239. These findings point towards a dependence on cGMP-PRKG1A. We showed a full absence of dTyr-tub in VASH1-KO hiPSC-CMs transduced with the phosphomimetic VASH1 7E, as seen by our collaborators in isolated MT. Still, we presented data indicating the lower enzymatic activity of VASH1 7E compared to 7A and WT. One could extend the knowledge about the relevance of dTyr-tub for HF by investigating its levels in other models of HF besides TAC. Such models could include ischemia reperfusion models or different genetic models (Van Der Velden et al., 2022). Our findings could be substantiated upon by evaluating dTyr-tub levels in cardiac biopsies of patients that were treated over longer periods of time with sacval. This evaluation could shed light on the question wheter or not the functional improvement of patients (McMurray et al., 2014) is linked to a decrease in dTyr-tub levels.

5.2 Generation of a MATCAP1-knockout hiPSC-line

As described before, the MATCAP1 detyrosinase represents a newly discovered enzyme that can modify MT (Landskron et al., 2022). Investigating the role of this enzyme is interesting because tissues (EHTs, mice) lacking VASH1 activity still show remaining levels of dTyr-tub. This might suggest the presence of additional enzymes involved in the cycle (Pagnamenta et al., 2019; Pietsch et al., 2024). Its MT binding mechanism differs from that of VASH1/SVBP. Thus far its action has been mostly described in neurons with data on CMs lacking (Landskron et al., 2022). We succeeded at generating a hiPSC line lacking the enzyme but not at creating a double KO on the background of the already established SVBP-KO.

5.2.1 Successful establishment of a new hiPSC-line targeting a novel detyrosinase

Importantly, we validated a full KO for MATCAP1 in hiPSCs. This cell line passed the quality measures routinely performed at the Institute of Experimental Pharmacology and Toxicology. Still, we did not perform whole genome sequencing but stuck to OT sequencing of the ten most likely ones. This was due to cost reasons and the low likelihood of unintended cuts beyond the predicted OTs. Unfortunately, there is always a chance of unpredicted OTs that could have been targeted with our CRISPR/Cas9 approach. In an academic setting, the quality measures at place can be sufficiently deemed. For a translational approach, only the highest degree of quality control would be appropriate. Cutting edge prediction tools utilize neuronal networks and outperform current ones. Those tools could pick up other potential OTs (Lin & Wong, 2018; Vakulskas & Behlke, 2019). What was not considered in our quality assessment was potential modulation of CRSPR/Cas9-binding by chromatin-status. This could critically influence binding and therefore nuclease activity (R. Singh et al., 2015).

Unfortunately, we could not generate a hiPSC-cell line deficient in both MATCAP1 and SVBP (MATCAP1/SVBP DKO). This could be due to the proliferative nature of hiPSCs. In the proliferation process, MTs play a central role as they are needed to separate the replicated chromosome sets properly (Bunning & Gupta Jr., 2023). It was shown that dTyr-tub is enriched in proximity of the spindle poles during cell division. It was implicated to play a central role in spindle positioning and correct chromosome segregation. Depletion of VASH1 resulted in abnormal mitotic spindle formation, which could be partially rescued by depletion of the MT severing enzyme mitotic centromere-associated kinesin (MCAK; S. Liao et al., 2019). KD of *MCAK* normalized the dTyr-tub levels, increasing MT stability. The same study has also interpreted this as evidence for the existence of other tubulin carboxypeptidases (e.g. MATCAP1; S. Liao et al., 2019). Along these lines, another study has shown that the fine tuning dTyr-tub plays a role in mitotic error correction via MCAK (Ferreira et al., 2020). Therefore cells lacking endogenous detyrosination activity could accumulate mitotic errors and undergo apoptosis (Ohashi et al., 2015). Still, the mitotic spindle apparatus is known to contain more dynamic, likely Tyr-tub, MTs (Bunning et al., 2023). The absence of any double-KO hiPSC clones suggests that dTyr-tub solely generated through TUBA4A, the only *de novo* detyrosinated isoform (Fu et al., 2023), is not sufficient in dividing cells. In contrast to that, we also only obtained one homozygous MATCAP1-KO clone. The lack of further clones could indicate insufficient efficiency of the crRNAs used in our approach. This is underlined by the fact that double-KO mice, lacking SVBP and MATCAP1 are viable (Landskron et al., 2022).

5.2.2 Does MATCAP1 impact force of contraction and kinetics in EHTs?

Interestingly, MATCAP1-KO EHTs started to beat 2-3 days earlier than RFP WT. Force amplitude was only slightly lower in MATCAP1-KO, while the beating frequency was consistently higher after day 35. The maximum generated force during spontaneous measurements was about 0.6 mN in both lines, which is on the higher end especially for RFP WT. These data were generated using stiff silicone posts (0.8 mN/mm). Our group had previously published a force of ~0.4 mN, but this discrepancy might be due to the relatively low EHT number in the current study. Neverthess, MATCAP1-KO EHTs thereby generated similar force to SVBP-KO EHTs (Pietsch et al., 2024). When EHTs were electrically stimulated at 2 Hz, TTP20 and TTP80 were consistently longer in MATCAP1-KO tissues after 30 and 60 days, while RT20 was longer only after 30 days. This time-dependent discrepancy was likely due to more homogenous results after 60 days in MATCAP1-KO EHTs. The significantly higher TTP in MATCAP1-KO (**Figure 66**, **Figure 67**) is comparable to what was published already by our group in SVBP-KO EHTs (Pietsch et al., 2024). As both of these cell lines are deficient in enzymes involved in detyrosination, effect was a common functional expected. This effect might be due to differential MT association to the force generating sarcomeres caused by decrease in dTyr-tub. Researchers have shown that decreasing dTyr-tub by overexpression of TTL in isolated ARCMs increased sarcomeric shortening and contraction velocity without altering Ca^{2+} transients (Robison et al., 2016).

The functional differences in EHTs were likely caused by the altered PTM state of the MTs. Eighty-four-day-old MATCAP1-EHTs did have almost 40% lower levels of dTyr-tub and ac-tub than RFP WT EHTs. Additionally, Tyr-tub levels were lower and α-tub level was 1.5-fold higher (**Figure 60**). As the classical PTMs associated with stability (dTyr-tub, ac-tub) were less abundant in MATCAP1-KO than in RFP WT EHTs, the higher α-tub level could be attributed to increased translation or a decrease in MT severing enzymes (Aillaud et al., 2017; Howes et al., 2014).

5.2.3 How does deficiency of MATCAP1 impact the proteome?

To analyze the changes in MATCAP1-KO EHTs more in detail, we also performed MS analysis. Overall, 97 proteins were significantly lower and 265 were significantly more abundant in the KO than in RFP WT (**Figure 62**, **Figure 60**). We specifically looked for alterations in tubulin isoform levels but we did not detect any difference, which contrasts the finding of the Western blot analysis where higher α-tub was observed. The higher number of proteins enriched in MATCAP1-KO EHTs suggests a role for the protein in translational regulation. Such a mechanism has already been proposed for VASH1. Hantelys et al. described a VASH1 dependent mechanism for translational regulation during hypoxia functioning via the trans-activation of internal ribosome entry sites (Hantelys et al., 2019).

In addition to the above discussed PTMs, MT stability could also be regulated further by other microtubule associated proteins (MAPs). Such MAPs are MAP2 and MAP4 but also the tau protein is known to induce MT stability (Al-Bassam et al., 2002; Shigematsu et al., 2018). In contrast to these factors, which were not detected in MS analysis of MATCAP1-KO EHTs, MAP1S was significantly higher in this cell line than in RFP WT. MAP1S has been found to also act as a MT stabilizer in neurons and its increased abundance in MATCAP1-KO EHTs could counteract decreased MT stability through decreased dTyr-tub (Orbán-Németh et al., 2005). Opposed to the EHTs, 2D MATCAP1-KO hiPSC-CMs exhibited 3-fold higher levels of dTyr-tub compared to RFP WT (**Figure 61**). RT-qPCR analysis comparing the expression of *VASH1* in RFP WT and MATCAP1-KO 2D hiPSC-CMs did not show significant differences (data not shown), arguing against a compensatory mechanism by VASH1 for the loss of MATCAP1. The differences could be a technical artifact or be caused by the vast structural differences in 2D and 3D cultures or a batch-dependent effect.

Because several of the significantly higher abundant proteins are structural ones, the proteomic alterations may indicate broader cytoskeletal remodeling similar to what was found in SVBP-KO (Pietsch et al., 2024). Among these proteins were NRAP, CSRP3, MYH11 and MYOM3 (**Figure 62**). CSRP3 and MYOM3 have been implicated in cardiomyopathy development. Interestingly, *CSRP3* genetic variants are more associated with HCM while MYOM3 genetic variants cause DCM (Geier et al., 2008; Nasir et al., 2023). NRAP plays a crucial tole in myofibril assembly and mechanotransduction (Raabe et al., 2025). Higher levels could therefore indicate a higher degree of tissue maturity. This is also compatible with our GO pathway analysis where terms like muscle contraction and muscle cell development were found (**Figure 64**). Supplementing this argument is the finding of higher CRYAB level in MATCAP1-KO. This protein functions as a chaperone for DES and was shown to promote maturation (Tanaka et al., 2023). Genetic variants in CRYAB can cause intracellular aggregates (Alizoti et al., 2025). Unpublished data from our group has also found higher CRYAB level in a CRISPR/Cas9 edited hiPSC-line that carries a heterozygous genetic variant. In concert with the change in CRYAB levels, my colleagues found lower DES and mislocalization of both DES and CRYAB (Alizoti et al., n.d.). For these reasons, MATCAP1-KO could also represent a model with increased proteotoxic stress or cytoskeletal remodeling. Dysregulation and mutations of both NRAP (Pietsch et al., 2024; Z. Zhang et al., 2023) and CRYAB have been reported to be involved in multiple models of hypertrophy arguing in favor of remodeling (**Figure 29**; Chou et al., 2023).

Another protein that was more abundant in MATCAP1 was VIM. Already three decades ago, circumstantial evidence has surfaced arguing for its expression in dedifferentiated more proliferative CMs that also co-express the proliferation marker Ki67 (Behr et al., 1995). Moreover, VIM is known to be the less mature intermediate filament protein compared to DES arguing against a higher degree of maturation in MATCAP1-KO EHTs (Vaittinen et al., 1999). VIM and CRYAB were also reported to be in close proximity in cultured human astocyte cells (Hagemann et al., 2009; Perng et al., 1999). In ocular tissues, where CRYAB is the most abundant protein, higher levels have been associated with an increase in VIM (H. Xu et al., 2018).

The significantly lower level of CALM1 can be tied into the lower dTyr-tub levels in MATCAP1-KO EHTs (**Figure 60**, **Figure 62**). It could lead to a mild destabilization of the network (Sanyal et al., 2023). Along those lines, a 2025 study showed increased expression of CALM1 and mislocalization through colchicine-mediated MT stabilization (Bogdanov et al., 2025). Therefore, our data and literature complement one another. CALM1 is also involved in calcium handling, meaning that alterations in its abundance could potentially explain the differential beating rate and contraction kinetics in MATCAP1-KO EHTs (**Figure 62**, **Figure 66**, **Figure 67**; Z. Liu et al., 2015).

5.3 Limitations

A major limitation of our study is the use of hiPSC-CMs. This model has to be considered as immature, although we already imply measures to increase metabolic and structural maturity (Knight et al., 2021; Meyer-Jens et al., 2024). In our setup, we solely control CM percentage of the differentiation without focusing on the remaining cell types, which usually make up between 5 and 20% of the resulting cells. Due to the molecular mechanisms utilized in our differentiation protocol (3.2.3.1), it is at least very likely that the non-myocytes are also of mesodermal origin. In sharp contrast to this, the CM percentage of adult heart ventricles is regularly reported to be around 50% (Litviňuková et al., 2020). Some groups have made advances in including other cell types in their (3D) models and reported superior *in vitro* model characteristics. These models more closely resemble the cellular composition of the heart and might be more suitable for disease modeling (Prondzynski et al., 2024; Wrona et al., 2022).

HiPSC-CMs also do not develop T-tubules, which are a central structural and functional feature of adult CMs. T-tubules are necessary to facilitate proximity between voltage gated Ca channels and the sarcoplasmic RYR2 channels (Bers, 2002). Calcium handling in CMs is furthermore critically regulated by the reuptake into the sarcoplasmic reticulum and extrusion towards the extracellular space. The former action is performed by SERCA2, which is tightly regulated by PLN. As PLN has been shown to be a target of cGMP-PRKG1A signaling, evaluation of PLN phosphorylation is indicated but was not performed here (Abdallah et al., 2005). Levels and PTMs of NFAT, which can crucially modulate gene expression influenced by Ca^{2+}, were also not assessed (Fiedler et al., 2002). One study has already shown positive effects of sac on pro arrhythmic Ca^{2+} leak in late stage HF (Eiringhaus et al., 2020). According to our study and the literature, this is likely caused by cGMP-PRKG1A signaling alterations.

One also has to address the concentration of ET1 that was applied for the treatments during this study. We have regularly used 100 nM of this substance to induce *in cellulo* hypertrophy while others reported comparable effects with only 10 nM (Johansson et al., 2020; Redwanz et al., 2024). However, this concentration has been used before in our institute and yielded no obvious adverse effects in our model.

The *PRKG1A* KD was highly effective on transcript level, reducing the abundance by 75-80% (**Figure 36**). This efficiency is comparable to what was reported by other in the literature and our own experience (L. Guo et al., 2015). Some groups even report up to 90% reduction of the targeted mRNA (Saroj et al., 2025). However, we only observed a 35-40% lower level of PRKG1A protein (**Figure 36**). Differences between transcript and protein levels can be due to various factors. First, half-life time of the protein might be vastly different from that of the mRNA. Although there is no data specifically outlining the turnover of PRKG1A in CMs, data from other cell types was published. The exact half-life is highly cell type dependent, as PRKG1B is highly expressed in platelets, which have a turnover of up to 60 days without possessing a nuceleus to continue mRNA synthesis. In vascular smooth muscle cells PRKG1 half-life time is estimated to be around 24 h (Sellak et al., 2013). In this regard, other proteins, like Connexin 43, have been investigated. It was found to have a half-life of 1-2 h in isolated CMs (Laird et al., 1991) while others observed a half-life of 2-4 h for TNNT2 and TNNI3 in patients after MI (Kristensen et al., 2024). Importantly, regulatory proteins like ANKRD1 have been reported to have a significantly slower turnover (13 h ± 2.5). Second, this turnover also depends on the cell type, with the same study reporting only about 12 min in endothelial cells (Samaras et al., 2012). As the hiPSC-CMs in our setup were incubated with the siRNAs for five days, this should have resulted in a more prominent decrease in protein levels. However, there are some pitfalls associated with that assumption. On the one hand, the level of PRKG1A is most likely much lower than that of sarcomeric (MYH7) or other structural proteins (α/β-tub) although no literature is available directly comparing them. PRKG1A was, in contrast to other kinases like protein kinase C, not detected in our MS data sets, emphasizing its low abundance. On the other hand, this low abundance increases the difficulty to detect the protein or changes in its levels. Finally, the translation of mRNA molecules can fluctuate drastically (Yan et al., 2016). Taken together, a low PRKG1A level, unknown turnover kinetics and unknown translation rates compound the issue of exact PRKG1A level evaluation.

During this study we have primarily focused on MTs, their PTMs and differentially influenced properties conferred by these. We have not evaluated cellular stiffness resulting from our cellular modulations. Most available literature considers TTN to be the main driver of passive stiffness in CMs with MTs only playing a minor role (Crocini & Gotthardt, 2021; Loescher et al., 2023; Loescher & Linke, 2024). Nevertheless, direct targeting of dTyr-tub in a recent paper from our group in a mouse model of HCM, increased compliance and decreased end-diastolic pressure volume relationship significantly. Therefore, arguing for a substantial role of MTs and MT PTMs for the regulation of cardiac stiffness especially when considering no observable shift in TTN isoform abundance in mice overexpressing TTL compared to empty control (Pietsch et al., 2024). Still TTN isoform levels and its phosphorylation status should have been considered as multiple studies indicate that PRKG1A can decrease passive CM stiffness via TTN phosphorylation and that a hypophosphorylation could increase risk for HFpEF development (Hamdani et al., 2013; Krüger et al., 2009). Assessment of TTN phosphorylation would have been especially important and interesting because a 2024 landmark study reported a decreased stiffness via increased TTN phosphorylation after sacval application in a mouse model of HFpEF (Furukawa et al., 2024). Nanoindentation measurement could be implied to analyze cellular stiffness (Mahmoud et al., 2024).

Another PTM we did not measure was the GSK3B-mediated MAP1B phosphorylation. This could be insightful to understand the mechanism because phosphorylated MAP1B was found to be preferentially associated with Tyr-tub (Barnat et al., 2016). Accordingly, we would expect to find less phosphorylated MAP1B after ET1 treatment compared to control and groups incubated with sac or NPs.

Additionally, we only investigated one clone for the KO of MATCAP1 due to a lack of availablility. It is frequently reported that clones that carry an identical genotype on the surface cannot be viewed as isogenic without implying further quality control steps (Panda et al., 2023; Westermann et al., 2022). In order to fully understand the gravitas of MATCAP1-KO in hiPSC-CMs, more clones should be tested, potentially using a different set of crRNAs to increase experimental yield.

Regarding the MATCAP1-KO EHT data, it has to be said that especially the later time points have limited experimental power due to low sample numbers. Although EHTs overall present a robust platform, batch-to-batch variability represents a hurdle in data interpretation and significance. This can only be overcome by applying stringent quality measures such as force thresholds or electrophysiological parameters or by increasing batch and sample numbers (Arefin et al., 2023). Furthermore, the evaluation of the MT PTMs should be substantiated as the current n numbers do not allow conclusive statements.

5.4 Conclusions and outlook

5.4.1 Conclusions

From our data and careful consideration of the available literature, we can conclude that the ET1-based model represents a valuable tool for future mechanistic studies of CM hypertrophy in a human background. It captures key features of hypertrophy including increased cell size, proteomic and transcriptomic changes as well as higher levels of dTyr-tub. Most of the maladaptive changes were prevented by sac and we were able to identify an inhibitory phosphorylation site on the most important detyrosination enzyme in the heart, VASH1, which is targeted by (sac)-cGMP-PRKG1 signaling.

We could also outline the importance of dTyr-tub in the development of hypertrophy (**Figure 68**). Importantly, TTL-KO hiPSC-CMs exhibited a baseline level of cellular hypertrophy. A similar finding stems from CM-specific NPR1-KO mice. These mice presented with a baseline hypertrophy as well as transcriptomic changes indicating the pathology (Holtwick et al., 2003). Less targeted whole-body NPR1-KO mice show hypertension, hypertrophy and sudden cardiac death (Oliver et al., 1997). Follow up studies have suggested hypertension as the main cause for hypertrophy in these mice but this has since been disproven as normalization of blood pressure had no effect on pathological hypertrophy (Knowles et al., 2001). Therefore, both the NP system and MT, must play a central role in maintaining normal cardiac physiology and dysregulation can lead to pathological remodeling without further stimuli. Contrary to the NPR1-KO, a CM specific PRKG1-KO did not induce hypertrophy at baseline or after AngII application or TAC surgery. These otherwise hypertrophic stimuli resulted in development of a DCM phenotype which was likely due to Ca mishandling (Frantz et al., 2013).

Finally, we provide indications that phosphorylation of VASH1 does influence its activity in hiPSC-CMs. This emphasizes the possibility to target VASH1 as a therapeutic option in patients suffering from hypertrophy and HF if increased dTyr-tub is observed. Still evaluating dTyr-tub in patients presents a hurdle, as tissue availability is sparse. This could in theory be overcome with patient-specific hiPSCs and differentiate them to CMs (Prondzynski et al., 2019).

5.4.2 Outlook

Looking forward, the dependence of (cellular) hypertrophy has also been linked to localized translation. This field has been pioneered by the group of Ben Prosser, who uncovered that the dTyr-tub increase precedes hypertrophy and that MT are the key component in localized translation (Phyo et al., 2022; Scarborough et al., 2021). They evaluated translation elegantly by first injecting mice with colchicine, then stimulating hypertrophy with PE and finally tracking newly translated proteins with puromycin. PE induced 2-fold higher protein translation rates without a significant increase in heart-weight-to-body-weight ratio, a classical parameter for hypertrophy assessment (Scarborough et al., 2021).

In the future, we would like to evaluate if dTyr-tub is necessary for cardiac hypertrophy development *in vivo*. We plan to subject WT or SVBP-KO mice to either vehicle or PE injections for 4 days. If dTyr-tub is necessary for PE-induced pathological hypertrophy, we should only observe hypertrophy and increased MT density in WT animals (**Figure 70**). To uncover the underlying mechanism, we will also track protein synthesis and activity of different degradation pathways such as the ubiquitin-proteasome system or macro-autophagy. If this approach is successful, sacval or other cGMP-PRKG1 modulators could also be applied in the PE hypertrophy mouse model.

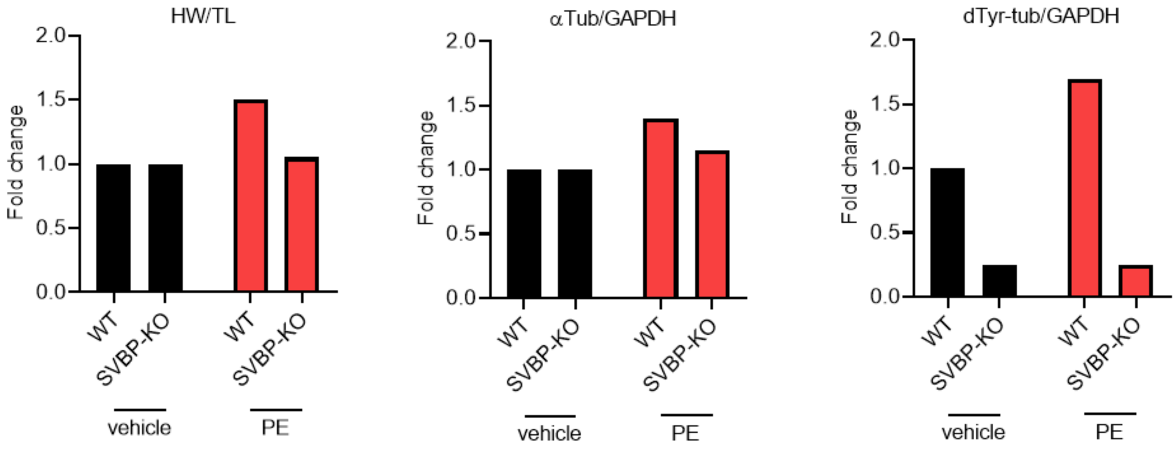

Figure 70: Expected hypertrophy, αTub and dTyr-tub in WT or SVBP-KO mice.

WT or SVBP-KO mice will be injected with 10 mg/kilogram bodyweight per day for 4 days. Heart weight (HW) and tibia length (TL) will be evaluated to determine hypertrophy (HW/TL). Also, αTub and dTyr-tub will be tested via Western blot. Graphs show expected results only. Abbreviations: HW, heart weight; TL, tibia length.

The outlined project is already fully funded with the EPICC grant awarded to Dr. Keita Uchida and me by the Leducq Cytoskeletal Network.

Moreover, one could evaluate the effectiveness of classical cGMP-PRKG1 modulators on VASH1 activity and dTyr-tub level. One option would be to use the PDE5 inhibitor sildenafil. Multiple studies have already proven that sildenafil application in TAC mice blunts hypertrophy (Hsu et al., 2009; Nagayama et al., 2009). Nagayama et al. showed a stabilization of cardiac function, reduced fibrosis and significantly lower heart weight to body weight ratio, overall comparable to sacval application in our study. At the same time Hsu et al. showed an independence of the beneficial effect of sildenafil from calcium-calmodulin signaling (Hsu et al., 2009; Nagayama et al., 2009). Accordingly, there must be a (structural) target in the myocardium which can modulate cardiac hypertrophy. As discussed before, we propose this to be VASH1.

For the translation of VASH1 activity modulation to patients, the development of small molecules is most promising. A newly developed VASHi has already been shown to be comparable to TTL overexpression in CMs isolated from HFpEF rats (Eaton et al., 2023). Contrary to the delivery of TTL, likely via a viral vector, drug application is much simpler for patients and physicians alike.

6. Acknowledgements

First, I would like to thank Prof. Dr. Thomas Eschenhagen, the director of the Institute of Experimental Phamarcology and Toxicoloy, for providing valuable insights and constructive criticism.

Second, I want to thank Prof. Dr. Lucie Carrier for the opportunity to work in her group. She provided me with the necessary funds, utilized her personal network to advance my project and was always available for scientific discussions. Also, it was her who enabled me to travel frequently, discover new places and who always challenged me and pushed me to become a better scientist.

Third, I thank Prof. Dr. Hartmut Schlüter for serving as both my primary thesis reviewer and head of disputation committee. Alongside, I want to thank Prof. Dr. Elke Oetjen for being the head of my thesis committee and Prof. Dr. Wolfram Brune and Prof. Dr. Friederike Cuello for serving on my disputation committee.

Also, I thank the members of AG Carrier, Ellen Orthey, Lisa Krämer, Dr. Saskia Schlossarek, Dr. Sonia Singh and of the IEPT, Grit Höppner, Thomas Schulze, Birgit Klampe and Dr. Ingke Braren.

I would also like to thank the members of the Leducq Cytoskeleton Network, especially Prof. Marie-Jo Moutin, Dr. Sacnite Ramirez-Rios and Dr. Chandi Sanyal for close collaboration on the mutant VASH1 project as well as Prof. Ben Prosser for hosting me during a stay at his lab in 2022.

Moreover, I would like to thank the labs of Slava Nikolaev and Stepahnie Könemann for support with FRET and mouse experiments.

Special thanks go out to Dr. Niels Pietsch who is both an outstanding researcher and close friend but also, especially in my early PhD days, a great bench-side scientific advisor. You know the answer to every possible question one could have while working in this institute because you have done everything already. We have shared many long days in the stem cell culture, sometimes discussing sports, politics or else, sometimes quiet. I knew that I was always able to count on you.

Moreover, I want to thank my friends and colleagues Erda Alizoti, Leonie Ewald and Dr. Marie “Lorns” Nehring for supporting me in any way possible, both experimentally and privately.

Another friend I would like to thank is Dr. Keita Uchida (UPenn, Philadelphia) who I met in 2022 during my first year of PhD studies. You are one of the most knowledgeable and humble people I have ever met. I am happy to have worked with you. You supported me in developing my own ideas and you were a great mentor.

Additionally, I want to thank my close friends, who I have known for almost ten years now, Sebastian Beier, Dr. Bryan Barcelona and Dr. Janina Behrens. We have shared struggles and joy. For all of us, graduation marks the end of an era as we progress in our careers.

Many thanks go out to Bruno Siebert, who has been my best friend for almost 20 years. We work in different fields but always find common ground, share values and the occasional drink.

Especially I would like to express my gratitude towards my parents, Dr. Thorsten Meyer-Jens and Ellen Meyer-Jens for always supporting me during my PhD and personal journey. You brought me up to be kind, confident and independent and did a great job at that (pat on the back for all of us). Also, you provided me with great role models, each of you in your own way.

I also thank my younger brother, Marius Meyer-Jens, with whom I shared an apartment for a substantial portion of my thesis. I admire your ability to always stay calm and collected and wish you succeed in art.

Lastly, I want to thank my partner, Lara Stock. You are the most amazing person I have met in my life. I am eternally thankful for having you by my side. Nothing compares to the support you provide, encouraging and believing in me even if I struggle. Without you, I would not have been able to accomplish what I did. You never criticized me for working late hours or on weekends but provided comfort and amazing dinners once I arrived home.

Appendix

I. Materials

I.I Media

Table 6: Used media and respective composition.

Medium	Composition
Basic medium for monolayer dissociation	DMEM low glucose Penicillin-streptomycin 1%
Blocking buffer for monolayer dissociation	Basic medium DNase 12 U/ml
EHT complete medium	DMEM low glucose Penicillin-streptomycin 1% Horse Serum, heat inactivated 10 % Insulin 10 µg/ml Aprotinin 33 µg/ml
FTDA	DMEM F-12 L-Glutamine 2 mM Transferrin 5 mg/ml Selen 5 µg/ml Human Serum Albumin 0.1 % Lipid Mix 1X Insulin 5 mg/ml Dorsomorphin 50 mM Activin A 2.5 ng/ml Transforming growth factor β1 0.5 ng/µl Stable fibroblast growth factor 30 ng/ml
Maturation medium	DMEM w/o Glucose Glucose 3 mM L-Lactate 10 mM Vitamin B12 5 µg/ml Biotin 0.82 µM

Medium	Composition
Maturation medium	Creatine monohydrate 5 mM Taurine 2 mM L-Carnitine 2 mM Ascorbic acid 0.5 mM NEAA 1X Albumax I 0.5 % B27 1X Knockout serum replacement 1X P/S 1% Insulin 10 µg/ml
Monolayer feeding medium	RPMI 1640 B27 5 % Insulin 3.21 µg/ml
Monolayer medium Stage 0	StemPro-34 SFM StemPro plus supplement 2.6 % BMP4 1 ng/ml L-Glutamine 2 mM Matrigel EHT 1 %
Monolayer medium Stage 1	StemPro-34 SFM StemPro plus supplement 2.6 % BMP4 10 ng/ml L-Glutamine 2 mM Activin A 8 ng/ml
Monolayer medium Stage 2.1	RPMI 1640 B27 2 % KYO2111 10 µM XAV939 10 µM
Monolayer medium Stage 2.2	RPMI 1640 B27 2 % KYO2111 10 µM XAV939 10 µM Insulin 3.21 µg/ml

I.II Buffers and reagents

Table 7: Used buffers and compositions.

Buffer	Composition
Blocking solution for Western blot	TBS-T 5 % (w/v) milk powder or BSA
blotting buffer 5X	Milli-Q H_2O Tris base 125 mM Glycine 950 mM
blotting buffer 1X	Milli-Q H_2O blotting buffer 5X 20 % Methanol 20 %
BTS solution	DMSO BTS 30 mM
Collagenase II solution	HBSS w/o Ca^{2+} Collagenase II 200 U/ml HEPES, pH 7.4 1 mM BTS solution 30 µM Y compound 10 µM
FASC staining buffer	PBS FBS 5 % (v/v) Sodium azide 0.05 % (v/v) Saponin 0.5 % (w/v)
DNase solution	PBS DNase II type V 2000 U/ml
EDTA	PBS EDTA 0.5 mM
Electrophoresis buffer 10X	Milli-Q H_2O Tris base 250 mM Glycine 1.92 M SDS 1 % (w/v)
Electrophoresis buffer 1X	Milli-Q H_2O 10 % (v/v) Electrophoresis buffer 10X
HEPES pH 7.4	PBS

Buffer	Composition
	HEPES 1 M pH 7.4 adjusted with KOH filtered sterile with 0.2 µM filter
Kranias buffer	Milli-Q H_2O Tris 1.5 M, pH 8.8 2 % (v/v) EDTA 5 mM NaF 30 mM SDS 3 % Glycerol 10 % (v/v)
Laemmli Buffer	Milli-Q H_2O SDS 12 % Bromphenol blue 0.06 % (w/v) Glyerol 60 % (w/v) Tris 0.5 M, pH 6.8 12 % (v/v) DTT 9.3 % (w/v)
Permeabilization buffer (IF)	PBS Milk powder 3 % Trition^{TM} X-100 0.1 %
TBS 10X	Milli-Q H_2O Tris base 1 M NaCl 1.5 M pH adjusted to 7.5
TBS-T	Milli-Q H_2O TBS 10X 10 % (v/v) Tween 20 0.1 % (v/v)

I.III Cells

Table 8: Used cell lines and sources.

Cell line/type	Source
mTagRFPT-TUBA1B (AICS-0031-035) (RFP WT)	Corriell Institute (IEPT stock)

Cell line/type	Source
SVBP-KO	Generated by Niels Pietsch (Pietsch et al., 2024)
TTL-KO	Generated by Niels Pietsch (Pietsch et al., 2024)
VASH1-KO	Generated by Niels Pietsch (Pietsch et al., n.d.)
MATCAP1-KO	Generated during this study
ERC001 WT	IEPT stock

I.IV Antibodies

Table 9: Used antibodies with manufacturers and supplementary information.

Target	Manufacturer	Dilution	Buffer	Application
dTyr-tub (rb)	Gift from Marie-Jo Moutin	1:2000	5% BSA/TBS-T	Western blot
dTyr-tub (rb)	Abcam	1:1000	5% BSA/TBS-T	Western blot
Tyr-tub (rat)	Gift from Marie-Jo Moutin	1:5000	5% BSA/TBS-T	Western blot
Δ2-Tub (rb)	Gift from Marie-Jo Moutin	1:5000	5% BSA/TBS-T	Western blot
αTub (ms)	Cell Signaling	1:1000	TBS-T	Western blot
ACTN2 (ms)	Sigma	1:800	PBS	Immunofluorescence
GAPDH (ms)	HyTest	1:5000	TBS-T	Western blot
GAPDH-680 (ms)	Thermo Fisher	1:3000	TBS-T	Western blot
PRGK1A	Cell Signaling	1:1000	TBS-T	Western blot
ac-tub	Cell Signaling	1:1000	TBS-T	Western blot

Target	Manufacturer	Dilution	Buffer	Application
pVASP S157	Cell Signaling	1:1000	TBS-T	Western blot
pVASP S239	Cell Signaling	1:1000	TBS-T	Western blot
VASH1	Gift from Marie-Jo Moutin	1:10,000	TBS-T	Western blot
XIRP2	Proteintech	1:2000	TBS-T	Western blot
Anti-rabbit HRP	Sigma	1:10,000	5% milk/TBS-T	Western blot
Anti-mouse HRP	Sigma	1:10,000	5% milk/TBS-T	Western blot
Anti-rat HRP	Jackson Immunores	1:10,000	5% milk/TBS-T	Western blot
Anti-rabbit DyLight680	Thermo Fisher	1:10,000	TBS-T	Western blot
Anti-mouse DyLight800	Thermo Fisher	1:10,000	TBS-T	Western blot
Anti-rat 546	Thermo Fisher	1:1000	TBS-T	Western blot
Anti-rat 546	Thermo Fisher	1:800	PBS	Immunofluorescence
Anti-mouse 488	Thermo Fisher	1:800	PBS	Immunofluorescence
SSEA3 PE	BD Biosciences	1:5	FACS buffer	FACS
Isotype control PE	BD Biosciences	1:100	FACS buffer	FACS
cTnT FITC	Milteny	1:100	FACS Buffer	FACS
Isotype control FITC	Milteny	1:100	FACS Buffer	FACS

I.V Consumables and chemicals

Table 10: Used consumables, chemicals and manufacturers.

Material	Manufacturer
12-well plates	Thermo Fisher
24-well plates	Thermo Fisher
6-well plates	Thermo Fisher
96-well plates	Greiner
Accutase	Sigma Aldrich
Aluminum foil	Quickpack
Amersham 0.22 µm nitrocellulose transfer paper	Carl Roth
CASYCups	Omni Life Sciences
Cell scraper	Thermo Fisher
Collagenase II	TCI Deutschland GmbH
DMEM/F12	Gibco
DPBS	Gibco
Eppendorf Safe Lock tubes (1.5/2 ml)	Eppendorf AG
Facial Tissues	Tapira
Falcon Tubes (15/50 ml)	Sarstedt
Flow Cytometry tubes 5 ml	Sarstedt
Geltrex	Gibco
Glass Pasteur-Pipettes	Th. Geyer GmbH
Glassware	Schott Duran
HBSS w/o Calcium	Gibco
Matrigel	Corning
Matrigel Growth Factor reduced	Corning
MICRO-TOUCH Nitra-Tex medical examination gloves	Ansell
NEAA	Gibco
Parafilm	Bemis Company
Pipette tips	Sarstedt

Material	Manufacturer
Precision Plus Protein standard DualColor	BioRad Laboratories
Precision Plus Protein standard Kaleidoscope	BioRad Laboratories
RPMI 1640	Gibco
Scalpel blade	Bayha
SDS-PAGE precast gels 4-15 % (10/15-well)	BioRad Laboratories
Serological pipettes	Sarstedt
StemPro34 medium and supplement	Gibco
Surgical mask	Farstar medical
Tweezers	Biochem Lab Supply
Spatulae	Biochem Lab Supply

I.VI Kits

Table 11: Used kits and manufacturers.

Kit	Manufacturer	Hazard statement	Precautionary statement
iScript cDNA synthesis Kit	BioRad Laboratories		
Clarity Western ECL substrate Kit	BioRad Laboratories		
SV Total RNA Isolation Kit	Promega		
TriZol RNA isolation kit	Invitrogen	301, 311, 331, 314, 335, 342, 373, 412	201, 261, 264, 280, 273, 301+310, 302+352, 303+361+353, 204+340,

Kit	Manufacturer	Hazard statement	Precautionary statement
			305+351+338, 403+233, 501
Silencer Select *PRKG1A s11131*	Thermo Fisher		
Silencer Select *PRKG1A s11132*	Thermo Fisher		
Trans blot Turbo RTA	BioRad Laboratories	228, 301, 311, 315, 319, 335	210, 240, 241, 280, 370+378
cGMP ELISA	Sigma		
Lipofectamine 3000	Thermo Fisher		
Silencer Select Negative control 2 4390847			
Blood and Tissue DNA extraction Kit	Quiagen		
ANP ELISA	Thermo Fisher		
In Fusion HD Cloning	Clonetech		

I.VII Laboratory equipment

Table 12: Used laboratory equipment and manufacturer.

Equipment	Manufacturer
7900HT fast real-time PCR system	Applied Biosystems
Accu-jet Pro	BRAND
BD FACS CANTO II	BD Biosciences
CASY Cell counter	Omni Life Sciences
Centrifuge 5810R	Eppendorf AG
Centrifuge MC 6	Sarstedt
ChemiDoc Touch	BioRad Laboratories
CO_2 Incubator	Memmert

Equipment	Manufacturer
DMI600/ROPER	Leica
Evos AMG XL Digital	Thermo Fisher
Fusion FX7	Vilber
pH meter	Mettler Toledo
Heracell 150	Thermo Fisher
Heracell 240	Thermo Fisher
Haraeus multifuge X3R	Thermo Fisher
Ice machine	Scotsman Ice Systems
LSM 800 confocal microscope	Zeiss
Mastercycler PCR cycler	Eppendorf AG
Milli-Q system	Merck Millipore
Mini Protean Tetra Electrophoresis chamber	Bio-Rad Laboratories
Mini Protean Trans-blot chamber	Bio-Rad Laboratories
NanoDrop 1000	Thermo Fisher
nCounter Sprint profiler	Nanostring Technologies
Nikon Eclipse Ti	Nikon
Pipettes	Eppendorf AG
Polymax 1040	Heidolph Instruments
PowerPac Basic Power Supply	BioRad Laboratories
Quant Studio 5 RT-qPCR cycler	Thermo Fisher
Safe2020 Biological Safety Cabinet	Thermo Fisher
Thermomixer comfort	Eppendorf AG
Trans blot Turbo	Bio-Rad Laboratories
Tube Roller R3005	Benchmark Scientific
Vortex Genie 2	Scientific Industries

I.VIII Primers

Table 13: Used primers and sequences.

Gene name	Accession or locus	Primer direction	Sequence	Amplicon size (bp)
GAPDH	NM_001256799	Forward	ATGTTCGTCATGGGTGTGAA	136
GAPDH	NM_001256799	Reverse	TGAGTCCTTCCACGATACCA	136
XIRP2	NM_001079810.04	Forward	CCAAAGCCAGGTCCATTTGAG	138
XIRP2	NM_001079810.04	Reverse	CCTTTGGGGGCTTTTGGAAG	138
MME	NM_000902	Forward	GCCCATCGATGAAAACCAGC	187
MME	NM_000902	Reverse	CAACCAGCTGAATGGCTTCC	187
GUSB	NM_000181	Forward	ACGATTGCAGGGTTTCACCA	171
GUSB	NM_000181	Reverse	CACTCTCGTCGGTGACTGTT	171
B2M	NM_004048	Forward	GCTCGCGCTACTCTCTCTTT	140
B2M	NM_004048	Reverse	CAATGTCGGATGGATGAAACCC	140
NPR1	NM_000906	Forward	CGTCAAGGGCATGCTGTTTC	179
NPR1	NM_000906	Reverse	CCGTCCACAGCTTTTTGGC	179
NPR2	NM_001378923	Forward	GACCCATCCTGTGATAAAACTCC	124
NPR2	NM_001378923	Reverse	GCATCAGCTTTCTGTAAGGACG	124
NPR3	NM_000908	Forward	TGGTCTACAGCGACGACAAG	181

Gene name	Accession or locus	Primer direction	Sequence	Amplicon size (bp)
NPR3	NM_000908	Reverse	GCACACATGATCA CCACTCTC	181
PRKG1A	NM_0010985 12	Forward	CTCCACAAATGCCA GTCGG	166
PRKG1A	NM_0010985 12	Reverse	TTATAAGATCCTTG GACCTTTCGG	166
CRIP2	NM_0012708 37.2	Forward	CATGTTTCTGGCCT GCTGTC	184
CRIP2	NM_0012708 37.2	Reverse	CTCACCTTCTCGGC TGTTCC	184
MATCAP1	NM_0010407 15.2	Forward	ATGATGGTGGAGA ACAGCCG	106/771
MATCAP1	NM_0010407 15.2	Reverse	GCAGGTAGTGGGT GCCTATC	106
MATCAP crRNA1 fw	NM_0010407 15.2	Forward	CACGAGTAAGGGG CTCAGTC	582
MATCAP crRNA1 rev	NM_0010407 15.2	Reverse	CAGGGATGGGGAC TGGTAG	582
MATCAP crRNA2 fw	NM_0010407 15.2	Forward	CCTCCCAGGTTGTT GTTTCAGCA	540
MATCAP crRNA2 rev	NM_0010407 15.2	Reverse	TCTCTCCAATCCAC CTCCCA	540
MATCAP internal rev	NM_0010407 15.2	Reverse	AACAGTCATGCTGA TGCCCC	771
OT1 MATCAP1 crRNA1	chrX:- 68685818	Forward	ATGCAAGTTTGCTT GCGGTG	473
OT1 MATCAP1 crRNA1	chrX:- 68685818	Reverse	ATGGCTCTGGCCA TCTTGAC	473
OT2 MATCAP1 crRNA1	chr4:+323558 20	Forward	CAACCTGAGGGAG CGTCTTC	312
OT2 MATCAP1 crRNA1	chr4:+323558 20	Reverse	TTCAACCTTGCCTC TGGTGG	312
OT3 MATCAP1 crRNA1	chr1:+169158 1	Forward	CCCCTGCACCAGA GGTTAAG	305

Gene name	Accession or locus	Primer direction	Sequence	Amplicon size (bp)
OT3 MATCAP1 crRNA1	chr1:+1691581	Reverse	TGAAGATGTGTAGGGCGCAG	305
OT4 MATCAP1 crRNA1	chr1:+1744856	Forward	ATCTCAACGCCGGGTTACTG	293
OT4 MATCAP1 crRNA1	chr1:+1744856	Reverse	TTGTGTGGTCTCCAGCTTCC	293
OT5 MATCAP1 crRNA1	chr5:+158975840	Forward	TGCTAAGTGCTGGCCTGAAG	265
OT5 MATCAP1 crRNA1	chr5:+158975840	Reverse	GCGTGCTTGCTGTCCTAATC	265
OT6 MATCAP1 crRNA1	chr14:+72877480	Forward	GCGGGCTTTTTCTTCCCAAG	455
OT6 MATCAP1 crRNA1	chr14:+72877480	Reverse	GATCCCAGCGAGTGTCAGAG	455
OT7 MATCAP1 crRNA1	chr1:+107716296	Forward	TGGCATGAATCAAGGCCAC	150
OT7 MATCAP1 crRNA1	chr1:+107716296	Reverse	TAAAAGTCTTTACTGGCTGGCTG	150
OT8 MATCAP1 crRNA1	chr20:+61704982	Forward	CCGGGATGTCTGAGTCTTGG	390
OT8 MATCAP1 crRNA1	chr20:+61704982	Reverse	AAGAGGGACATGCCAACGAG	390
OT9 MATCAP1 crRNA1	chrX:-77282894	Forward	CCAGACACTGTGCTTTTCCC	173
OT9 MATCAP1 crRNA1	chrX:-77282894	Reverse	GGAGTTTCTTGTGCCACTGG	173
OT10 MATCAP1 crRNA1	chr8:+76502555	Forward	ATGGCCTCTGTCTCAAGCTG	402
OT10 MATCAP1 crRNA1	chr8:+76502555	Reverse	GTGGAGGTTCCCGAGTCATC	402
OT1 MATCAP1 crRNA2	chrX:-121197635	Forward	TTTAGGTGGGCACTCTACTTTC	1273
OT1 MATCAP1 crRNA2	chrX:-121197635	Reverse	TGCATCTCCCCACCTCATTTC	1273
OT2 MATCAP1 crRNA2	chr15:-60413682	Forward	ACTGTGACTTCACACGCTCC	246

Gene name	Accession or locus	Primer direction	Sequence	Amplicon size (bp)
OT2 MATCAP1 crRNA2	chr15:-60413682	Reverse	TCATGGGTCCCAACAATACCC	246
OT3 MATCAP1 crRNA2	chr3:+100241571	Forward	TCCACTCACCAAGGATGACC	173
OT3 MATCAP1 crRNA2	chr3:+100241571	Reverse	CAAACCTCTGCCATTTCCATG	173
OT4 MATCAP1 crRNA2	chr2:+212395648	Forward	GTTAGCATCTTTGGCTTGGGAG	400
OT4 MATCAP1 crRNA2	chr2:+212395648	Reverse	CACTGGGTTGATCTTCATGCTG	400
OT5 MATCAP1 crRNA2	chrX:-113827860	Forward	ACTAGTGAAGCTGCTATGGAAG	560
OT5 MATCAP1 crRNA2	chrX:-113827860	Reverse	CCCGTATCACAACCATCACC	560
OT6 MATCAP1 crRNA2	chr14:+58132614	Forward	CCTTTGAGGACCCAGAGGTG	402
OT6 MATCAP1 crRNA2	chr14:+58132614	Reverse	TTGAAGAGGTGTGGCAGAGC	402
OT7 MATCAP1 crRNA2	chr22:+48379613	Forward	GGCACCATTGTCAAGAGCAC	183
OT7 MATCAP1 crRNA2	chr22:+48379613	Reverse	CTCTGCCCACCTTTCCACTC	183
OT8 MATCAP1 crRNA2	chr10:+98069332	Forward	AGAGTGACTAGCTGCATCCC	425
OT8 MATCAP1 crRNA2	chr10:+98069332	Reverse	AGGCAAGATCCAGACACTGAG	425
OT9 MATCAP1 crRNA2	chr10:-16166816	Forward	GTGATGACGAACTTCTGCCC	185
OT9 MATCAP1 crRNA2	chr10:-16166816	Reverse	GGACTTCTGCTCACCAATGC	185

Gene name	Accession or locus	Primer direction	Sequence	Amplicon size (bp)
OT10 MATCAP1 crRNA2	chr2:-10721987	Forward	CTGGTAGCATCTCCGCAGG	152
OT10 MATCAP1 crRNA2	chr2:-10721987	Reverse	CTCTTCCTTTCGGACTCCCG	152

I.IX Viruses

Table 14: Used viruses and sources.

Virus	Source
Adv-cGi500	Gift from Slava Nikolaev
LV-YFP-VASH1-IRES-SVBP	Plasmid from Marie-Jo Moutin; virus produced by Ingke Braren
LV-YFP-VASH1(S347E)-IRES-SVBP	Plasmid from Marie-Jo Moutin; virus produced by Ingke Braren
LV-YFP-VASH1(S347A)-IRES-SVBP	Plasmid from Marie-Jo Moutin; virus produced by Ingke Braren
LV-YFP-VASH1(7E)-IRES-SVBP	Plasmid from Marie-Jo Moutin; virus produced by Ingke Braren
LV-YFP-VASH1(7A)-IRES-SVBP	Plasmid from Marie-Jo Moutin; virus produced by Ingke Braren

I.X Software

Table 15: Used software and publishers.

Software	Publisher
BD FACS Diva	BD Biosciences
FlowJo v10.6.1	BD Biosciences
ImageLab 5.2.1	BioRad Laboratories
Microsoft Office	Microsoft
n-Solver	NanoString Technologies
Prism 8.0	GraphPad Software

Software	Publisher
Bio1D	Vilber Lourmat
R	R Foundation
Fiji/ImageJ	Open source/NIH
ZEN 2012	Zeiss

II. Safety and waste disposal

All used substances were used according to the safety standards required in S1 and S2 laboratories. Cell culture material was autoclaved to inactivate any genetically modified organisms and the used work benches were cleaned with 70 % ethanol and pursept solution. Chemicals, buffers, and solutions were disposed in the appropriate containers.

Table 16: Relevant GHS symbols.
From: GESTIS Stoffdatenbank.

GHS symbol number	GHS symbol
GHS02	
GHS04	
GHS05	
GHS06	
GHS07	
GHS08	
GHS09	

Table 17: Used chemicals with hazard and precautionary statements.

Chemical	Manufacturer	Hazard statement	Precautionary statement
1,4-DTT	Applichem	302, 315, 319, 412	264, 270, 273, 280, 337+313, 501
2-Propanol	BioRad Laboratories	225, 319, 336	210, 261, 305+351+338
Activin A	R&D Systems		
Albumax I	Thermo Fisher		
ANP	Tocris		
Aprotinin	Sigma-Aldrich		
Ascorbic acid	Sigma-Aldrich		
B12	Sigma-Aldrich		
B27	Thermo Fisher		
Biotin	Sigma-Aldrich		
BTS	Gibco	301	264, 270, 301+310, 321, 330, 405, 501
BSA	Sigma-Aldrich; Serva		
L-Carnitine	Sigma-Aldrich	315, 319, 335	261, 305+351+338
CASY-Clean	Omni Life Sciences		
CASY-Ton	Omni Life Sciences		
CNP	Tocris		
Collagenase II	Worthington	334	261, 284, 304+340, 342+311
Creatine monohydrate	Sigma-Aldrich		
Dorsomorphin	Tocris	302, 312, 332	261, 264, 270, 271, 280, 301+312, 302+352, 304+312, 304+340, 312, 322, 330, 363, 501

Chemical	Manufacturer	Hazard statement	Precautionary statement
Endothelin 1	Merck		
Ethanol	Chemsolute; Carl Roth	225, 319	210, 240, 305+351+338, 403+233
bFGF	Peprotech		
Glucose	Carl Roth		
Glutamine	Gibco		
Glycerol	Merck		
Glycine	Carl Roth		
HEPES	Carl Roth		
Hoechst 33342	Carl Roth	302, 315, 319	264, 280, 301+312, 302+352, 305+351+338, 330, 332+313, 337+313, 362+364
Horse Serum	Gibco		
Human Serum Albumin	Biological Industries		
Hydrocortisone	Sigma-Aldrich	360Df, 373	202, 260, 280, 308+313, 405, 501
Insulin	Sigma-Aldrich		
KOSR	Thermo Fisher		
KY 02111	Tocris	302, 400	273
L-Lactate	Sigma-Aldrich		
Methanol	J T Baker	225, 331, 311, 301, 370	210, 233, 280, 302+352
Milk powder	Carl Roth		
Nitrogen	Cryotherm	281	282, 336+315, 403

Chemical	Manufacturer	Hazard statement	Precautionary statement
Penicillin/Streptomycin	Gibco	315, 317, 334, 335	280, 261, 264, 284, 271, 302+352, 304+340
Ponceau S solution	Sigma-Aldrich	315, 319, 335	261, 305+351+338
Pursept	Schülke	226, 319	210, 280, 305+351+338, 337+313, 403+235
Roti-Histofix	Carl Roth	302, 317, 341, 350	261, 280, 302+352, 308+313
RP-8-Br-cGMPs-PET	Tocris		
Sacubitrilat	Sigma Aldrich		
Saponin	Sigma Aldrich	319, 335	261, 305+351+338
Selen	Sigma Aldrich	331, 301, 373, 413	273, 304+340
Sodium azide	Merck	300, 400, 410	273, 309, 310
SDS	Carl Roth	228, 302+332, 315, 318, 335, 412	210, 261, 280, 302+352, 305+351+338, 312
StemPro-34 SFM	Gibco		
StemPro Supplement	Gibco		
T3	Gibco	315, 319, 335	261, 305+351+338
Taurine	Sigma Aldrich	315, 319, 335	261, 305+351+338
Transferrin human	Sigma Aldrich		
TGF β1	Pepro Tech		
Tris base	Merck	315, 319, 335	261, 305+351+338
Tris HCl	Merck	315, 319, 335	280, 302+352, 305+351+338
Trypan blue	Gibco	350	201, 308+313
Tween 20	Sigma Aldrich		
Valsartan	Sigma Aldrich		

Chemical	Manufacturer	Hazard statement	Precautionary statement
XAV939	Tocris	301, 319	301+310, 305+351+338
Y-2732	Biorbyt	302, 312, 332	280

Bibliography

Abdallah, Y., Gkatzoflia, A., Pieper, H., Zoga, E., Walther, S., Kasseckert, S., Schäfer, M., Schlüter, K. D., Piper, H. M., & Schäfer, C. (2005). Mechanism of cGMP-mediated protection in a cellular model of myocardial reperfusion injury. *Cardiovascular Research*, *66*(1), 123–131. https://doi.org/10.1016/j.cardiores.2005.01.007

Ackers-Johnson, M., Li, P. Y., Holmes, A. P., O'Brien, S.-M., Pavlovic, D., & Foo, R. S. (2016). A Simplified, Langendorff-Free Method for Concomitant Isolation of Viable Cardiac Myocytes and Nonmyocytes From the Adult Mouse Heart. *Circulation Research*, *119*(8), 909–920. https://doi.org/10.1161/CIRCRESAHA.116.309202

Adamczak, D. M., Oduah, M. T., Kiebalo, T., Nartowicz, S., Bęben, M., Pochylski, M., Ciepłucha, A., Gwizdała, A., Lesiak, M., & Straburzyńska-Migaj, E. (2020). Heart Failure with Preserved Ejection Fraction—a Concise Review. *Current Cardiology Reports*, *22*(9). https://doi.org/10.1007/s11886-020-01349-3

Agostinucci, K., Grant, M. K. O., Seelig, D., Yücel, D., van Berlo, J., Bartolomucci, A., Dyck, J. R. B., & Zordoky, B. N. (2022). Divergent Cardiac Effects of Angiotensin II and Isoproterenol Following Juvenile Exposure to Doxorubicin. *Frontiers in Cardiovascular Medicine*, *9*(March), 1–17. https://doi.org/10.3389/fcvm.2022.742193

Aillaud, C., Bosc, C., Peris, L., Bosson, A., Heemeryck, P., Van Dijk, J., Le Friec, J., Boulan, B., Vossier, F., Sanman, L. E., Syed, S., Amara, N., Couté, Y., Lafanechère, L., Denarier, E., Delphin, C., Pelletier, L., Humbert, S., Bogyo, M., Moutin, M.-J. (2017). Vasohibins/SVBP are tubulin carboxypeptidases (TCPs) that regulate neuron differentiation. *Science*, *358*(6369), 1448–1453. https://doi.org/10.1126/science.aao4165

Al-Bassam, J., Ozer, R. S., Safer, D., Halpain, S., & Milligan, R. A. (2002). MAP2 and tau bind longitudinally along the outer ridges of microtubule protofilaments. *The Journal of Cell Biology*, *157*(7), 1187–1196. https://doi.org/10.1083/jcb.200201048

Alanis-Lobato, G., Zohren, J., McCarthy, A., Fogarty, N. M. E., Kubikova, N., Hardman, E., Greco, M., Wells, D., Turner, J. M. A., & Niakan, K. K. (2021). Frequent loss of heterozygosity in CRISPR-Cas9–edited early human embryos. *Proceedings of the National Academy of Sciences*, *118*(22). https://doi.org/10.1073/pnas.2004832117

Algül, S., Dorsch, L. M., Sorop, O., Vink, A., Michels, M., dos Remedios, C. G., Dalinghaus, M., Merkus, D., Duncker, D. J., Kuster, D. W. D., & van der Velden, J. (2023). The microtubule signature in cardiac disease: etiology, disease stage, and age dependency. *Journal of Comparative Physiology B*, *193*(5), 581–595. https://doi.org/10.1007/s00360-023-01509-1

Alizoti, E, Ewald, L., Parretta, S., Meyer-Jens, M., Orthey, E., Conze, C., Carrier, L., Robbins, J., & Singh, S. R. (2025). Ruxolitinib clears CRYAB p.Arg120Gly aggregates through the ubiquitin-proteasome system. *BioRxiv*, 1–25. https://www.embase.com/search/results?subaction=viewrecord&id=L2035792150&from=export%0Ahttp://dx.doi.org/10.1101/2024.10.11.615348

Alizoti, Erda, Pietsch, N., Fazio, A., Cheng, J., Orthey, E., Carrier, L., & Singh, S. R. (n.d.). *A CRYAB p.Arg120Gly Human Disease Model Exhibits Important Hallmarks of Desmin-related Cardiomyopathy*.

Allen Institute. (n.d.). *mTagRFPTuba1b hiPSC line*. https://www.allencell.org/cell-catalog.html

Andreu-Carbó, M., Egoldt, C., Velluz, M. C., & Aumeier, C. (2024). Microtubule damage shapes the acetylation gradient. *Nature Communications*, *15*(1). https://doi.org/10.1038/s41467-024-46379-5

Andrews, P. W., & Gokhale, P. J. (2024). A short history of pluripotent stem cells markers. *Stem Cell Reports*, *19*(1), 1–10. https://doi.org/10.1016/j.stemcr.2023.11.012

Arefin, A., Mendoza, M., Dame, K., Garcia, M. I., Strauss, D. G., & Ribeiro, A. J. S. (2023). Reproducibility of drug-induced effects on the contractility of an engineered heart tissue derived from human pluripotent stem cells. *Frontiers in Pharmacology*, *14*(July), 1–15. https://doi.org/10.3389/fphar.2023.1212092

Assaf, K. I., Faraj, A. N., Abu-Nameh, E. S. M., & Alnajjar, M. A. (2024). Supramolecular complexation of phenylephrine by cucurbit[7]uril in aqueous solution. *RSC Advances*, *14*(19), 13286–13290. https://doi.org/10.1039/D4RA01910E

Bacmeister, L., Schwarzl, M., Warnke, S., Stoffers, B., Blankenberg, S., Westermann, D., & Lindner, D. (2019). Inflammation and fibrosis in murine models of heart failure. *Basic Research in Cardiology 2019 114:3*, *114*(3), 1–35. https://doi.org/10.1007/S00395-019-0722-5

Bance, B., Seetharaman, S., Leduc, C., Boeda, B., & Etienne-Manneville, S. (2019). Microtubule acetylation but not detyrosination promotes focal adhesion dynamics and astrocyte migration. *Journal of Cell Science*, *132*(7). https://doi.org/10.1242/jcs.225805

Banfeng, P. (2022). *Atrial Fibrillation Modelling and Targeted DNA Methylation Editing in Human Engineered Heart Tissue-Based Disease Models*.

Banko, M. R., Allen, J. J., Schaffer, B. E., Wilker, E. W., Tsou, P., White, J. L., Villén, J., Wang, B., Kim, S. R., Sakamoto, K., Gygi, S. P., Cantley, L. C., Yaffe, M. B., Shokat, K. M., & Brunet, A. (2011). Chemical Genetic Screen for AMPKα2 Substrates Uncovers a Network of Proteins Involved in Mitosis. *Molecular Cell*, *44*(6), 878–892. https://doi.org/10.1016/j.molcel.2011.11.005

Barnat, M., Benassy, M. N., Vincensini, L., Soares, S., Fassier, C., Propst, F., Andrieux, A., von Boxberg, Y., & Nothias, F. (2016). The GSK3-MAP1B pathway controls neurite branching and microtubule dynamics. *Molecular and Cellular Neuroscience*, *72*, 9–21. https://doi.org/10.1016/j.mcn.2016.01.001

Batalov, I., & Feinberg, A. W. (2015). Differentiation of cardiomyocytes from human pluripotent stem cells using monolayer culture. *Biomarker Insights*, *10*, 71–76. https://doi.org/10.4137/BMI.S20050

Beghini, A., Sammartino, A. M., Papp, Z., von Haehling, S., Biegus, J., Ponikowski, P., Adamo, M., Falco, L., Lombardi, C. M., Pagnesi, M., Savarese, G., Metra, M., & Tomasoni, D. (2025). 2024 Update in Heart Failure. *ESC Heart Failure*, *12*(1), 8–42. https://doi.org/10.1002/ehf2.14857

Behr, T. M., Fischer, P., Spes, C. H., Kur, F., Ziegler, U., Pongratz, D. E., & Angermann, C. E. (1995). 901-26 Coexpression of Vimentin and Ki 67 Indicates Cardiomyocyte Regeneration After Acute Rejection in Human Cardiac Allografts. *Journal of the American College of Cardiology*, *25*(2), 11A. https://doi.org/10.1016/0735-1097(95)91503-P

Bensley, J. G., De Matteo, R., Harding, R., & Black, M. J. (2016). Three-dimensional direct measurement of cardiomyocyte volume, nuclearity, and ploidy in thick histological sections. *Scientific Reports 2016 6:1*, *6*(1), 1–10. https://doi.org/10.1038/srep23756

Benza, R. L., Simonneau, G., Grünig, E., Sandner, P., & Stasch, J. P. (2024). The nitric oxide–soluble guanylate cyclase–cGMP pathway in pulmonary hypertension: from PDE5 to soluble guanylate cyclase. *European Respiratory Review*, *33*(171). https://doi.org/10.1183/16000617.0183-2023

Blanton, R. M., Takimoto, E., Lane, A. M., Aronovitz, M., Piotrowski, R., Karas, R. H., Kass, D. A., & Mendelsohn, M. E. (2012). Protein kinase g iα inhibits pressure overload-induced cardiac remodeling and is required for the cardioprotective effect of sildenafil in vivo. *Journal of the American Heart Association*, *1*(5), 1–10. https://doi.org/10.1161/JAHA.112.003731

Bogdanov, V., Mariangelo, J. I. E., Soltisz, A. M., Sakuta, G., Pokrass, A., Beard, C., Orengo, B. H., Kalinin, R., Ulker, A., Yunker, B., Tikunova, S., Thuma, J., Xu, X., Hund, T. J., Veeraraghavan, R., Davis, J. P., & Gyorke, S. (2025). Distinct intracellular spatiotemporal expression of Calmodulin genes underlies functional diversity of Calmodulin-dependent signalling in cardiac myocytes. *Cardiovascular Research*, *121*(7), 1052–1065. https://doi.org/10.1093/cvr/cvaf059

Bonne, G., Carrier, L., Bercovici, J., Cruaud, C., Richard, P., Hainque, B., Gautel, M., Labeit, S., James, M., Beckmann, J., Weissenbach, J., Vosberg, H. P., Fiszman, M., Komajda, M., & Schwartz, K. (1995). Cardiac myosin binding protein–C gene splice acceptor site mutation is associated with familial hypertrophic cardiomyopathy. *Nature Genetics 1995 11:4*, *11*(4), 438–440. https://doi.org/10.1038/ng1295-438

Bork, N., & Nikolaev, V. (2018). cGMP Signaling in the Cardiovascular System—The Role of

Compartmentation and Its Live Cell Imaging. *International Journal of Molecular Sciences*, *19*(3), 801. https://doi.org/10.3390/ijms19030801

Bozkurt, B. (2024). Contemporary pharmacological treatment and management of heart failure. *Nature Reviews Cardiology*, *21*(8), 545–555. https://doi.org/10.1038/s41569-024-00997-0

Brown, A., Slaughter, T., & Black, M. M. (1992). Newly assembled microtubules are concentrated in the proximal and distal regions of growing axons. *The Journal of Cell Biology*, *119*(4), 867–882. https://doi.org/10.1083/jcb.119.4.867

Bunning, A. R., & Gupta Jr., M. L. (2023). The importance of microtubule-dependent tension in accurate chromosome segregation. *Frontiers in Cell and Developmental Biology*, *11*. https://doi.org/10.3389/fcell.2023.1096333

Burridge, P. W., Matsa, E., Shukla, P., Lin, Z. C., Churko, J. M., Ebert, A. D., Lan, F., Diecke, S., Huber, B., Mordwinkin, N. M., Plews, J. R., Abilez, O. J., Cui, B., Gold, J. D., Wu, J. C., & Paul Burridge, or W. (2014). Chemically Defined and Small Molecule-Based Generation of Human Cardiomyocytes HHS Public Access. *Nat Methods*, *11*(8), 855–860. https://doi.org/10.1038/nmeth.2999.Chemically

Calamera, G., Moltzau, L. R., Levy, F. O., & Andressen, K. W. (2022). Phosphodiesterases and Compartmentation of cAMP and cGMP Signaling in Regulation of Cardiac Contractility in Normal and Failing Hearts. *International Journal of Molecular Sciences*, *23*(4). https://doi.org/10.3390/ijms23042145

Cambray-Deakin, M. A., & Burgoyne, R. D. (1987). Posttranslational modifications of α-tubulin: Acetylated and detyrosinated forms in axons of rat cerebellum. *Journal of Cell Biology*, *104*(6), 1569–1574. https://doi.org/10.1083/jcb.104.6.1569

Caporizzo, M. A., Chen, C. Y., Bedi, K., Margulies, K. B., & Prosser, B. L. (2020). Microtubules increase diastolic stiffness in failing human cardiomyocytes and myocardium. *Circulation*, *141*(11), 902. https://doi.org/10.1161/CIRCULATIONAHA.119.043930

Casteel, D. E., Smith-Nguyen, E. V., Sankaran, B., Roh, S. H., Pilz, R. B., & Kim, C. (2010). A crystal structure of the cyclic GMP-dependent protein kinase Iβ dimerization/docking domain reveals molecular details of isoform-specific anchoring. *Journal of Biological Chemistry*, *285*(43), 32684–32688. https://doi.org/10.1074/jbc.C110.161430

Castro, L. R. V., Schittl, J., & Fischmeister, R. (2010). Feedback control through cGMP-dependent protein kinase contributes to differential regulation and compartmentation of cGMP in rat cardiac myocytes. *Circulation Research*, *107*(10), 1232–1240. https://doi.org/10.1161/CIRCRESAHA.110.226712

Cerneckis, J., Cai, H., & Shi, Y. (2024). Induced pluripotent stem cells (iPSCs): molecular mechanisms of induction and applications. *Signal Transduction and Targeted Therapy*, *9*(1), 1–26. https://doi.org/10.1038/s41392-024-01809-0

Chen, C. Y., Caporizzo, M. A., Bedi, K., Vite, A., Bogush, A. I., Robison, P., Heffler, J. G., Salomon, A. K., Kelly, N. A., Babu, A., Morley, M. P., Margulies, K. B., & Prosser, B. L. (2018). Suppression of detyrosinated microtubules improves cardiomyocyte function in human heart failure. *Nature Medicine*, *24*(8), 1225–1233. https://doi.org/10.1038/s41591-018-0046-2

Chen, C. Y., Salomon, A. K., Caporizzo, M. A., Curry, S., Kelly, N. A., Bedi, K., Bogush, A. I., Krämer, E., Schlossarek, S., Janiak, P., Moutin, M. J., Carrier, L., Margulies, K. B., & Prosser, B. L. (2020). Depletion of Vasohibin 1 Speeds Contraction and Relaxation in Failing Human Cardiomyocytes. *Circulation Research*, *127*, E14–E27. https://doi.org/10.1161/CIRCRESAHA.119.315947

Chen, X., Wu, Y., Xing, Y., & Zhong, P. (2025). CENPF as a prognostic marker of glioma: unraveling the molecular mechanisms. *Journal of Cancer Research and Clinical Oncology*, *151*(2), 96. https://doi.org/10.1007/s00432-025-06144-7

Chen, Yuanjian, Xu, F., Munkhsaikhan, U., Boyle, C., Borcky, T., Zhao, W., Purevjav, E., Towbin, J. A., Liao, F., Williams, R. W., Bhattacharya, S. K., Lu, L., & Sun, Y. (2020). Identifying modifier genes for hypertrophic cardiomyopathy. *Journal of Molecular and Cellular Cardiology*, *144*(November 2019), 119–126. https://doi.org/10.1016/j.yjmcc.2020.05.006

Chen, Yuntao, Voors, A. A., Jaarsma, T., Lang, C. C., Sama, I. E., Akkerhuis, K. M., Boersma, E., Hillege, H. L., & Postmus, D. (2021). A heart failure phenotype stratified model for predicting 1-year mortality in patients admitted with acute heart failure: results from an individual participant data meta-analysis of four prospective European cohorts. *BMC Medicine*, *19*(1), 21. https://doi.org/10.1186/s12916-020-01894-2

Chou, C., Martin, G. L., Perera, G., Awata, J., Larson, A., Blanton, R., & Chin, M. T. (2023). A novel αB-crystallin R123W variant drives hypertrophic cardiomyopathy by promoting maladaptive calcium-dependent signal transduction. *Frontiers in Cardiovascular Medicine*, *10*. https://doi.org/10.3389/fcvm.2023.1223244

Colyer, J. (1998). Phosphorylation States of Phospholamban a. *Annals of the New York Academy of Sciences*, *853*(1), 79–91. https://doi.org/10.1111/j.1749-6632.1998.tb08258.x

Coombes, C., Yamamoto, A., McClellan, M., Reid, T. A., Plooster, M., Luxton, G. W. G., Alper, J., Howard, J., & Gardner, M. K. (2016). Mechanism of microtubule lumen entry for the α-tubulin acetyltransferase enzyme αTAT1. *Proceedings of the National Academy of Sciences*, *113*(46). https://doi.org/10.1073/pnas.1605397113

Crocini, C., & Gotthardt, M. (2021). Cardiac sarcomere mechanics in health and disease. *Biophysical Reviews*, *13*(5), 637–652. https://doi.org/10.1007/s12551-021-00840-7

Cui, M., Wu, W., Li, Q., Qi, G., Liu, X., Bai, J., Chen, M., Li, P., & Sun, X. (2024). Unlocking the Potential of Human-Induced Pluripotent Stem Cells: Cellular Responses and Secretome Profiles in Peptide Hydrogel 3D Culture. *Cells*, *13*(2), 1–20. https://doi.org/10.3390/cells13020143

Das, A., Xi, L., & Kukreja, R. C. (2008). Protein kinase G-dependent cardioprotective mechanism of phosphodiesterase-5 inhibition involves phosphorylation of ERK and GSK3β. *Journal of Biological Chemistry*, *283*(43), 29572–29585. https://doi.org/10.1074/jbc.M801547200

de Villiers, C., & Riley, P. R. (2020). Mouse models of myocardial infarction: Comparing permanent ligation and ischaemia-reperfusion. *DMM Disease Models and Mechanisms*, *13*(11), 1–5. https://doi.org/10.1242/dmm.046565

deAlmeida, A. C., van Oort, R. J., & Wehrens, X. H. T. (2010). Transverse aortic constriction in mice. *Journal of Visualized Experiments : JoVE*, *38*. https://doi.org/10.3791/1729

Del Buono, M. G., Moroni, F., Montone, R. A., Azzalini, L., Sanna, T., & Abbate, A. (2022). Ischemic Cardiomyopathy and Heart Failure After Acute Myocardial Infarction. *Current Cardiology Reports*, *24*(10), 1505–1515. https://doi.org/10.1007/s11886-022-01766-6

Del Gobbo, L. C., Kalantarian, S., Imamura, F., Lemaitre, R., Siscovick, D. S., Psaty, B. M., & Mozaffarian, D. (2015). Contribution of Major Lifestyle Risk Factors for Incident Heart Failure in Older Adults. *JACC: Heart Failure*, *3*(7), 520–528. https://doi.org/10.1016/j.jchf.2015.02.009

Dewing, J. M., Saunders, V., O'Kelly, I., & Wilson, D. I. (2021). *Defining Cardiac Cell Populations and Relative Cellular Composition of the Early Fetal Human Heart*. https://doi.org/10.1101/2021.10.21.465281

Di Baldassarre, A., Cimetta, E., Bollini, S., Gaggi, G., & Ghinassi, B. (2018). Human-induced pluripotent stem cell technology and cardiomyocyte generation: Progress and clinical applications. *Cells*, *7*(6). https://doi.org/10.3390/cells7060048

Donald M. Bers. (2002). *Cardiac excitation–contractioncoupling*. www.nature.com

Doudna, J. A., & Charpentier, E. (2014). The new frontier of genome engineering with CRISPR-Cas9. *Science*, *346*(6213). https://doi.org/10.1126/science.1258096

Dumoulin, A., Ter-Avetisyan, G., Schmidt, H., & Rathjen, F. G. (2018). Molecular analysis of sensory axon branching unraveled a cGMP-dependent signaling cascade. *International Journal of Molecular Sciences*, *19*(5). https://doi.org/10.3390/ijms19051266

Eaton, D. M., Lee, B. W., Caporizzo, M. A., Chen, Y., Iyengar, A., Meldrum, D., Dominic, J., Weingarten, N., Hached, K., Bedi, K., Atluri, P., Van Der Laan, S., Prosser, B. L., & Margulies, K. B. (2023). Vasohibin Inhibition Improves Myocardial Relaxation In A Rodent Model Of Heart Failure With Preserved Ejection Fraction. *Circulation Research*, *133*(Suppl_1). https://doi.org/10.1161/res.133.suppl_1.p2078

Eckert, R. E., & Jones, S. L. (2007). Regulation of VASP serine 157 phosphorylation in human neutrophils after stimulation by a chemoattractant. *Journal of Leukocyte Biology*, *82*(5), 1311–1321. https://doi.org/https://doi.org/10.1189/jlb.0206107

Eiringhaus, J., Wünsche, C. M., Tirilomis, P., Herting, J., Bork, N., Nikolaev, V. O., Hasenfuss, G., Sossalla, S., & Fischer, T. H. (2020). Sacubitrilat reduces pro-arrhythmogenic sarcoplasmic reticulum Ca $^{2+}$ leak in human ventricular cardiomyocytes of patients with end-stage heart failure. *ESC Heart Failure*, *7*(5). https://doi.org/10.1002/ehf2.12918

Eisner, D. A., Caldwell, J. L., Kistamás, K., & Trafford, A. W. (2017). Calcium and Excitation-Contraction Coupling in the Heart. In *Circulation Research* (Vol. 121, Issue 2, pp. 181–195). Lippincott Williams and Wilkins. https://doi.org/10.1161/CIRCRESAHA.117.310230

Ellmers, L. J., Scott, N. J. A., Piuhola, J., Maeda, N., Smithies, O., Frampton, C. M., Richards, A. M., & Cameron, V. A. (2007). Npr1-regulated gene pathways contributing to cardiac hypertrophy and fibrosis. *Journal of Molecular Endocrinology*, *38*(2), 245–257. https://doi.org/10.1677/jme.1.02138

Eschenhagen, T., Fink, C., Remmers, U., Scholz, H., Wattchow, J., Weil, J., Zimmermann, W., Dohmen, H. H., Schäfer, H., Bishopric, N., Wakatsuki, T., & Elson, E. L. (1997). Three-dimensional reconstitution of embryonic cardiomyocytes in a collagen matrix: a new heart muscle model system. *The FASEB Journal*, *11*(8), 683–694. https://doi.org/10.1096/fasebj.11.8.9240969

Essandoh, K., Subramani, A., Teuber, J. P., Koripella, S., & Brody, M. J. (2023). Regulation of atrial natriuretic peptide secretion in cardiomyocytes by Rab3a and zDHHC9-mediated palmitoylation of Rab3gap1. *Biophysical Journal*, *122*(3), 517a. https://doi.org/10.1016/j.bpj.2022.11.2750

Faleeva, M., Diakonov, I., Srivastava, P., Ramuz, M., Calamera, G., Andressen, K. W., Bork, N., Tsansizi, L., Cosson, M. V., Bernardo, A. S., Nikolaev, V., & Gorelik, J. (2022). Compartmentation of cGMP Signaling in Induced Pluripotent Stem Cell Derived Cardiomyocytes during Prolonged Culture. *Cells*, *11*(20), 1–17. https://doi.org/10.3390/cells11203257

Felker, G. M., Hasselblad, V., Tang, W. H. W., Hernandez, A. F., Armstrong, P. W., Fonarow, G. C., Voors, A. A., Metra, M., McMurray, J. J. V., Butler, J., Heizer, G. M., Dickstein, K., Massie, B. M., Atar, D., Troughton, R. W., Anker, S. D., Califf, R. M., Starling, R. C., & O'Connor, C. M. (2012). Troponin I in acute decompensated heart failure: insights from the ASCEND-HF study. *European Journal of Heart Failure*, *14*(11), 1257–1264. https://doi.org/10.1093/eurjhf/hfs110

Ferrari, S., Jacob, A., Cesana, D., Laugel, M., Beretta, S., Varesi, A., Unali, G., Conti, A., Canarutto, D., Albano, L., Calabria, A., Vavassori, V., Cipriani, C., Castiello, M. C., Esposito, S., Brombin, C., Cugnata, F., Adjali, O., Ayuso, E., Naldini, L. (2022). Choice of template delivery mitigates the genotoxic risk and adverse impact of editing in human hematopoietic stem cells. *Cell Stem Cell*, *29*(10), 1428-1444.e9. https://doi.org/10.1016/j.stem.2022.09.001

Ferreira, L. T., Orr, B., Rajendraprasad, G., Pereira, A. J., Lemos, C., Lima, J. T., Boldú, C. G., Ferreira, J. G., Barisic, M., & Maiato, H. (2020). α-Tubulin detyrosination impairs mitotic error correction by suppressing MCAK centromeric activity. *Journal of Cell Biology*, *219*(4). https://doi.org/10.1083/JCB.201910064

Feyen, D. A. M., McKeithan, W. L., Bruyneel, A. A. N., Spiering, S., Hörmann, L., Ulmer, B., Zhang, H., Briganti, F., Schweizer, M., Hegyi, B., Liao, Z., Pölönen, R. P., Ginsburg, K. S., Lam, C. K., Serrano, R., Wahlquist, C., Kreymerman, A., Vu, M., Amatya, P. L., Mercola, M. (2020). Metabolic Maturation Media Improve Physiological Function of Human iPSC-Derived Cardiomyocytes. *Cell Reports*, *32*(3), 107925. https://doi.org/10.1016/J.CELREP.2020.107925

Fiedler, B., Lohmann, S. M., Smolenski, A., Linnemüller, S., Pieske, B., Schröder, F., Molkentin, J. D., Drexler, H., & Wollert, K. C. (2002). Inhibition of calcineurin-NFAT hypertrophy signaling by cGMP-dependent protein kinase type I in cardiac myocytes. *Proceedings of the National Academy of Sciences of the United States of America*, *99*(17), 11363–11368. https://doi.org/10.1073/pnas.162100799

Fischer, B., Meier, A., Dehne, A., Salhotra, A., Tran, T. A., Neumann, S., Schmidt, K., Meiser, I., Neubauer, J. C., Zimmermann, H., & Gentile, L. (2018). A complete workflow for the differentiation and the dissociation of hiPSC-derived cardiospheres. *Stem Cell Research*, *32*, 65–72. https://doi.org/10.1016/j.scr.2018.08.015

Forsten, R. (2020). *Evaluation of maturation in human induced pluripotent stem cell-derived cardiomyocytes under different surface and media conditions*.

Frank, D., & Frey, N. (2011). Cardiac Z-disc Signaling Network. *Journal of Biological Chemistry*, *286*(12), 9897–9904. https://doi.org/10.1074/jbc.R110.174268

Frantz, S., Klaiber, M., Baba, H. A., Oberwinkler, H., Völker, K., Gaβner, B., Bayer, B., Abeβer, M., Schuh, K., Feil, R., Hofmann, F., & Kuhn, M. (2013). Stress-dependent dilated cardiomyopathy in mice with cardiomyocyte-restricted inactivation of cyclic GMP-dependent protein kinase I. *European Heart Journal*, *34*(16), 1233–1244. https://doi.org/10.1093/eurheartj/ehr445

Friedrich, F. W., Reischmann, S., Schwalm, A., Unger, A., Ramanujam, D., Münch, J., Müller, O. J., Hengstenberg, C., Galve, E., Charron, P., Linke, W. A., Engelhardt, S., Patten, M., Richard, P., van der Velden, J., Eschenhagen, T., Isnard, R., & Carrier, L. (2014). FHL2 expression and variants in hypertrophic cardiomyopathy. *Basic Research in Cardiology*, *109*(6). https://doi.org/10.1007/S00395-014-0451-8

Fu, G., Yan, S., Khoo, C. J., Chao, V. C., Liu, Z., Mukhi, M., Hervas, R., Li, X. D., & Ti, S.-C. (2023). Integrated regulation of tubulin tyrosination and microtubule stability by human α-tubulin isotypes. *Cell Reports*, *42*(6), 112653. https://doi.org/10.1016/j.celrep.2023.112653

Funakoshi, S., Fernandes, I., Mastikhina, O., Wilkinson, D., Tran, T., Dhahri, W., Mazine, A., Yang, D., Burnett, B., Lee, J., Protze, S., Bader, G. D., Nunes, S. S., Laflamme, M., & Keller, G. (2021). Generation of mature compact ventricular cardiomyocytes from human pluripotent stem cells. *Nature Communications*, *12*(1). https://doi.org/10.1038/s41467-021-23329-z

Furukawa, N., Matsui, H., Sunaga, H., Nagata, K., Hirayama, M., Obinata, H., Yokoyama, T., Ohno, K., Kurabayashi, M., & Koitabashi, N. (2024). Sacubitril/valsartan improves diastolic left ventricular stiffness with increased titin phosphorylation via cGMP-PKG activation in diabetic mice. *Scientific Reports*, *14*(1). https://doi.org/10.1038/s41598-024-75757-8

Gaj, T., Sirk, S. J., Shui, S., & Liu, J. (2016). Genome-Editing Technologies: Principles and Applications. *Cold Spring Harbor Perspectives in Biology*, *8*(12), a023754. https://doi.org/10.1101/cshperspect.a023754

Gasic, I., Boswell, S. A., & Mitchison, T. J. (2019). Tubulin mRNA stability is sensitive to change in microtubule dynamics caused by multiple physiological and toxic cues. *PLOS Biology*, *17*(4). https://doi.org/10.1371/journal.pbio.3000225

Geier, C., Gehmlich, K., Ehler, E., Hassfeld, S., Perrot, A., Hayess, K., Cardim, N., Wenzel, K., Erdmann, B., Krackhardt, F., Posch, M. G., Bublak, A., Nägele, H., Scheffold, T., Dietz, R., Chien, K. R., Spuler, S., Fürst, D. O., Nürnberg, P., & Özcelik, C. (2008). Beyond the sarcomere: CSRP3 mutations cause hypertrophic cardiomyopathy. *Human Molecular Genetics*, *17*(18), 2753–2765. https://doi.org/10.1093/hmg/ddn160

Goetze, J. P., Bruneau, B. G., Ramos, H. R., Ogawa, T., de Bold, M. K., & de Bold, A. J. (2020). Cardiac natriuretic peptides. *Nature Reviews Cardiology*, *17*(11), 698–717. https://doi.org/10.1038/s41569-020-0381-0

Goldstein, L. S. B., & Yang, Z. (2000). Microtubule-Based Transport Systems in Neurons: The Roles of Kinesins and Dyneins. *Annual Review of Neuroscience*, *23*(1), 39–71. https://doi.org/10.1146/annurev.neuro.23.1.39

Grigioni, F., Detaint, D., Avierinos, J. F., Scott, C., Tajik, J., & Enriquez-Sarano, M. (2005). Contribution of ischemic mitral regurgitation to congestive heart failure after myocardial infarction. *Journal of the American College of Cardiology*, *45*(2), 260–267. https://doi.org/10.1016/j.jacc.2004.10.030

Groenewegen, A., Rutten, F. H., Mosterd, A., & Hoes, A. W. (2020). Epidemiology of heart failure. *European Journal of Heart Failure*, *22*(8), 1342–1356.

https://doi.org/10.1002/ejhf.1858

Guo, C., Ma, X., Gao, F., & Guo, Y. (2023). Off-target effects in CRISPR/Cas9 gene editing. *Frontiers in Bioengineering and Biotechnology*, *11*. https://doi.org/10.3389/fbioe.2023.1143157

Guo, L., Eldridge, S., Furniss, M., Mussio, J., & Davis, M. (2015). Use of Human Induced Pluripotent Stem Cell–Derived Cardiomyocytes (hiPSC-CMs) to Monitor Compound Effects on Cardiac Myocyte Signaling Pathways. *Current Protocols in Chemical Biology*, *7*(3), 141–185. https://doi.org/10.1002/9780470559277.ch150035

Haddad, R., Sadeh, O., Ziv, T., Erlich, I., Haimovich-Caspi, L., Shemesh, A., van der Velden, J., & Kehat, I. (2024). Localized translation and sarcomere maintenance requires ribosomal protein SA in mice. *Journal of Clinical Investigation*, *134*(13), 1–15. https://doi.org/10.1172/JCI174527

Hagemann, T. L., Boelens, W. C., Wawrousek, E. F., & Messing, A. (2009). Suppression of GFAP toxicity by αB-crystallin in mouse models of Alexander disease. *Human Molecular Genetics*, *18*(7), 1190–1199. https://doi.org/10.1093/hmg/ddp013

Hamdani, N., Franssen, C., Lourenço, A., Falca o-Pires, I., Fontoura, D., Leite, S., Plettig, L., Lopez, B., Ottenheijm, C. A., Becher, P. M., Gonzalez, A., Tscho pe, C., Diez, J., Linke, W. A., Leite-Moreira, A. F., & Paulus, W. J. (2013). Myocardial titin hypophosphorylation importantly contributes to heart failure with preserved ejection fraction in a rat metabolic risk model. *Circulation: Heart Failure*, *6*(6), 1239–1249. https://doi.org/10.1161/CIRCHEARTFAILURE.113.000539

Hantelys, F., Godet, A. C., David, F., Tatin, F., Renaud-Gabardos, E., Pujol, F., Diallo, L., Ader, I., Ligat, L., Henras, A. K., Sato, Y., Parini, A., Lacazette, E., Garmy-Susini, B., & Prats, A. C. (2019). Vasohibin1, a new mouse cardiomyocyte ires trans-acting factor that regulates translation in early hypoxia. *ELife*, *8*, 1–26. https://doi.org/10.7554/eLife.50094

Haubner, B. J., Schuetz, T., & Penninger, J. M. (2016). A reproducible protocol for neonatal ischemic injury and cardiac regeneration in neonatal mice. *Basic Research in Cardiology*, *111*(6), 64. https://doi.org/10.1007/s00395-016-0580-3

Heusch, G. (2022). Coronary blood flow in heart failure: cause, consequence and bystander. *Basic Research in Cardiology*, *117*(1), 1. https://doi.org/10.1007/s00395-022-00909-8

Hirokawa, N., & Tanaka, Y. (2015). Kinesin superfamily proteins (KIFs): Various functions and their relevance for important phenomena in life and diseases. *Experimental Cell Research*, *334*(1), 16–25. https://doi.org/10.1016/j.yexcr.2015.02.016

Hirt, M. N., Sörensen, N. A., Bartholdt, L. M., Boeddinghaus, J., Schaaf, S., Eder, A., Vollert, I., Stöhr, A., Schulze, T., Witten, A., Stoll, M., Hansen, A., & Eschenhagen, T. (2012). Increased afterload induces pathological cardiac hypertrophy: a new in vitro model. *Basic Research in Cardiology*, *107*(6). https://doi.org/10.1007/S00395-012-0307-Z

Ho, C. Y., Day, S. M., Axelsson, A., Russell, M. W., Zahka, K., Lever, H. M., Pereira, A. C., Colan, S. D., Margossian, R., Murphy, A. M., Canter, C., Bach, R. G., Wheeler, M. T., Rossano, J. W., Owens, A. T., Bundgaard, H., Benson, L., Mestroni, L., Taylor, M. R. G., … Braunwald, E. (2021). Valsartan in early-stage hypertrophic cardiomyopathy: a randomized phase 2 trial. *Nature Medicine*, *27*(10), 1818–1824. https://doi.org/10.1038/s41591-021-01505-4

Hohmann, T., & Dehghani, F. (2019). The Cytoskeleton—A Complex Interacting Meshwork. *Cells*, *8*(4), 362. https://doi.org/10.3390/cells8040362

Holtwick, R., van Eickels, M., Skryabin, B. V., Baba, H. A., Bubikat, A., Begrow, F., Schneider, M. D., Garbers, D. L., & Kuhn, M. (2003). Pressure-independent cardiac hypertrophy in mice with cardiomyocyte-restricted inactivation of the atrial natriuretic peptide receptor guanylyl cyclase-A. *Journal of Clinical Investigation*, *111*(9), 1399–1407. https://doi.org/10.1172/jci200317061

Horikoshi, Y., Yan, Y., Terashvili, M., Wells, C., Horikoshi, H., Fujita, S., Bosnjak, Z., & Bai, X. (2019). Fatty Acid-Treated Induced Pluripotent Stem Cell-Derived Human Cardiomyocytes Exhibit Adult Cardiomyocyte-Like Energy Metabolism Phenotypes. *Cells*, *8*(9), 1095. https://doi.org/10.3390/cells8091095

Hotta, T., Haynes, S. E., Blasius, T. L., Gebbie, M., Eberhardt, E. L., Sept, D., Cianfrocco, M., Verhey, K. J., Nesvizhskii, A. I., & Ohi, R. (2021). Parthenolide Destabilizes Microtubules by Covalently Modifying Tubulin. *Current Biology*, *31*(4), 900-907.e6. https://doi.org/10.1016/j.cub.2020.11.055

Hou, P.-F., Jiang, T., Chen, F., Shi, P.-C., Li, H.-Q., Bai, J., & Song, J. (2018). KIF4A facilitates cell proliferation via induction of p21-mediated cell cycle progression and promotes metastasis in colorectal cancer. *Cell Death & Disease*, *9*(5), 477. https://doi.org/10.1038/s41419-018-0550-9

Howes, S. C., Alushin, G. M., Shida, T., Nachury, M. V., & Nogales, E. (2014). Effects of tubulin acetylation and tubulin acetyltransferase binding on microtubule structure. *Molecular Biology of the Cell*, *25*(2), 257–266. https://doi.org/10.1091/mbc.e13-07-0387

Hsu, S., Nagayama, T., Koitabashi, N., Zhang, M., Zhou, L., Bedja, D., Gabrielson, K. L., Molkentin, J. D., Kass, D. A., & Takimoto, E. (2009). Phosphodiesterase 5 inhibition blocks pressure overload-induced cardiac hypertrophy independent of the calcineurin pathway. *Cardiovascular Research*, *81*(2), 301–309. https://doi.org/10.1093/cvr/cvn324

Hu, Y., Liu, G., Yuan, J., Yin, D., & Lin, Y. (2025). Mutations in the TCAP gene may lead to restrictive phenotype hypertrophic cardiomyopathy with poor prognosis: case report. *European Heart Journal - Case Reports*, *9*(5). https://doi.org/10.1093/ehjcr/ytaf180

Huxley, H., & Hanson, J. (1954). Changes in the Cross-Striations of Muscle during Contraction and Stretch and their Structural Interpretation. *Nature*, *173*(4412), 973–976. https://doi.org/10.1038/173973a0

IDT. (2025). *CRISPR Design Tool*. https://eu.idtdna.com/site/order/designtool/index/CRISPR_CUSTOM

Immohr, M. B., Aubin, H., Westenfeld, R., Erbel-Khurtsidze, S., Tudorache, I., Akhyari, P., Lichtenberg, A., & Boeken, U. (2022). Heart Transplantation of the Elderly—Old Donors for Old Recipients: Can We Still Achieve Acceptable Results? *Journal of Clinical Medicine*, *11*(4), 929. https://doi.org/10.3390/jcm11040929

Iyama, T., & Wilson, D. M. (2013). DNA repair mechanisms in dividing and non-dividing cells. *DNA Repair*, *12*(8), 620–636. https://doi.org/10.1016/j.dnarep.2013.04.015

James, S. L., Abate, D., Abate, K. H., Abay, S. M., Abbafati, C., Abbasi, N., Abbastabar, H., Abd-Allah, F., Abdela, J., Abdelalim, A., Abdollahpour, I., Abdulkader, R. S., Abebe, Z., Abera, S. F., Abil, O. Z., Abraha, H. N., Abu-Raddad, L. J., Abu-Rmeileh, N. M. E., Accrombessi, M. M. K., Murray, C. J. L. (2018). Global, regional, and national incidence, prevalence, and years lived with disability for 354 Diseases and Injuries for 195 countries and territories, 1990-2017: A systematic analysis for the Global Burden of Disease Study 2017. *The Lancet*, *392*(10159), 1789–1858. https://doi.org/10.1016/S0140-6736(18)32279-7

Janke, C., & Magiera, M. M. (2020). The tubulin code and its role in controlling microtubule properties and functions. *Nature Reviews Molecular Cell Biology*, *21*(6), 307–326. https://doi.org/10.1038/s41580-020-0214-3

Jebran, A.-F., Seidler, T., Tiburcy, M., Daskalaki, M., Kutschka, I., Fujita, B., Ensminger, S., Bremmer, F., Moussavi, A., Yang, H., Qin, X., Mißbach, S., Drummer, C., Baraki, H., Boretius, S., Hasenauer, C., Nette, T., Kowallick, J., Ritter, C. O., Zimmermann, W.-H. (2025). Engineered heart muscle allografts for heart repair in primates and humans. *Nature*, *639*(8054), 503–511. https://doi.org/10.1038/s41586-024-08463-0

Jia, T., Wang, X., Tang, Y., Yu, W., Li, C., Cui, S., Zhu, J., Meng, W., Wang, C., & Wang, Q. (2021). Sacubitril Ameliorates Cardiac Fibrosis Through Inhibiting TRPM7 Channel. *Frontiers in Cell and Developmental Biology*, *9*. https://doi.org/10.3389/fcell.2021.760035

Johansson, M., Ulfenborg, B., Andersson, C. X., Heydarkhan-Hagvall, S., Jeppsson, A., Sartipy, P., & Synnergren, J. (2020). Cardiac hypertrophy in a dish: a human stem cell based model. *Biology Open*, *9*(9). https://doi.org/10.1242/bio.052381

Joung, J., Konermann, S., Gootenberg, J. S., Abudayyeh, O. O., Platt, R. J., Brigham, M. D., Sanjana, N. E., & Zhang, F. (2016). *Protocol: Genome-scale CRISPR-Cas9 Knockout and Transcriptional Activation Screening*. https://doi.org/10.1101/059626

Juarros, M., Dhand, A., Martin, T., Valle-Ayala, H., Hunt, D., Burdick, J., & Leinwand, L. (2024). Abstract We007: High Throughput 3D-Printed Human Engineered Heart Tissues for

Cardiac Disease Modeling. *Circulation Research*, *135*(Suppl_1), AWe007–AWe007. https://doi.org/10.1161/res.135.suppl_1.We007

Kadota, S., Pabon, L., Reinecke, H., & Murry, C. E. (2017). In Vivo Maturation of Human Induced Pluripotent Stem Cell-Derived Cardiomyocytes in Neonatal and Adult Rat Hearts. *Stem Cell Reports*, *8*(2), 278–289. https://doi.org/10.1016/j.stemcr.2016.10.009

Kahn-Krell, A., Pretorius, D., Ou, J., Fast, V. G., Litovsky, S., Berry, J., Liu, X. (Margaret), & Zhang, J. (2021). Bioreactor Suspension Culture: Differentiation and Production of Cardiomyocyte Spheroids From Human Induced Pluripotent Stem Cells. *Frontiers in Bioengineering and Biotechnology*, *9*. https://doi.org/10.3389/fbioe.2021.674260

Kamps, J. A. (2016). Micromanaging cardiac regeneration: Targeted delivery of microRNAs for cardiac repair and regeneration. *World Journal of Cardiology*, *8*(2), 163. https://doi.org/10.4330/wjc.v8.i2.163

Karvelis, T., Gasiunas, G., Miksys, A., Barrangou, R., Horvath, P., & Siksnys, V. (2013). crRNA and tracrRNA guide Cas9-mediated DNA interference in Streptococcus thermophilus. *RNA Biology*, *10*(5), 841–851. https://doi.org/10.4161/rna.24203

Khan, M. S., Shahid, I., Bennis, A., Rakisheva, A., Metra, M., & Butler, J. (2024). Global epidemiology of heart failure. *Nature Reviews Cardiology*, *21*(10), 717–734. https://doi.org/10.1038/s41569-024-01046-6

Khan, M. S., Shahid, I., Fonarow, G. C., & Greene, S. J. (2022). Classifying heart failure based on ejection fraction: imperfect but enduring. *European Journal of Heart Failure*, *24*(7), 1154–1157. https://doi.org/10.1002/ejhf.2470

Kim, C., & Sharma, R. (2021). Cyclic nucleotide selectivity of protein kinase G isozymes. *Protein Science*, *30*(2), 316–327. https://doi.org/10.1002/pro.4008

Kim, Y. T., Hur, E.-M., Snider, W. D., & Zhou, F.-Q. (2011). Role of GSK3 Signaling in Neuronal Morphogenesis. *Frontiers in Molecular Neuroscience*, *4*(November), 1–11. https://doi.org/10.3389/fnmol.2011.00048

Kitazawa, H., Iida, J., Ichida, A., Haino-Fukushima, K., Itoh, T. J., Hotani, H., Ookata, K., Murofushi, H., Bulinski, J. C., Kishimoto, T., & Hisanaga, S. I. (2000). Ser787 in the proline-rich region of human MAP4 is a critical phosphorylation site that reduces its activity to promote tubulin polymerization. *Cell Structure and Function*, *25*(1), 33–39. https://doi.org/10.1247/csf.25.33

Kliesow Remes, A., Ruf, T., Zurashvili, T., Ding, L., Meyer-Jens, M., Schwab, D. M., Hille, S., Matzen, A., Michalewski, S., Kilian, L., Shetty, P. M. V., Fuchs, M.-C. C., Eden, M., Gröne, H.-J. J., Rapti, K., Jungmann, A., Milting, H., Katus, H. A., Carrier, L., Müller, O. J. (2025). AAV-mediated overexpression of CPT1B protects from cardiac hypertrophy and heart failure in a murine pressure overload model. *Basic Research in Cardiology*, *0123456789*. https://doi.org/10.1007/s00395-025-01123-y

Knight, W. E., Cao, Y., Dillon, P., & Song, K. (2021). A simple protocol to produce mature human-induced pluripotent stem cell-derived cardiomyocytes. *STAR Protocols*, *2*(4), 100912. https://doi.org/10.1016/j.xpro.2021.100912

Knight, W. E., Cao, Y., Lin, Y. H., Chi, C., Bai, B., Sparagna, G. C., Zhao, Y., Du, Y., Londono, P., Reisz, J. A., Brown, B. C., Taylor, M. R. G., Ambardekar, A. V., Cleveland, J. C., McKinsey, T. A., Jeong, M. Y., Walker, L. A., Woulfe, K. C., D'Alessandro, A., Song, K. (2021). Maturation of Pluripotent Stem Cell-Derived Cardiomyocytes Enables Modeling of Human Hypertrophic Cardiomyopathy. *Stem Cell Reports*, *16*(3), 519–533. https://doi.org/10.1016/j.stemcr.2021.01.018

Knowles, J. W., Esposito, G., Mao, L., Hagaman, J. R., Fox, J. E., Smithies, O., Rockman, H. A., & Maeda, N. (2001). Pressure-independent enhancement of cardiac hypertrophy in natriuretic peptide receptor A-deficient mice. *Journal of Clinical Investigation*, *107*(8), 975–984. https://doi.org/10.1172/JCI11273

Kokkonen, K., & Kass, D. A. (2017). Nanodomain Regulation of Cardiac Cyclic Nucleotide Signaling by Phosphodiesterases. *Annual Review of Pharmacology and Toxicology*, *57*, 455–479. https://doi.org/10.1146/annurev-pharmtox-010716-104756

Kondo, T., Takahashi, M., Yamasaki, G., Sugimoto, M., Kuse, A., Morichika, M., Nakagawa, K., Sakurada, M., Asano, M., & Ueno, Y. (2022). Immunohistochemical analysis of vimentin expression in myocardial tissue from autopsy cases of ischemic heart disease. *Legal Medicine*, *54*, 102003. https://doi.org/10.1016/j.legalmed.2021.102003

Kong, Q., & Blanton, R. M. (2013). Protein Kinase G I and Heart Failure. *Circulation: Heart Failure*, *6*(6), 1268–1283. https://doi.org/10.1161/CIRCHEARTFAILURE.113.000575

Kontis, V., Bennett, J. E., Mathers, C. D., Li, G., Foreman, K., & Ezzati, M. (2017). Future life expectancy in 35 industrialised countries: projections with a Bayesian model ensemble. *The Lancet*, *389*(10076), 1323–1335. https://doi.org/10.1016/S0140-6736(16)32381-9

Kristensen, J. H., Hasselbalch, R. B., Strandkjær, N., Jørgensen, N., Østergaard, M., Møller-Sørensen, P. H., Nilsson, J. C., Afzal, S., Kamstrup, P. R., Dahl, M., Bor, M. V., Frikke-Schmidt, R., Jørgensen, N. R., Rode, L., Holmvang, L., Kjærgaard, J., Bang, L. E., Forman, J., Dalhoff, K., Iversen, K. K. (2024). Half-Life and Clearance of Cardiac Troponin I and Troponin T in Humans. *Circulation*, *150*(15), 1187–1198. https://doi.org/10.1161/CIRCULATIONAHA.123.066565

Krüger, M., Kötter, S., Grützner, A., Lang, P., Andresen, C., Redfield, M. M., Butt, E., Dos Remedios, C. G., & Linke, W. A. (2009). Protein kinase G modulates human myocardial passive stiffness by phosphorylation of the titin springs. *Circulation Research*, *104*(1), 87–94. https://doi.org/10.1161/CIRCRESAHA.108.184408

Kubin, T., Cetinkaya, A., Kubin, N., Bramlage, P., Sen Hild, B., Gajawada, P., Akintürk, H., Schönburg, M., Schaper, W., Choi, Y.-H., Barancik, M., & Richter, M. (2020). The mek/erk module is reprogrammed in remodeling adult cardiomyocytes. *International Journal of Molecular Sciences*, *21*(17), 1–18. https://doi.org/10.3390/ijms21176348

Kyselovic, J., Cervenak, Z., Hulman, M., & Gazova, A. (2024). The essential role of the miRNA-208a/TARBP2/Sox6 axis in myosin expression in the end stage human heart failure. *European Heart Journal*, *45*(Supplement_1). https://doi.org/10.1093/eurheartj/ehae666.755

Lafanechère, L., Courtay-Cahen, C., Kawakami, T., Jacrot, M., Rüdiger, M., Wehland, J., Job, D., & Margolis, R. L. (1998). Suppression of tubulin tyrosine ligase during tumor growth. *Journal of Cell Science*, *111*(2), 171–181. https://doi.org/10.1242/jcs.111.2.171

Laird, D. W., Puranam, K. L., & Revel, J. P. (1991). Turnover and phosphorylation dynamics of connexin43 gap junction protein in cultured cardiac myocytes. *Biochemical Journal*, *273*(1), 67–72. https://doi.org/10.1042/bj2730067

Landskron, L., Bak, J., Adamopoulos, A., Kaplani, K., Moratti, M., Van den Hengel, L. G., Song, J.-Y., Bleijerveld, O. B., Nieuwenhuis, J., Heidebrecht, T., Henneman, L., Moutin, M., Barisic, M., Taraviras, S., Perrakis, A., & Brummelkamp, T. R. (2022). Posttranslational modification of microtubules by the MATCAP detyrosinase. *Science*, *6020*(8.5.2017), 2003–2005. https://doi.org/DOI: 10.1126/science.abn6020

Larsson, S. C., Tektonidis, T. G., Gigante, B., Åkesson, A., & Wolk, A. (2016). Healthy Lifestyle and Risk of Heart Failure. *Circulation: Heart Failure*, *9*(4). https://doi.org/10.1161/CIRCHEARTFAILURE.115.002855

Laskary, A. R., Hudson, J. E., & Porrello, E. R. (2025). Designing multicellular cardiac tissue engineering technologies for clinical translation. *Seminars in Cell & Developmental Biology*, *171*, 103612. https://doi.org/10.1016/j.semcdb.2025.103612

Lee, D. I., Zhu, G., Sasaki, T., Cho, G. S., Hamdani, N., Holewinski, R., Jo, S. H., Danner, T., Zhang, M., Rainer, P. P., Bedja, D., Kirk, J. A., Ranek, M. J., Dostmann, W. R., Kwon, C., Margulies, K. B., Van Eyk, J. E., Paulus, W. J., Takimoto, E., & Kass, D. A. (2015). Phosphodiesterase 9A controls nitric-oxide-independent cGMP and hypertrophic heart disease. *Nature*, *519*(7544), 472–476. https://doi.org/10.1038/nature14332

Leibinger, M., Zeitler, C., Paulat, M., Gobrecht, P., Hilla, A., Andreadaki, A., Guthoff, R., & Fischer, D. (2023). Inhibition of microtubule detyrosination by parthenolide facilitates functional CNS axon regeneration. *ELife*, *12*. https://doi.org/10.7554/eLife.88279

Leitolis, A., Robert, A. W., Pereira, I. T., Correa, A., & Stimamiglio, M. A. (2019). Cardiomyogenesis Modeling Using Pluripotent Stem Cells: The Role of Microenvironmental Signaling. *Frontiers in Cell and Developmental Biology*, *7*. https://doi.org/10.3389/fcell.2019.00164

Lemme, M., Ulmer, B. M., Lemoine, M. D., Zech, A. T. L., Flenner, F., Ravens, U., Reichenspurner, H., Rol-Garcia, M., Smith, G., Hansen, A., Christ, T., & Eschenhagen, T. (2018). Atrial-like Engineered Heart Tissue: An In Vitro Model of the Human Atrium. *Stem Cell Reports*, *11*(6), 1378–1390. https://doi.org/10.1016/j.stemcr.2018.10.008

Li, F., Li, Y., Ye, X., Gao, H., Shi, Z., Luo, X., Rice, L. M., & Yu, H. (2020). Cryo-em structure of vash1-svbp bound to microtubules. *ELife*, *9*, 1–19. https://doi.org/10.7554/ELIFE.58157

Li, J. M., Pan, X. C., Ding, Y. Y., Tong, Y. F., Chen, X. H., Liu, Y., & Zhang, H. G. (2020). Effect of Triptolide on Temporal Expression of Cell Cycle Regulators During Cardiac Hypertrophy. *Frontiers in Pharmacology*, *11*(September), 1–12. https://doi.org/10.3389/fphar.2020.566938

Liao, H., Wu, J., VanDusen, N. J., Li, Y., & Zheng, Y. (2024). CRISPR-Cas9-mediated homology-directed repair for precise gene editing. *Molecular Therapy - Nucleic Acids*, *35*(4), 102344. https://doi.org/10.1016/j.omtn.2024.102344

Liao, S., Rajendraprasad, G., Wang, N., Eibes, S., Gao, J., Yu, H., Wu, G., Tu, X., Huang, H., Barisic, M., & Xu, C. (2019). Molecular basis of vasohibins-mediated detyrosination and its impact on spindle function and mitosis. *Cell Research*, *29*(7), 533–547. https://doi.org/10.1038/s41422-019-0187-y

Lin, J., & Wong, K. C. (2018). Off-target predictions in CRISPR-Cas9 gene editing using deep learning. *Bioinformatics*, *34*(17), i656–i663. https://doi.org/10.1093/bioinformatics/bty554

Litviňuková, M., Talavera-López, C., Maatz, H., Reichart, D., Worth, C. L., Lindberg, E. L., Kanda, M., Polanski, K., Heinig, M., Lee, M., Nadelmann, E. R., Roberts, K., Tuck, L., Fasouli, E. S., DeLaughter, D. M., McDonough, B., Wakimoto, H., Gorham, J. M., Samari, S., … Teichmann, S. A. (2020). Cells of the adult human heart. *Nature*, *588*(7838), 466–472. https://doi.org/10.1038/s41586-020-2797-4

Liu, B., Li, A., Qin, Y., Tian, X., Gao, M., Jiang, W., & Gong, G. (2019). Comparative study on isolation and mitochondrial function of adult mouse and rat cardiomyocytes. *Journal of Molecular and Cellular Cardiology*, *136*, 64–71. https://doi.org/10.1016/j.yjmcc.2019.09.006

Liu, E., & Lampert, B. C. (2022). Heart Failure in Older Adults: Medical Management and Advanced Therapies. *Geriatrics (Switzerland)*, *7*(2). https://doi.org/10.3390/geriatrics7020036

Liu, S., Deshmukh, V., Meng, F., Wang, Y., & Morikawa, Y. (2024). *Microtubules Sequester Acetylated YAP in the Cytoplasm and Inhibit Heart Regeneration*. 1–17. https://doi.org/10.1161/CIRCULATIONAHA.123.067646

Liu, X., & Liu, Y. (2022). Comprehensive Analysis of the Expression and Prognostic Significance of the CENP Family in Breast Cancer. *International Journal of General Medicine*, *Volume 15*, 3471–3482. https://doi.org/10.2147/IJGM.S354200

Liu, Z., Liu, X., Yu, H., Pei, J., Zhang, Y., Gong, J., & Pu, J. (2015). Common Variants in TRDN and CALM1 Are Associated with Risk of Sudden Cardiac Death in Chronic Heart Failure Patients in Chinese Han Population. *PLOS ONE*, *10*(7), e0132459. https://doi.org/10.1371/journal.pone.0132459

Lobo, S., Barbosa-Matos, R., Doria, S., Pedro, A. M., Brito, A., Ferreira, D., & Oliveira, C. (2025). A protocol for karyotyping and genetic editing of induced pluripotent stem cells with homology-directed repair mediated CRISPR/Cas9. *Biology Methods and Protocols*, *10*(1). https://doi.org/10.1093/biomethods/bpaf018

Loescher, C. M., Freundt, J. K., Unger, A., Hessel, A. L., Kühn, M., Koser, F., & Linke, W. A. (2023). Titin governs myocardial passive stiffness with major support from microtubules and actin and the extracellular matrix. *Nature Cardiovascular Research*, *2*(11), 991–1002. https://doi.org/10.1038/s44161-023-00348-1

Loescher, C. M., & Linke, W. A. (2024). Titin takes centerstage among cytoskeletal contributions to myocardial passive stiffness. *Cytoskeleton*, *81*(2–3), 184–187. https://doi.org/10.1002/cm.21827

Loos, M., Klampe, B., Schulze, T., Yin, X., Theofilatos, K., Ulmer, B. M., Schulz, C., Behrens, C. S., van Bergen, T. D., Adami, E., Maatz, H., Schweizer, M., Brodesser, S., Skryabin, B. V., Rozhdestvensky, T. S., Bodbin, S., Stathopoulou, K., Christ, T., Denning, C., Hansen, A. (2023). Human model of primary carnitine deficiency cardiomyopathy reveals ferroptosis as a novel mechanism. *Stem Cell Reports*, *18*(11), 2123–2137. https://doi.org/10.1016/j.stemcr.2023.09.002

Lou, Y., Lu, J., Zhang, Y., Gu, P., Wang, H., Qian, F., Zhou, W., Zhang, W., Zhong, H., & Han, B. (2022). The centromere-associated protein CENPU promotes cell proliferation, migration, and invasiveness in lung adenocarcinoma. *Cancer Letters*, *532*, 215599. https://doi.org/10.1016/j.canlet.2022.215599

Luengo-Fernandez, R., Walli-Attaei, M., Gray, A., Torbica, A., Maggioni, A. P., Huculeci, R., Bairami, F., Aboyans, V., Timmis, A. D., Vardas, P., & Leal, J. (2023). Economic burden of cardiovascular diseases in the European Union: a population-based cost study. *European Heart Journal*, *44*(45), 4752–4767. https://doi.org/10.1093/eurheartj/ehad583

Lund, L. H., Pitt, B., & Metra, M. (2022). Left ventricular ejection fraction as the primary heart failure phenotyping parameter. *European Journal of Heart Failure*, *24*(7), 1158–1161. https://doi.org/10.1002/ejhf.2576

Machiraju, P., & Greenway, S. C. (2019). Current methods for the maturation of induced pluripotent stem cell-derived cardiomyocytes. *World Journal of Stem Cells*, *11*(1). https://doi.org/10.4252/wjsc.v11.i1.33

Mahmoud, Z. H., AL-Salman, H. N. K., & Kianfar, E. (2024). Nanoindentation: Introduction and applications of a non-destructive analysis. *Nano TransMed*, *3*, 100057. https://doi.org/10.1016/j.ntm.2024.100057

Malliaras, K., Zhang, Y., Seinfeld, J., Galang, G., Tseliou, E., Cheng, K., Sun, B., Aminzadeh, M., & Marbán, E. (2013). Cardiomyocyte proliferation and progenitor cell recruitment underlie therapeutic regeneration after myocardial infarction in the adult mouse heart. *EMBO Molecular Medicine*, *5*(2), 191–209. https://doi.org/10.1002/emmm.201201737

Manka, S. W., & Moores, C. A. (2018). Microtubule structure by cryo-EM: snapshots of dynamic instability. *Essays in Biochemistry*, *62*(6), 737. https://doi.org/10.1042/EBC20180031

Martin, A. A., Thompson, B. R., Hahn, D., Angulski, A. B. B., Hosny, N., Cohen, H., & Metzger, J. M. (2022). Cardiac Sarcomere Signaling in Health and Disease. In *International Journal of Molecular Sciences* (Vol. 23, Issue 24). MDPI. https://doi.org/10.3390/ijms232416223

Masarone, D., Limongelli, G., Rubino, M., Valente, F., Vastarella, R., Ammendola, E., Gravino, R., Verrengia, M., Salerno, G., & Pacileo, G. (2017). Management of Arrhythmias in Heart Failure. *Journal of Cardiovascular Development and Disease*, *4*(1), 3. https://doi.org/10.3390/jcdd4010003

MATCAP1 Gene Card. (2025). https://www.genecards.org/cgi-bin/carddisp.pl?gene=MATCAP1

McMurray, J. J. V., Packer, M., Desai, A. S., Gong, J., Lefkowitz, M. P., Rizkala, A. R., Rouleau, J. L., Shi, V. C., Solomon, S. D., Swedberg, K., & Zile, M. R. (2014). Angiotensin–Neprilysin Inhibition versus Enalapril in Heart Failure. *New England Journal of Medicine*, *371*(11). https://doi.org/10.1056/NEJMoa1409077

Menendez, J. T. (2016). The Mechanism of Action of LCZ696. *Cardiac Failure Review*, *2*(1), 40. https://doi.org/10.15420/cfr.2016:1:1

Meyer-Jens, M., Wenzel, K., Grube, K., Rüdebusch, J., Krämer, E., Bahls, M., Müller, K., Voß, H., Schlüter, H., Felix, S. B., Carrier, L., Könemann, S., & Schlossarek, S. (2024). Sacubitril/valsartan reduces proteasome activation and cardiomyocyte area in an experimental mouse model of hypertrophy. *Journal of Molecular and Cellular Cardiology Plus*, *7*, 100059. https://doi.org/10.1016/J.JMCCPL.2023.100059

Mezzasoma, L., Talesa, V. N., Romani, R., & Bellezza, I. (2021). Anp and bnp exert anti-inflammatory action via npr-1/cgmp axis by interfering with canonical, non-canonical, and alternative routes of inflammasome activation in human thp1 cells. *International Journal of Molecular Sciences*, *22*(1), 1–17. https://doi.org/10.3390/ijms22010024

Michel, K., Herwig, M., Werner, F., Spes, K. Š., Abeßer, M., Schuh, K., Dabral, S., Mügge, A., Baba, H. A., Skryabin, B. V., Hamdani, N., & Kuhn, M. (2020). C-type natriuretic peptide moderates titin-based cardiomyocyte stiffness. *JCI Insight*, *5*(22), 1–17. https://doi.org/10.1172/jci.insight.139910

Mishra, S., Sadagopan, N., Dunkerly-Eyring, B., Rodriguez, S., Sarver, D. C., Ceddia, R. P., Murphy, S. A., Knutsdottir, H., Jani, V. P., Ashok, D., Oeing, C. U., O'Rourke, B., Gangoiti, J. A., Sears, D. D., Wong, G. W., Collins, S., & Kass, D. A. (2021). Inhibition of phosphodiesterase type 9 reduces obesity and cardiometabolic syndrome in mice. *Journal of Clinical Investigation*, *131*(21), 1–17. https://doi.org/10.1172/JCI148798

Miyoshi, T., Nakamura, K., Miura, D., Yoshida, M., Saito, Y., Akagi, S., Ohno, Y., Kondo, M., & Ito, H. (2019). Effect of lcz696, a dual angiotensin receptor neprilysin inhibitor, on isoproterenol-induced cardiac hypertrophy, fibrosis, and hemodynamic change in rats. *Cardiology Journal*, *26*(5), 575–583. https://doi.org/10.5603/CJ.a2018.0048

Mosqueira, D., Mannhardt, I., Bhagwan, J. R., Lis-Slimak, K., Katili, P., Scott, E., Hassan, M., Prondzynski, M., Harmer, S. C., Tinker, A., Smith, J. G. W., Carrier, L., Williams, P. M., Gaffney, D., Eschenhagen, T., Hansen, A., & Denning, C. (2018). CRISPR/Cas9 editing in human pluripotent stem cell-cardiomyocytes highlights arrhythmias, hypocontractility, and energy depletion as potential therapeutic targets for hypertrophic cardiomyopathy. *European Heart Journal*, *39*(43), 3879–3892. https://doi.org/10.1093/eurheartj/ehy249

Moutin, M., Bosc, C., Peris, L., & Andrieux, A. (2020). Tubulin post-translational modifications control neuronal development and functions. *Developmental Neurobiology*, *81*(3), 253–272. https://doi.org/10.1002/dneu.22774

Murphy, S. P., Ibrahim, N. E., & Januzzi, J. L. (2020). Heart Failure with Reduced Ejection Fraction: A Review. *JAMA - Journal of the American Medical Association*, *324*(5), 488–504. https://doi.org/10.1001/jama.2020.10262

Murray, C. J. L., & Lopez, A. D. (2013). Measuring the Global Burden of Disease. *New England Journal of Medicine*, *369*(5), 448–457. https://doi.org/10.1056/nejmra1201534

Nagayama, T., Hsu, S., Zhang, M., Koitabashi, N., Bedja, D., Gabrielson, K. L., Takimoto, E., & Kass, D. A. (2009). Sildenafil Stops Progressive Chamber, Cellular, and Molecular Remodeling and Improves Calcium Handling and Function in Hearts With Pre-Existing Advanced Hypertrophy Caused by Pressure Overload. *Journal of the American College of Cardiology*, *53*(2), 207–215. https://doi.org/10.1016/j.jacc.2008.08.069

Naito, H., Melnychenko, I., Didié, M., Schneiderbanger, K., Schubert, P., Rosenkranz, S., Eschenhagen, T., & Zimmermann, W.-H. (2006). Optimizing Engineered Heart Tissue for Therapeutic Applications as Surrogate Heart Muscle. *Circulation*, *114*(1_supplement). https://doi.org/10.1161/CIRCULATIONAHA.105.001560

Nakamura, T., & Tsujita, K. (2021). Current trends and future perspectives for heart failure treatment leveraging cGMP modifiers and the practical effector PKG. *Journal of Cardiology*, *78*(4), 261–268. https://doi.org/10.1016/j.jjcc.2021.03.004

Nasir, M., Khan, M. N., Soomro, N. A., Naseeb, K., Jahanzaib, M., Irfan, M., Qazi, S. R., Khan, I. A., & Ashraf, T. (2023). Analysis of genetic mutation in dilated cardiomyopathy. *Gene Reports*, *33*, 101821. https://doi.org/10.1016/j.genrep.2023.101821

NCBI. (2025). *MATCAP1 locus*. https://www.ncbi.nlm.nih.gov/gene/653319

Nieuwenhuis, J., Adamopoulos, A., Bleijerveld, O. B., Mazouzi, A., Stickel, E., Celie, P., Altelaar, M., Knipscheer, P., Perrakis, A., Blomen, V. A., & Brummelkamp, T. R. (2017). Vasohibins encode tubulin detyrosinating activity. *Science (New York, N.Y.)*, *358*(6369), 1453–1456. https://doi.org/10.1126/SCIENCE.AAO5676

Nieuwenhuis, J., & Brummelkamp, T. R. (2019). The Tubulin Detyrosination Cycle: Function and Enzymes. *Trends in Cell Biology*, 80–92. https://doi.org/10.1016/j.tcb.2018.08.003

Numata, G., & Takimoto, E. (2022). Cyclic GMP and PKG Signaling in Heart Failure. *Frontiers in Pharmacology*, *13*. https://doi.org/10.3389/fphar.2022.792798

Oeing, C. U., Jun, S., Mishra, S., Dunkerly-Eyring, B. L., Chen, A., Grajeda, M. I., Tahir, U. A., Gerszten, R. E., Paolocci, N., Ranek, M. J., & Kass, D. A. (2021). MTORC1-Regulated Metabolism Controlled by TSC2 Limits Cardiac Reperfusion Injury. *Circulation Research*, *128*(5), 639. https://doi.org/10.1161/CIRCRESAHA.120.317710

Oeing, C. U., Nakamura, T., Pan, S., Mishra, S., Dunkerly-Eyring, B. L., Kokkonen-Simon, K. M., Lin, B. L., Chen, A., Zhu, G., Bedja, D., Lee, D. I., Kass, D. A., & Ranek, M. J. (2020). PKG1α Cysteine-42 Redox State Controls mTORC1 Activation in Pathological Cardiac Hypertrophy. *Circulation Research*, *127*(4), 522–533.

https://doi.org/10.1161/CIRCRESAHA.119.315714

Ohashi, A., Ohori, M., Iwai, K., Nakayama, Y., Nambu, T., Morishita, D., Kawamoto, T., Miyamoto, M., Hirayama, T., Okaniwa, M., Banno, H., Ishikawa, T., Kandori, H., & Iwata, K. (2015). Aneuploidy generates proteotoxic stress and DNA damage concurrently with p53-mediated post-mitotic apoptosis in SAC-impaired cells. *Nature Communications*, *6*. https://doi.org/10.1038/ncomms8668

Oka, T., Xu, J., Kaiser, R. A., Melendez, J., Hambleton, M., Sargent, M. A., Lorts, A., Brunskill, E. W., Dorn, G. W., Conway, S. J., Aronow, B. J., Robbins, J., & Molkentin, J. D. (2007). Genetic Manipulation of Periostin Expression Reveals a Role in Cardiac Hypertrophy and Ventricular Remodeling. *Circulation Research*, *101*(3), 313–321. https://doi.org/10.1161/CIRCRESAHA.107.149047

Okada, K., Minamino, T., Tsukamoto, Y., Liao, Y., Tsukamoto, O., Takashima, S., Hirata, A., Fujita, M., Nagamachi, Y., Nakatani, T., Yutani, C., Ozawa, K., Ogawa, S., Tomoike, H., Hori, M., & Kitakaze, M. (2004). Prolonged Endoplasmic Reticulum Stress in Hypertrophic and Failing Heart After Aortic Constriction. *Circulation*, *110*(6), 705–712. https://doi.org/10.1161/01.CIR.0000137836.95625.D4

Oliver, P. M., Fox, J. E., Kim, R., Rockman, H. A., Kim, H.-S. S., Reddick, R. L., Pandey, K. N., Milgram, S. L., Smithies, O., & Maeda, N. (1997). Hypertension, cardiac hypertrophy, and sudden death in mice lacking natriuretic peptide receptor A. *Proceedings of the National Academy of Sciences*, *94*(26), 14730–14735. https://doi.org/10.1073/pnas.94.26.14730

Orbán-Németh, Z., Simader, H., Badurek, S., Trančiková, A., & Propst, F. (2005). Microtubule-associated protein 1S, a short and ubiquitously expressed member of the microtubule-associated protein 1 family. *Journal of Biological Chemistry*, *280*(3), 2257–2265. https://doi.org/10.1074/jbc.M408984200

Pagnamenta, A. T., Heemeryck, P., Martin, H. C., Bosc, C., Peris, L., Uszynski, I., Gory-Fauré, S., Couly, S., Deshpande, C., Siddiqui, A., Elmonairy, A. A., Jayawant, S., Murthy, S., Walker, I., Loong, L., Bauer, P., Vossier, F., Denarier, E., Maurice, T., Moutin, M.-J. (2019). Defective tubulin detyrosination causes structural brain abnormalities with cognitive deficiency in humans and mice. *Human Molecular Genetics*, *28*(20), 3391–3405. https://doi.org/10.1093/hmg/ddz186

Panda, A., Suvakov, M., Mariani, J., Drucker, K. L., Park, Y., Jang, Y., Kollmeyer, T. M., Sarkar, G., Bae, T., Kim, J. J., Yoon, W. H., Jenkins, R. B., Vaccarino, F. M., & Abyzov, A. (2023). Clonally Selected Lines After CRISPR-Cas Editing Are Not Isogenic. *The CRISPR Journal*, *6*(2), 176–182. https://doi.org/10.1089/crispr.2022.0050

Pandey, K. N. (2014). Guanylyl cyclase/natriuretic peptide receptor-A signaling antagonizes phosphoinositide hydrolysis, Ca2+ release, and activation of protein kinase C. *Frontiers in Molecular Neuroscience*, *7*(AUG), 1–14. https://doi.org/10.3389/fnmol.2014.00075

Papathanasiou, S., Markoulaki, S., Blaine, L. J., Leibowitz, M. L., Zhang, C.-Z., Jaenisch, R., & Pellman, D. (2021). Whole chromosome loss and genomic instability in mouse embryos after CRISPR-Cas9 genome editing. *Nature Communications*, *12*(1), 5855. https://doi.org/10.1038/s41467-021-26097-y

Patel, S. R., Sileo, A., Bello, R., Gunda, S., Nguyen, J., & Goldstein, D. (2015). Heart Transplantation Versus Continuous-Flow Left Ventricular Assist Device: Comprehensive Cost at 1 Year. *Journal of Cardiac Failure*, *21*(2), 160–166. https://doi.org/10.1016/j.cardfail.2014.11.007

Paturle-Lafanechère, L., Manier, M., Trigault, N., Pirollet, F., Mazarguil, H., & Job, D. (1994). Accumulation of delta 2-tubulin, a major tubulin variant that cannot be tyrosinated, in neuronal tissues and in stable microtubule assemblies. *Journal of Cell Science*, *107*(6), 1529–1543. https://doi.org/10.1242/jcs.107.6.1529

Perera, R. K., Sprenger, J. U., Steinbrecher, J. H., Hübscher, D., Lehnart, S. E., Abesser, M., Schuh, K., El-Armouche, A., & Nikolaev, V. O. (2015). Microdomain Switch of cGMP-Regulated Phosphodiesterases Leads to ANP-Induced Augmentation of β-Adrenoceptor-Stimulated Contractility in Early Cardiac Hypertrophy. *Circulation Research*, *116*(8), 1304–1311. https://doi.org/10.1161/CIRCRESAHA.116.306082

Perng, M. Der, Cairns, L., van den Ijssel, P., Prescott, A., Hutcheson, A. M., & Quinlan, R. A. (1999). Intermediate filament interactions can be altered by HSP27 and αB-crystallin. *Journal of Cell Science*, *112*(13), 2099–2112. https://doi.org/10.1242/jcs.112.13.2099

Pero, M. E., Meregalli, C., Qu, X., Shin, G. J., Kumar, A., Shorey, M., Rolls, M. M., Tanji, K., Brannagan, T. H., Alberti, P., Fumagalli, G., Monza, L., Grueber, W. B., Cavaletti, G., & Bartolini, F. (2021). Pathogenic role of delta 2 tubulin in bortezomib-induced peripheral neuropathy. *Proceedings of the National Academy of Sciences*, *118*(4). https://doi.org/10.1073/pnas.2012685118

Phyo, S. A., Uchida, K., Chen, C. Y., & Caporizzo, M. A. (2022). *Rewrite the Tubulin Code During Cardiac Hypertrophy and Failure*.

Pietsch, N., Chen, C. Y., Kupsch, S., Bacmeister, L., Geertz, B., Herrera-Rivero, M., Siebels, B., Voß, H., Krämer, E., Braren, I., Westermann, D., Schlüter, H., Mearini, G., Schlossarek, S., van der Velden, J., Caporizzo, M., Lindner, D., Prosser, B. L., & Carrier, L. (2024). Chronic Activation of Tubulin Tyrosination Improves Heart Function. *Circulation Research*. https://doi.org/10.1161/CIRCRESAHA.124.324387

Pietsch, N., Krämer, E., Moutin, M., Ramirez-Rios, S., & Carrier, L. (n.d.). *SVBP deficiency causes proliferation in hiPSC-CMs*.

Pietsch, N., Moutin, M.-J., & Carrier, L. (n.d.). *Creation of VASH1/2 knockout and mutant hiPSC-lines*.

Pocock, S. J., Wang, D., Pfeffer, M. A., Yusuf, S., McMurray, J. J. V., Swedberg, K. B., Östergren, J., Michelson, E. L., Pieper, K. S., & Granger, C. B. (2006). Predictors of mortality and morbidity in patients with chronic heart failure. *European Heart Journal*, *27*(1), 65–75. https://doi.org/10.1093/eurheartj/ehi555

Ponikowski, P., Voors, A. A., Anker, S. D., Bueno, H., Cleland, J. G. F., Coats, A. J. S., Falk, V., González-Juanatey, J. R., Harjola, V.-P., Jankowska, E. A., Jessup, M., Linde, C., Nihoyannopoulos, P., Parissis, J. T., Pieske, B., Riley, J. P., Rosano, G. M. C., Ruilope, L. M., Ruschitzka, F., Davies, C. (2016). 2016 ESC Guidelines for the diagnosis and treatment of acute and chronic heart failureThe Task Force for the diagnosis and treatment of acute and chronic heart failure of the European Society of Cardiology (ESC)Developed with the special contribution of the Heart Failure Association (HFA) of the ESC. *European Heart Journal*, *37*(27), 2129–2200. https://doi.org/10.1093/EURHEARTJ/EHW128

Potter, L. R., Yoder, A. R., Flora, D. R., Antos, L. K., & Dickey, D. M. (2009). *Natriuretic Peptides: Their Structures, Receptors, Physiologic Functions and Therapeutic Applications* (pp. 341–366). https://doi.org/10.1007/978-3-540-68964-5_15

Prondzynski, M., Berkson, P., Trembley, M. A., Tharani, Y., Shani, K., Bortolin, R. H., Sweat, M. E., Mayourian, J., Yucel, D., Cordoves, A. M., Gabbin, B., Hou, C., Anyanwu, N. J., Nawar, F., Cotton, J., Milosh, J., Walker, D., Zhang, Y., Lu, F., Pu, W. T. (2024). Efficient and reproducible generation of human iPSC-derived cardiomyocytes and cardiac organoids in stirred suspension systems. *Nature Communications*, 1–17. https://doi.org/10.1038/s41467-024-50224-0

Prondzynski, M., Lemoine, M. D., Zech, A. T., Horváth, A., Di Mauro, V., Koivumäki, J. T., Kresin, N., Busch, J., Krause, T., Krämer, E., Schlossarek, S., Spohn, M., Friedrich, F. W., Münch, J., Laufer, S. D., Redwood, C., Volk, A. E., Hansen, A., Mearini, G., Carrier, L. (2019). Disease modeling of a mutation in α-actinin 2 guides clinical therapy in hypertrophic cardiomyopathy. *EMBO Molecular Medicine*, *11*(12), 1–18. https://doi.org/10.15252/emmm.201911115

Querdel, E., Reinsch, M., Castro, L., Köse, D., Bähr, A., Reich, S., Geertz, B., Ulmer, B., Schulze, M., Lemoine, M. D., Krause, T., Lemme, M., Sani, J., Shibamiya, A., Stüdemann, T., Köhne, M., Bibra, C. von, Hornaschewitz, N., Pecha, S., Weinberger, F. (2021). Human Engineered Heart Tissue Patches Remuscularize the Injured Heart in a Dose-Dependent Manner. *Circulation*, *143*(20), 1991–2006. https://doi.org/10.1161/CIRCULATIONAHA.120.047904

Raabe, J., Lewandowski, V., Fuchs, S., Hammerschmidt, A., Piasecki, A., Orthey, E., Krämer, E., Ehler, E., & Cuello, F. (2025). Generation of a biallelic NRAP-knockout mutant from a human iPSC line. *Stem Cell Research*, *88*, 103829. https://doi.org/10.1016/j.scr.2025.103829

Rajamohan, D., Kalra, S., Duc Hoang, M., George, V., Staniforth, A., Russell, H., Yang, X., & Denning, C. (2016). Automated electrophysiological and pharmacological evaluation of human pluripotent stem cell-derived cardiomyocytes. *Stem Cells and Development*, *25*(6), 439–452. https://doi.org/10.1089/scd.2015.0253

Ramirez-Rios, S., Choi, S. R., Sanyal, C., Blum, T. B., Bosc, C., Krichen, F., Denarier, E., Soleilhac, J. M., Blot, B., Janke, C., Stoppin-Mellet, V., Magiera, M. M., Arnal, I., Steinmetz, M. O., & Moutin, M. J. (2023). VASH1–SVBP and VASH2–SVBP generate different detyrosination profiles on microtubules. *Journal of Cell Biology*, *222*(2). https://doi.org/10.1083/jcb.202205096

Ran, F. A., Hsu, P. D., Wright, J., Agarwala, V., Scott, D. A., & Zhang, F. (2013). Genome engineering using the CRISPR-Cas9 system. *Nature Protocols*, *8*(11), 2281–2308. https://doi.org/10.1038/nprot.2013.143

Ranek, M. J., Kokkonen-Simon, K. M., Chen, A., Dunkerly-Eyring, B. L., Vera, M. P., Oeing, C. U., Patel, C. H., Nakamura, T., Zhu, G., Bedja, D., Sasaki, M., Holewinski, R. J., Van Eyk, J. E., Powell, J. D., Lee, D. I., & Kass, D. A. (2019). PKG1-modified TSC2 regulates mTORC1 activity to counter adverse cardiac stress. *Nature*, *566*(7743), 264–269. https://doi.org/10.1038/s41586-019-0895-y

Rangrez, A. Y., Eden, M., Poyanmehr, R., Kuhn, C., Stiebeling, K., Dierck, F., Bernt, A., Lüllmann-Rauch, R., Weiler, H., Kirchof, P., Frank, D., & Frey, N. (2016). Myozap Deficiency Promotes Adverse Cardiac Remodeling via Differential Regulation of Mitogen-activated Protein Kinase/Serum-response Factor and β-Catenin/GSK-3β Protein Signaling. *Journal of Biological Chemistry*, *291*(8), 4128–4143. https://doi.org/10.1074/jbc.M115.689620

Rau, C. D., Romay, M. C., Tuteryan, M., Wang, J. J. C., Santolini, M., Ren, S., Karma, A., Weiss, J. N., Wang, Y., & Lusis, A. J. (2017). Systems Genetics Approach Identifies Gene Pathways and Adamts2 as Drivers of Isoproterenol-Induced Cardiac Hypertrophy and Cardiomyopathy in Mice. *Cell Systems*, *4*(1), 121-128.e4. https://doi.org/10.1016/j.cels.2016.10.016

Redwanz, C., Pires, R. H., Biedenweg, D., Groß, S., Otto, O., & Könemann, S. (2024). Endothelin-1 influences mechanical properties and contractility of hiPSC derived cardiomyocytes resulting in diastolic dysfunction. *Journal of Molecular and Cellular Cardiology*, *194*, 105–117. https://doi.org/10.1016/j.yjmcc.2024.07.004

Ribeiro, J. de S., & de Oliveira, M. L. C. (2022). Demographic and Epidemiological Profile of Aging and Elderly Patients Receiving Heart Transplant During the Period from 2009 to 2018. *International Journal of Cardiovascular Sciences*. https://doi.org/10.36660/ijcs.20210176

Rich, J. D., Burns, J., Freed, B. H., Maurer, M. S., Burkhoff, D., & Shah, S. J. (2018). Meta-Analysis Global Group in Chronic (MAGGIC) Heart Failure Risk Score: Validation of a Simple Tool for the Prediction of Morbidity and Mortality in Heart Failure With Preserved Ejection Fraction. *Journal of the American Heart Association*, *7*(20). https://doi.org/10.1161/JAHA.118.009594

Robison, P., Caporizzo, M. A., Ahmadzadeh, H., Bogush, A. I., Chen, C. Y., Margulies, K. B., Shenoy, V. B., & Prosser, B. L. (2016). Detyrosinated microtubules buckle and bear load in contracting cardiomyocytes. *Science (New York, N.Y.)*, *352*(6284). https://doi.org/10.1126/SCIENCE.AAF0659

Rockman, H. A., Ross, R. S., Harris, A. N., Knowlton, K. U., Steinhelper, M. E., Field, L. J., Ross, J., & Chien, K. R. (1991). Segregation of atrial-specific and inducible expression of an atrial natriuretic factor transgene in an in vivo murine model of cardiac hypertrophy. *Proceedings of the National Academy of Sciences*, *88*(18), 8277–8281. https://doi.org/10.1073/PNAS.88.18.8277

Roger, V. L. (2021). Epidemiology of Heart Failure: A Contemporary Perspective. *Circulation Research*, *128*(10), 1421–1434. https://doi.org/10.1161/CIRCRESAHA.121.318172

Roll-Mecak, A. (2020). The Tubulin Code in Microtubule Dynamics and Information Encoding.

Developmental Cell, *54*(1), 7–20. https://doi.org/10.1016/J.DEVCEL.2020.06.008

Rossignol, P., Hernandez, A. F., Solomon, S. D., & Zannad, F. (2019). Heart failure drug treatment. *The Lancet*, *393*(10175), 1034–1044. https://doi.org/10.1016/S0140-6736(18)31808-7

Saleem, U., Meer, B. J. V., Katili, P. A., Yusof, N. A. N. M., Mannhardt, I., Garcia, A. K., Tertoolen, L., Korte, T. De, Vlaming, M. L. H., McGlynn, K., Nebel, J., Bahinski, A., Harris, K., Rossman, E., Xu, X., Burton, F. L., Smith, G. L., Clements, P., Mummery, C. L., Denning, C. (2020). Blinded, Multicenter Evaluation of Drug-induced Changes in Contractility Using Human-induced Pluripotent Stem Cell-derived Cardiomyocytes. *Toxicological Sciences*, *176*(1), 103–123. https://doi.org/10.1093/toxsci/kfaa058

Salomon, A. K., Okami, N., Heffler, J., Lee, J.-J., Robinson, P., Bogush, A. I., & Prosser, B. L. (2021). Desmin intermediate filaments and tubulin detyrosination stabilize growing microtubules in the cardiomyocyte. *BioRxiv*, *3*(2), 6. https://doi.org/10.1007/s00395-022-00962-3

Samaras, S. E., Chen, B., Koch, S. R., Sawyer, D. B., Lim, C. C., & Davidson, J. M. (2012). 26S Proteasome regulation of Ankrd1/CARP in adult rat ventricular myocytes and human microvascular endothelial cells. *Biochemical and Biophysical Research Communications*, *425*(4), 830–835. https://doi.org/10.1016/j.bbrc.2012.07.162

Sanyal, C. (2024). *Understanding the functional interaction of VASH-SVBP with microtubules and their regulation by phosphorylation*.

Sanyal, C., Pietsch, N., Ramirez Rios, S., Peris, L., Carrier, L., & Moutin, M.-J. (2023). The detyrosination/re-tyrosination cycle of tubulin and its role and dysfunction in neurons and cardiomyocytes. *Seminars in Cell & Developmental Biology*, *137*, 46–62. https://doi.org/10.1016/j.semcdb.2021.12.006

Saroj, N., Dholaniya, P. S., Alvi, S. B., Sridharan, D., Soni, N., Ashraf, S. A., Choudhry, A., Ashraf, Y. A., Mikula, S. K., Singla, D. K., & Khan, M. (2025). SiRNA-mediated knockdown of TOP2B protects hiPSC-derived cardiomyocytes from doxorubicin-induced toxicity. *Life Sciences*, *371*(March), 123595. https://doi.org/10.1016/j.lfs.2025.123595

Savarese, G., Stolfo, D., Sinagra, G., & Lund, L. H. (2022). Heart failure with mid-range or mildly reduced ejection fraction. *Nature Reviews Cardiology*, *19*(2), 100–116. https://doi.org/10.1038/s41569-021-00605-5

Scarborough, E. A., Uchida, K., Vogel, M., Erlitzki, N., Iyer, M., Phyo, S. A., Bogush, A., Kehat, I., & Prosser, B. L. (2021). Microtubules orchestrate local translation to enable cardiac growth. *Nature Communications*, *12*(1). https://doi.org/10.1038/s41467-021-21685-4

Schaaf, S., Shibamiya, A., Mewe, M., Eder, A., Stöhr, A., Hirt, M. N., Rau, T., Zimmermann, W. H., Conradi, L., Eschenhagen, T., & Hansen, A. (2011). Human engineered heart tissue as a versatile tool in basic research and preclinical toxicology. *PloS One*, *6*(10). https://doi.org/10.1371/JOURNAL.PONE.0026397

Schlossarek, S., & Carrier, L. (2011). The ubiquitin-proteasome system in cardiomyopathies. *Current Opinion in Cardiology*, *26*(3), 190–195. https://doi.org/10.1097/HCO.0b013e32834598fe

Schuldt, M., Pei, J., Harakalova, M., Dorsch, L. M., Schlossarek, S., Mokry, M., Knol, J. C., Pham, T. V., Schelfhorst, T., Piersma, S. R., dos Remedios, C., Dalinghaus, M., Michels, M., Asselbergs, F. W., Moutin, M.-J. J., Carrier, L., Jimenez, C. R., Van Der Velden, J., & Kuster, D. W. D. (2021). Proteomic and Functional Studies Reveal Detyrosinated Tubulin as Treatment Target in Sarcomere Mutation-Induced Hypertrophic Cardiomyopathy. *Circulation: Heart Failure*, *14*(1). https://doi.org/10.1161/CIRCHEARTFAILURE.120.007022

Schulz, C., Lemoine, M. D., Mearini, G., Koivumäki, J., Sani, J., Schwedhelm, E., Kirchhof, P., Ghalawinji, A., Stoll, M., Hansen, A., Eschenhagen, T., & Christ, T. (2023). PITX2 Knockout Induces Key Findings of Electrical Remodeling as Seen in Persistent Atrial Fibrillation. *Circulation: Arrhythmia and Electrophysiology*, *16*(3). https://doi.org/10.1161/CIRCEP.122.011602

Schwaerzer, G. K., Casteel, D. E., Cividini, F., Kalyanaraman, H., Zhuang, S., Gu, Y., Dalton, N. D., Kirk, |, Peterson, L., Dillmann, W. H., Boss, G. R., & Pilz, R. B. (2021). *Constitutive* *protein kinase G activation exacerbates stress-induced cardiomyopathy*. https://doi.org/10.1111/bph.v179.11/issuetoc

Seferović, P. M., Polovina, M., Bauersachs, J., Arad, M., Ben Gal, T., Lund, L. H., Felix, S. B., Arbustini, E., Caforio, A. L. P., Farmakis, D., Filippatos, G. S., Gialafos, E., Kanjuh, V., Krljanac, G., Limongelli, G., Linhart, A., Lyon, A. R., Maksimović, R., Miličić, D., Tschöpe, C. (2019). Heart failure in cardiomyopathies: a position paper from the Heart Failure Association of the European Society of Cardiology. *European Journal of Heart Failure*, *21*(5), 553–576. https://doi.org/10.1002/ejhf.1461

Sellak, H., Choi, C. -s., Dey, N. B., & Lincoln, T. M. (2013). Transcriptional and post-transcriptional regulation of cGMP-dependent protein kinase (PKG-I): pathophysiological significance. *Cardiovascular Research*, *97*(2), 200–207. https://doi.org/10.1093/cvr/cvs327

Shahim, A., Linde, C., Savarese, G., Dahlström, U., Lund, L. H., & Hage, C. (2025). Implementation of guideline-recommended therapies in heart failure with reduced ejection fraction according to heart failure duration: An analysis of 55 581 patients from the Swedish Heart Failure (SwedeHF) Registry. *European Journal of Heart Failure*, *27*(3), 421–431. https://doi.org/10.1002/ejhf.3565

Sharma, A., Sances, S., Workman, M. J., & Svendsen, C. N. (2020). Multi-lineage Human iPSC-Derived Platforms for Disease Modeling and Drug Discovery. *Cell Stem Cell*, *26*(3), 309–329. https://doi.org/10.1016/j.stem.2020.02.011

Sharma, R., Kim, J. J., Qin, L., Henning, P., Akimoto, M., Vanschouwen, B., Kaur, G., Sankaran, B., Mackenzie, K. R., Melacini, G., Casteel, D. E., Herberg, F. W., & Kim, C. (2022). An auto-inhibited state of protein kinase G and implications for selectiveactivation. *ELife*, *11*, 1–25. https://doi.org/10.7554/eLife.79530

Shehata, N., Srikantharajah, R., Baier, E., Manthey, C., Stüdemann, T., Nehring, M., Covic, A., Müller, C., Siebels, B., Nissen, P., Witten, A., Castellano, M. Z., Rodriguez, Y., Gomez, L. Z., Janssen, I., Rodriguez, J., Enriquez, A. G., Romero, M. A. G., Di Mattia, R., … Weinberger, F. (2025). *Contractility governs cardiomyocyte cell cycle activity*. https://doi.org/10.1101/2025.08.19.671096

Shigematsu, H., Imasaki, T., Doki, C., Sumi, T., Aoki, M., Uchikubo-Kamo, T., Sakamoto, A., Tokuraku, K., Shirouzu, M., & Nitta, R. (2018). Structural insight into microtubule stabilization and kinesin inhibition by Tau family MAPs. *Journal of Cell Biology*, *217*(12), 4155–4163. https://doi.org/10.1083/jcb.201711182

Singh, R., Kuscu, C., Quinlan, A., Qi, Y., & Adli, M. (2015). Cas9-chromatin binding information enables more accurate CRISPR off-target prediction. *Nucleic Acids Research*, *43*(18), 1–8. https://doi.org/10.1093/nar/gkv575

Singh, S. R., Meyer-Jens, M., Alizoti, E., Bacon, W. C., Davis, G., Osinska, H., Gulick, J., Reischmann-Düsener, S., Orthey, E., McLendon, P. M., Molkentin, J. D., Schlossarek, S., Robbins, J., & Carrier, L. (2021). A high-throughput screening identifies ZNF418 as a novel regulator of the ubiquitin-proteasome system and autophagy-lysosomal pathway. *Autophagy*, *17*(10), 3124–3139. https://doi.org/10.1080/15548627.2020.1856493

Skultetyova, L., Ustinova, K., Kutil, Z., Novakova, Z., Pavlicek, J., Mikesova, J., Trapl, D., Baranova, P., Havlinova, B., Hubalek, M., Lansky, Z., & Barinka, C. (2017). Human histone deacetylase 6 shows strong preference for tubulin dimers over assembled microtubules. *Scientific Reports*, *7*(1), 11547. https://doi.org/10.1038/s41598-017-11739-3

Solomon, S. D., Vaduganathan, M., L. Claggett, B., Packer, M., Zile, M., Swedberg, K., Rouleau, J., A. Pfeffer, M., Desai, A., H. Lund, L., Kober, L., Anand, I., Sweitzer, N., Linssen, G., Merkely, B., Luis Arango, J., Vinereanu, D., Chen, C. H., Senni, M., McMurray, J. J. V. (2020). Sacubitril/Valsartan across the Spectrum of Ejection Fraction in Heart Failure. *Circulation*, 352–361. https://doi.org/10.1161/CIRCULATIONAHA.119.044586

Solomon, S. D., Zile, M., Pieske, B., Voors, A., Shah, A., Kraigher-Krainer, E., Shi, V., Bransford, T., Takeuchi, M., Gong, J., Lefkowitz, M., Packer, M., & McMurray, J. J. (2012). The angiotensin receptor neprilysin inhibitor LCZ696 in heart failure with preserved ejection fraction: A phase 2 double-blind randomised controlled trial. *The Lancet*, *380*(9851), 1387–1395. https://doi.org/10.1016/S0140-6736(12)61227-6

Souphron, J., Bodakuntla, S., Jijumon, A. S., Lakisic, G., Gautreau, A. M., Janke, C., & Magiera, M. M. (2024). Purification of tubulin with controlled post-translational modifications by polymerization–depolymerization cycles. *Nature Protocols*. https://doi.org/10.1038/s41596-024-01127-3

Sprenger, J. U., Bork, N. I., Herting, J., Fischer, T. H., & Nikolaev, V. O. (2016). Interactions of Calcium Fluctuations during Cardiomyocyte Contraction with Real-Time cAMP Dynamics Detected by FRET. *PLOS ONE*, *11*(12), e0167974. https://doi.org/10.1371/journal.pone.0167974

Srivastava, P. K., Hsu, J. J., Ziaeian, B., & Fonarow, G. C. (2020). Heart Failure With Mid-range Ejection Fraction. *Current Heart Failure Reports*, *17*(1), 1–8. https://doi.org/10.1007/s11897-019-00451-0

Stüdemann, T., Rössinger, J., Manthey, C., Geertz, B., Srikantharajah, R., von Bibra, C., Shibamiya, A., Köhne, M., Wiehler, A., Wiegert, J. S., Eschenhagen, T., & Weinberger, F. (2022). Contractile Force of Transplanted Cardiomyocytes Actively Supports Heart Function After Injury. *Circulation*, *146*(15), 1159–1169. https://doi.org/10.1161/CIRCULATIONAHA.122.060124

Stuehr, D. J., Misra, S., Dai, Y., & Ghosh, A. (2021). Maturation, inactivation, and recovery mechanisms of soluble guanylyl cyclase. *Journal of Biological Chemistry*, *296*, 100336. https://doi.org/10.1016/J.JBC.2021.100336

Swiss Institute of Bioinformatics, Novo Nordisk Foundation Center Protein Research, & European Molecular Biology Laboratory. (n.d.). *String Multiple Protein Search*. https://string-db.org/cgi/input?sessionId=blyLqWR7iMgo&input_page_active_form=multiple_identifiers

Szyk, A., Deaconescu, A. M., Piszczek, G., & Roll-Mecak, A. (2011). Tubulin tyrosine ligase structure reveals adaptation of an ancient fold to bind and modify tubulin. *Nature Structural & Molecular Biology*, *18*(11), 1250–1258. https://doi.org/10.1038/nsmb.2148

Takahashi, K., Tanabe, K., Ohnuki, M., Narita, M., Ichisaka, T., Tomoda, K., & Yamanaka, S. (2007). Induction of Pluripotent Stem Cells from Adult Human Fibroblasts by Defined Factors. *Cell*, *131*(5), 861–872. https://doi.org/10.1016/j.cell.2007.11.019

Takahashi, K., & Yamanaka, S. (2006). Induction of Pluripotent Stem Cells from Mouse Embryonic and Adult Fibroblast Cultures by Defined Factors. *Cell*, *126*(4), 663–676. https://doi.org/10.1016/j.cell.2006.07.024

Takimoto, E., & Kass, D. A. (2007). Role of Oxidative Stress in Cardiac Hypertrophy and Remodeling. *Hypertension*, *49*(2), 241–248. https://doi.org/10.1161/01.HYP.0000254415.31362.a7

Tanaka, Y., Kadota, S., Zhao, J., Kobayashi, H., Okano, S., Izumi, M., Honda, Y., Ichimura, H., Shiba, N., Uemura, T., Wada, Y., Chuma, S., Nakada, T., Tohyama, S., Fukuda, K., Yamada, M., Seto, T., Kuwahara, K., & Shiba, Y. (2023). Mature human induced pluripotent stem cell-derived cardiomyocytes promote angiogenesis through alpha-B crystallin. *Stem Cell Research and Therapy*, *14*(1), 1–20. https://doi.org/10.1186/s13287-023-03468-4

Tang, Q., Sensale, S., Bond, C., Arab, A., Tang, Q., Sensale, S., Bond, C., Xing, J., Qiao, A., Hugelier, S., & Arab, A. (2023). Interplay between stochastic enzyme activity and microtubule stability drives detyrosination enrichment on microtubule subsets Article Interplay between stochastic enzyme activity and microtubule stability drives detyrosination enrichment on micro. *Current Biology*, 1–16. https://doi.org/10.1016/j.cub.2023.10.068

Tcheudji, J. F. K., Lebeau, L., Virmaux, N., Maftei, C. G., Cote, R. H., Lugnier, C., & Schultz, P. (2001). Molecular organization of bovine rod cGMP-phosphodiesterase 6. *Journal of Molecular Biology*, *310*(4), 781–791. https://doi.org/10.1006/jmbi.2001.4813

Thakur, S., Mohanty, P., Jadhav, M. S., Gaikwad, A. B., & Jadhav, H. R. (2024). A perspective on the development of small molecular neprilysin inhibitors (NEPi) with emphasis on cardiorenal disease. *European Journal of Medicinal Chemistry*, *280*, 116932. https://doi.org/10.1016/j.ejmech.2024.116932

Thunemann, M., Schmidt, K., de Wit, C., Han, X., Jain, R. K., Fukumura, D. D., & Feil, R. (2014). Correlative intravital imaging of cGMP signals and vasodilation in mice. *Frontiers in Physiology*, *5*(OCT), 1–15. https://doi.org/10.3389/fphys.2014.00394

Thürmann, P. A., Kenedi, ; Peter, Schmidt, A., Harder, S., & Rietbrock, N. (1998). *Influence of the Angiotensin II Antagonist Valsartan on Left Ventricular Hypertrophy in Patients With Essential Hypertension*. http://www.circulationaha.org

Trivedi, N., Marsh, P., Goold, R. G., Wood-Kaczmar, A., & Gordon-Weeks, P. R. (2005). Glycogen synthase kinase-3β phosphorylation of MAP1B at Ser1260 and Thr1265 is spatially restricted to growing axons. *Journal of Cell Science*, *118*(5), 993–1005. https://doi.org/10.1242/jcs.01697

Uchida, K., Scarborough, E. A., & Prosser, B. L. (2021). *Cardiomyocyte Microtubules: Control of Mechanics, Transport, and Remodeling. Annual Review of Physiology and Remodeling*. https://doi.org/10.1146/annurev-physiol-062421

Uniprot. (2025). *PRKG1 Uniprot*. https://www.uniprot.org/uniprotkb/Q13976/entry

Vaittinen, S., Lukka, R., Sahlgren, C., Rantanen, J., Hurme, T., Lendahl, U., Eriksson, J. E., & Kalimo, H. (1999). Specific and innervation-regulated expression of the intermediate filament protein nestin at neuromuscular and myotendinous junctions in skeletal muscle. *American Journal of Pathology*, *154*(2), 591–600. https://doi.org/10.1016/S0002-9440(10)65304-7

Vakulskas, C. A., & Behlke, M. A. (2019). Evaluation and reduction of crispr off-target cleavage events. *Nucleic Acid Therapeutics*, *29*(4), 167–174. https://doi.org/10.1089/nat.2019.0790

Valtcheva, N., Nestorov, P., Beck, A., Russwurm, M., Hillenbrand, M., Weinmeister, P., & Feil, R. (2009). The commonly used cGMP-dependent protein kinase type i (cGKI) inhibitor Rp-8-Br-PET-cGMPS can activate cGKI in vitro and in intact cells. *Journal of Biological Chemistry*, *284*(1), 556–562. https://doi.org/10.1074/jbc.M806161200

Van Der Velden, J., Asselbergs, F. W., Bakkers, J., Batkai, S., Bertrand, L., Bezzina, C. R., Bot, I., Brundel, B. J. J. M., Carrier, L., Chamuleau, S., Ciccarelli, M., Dawson, D., Davidson, S. M., Dendorfer, A., Duncker, D. J., Eschenhagen, T., Fabritz, L., Falc, I., Hilfiker-kleiner, D., Vlasman, P. (2022). *Animal models and animal-free innovations for cardiovascular research : current status and routes to be explored . Consensus document of the ESC Working Group on Myocardial Function and the ESC Working Group on Cellular Biology of the Heart*. *0031*, 1–36.

Vaskova, E., Ikeda, G., Tada, Y., Wahlquist, C., Mercola, M., & Yang, P. C. (2020). Sacubitril/valsartan improves cardiac function and decreases myocardial fibrosis via downregulation of exosomal mir-181a in a rodent chronic myocardial infarction model. *Journal of the American Heart Association*, *9*(13). https://doi.org/10.1161/JAHA.119.015640

Vite, A., Caporizzo, M. A., Corbin, E. A., Brandimarto, J., McAfee, Q., Livingston, C. E., Prosser, B. L., & Margulies, K. B. (2022). Extracellular stiffness induces contractile dysfunction in adult cardiomyocytes via cell-autonomous and microtubule-dependent mechanisms. *Basic Research in Cardiology*, *117*(1), 41. https://doi.org/10.1007/s00395-022-00952-5

Wang, F., Gao, L., Fu, X., Yan, Q., Hu, L., & Mao, J. (2023). Comparison of Two Representative Methods for Differentiation of Human Induced Pluripotent Stem Cells into Mesenchymal Stromal Cells. *Journal of Visualized Experiments*, *200*. https://doi.org/10.3791/65729

Wang, Q., Lin, J. L. C., Erives, A. J., Lin, C. I., & Lin, J. J. C. (2014). New insights into the roles of xin repeat-containing proteins in cardiac development, function, and disease. In *International Review of Cell and Molecular Biology* (Vol. 310). https://doi.org/10.1016/B978-0-12-800180-6.00003-7

Wang, Q., Lin, J. L. C., Wu, K. H., Wang, D. Z., Reiter, R. S., Sinn, H. W., Lin, C. I., & Lin, J. J. C. (2012). Xin proteins and intercalated disc maturation, signaling and diseases.

Frontiers in Bioscience (Landmark Edition), *17*(7), 2566–2593. https://doi.org/10.2741/4072

Warnecke, N., Ulmer, B. M., Laufer, S. D., Shibamiya, A., Krämer, E., Neuber, C., Hanke, S., Behrens, C., Loos, M., Münch, J., Kühnisch, J., Klaassen, S., Eschenhagen, T., Patten-Hamel, M., Carrier, L., & Mearini, G. (2021). Generation of bi-allelic MYBPC3 truncating mutant and isogenic control from an iPSC line of a patient with hypertrophic cardiomyopathy. *Stem Cell Research*, *55*. https://doi.org/10.1016/J.SCR.2021.102489

Wehland, J., Schröder, H. C., & Weber, K. (1986). *Isolation and purification of tubulin tyrosine ligase* (pp. 170–179). https://doi.org/10.1016/0076-6879(86)34086-2

Westermann, L., Li, Y., Göcmen, B., Niedermoser, M., Rhein, K., Jahn, J., Cascante, I., Schöler, F., Moser, N., Neubauer, B., Hofherr, A., Behrens, Y. L., Göhring, G., Köttgen, A., Köttgen, M., & Busch, T. (2022). Wildtype heterogeneity contributes to clonal variability in genome edited cells. *Scientific Reports*, *12*(1), 18211. https://doi.org/10.1038/s41598-022-22885-8

Wloga, D., Joachimiak, E., Louka, P., & Gaertig, J. (2017). Posttranslational Modifications of Tubulin and Cilia. *Cold Spring Harbor Perspectives in Biology*, *9*(6), a028159. https://doi.org/10.1101/cshperspect.a028159

Wrona, K. M., Albert, A. M. M., Eckardt, D., Herbel, C., Krause, J., Starbatty, J., Hemkemeyer, S. A. A., Frye, M., Cuello, F., Eschenhagen, T., & Hirt, M. N. (2022). Abstract 13973: Human iPSC-Derived Multi-Cell-Type Engineered Heart Tissues as an in vitro Model to Study Pathological Cardiac Hypertrophy. *Circulation*, *146*(Suppl_1). https://doi.org/10.1161/circ.146.suppl_1.13973

Wrona, K. M., Krause, J., Starbatty, J., Cuello, F., Eschenhagen, T., & Hirt, M. N. (2022). Human iPSC-derived multi-cell-type engineered heart tissues as an advanced model for pathological hypertrophy. *Journal of Molecular and Cellular Cardiology*, *173*, S176–S177. https://doi.org/10.1016/j.yjmcc.2022.08.337

Xia, C., Nguyen, M., Garrison, A. K., Zhao, Z., Wang, Z., Sutherland, C., & Ma, L. (2013). CNP/cGMP signaling regulates axon branching and growth by modulating microtubule polymerization. *Developmental Neurobiology*, *73*(9), 673–687. https://doi.org/10.1002/dneu.22078

Xu, H., Zhu, L., Wang, Y., & Bao, Y. (2018). Effect of Exogenous Alpha-B Crystallin on the Structures and Functions of Trabecular Meshwork Cells. *Journal of Ophthalmology*, *2018*, 1–8. https://doi.org/10.1155/2018/7875318

Xu, Z., Schaedel, L., Portran, D., Aguilar, A., Gaillard, J., Peter Marinkovich, M., Théry, M., & Nachury, M. V. (2017). Microtubules acquire resistance from mechanical breakage through intralumenal acetylation. *Science*, *356*(6335), 328–332. https://doi.org/10.1126/science.aai8764

Yan, X., Hoek, T. A., Vale, R. D., & Tanenbaum, M. E. (2016). Dynamics of Translation of Single mRNA Molecules in Vivo. *Cell*, *165*(4), 976–989. https://doi.org/10.1016/j.cell.2016.04.034

Yang, D., Xi, J., Xing, Y., Tang, X., Dai, X., Li, K., Li, H., Lv, X., Lu, D., & Wang, H. (2018). A new method for neonatal rat ventricular myocyte purification using superparamagnetic iron oxide particles. *International Journal of Cardiology*, *270*, 293–301. https://doi.org/10.1016/j.ijcard.2018.05.133

Yang, X., Rodriguez, M. L., Leonard, A., Sun, L., Fischer, K. A., Wang, Y., Ritterhoff, J., Zhao, L., Kolwicz, S. C., Pabon, L., Reinecke, H., Sniadecki, N. J., Tian, R., Ruohola-Baker, H., Xu, H., & Murry, C. E. (2019). Fatty Acids Enhance the Maturation of Cardiomyocytes Derived from Human Pluripotent Stem Cells. *Stem Cell Reports*, *13*(4), 657–668. https://doi.org/10.1016/j.stemcr.2019.08.013

Yu, J., Vodyanik, M. A., Smuga-Otto, K., Antosiewicz-Bourget, J., Frane, J. L., Tian, S., Nie, J., Jonsdottir, G. A., Ruotti, V., Stewart, R., Slukvin, I. I., & Thomson, J. A. (2007). Induced Pluripotent Stem Cell Lines Derived from Human Somatic Cells. *Science*, *318*(5858), 1917–1920. https://doi.org/10.1126/science.1151526

Zech, A. T. L., Prondzynski, M., Singh, S. R., Pietsch, N., Orthey, E., Alizoti, E., Busch, J., Madsen, A., Behrens, C. S., Meyer-Jens, M., Mearini, G., Lemoine, M. D., Krämer, E., Mosqueira, D., Virdi, S., Indenbirken, D., Depke, M., Salazar, M. G., Völker, U., … Carrier, L. (2022). ACTN2 Mutant Causes Proteopathy in Human iPSC-Derived Cardiomyocytes. *Cells*, *11*(17), 1–17. https://doi.org/10.3390/cells11172745

Zhang, J., Klos, M., Wilson, G. F., Herman, A. M., Lian, X., Raval, K. K., Barron, M. R., Hou, L., Soerens, A. G., Yu, J., Palecek, S. P., Lyons, G. E., Thomson, J. A., Herron, T. J., Jalife, J., & Kamp, T. J. (2012). Extracellular matrix promotes highly efficient cardiac differentiation of human pluripotent stem cells: The matrix sandwich method. *Circulation Research*, *111*(9), 1125–1136. https://doi.org/10.1161/CIRCRESAHA.112.273144

Zhang, R., Qu, Y., Ji, Z., Hao, C., Su, Y., Yao, Y., Zuo, W., Chen, X., Yang, M., & Ma, G. (2022). METTL3 mediates Ang-II-induced cardiac hypertrophy through accelerating pri-miR-221/222 maturation in an m6A-dependent manner. *Cellular & Molecular Biology Letters*, *27*(1), 55. https://doi.org/10.1186/s11658-022-00349-1

Zhang, X., Li, Z. L., Crane, J. A., Jordan, K. L., Pawar, A. S., Textor, S. C., Lerman, A., & Lerman, L. O. (2014). Valsartan regulates myocardial autophagy and mitochondrial turnover in experimental hypertension. *Hypertension*, *64*(1), 87–93. https://doi.org/10.1161/HYPERTENSIONAHA.113.02151

Zhang, Z., Xu, K., Ji, L., Zhang, H., Yin, J., Zhou, M., Wang, C., & Yang, S. (2023). A novel loss-of-function mutation in NRAP is associated with left ventricular non-compaction cardiomyopathy. *Frontiers in Cardiovascular Medicine*, *10*. https://doi.org/10.3389/fcvm.2023.1097957

Zhao, X., Zhou, L., Li, X., Ni, J., Chen, P., Ma, R., Wu, J., & Feng, J. (2018). Overexpression of KIF20A confers malignant phenotype of lung adenocarcinoma by promoting cell proliferation and inhibiting apoptosis. *Cancer Medicine*, *7*(9), 4678–4689. https://doi.org/10.1002/cam4.1710

Zhong, J., Basu, R., Guo, D., Chow, F. L., Byrns, S., Schuster, M., Loibner, H., Wang, X., Penninger, J. M., Kassiri, Z., & Oudit, G. Y. (2010). Angiotensin-Converting Enzyme 2 Suppresses Pathological Hypertrophy, Myocardial Fibrosis, and Cardiac Dysfunction. *Circulation*, *122*(7), 717–728. https://doi.org/10.1161/CIRCULATIONAHA.110.955369

Zhou, Z., Hughes, K., Saif, N., Kim, H., Massett, M. P., Zheng, M., Cecchi, A. C., Guo, D., Murdock, D. R., Pan, P., Clinton, J. S., Wang, J., Greally, J. M., & Milewicz, D. M. (2024). *MYH11 rare variant augments aortic growth and induces cardiac hypertrophy and heart failure with pressure overload*. https://doi.org/10.1101/2024.08.15.608063

Eidesstattliche Versicherung/Affadavit

Hiermit versichere ich an Eides statt, die vorliegende Dissertationsschrift selbst verfasst und keine anderen als die angegebenen Hilfsmittel und Quellen benutzt zu haben. Sofern im Zuge der Erstellung der vorliegenden Dissertationsschrift generative Künstliche Intelligenz (gKI) basierte elektronische Hilfsmittel verwendet wurden, versichere ich, dass meine eigene Leistung im Vordergrund stand und dass eine vollständige Dokumentation aller verwendeten Hilfsmittel gemäß der Guten wissenschaftlichen Praxis vorliegt. Ich trage die Verantwortung für eventuell durch die gKI generierte fehlerhafte oder verzerrte Inhalte, fehlerhafte Referenzen, Verstöße gegen das Datenschutz- und Urheberrecht oder Plagiate.

I hereby declare and affirm that this doctoral dissertation is my own work and that I have not used any aids and sources other than those indicated. If electronic resources based on generative artificial intelligence (gAI) were used in the course of writing this dissertation, I confirm that my own work was the main and value-adding contribution and that complete documentation of all resources used is available in accordance with good scientific practice. I am responsible for any erroneous or distorted content, incorrect references, violations of data protection and copyright law or plagiarism that may have been generated by the gAI.

Hamburg den 24.05.2026

Moritz Meyer-Jens

Erklärung zur Druckfassung

Ich versichere, dass das in elektronischer Form eingereichte Dissertationsexemplar (über den Docata-Upload) und das bei der Fakultät (zuständiges Studienbüro bzw. Promotionsbüro Physik) zur Archivierung eingereichte gedruckte gebundene Exemplar der Dissertationsschrift identisch sind.

I, the undersigned, declare that the dissertation submitted in electronic form (via the Docata upload) and the printed bound copy of the dissertation submitted to the faculty (responsible Academic Office or the Doctoral Office Physics) for archiving are identical.

Hamburg den 24.05.2026

Moritz Meyer-Jens